Lasers in Manufacturing

Lasers in Manufacturing

Edited by
J. Paulo Davim

ISTE WILEY

First published 2012 in Great Britain and the United States by ISTE Ltd and John Wiley & Sons, Inc.

ISTE Ltd
27-37 St George's Road
London SW19 4EU
UK

www.iste.co.uk

John Wiley & Sons, Inc.
111 River Street
Hoboken, NJ 07030
USA

www.wiley.com

Library of Congress Cataloging-in-Publication Data

Lasers in manufacturing / edited by J. Paulo Davim.
p. cm.
Includes bibliographical references and index.
ISBN 978-1-84821-369-2
1. Lasers--Industrial applications. I. Davim, J. Paulo.
TA1675.L374 2012
621.36'6--dc23

2012003364

British Library Cataloguing-in-Publication Data
A CIP record for this book is available from the British Library
ISBN: 978-1-84821-369-2

Printed and bound in Great Britain by CPI Group (UK) Ltd., Croydon, Surrey CR0 4YY

Table of Contents

Preface

Generally LASER (light amplification by stimulated emission of radiation) is defined as "*a device which uses a quantum mechanical effect, stimulated emission, to generate a coherent beam of light from a lasing medium of controlled purity, size, and shape*". Laser material processing represents a great number of methods, which are rapidly growing in current and different industrial applications as new alternatives to traditional manufacturing processes. Nowadays, the use of lasers in manufacturing is an emerging field with a wide variety of applications, for example, in electronics, molds and dies and biomedical applications.

The purpose of this book is to present a collection of examples illustrating the state-of-the-art and research developments relating to lasers in manufacturing. Chapter 1 presents laser rapid manufacturing. Chapter 2 discusses lasers in metal forming applications. Chapter 3 contains information on laser forming of metal foams. Chapter 4 is dedicated to mathematical modeling of laser drilling. Chapter 5 presents laser cutting of a small diameter hole (thermal stress analysis). Chapter 6 covers modeling and simulation of laser welding. Finally, Chapter 7 presents lasers in surface engineering.

The present book can be used as a research tool for a final undergraduate engineering course (for example, mechanical, manufacturing, materials; physics, etc) or for a subject on laser in manufacturing at the postgraduate level. This book can also serve as a useful reference for academics, laser researchers, mechanical, manufacturing, materials, physics engineers and professionals familiar with modern manufacturing technology. The interest of this book is evident for many important centers of the research, laboratories and universities throughout the world. Therefore, it is hoped that this book will encourage and enthuse other researchers in this important field of science and engineering.

As the Editor I would like to acknowledge my gratitude to ISTE for this opportunity and for their professional support. Finally, I would like to thank all the chapter authors for dedicating time to working on this project.

J. Paulo DAVIM
Aveiro, Portugal
February 2012

Chapter 1

Laser Rapid Manufacturing: Technology, Applications, Modeling and Future Prospects

This chapter deals with the various aspects of laser rapid manufacturing (LRM) and provides an insight into the underlying basic principles and applications of this revolutionizing laser based manufacturing technology. The details of the LRM system, relevant processing parameters, process modeling, control systems and future prospects of LRM are presented and discussed.

1.1. Introduction

Theodore H. Maiman, the inventor of the first working laser, described it as "a solution looking for a problem" because few appreciated its manifold potential applications [EVA 04]. However, the scenario after a journey of five decades is vivid and today lasers find applications in everyday life.

Due to unique properties, lasers have established themselves from "a solution looking for a problem" to "a solution for many problems". The field of manufacturing has also not been left untouched. As lasers can heat, melt and vaporize any material, they are exploited in manufacturing for cutting, welding, surface hardening, cladding, alloying, peening and additive manufacturing.

Chapter written by Christ P. PAUL, Pankaj BHARGAVA, Atul KUMAR, Ayukt K. PATHAK and Lalit M. KUKREJA.

Lasers in Manufacturing Edited by J. Paulo Davim

In 1986, lasers stepped into the arena of additive manufacturing with the invention of stereolithography – the first additive manufacturing process by Chuck Hull [CHU 86]. In this process, a UV laser beam is scanned on the surface of a liquid UV-curable photopolymer "resin" to selectively cure and form a cross-section of an indented object. A number of cross-sections are thus formed one over another to shape the whole object. This evolved the concept of additive manufacturing into a rapid prototyping process. Soon after the invention of stereolithography, the laser was deployed in "selective laser sintering" to fuse the polymer/polymer coated metal powders to shape the prototype components [DEC 89].

The subsequent advances in the field of high power lasers, computer aided design and manufacturing (CAD/CAM), powder metallurgy and allied electronics translated the rapid prototyping into 3D metallic components for various engineering applications [KRE 95].

Moreover, the paradigm shift in global economics, from a seller's market to a buyer's market, challenged industries for the immediate delivery of the best quality product with all possible features at the lowest possible price in order to ensure survival [CHI 11]. This propelled research and development in the area of rapid manufacturing at various renowned universities and national laboratories. In this growing list of rapid manufacturing, laser rapid manufacturing (LRM) is one of the leading manufacturing techniques.

1.2. Laser rapid manufacturing

LRM is one of the advanced additive manufacturing processes that is capable of fabricating engineering components directly from a solid model. In this technique, a solid model of the component to be fabricated is made either by a 3D imaging system, a designer using computer aided design (CAD) software or by math data as an output of numerical analysis. The model obtained thus is sliced into thin layers along the vertical axis. The thin layers are converted into corresponding numerical controlled (NC) code and are sent to a LRM station in a suitable format (e.g. G&M code).

A LRM station employs a laser beam as a heat source to melt a thin layer onto the surface of the substrate/deposited material and fed material to deposit a new layer as per the shape and dimensions defined in NC code. A number of such layers deposited one over another result in 3D components directly from the solid model. Figure 1.1 presents the general scheme of the LRM technique.

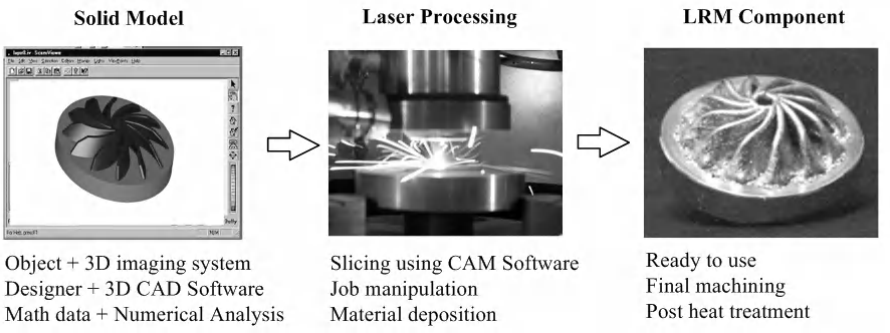

Figure 1.1. *General scheme of LRM*

LRM eliminates many manufacturing steps such as materials-machine planning, man-machine interaction, intermittent quality checks, assembly and related human errors, etc. Therefore, LRM offers many advantages over conventional subtractive techniques, such as reduced production time, better process control and the capability to form functionally graded parts. It is also an attractive candidate for refurbishing applications because of the low heat input, limited dilution with minimal distortion and capability of adding finer near-net shaped features to the components.

Manufacturing techniques, similar to LRM, are being developed with different names at various laboratories around the world. At Sandia National Laboratory, USA, laser engineered net shaping (LENS^{TM}) is being developed with the prime focus on creating complex metal parts in a single day [SAN 10]. The National Research Council, Canada is developing freeform laser consolidation for manufacturing structural components for advanced robotic mechatronic systems [XUE 01].

Automated laser fabrication (ALFa) is being developed, at the University of Waterloo, Canada, to produce low cost tungsten carbide components [PAU 08]. Selective laser cladding (SLC) at the University of Liverpool, UK and direct metal deposition at the University of Michigan, USA are being used to deposit critical surfaces on prime components [DAV 06, HE 10]. Laser powder deposition (LPD) at the University of Manchester UK and direct metal deposition/laser additive manufacturing at Fraunhofer Institute, Germany are being augmented for the fabrication of high performance materials [MOA 09]. Researchers at Tsinghua University, China, are working on diverse area and evaluating the technology for the potential development of graded Ti alloys for aeronautical applications, nickel alloys for power plants and various *in situ* repair applications [ZHO 10]. Thus, the ongoing global research is spearheading towards the deployment of this novel fabrication

technology for improving the quality of the products, the possibility of engineer integrated multi-materials and multi-functional components and enhancing economic or procedural benefits.

1.3. Laser rapid manufacturing system

A LRM system consists of the following three primary subsystems:

a) a high power laser system;

b) a material feeding system;

c) a computerized numerically controlled (CNC) workstation.

Figure 1.2 presents the various options used for primary LRM subsystems.

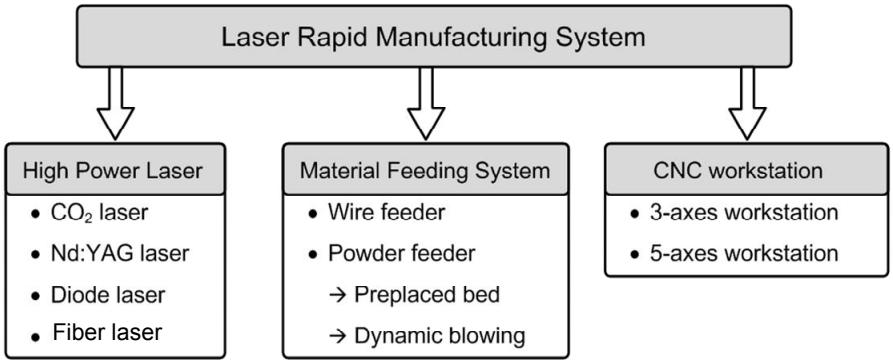

Figure 1.2. *Primary subsystems of a LRM system*

1.3.1. *High power laser system*

In LRM, a high power laser system is used as a heat source to melt a thin layer of substrate/previously deposited layer and fed material. CO_2 laser, Nd:YAG and diode lasers are most widely used for the application. High power fiber lasers are the new entrant in this application domain [VAL 10]. For laser material processing involving metals, Nd:YAG, diode and fiber lasers have better absorption due to shorter wavelengths, but CO_2 lasers are still used because of established systems and procedures. Generally, laser energy intensities of 20 kW/cm^2 to 60 kW/cm^2 are used for CO_2 lasers, while 150 kW/cm^2 to 200 kW/cm^2 are used for pulsed Nd:YAG lasers [KRE 95, SUN 05].

The high energy intensity requirements for pulsed Nd:YAG lasers are attributed to re-melting and solidification of a molten pool during the processing. The basic pre-requisite for laser beam energy intensity distribution is symmetry along the laser beam's axis of propagation. This allows uniform material deposition independent of the processing direction. Therefore, a multimode laser beam with a flat top distribution is the most widely used. Gedda *et al.* studied the energy distribution during a LRM process, using a CO_2 laser and a Nd:YAG laser [GED 02]. The observations are summarized in Table 1.1.

Use of laser power	CO_2 laser	Nd:YAG laser
Reflected off the cladding melt	50%	40%
Reflected off the powder cloud	10%	10%
Heat the substrate	30%	30%
Melt the substrate/previously deposited layer	10%	20%

Table 1.1. *Redistribution of laser power during laser cladding*

Table 1.1 clearly indicates that 10% of the laser energy is utilized to melt the substrate layer/previously deposited layer in the case of a CO_2 laser, while 20% of the energy of a Nd:YAG laser is used due to increased absorption. When metals (such as SS316L) are in solid state, the laser energy utilization for Nd: YAG laser is increased by a factor of 1.3. This factor reduces as the temperature rises and is the same for both the lasers in molten/liquid states. Thus, about 769 W of the continuous wave Nd:YAG laser replaces 1 kW of the continuous wave CO_2 laser with the same beam product parameter for almost the same results during LRM. Since the wave length of other commonly used lasers (diode and fibre) is close to the Nd:YAG laser, similar results compared to the CO_2 laser are pertinent.

1.3.2. *Material feeding system*

Among material feeders, there are three main types of feeding techniques: wire feeding, pre-placed powder bed and dynamic powder blowing.

1.3.2.1. *Wire feeders*

Wire feeders are generally used in various industrial applications, including gas metal arc welding. These standard wire feeders are customized and used in many LRM systems. Wire feeding is preferred for the fabrication of components as it involves continuous deposition [DRA 94, HEN 92], as intermittent start/stops results in discontinuity in deposited material. In wire feeding, the wire is always in direct

contact with the melt-pool on the substrate. Any inaccuracy in wire positioning and the wire-feed rate disturbs the shape and size of the melt-pool. This disturbance leads to a non-uniform/unsymmetrical shape of the deposited materials/tracks. Moreover, a definite ratio between the beam diameter and the wire diameter (>3) is used for good quality deposition. Here, good quality deposition means the deposited material has well-bonded to the substrate and the fed material spreads out during deposition resulting in a uniform smooth surface. Therefore, the positioning of the wire in relation to the beam spot on the substrate and its size are critical in wire feeder based LRM.

This method is not adopted as a universal method, because of poor wire/laser coupling leading to poor energy efficiency, unavailability of various materials in wire forms and their cost.

1.3.2.2. *Pre-placed powder bed*

Figure 1.3a-d shows the schematic arrangement of LRM with a pre-placed powder bed. In this scheme, the powder is spread over the substrate through a powder filled hopper and subsequently, it is uniformly leveled with a wiper. Thereafter, LRM is performed by scanning the laser beam over a pre-placed bed of metal/ceramic powders. When the laser beam heats the powder layer, the melt-front advances through the low conductive powder layer, from the surface to the bulk. When the melt-front reaches the substrate, heat conduction increases sharply because of the high conductivity of the substrate/previous deposited layer. If laser energy is sufficient to melt a thin layer of substrate/previous deposited layer, the melted powder is fused and deposited, forming a metallurgical bond. Excessive energy causes excessive re-melting and thermal distortion, while insufficient energy causes poor adherence and incomplete melting of the powder. For any particular deposited height (h) of a specific material, a specific laser energy (*E)* can be calculated by

$$E = \frac{P}{D\,V} \qquad [1.1]$$

where P is the laser power, D is the beam diameter and V is the scan velocity [EBO 85, CHE 89, POW 88]. The value of specific laser energy (E) has to be within a certain range for the controlled re-melting of the substrate and to achieve good powder consolidation for a specific material. This method requires a special laser scanning strategy to achieve nearly 100% density [YUS 08].

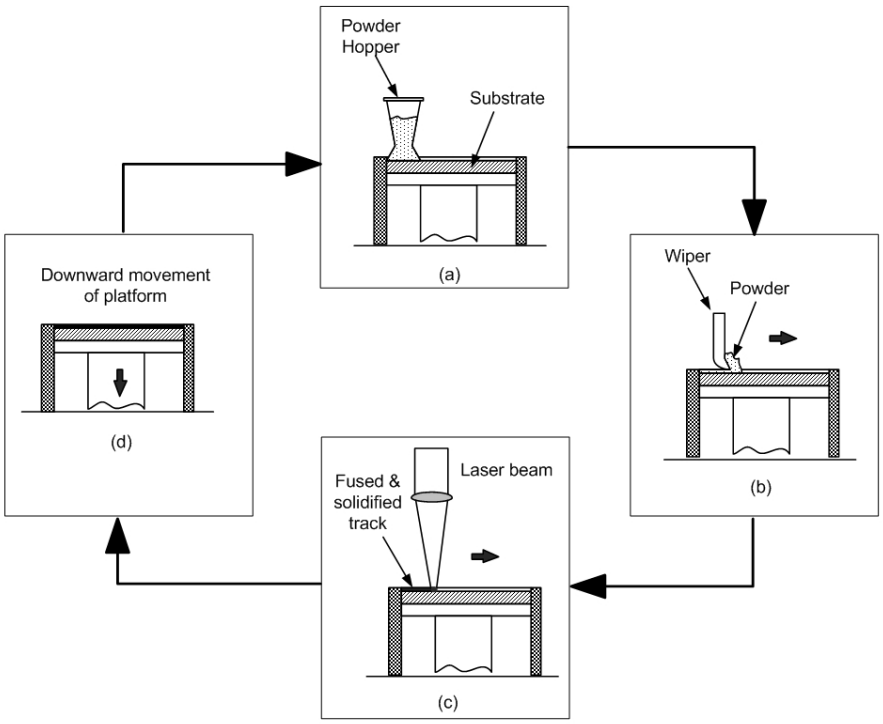

Figure 1.3. *Schematic arrangement of pre-placed powder bed*

1.3.2.3. *Dynamic powder blowing*

Dynamic powder blowing is convenient and the most widely used approach for material feeding in LRM systems. It allows online variation in feed rate and multi-material feeding. Moreover, laser energy utilization is also greater in dynamic powder blowing, as the laser beam passes through the powder cloud to the substrate/previously deposited layer, resulting in the preheating of powder particles by multiple reflections. Various powder feeders are used for this application. They are based on the following working principles:

a) a pneumatic screw type powder feeder;

b) a vibration assisted gravity powder feeder;

c) a volumetric controlled powder feeder.

A pneumatic screw type powder feeder is one of oldest methods. The powder is fed by a rotating screw mounted at the bottom of the hopper, as shown in

Figure 1.4a. The controlled amount of the powder is fed into a pneumatic line and transported to the powder nozzle with an inert gas like Argon (Ar), Helium (He), etc. The rotational speed and dimensions of the screw control the powder feed rate [LI 85]. Frequent choking and the need for cleaning are the problems observed in this feeder.

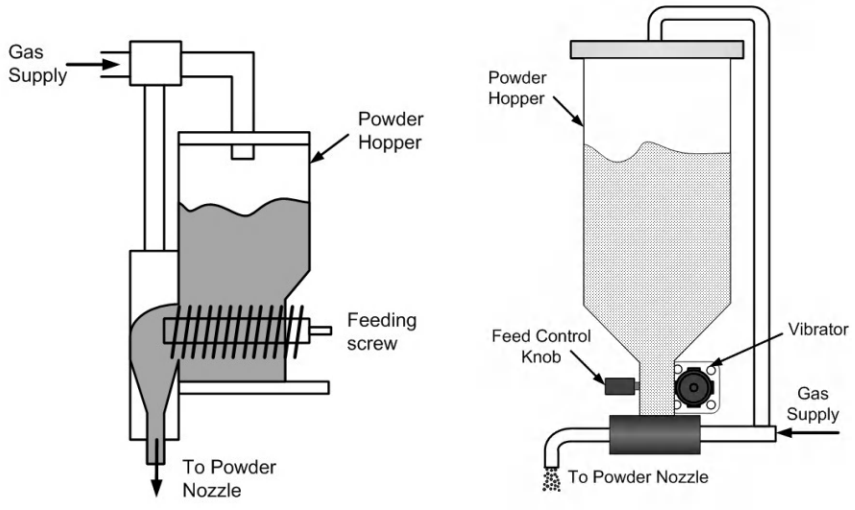

(a) (b)

Figure 1.4. *Schematic arrangement of (a) a pneumatic screw type and (b) a vibration assisted gravity powder feeder*

In a vibration assisted gravity powder feeder, a combination of pneumatic and vibration forces are used to feed the powder into a pneumatic line [PAU 97]. The powder is taken in a hopper and some vibrating device, such as a rotating wheel or standard ultrasonic vibrator, is fitted at the bottom of the hopper. The powder flows freely through an orifice. The dimensions of the orifice are controlled to regulate the powder flow rate. The vibrating device generates the vibration and maintains the free flow of powder under gravity into the pneumatic line. Thus, the powder is delivered to the substrate with the help of an inert gas, as shown in Figure 1.4b. This approach has limitations in regulating the powder flow rate in finer steps and it is widely used for applications involving a constant powder flow rate.

In a volumetric controlled powder feeder, the powder is filled in the hopper and it falls on the annular slot of rotating disc. The hopper and the chamber enclosing the rotating disc are pressurized equally. The rotating disc carries the powder to an exit with a descending pressure gradient. This pressure gradient sucks the powder

particles into a pneumatic line and the powder is delivered to the desired point. One such powder feeder is designed, fabricated and integrated at the Laser Rapid Manufacturing (LRM) laboratory at the Raja Ramanna Centre for Advanced Technology (RRCAT), Indore INDIA. Figure 1.5a presents the schematic arrangement of the developed volumetric controlled powder feeder. The pressure gradient resulting in a gas flow must exceed a minimum value to be able to suck the powder. This minimum gas flow rate is a function of the powder material density and particle size. A higher gas flow rate does not increase the powder flow, as the rotating disc is not able to deliver more powder. Moreover, a higher gas flow rate results in a higher gas velocity leading to a higher probability of the powder ricocheting at the impinging point. This results in lower powder catchment efficiency (which is equivalent to deposited material/fed material). In this system, the gap between the hopper and rotating disc inside the diameter of connecting tube, the density of powder material and rotation speed of the rotating disc define the volume of the powder displaced out of the feed tube from the rotating disc, i.e.:

$$m_p = \rho d t \pi D N \qquad [1.2]$$

where:

m_p = mass flow rate of the powder;

ρ = density of the feed material;

t = gap between the hopper and the disc;

d = inside diameter of the connecting tube;

D = mean diameter of the annular slot;

N = rotating disc speed.

In this feeder, there is a direct dependence of the powder flow rate on the speed of the rotating disc for a particular configuration and material. As the rotating disc is driven by a motor through a gear ratio, the disc speed can be effectively controlled in increments of 0.1 rpm. This results in a finer control of the powder feed rate.

The powder feeder is tested for SS316L, Cr_3C_2 and WC powders with particle sizes between 45 microns and 106 microns. The performance curve of the powder feeder is presented in Figure 1.5b. It is observed that for a regular and reproducible powder flow, a minimum N_2 gas flow of 6.5 slpm, 7.5 slpm and 15.5 slpm is required for Cr_3C_2, SS316L and WC powders respectively. Thus, this system allows online variation of the powder feed rate by simply changing the speed of the rotating disc. The ramp-up and ramp-down time from lowest to maximum feed rate is less than 5 seconds, this feature enables this feeder to be used for the development of functionally graded materials, by using two similar powder feeders simultaneously. Due to the above, all kinds of powders required for laser rapid manufacturing including ceramic powders can be fed.

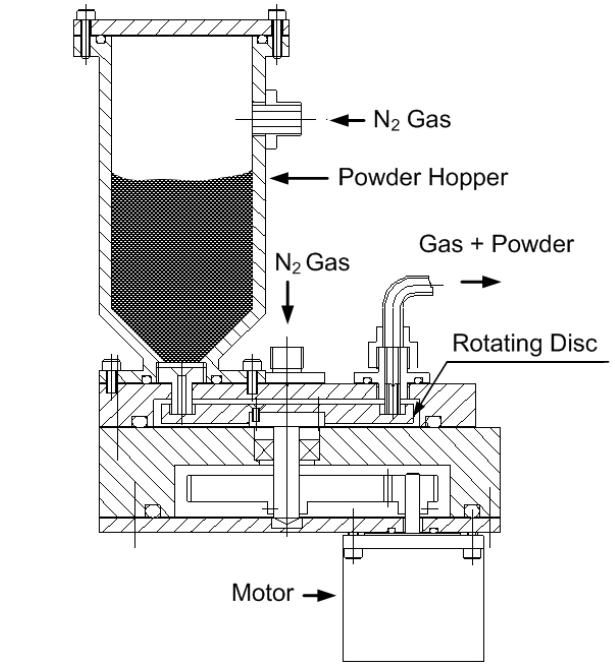

(a)

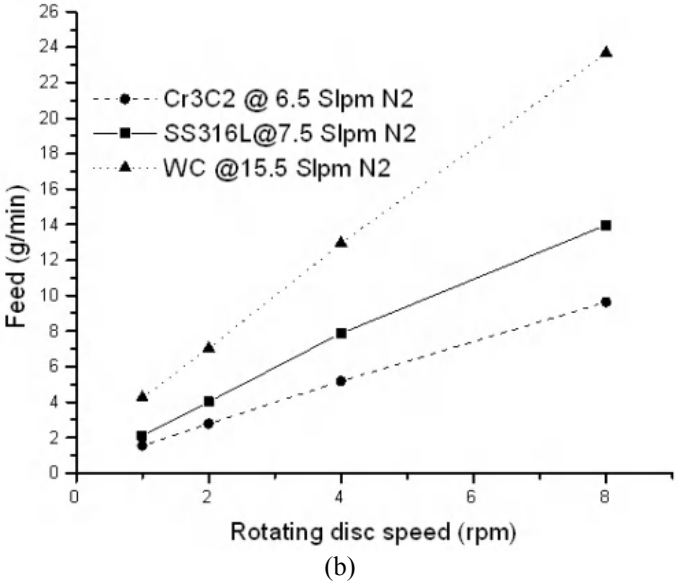

(b)

Figure 1.5. *Volumetric controlled powder feeder: (a) schematic arrangement; (b) rotating disc speed versus powder feed rate performance curve*

In the dynamic powder blowing method, there are two basic configurations for powder delivery to the substrate, i.e., lateral and co-axial powder feedings. Lateral feeding is very common in laser cladding. Since the powder stream is injected off-axis from the laser beam in lateral feeding, substrate movement determines different local deposition. For instance, a so-called "up-hill" deposition condition takes place when the powder stream is applied from the side from which the substrate moves. In this case, the powder is trapped temporarily in a corner formed between the molten track and the flat substrate. This leads to a higher powder catchment efficiency compared to the so-called "down-hill" deposition condition where the powder is from the opposite side. In the lateral powder feeding method, the nozzle is kept between 35º and 60º to the laser beam axis. Marsden *et al.* studied the effect of various parameters pertaining to nozzle geometry [MAR 90].

When the powder is delivered coaxially with the laser beam, all the directions of the substrate movement in a plane perpendicular to the laser beam are equivalent. The coaxial feeding of powder is preferred in LRM due to the advantages in terms of powder catchment efficiency and the omnidirectional material deposition. Various designs of co-axial nozzles have been reported in the literature. Vetter *et al.* designed a co-axial nozzle that had a cone shaped nozzle with two concentric internal spaces [VET 94]. In the outer interstice, carrier or primary gas was used to blow the powder, while in the inner space a secondary gas jet was injected to shield the laser optics. This secondary gas also improved powder homogenization in the stream, ensuring an optimum confinement of the powder stream along the beam axis. This prevented the deviation of the particles towards the focus, where breakdown could occur.

Lin *et al.* designed a coaxial powder-feeding nozzle and extensively studied its characteristics [LIN 98, LIN 99a, LIN 99b, LIN 99c, LIU 03a]. As shown in Figure 1.6a, it had three concentric internal spaces: the inner most space was for a laser beam with an optics shielding gas; the subsequent outer space was for powder and carrier gas; the outer most space was used for shielding gas. The double shielding envelope enables better control of the powder stream by varying the respective gas flow rates.

Some of the common problems with a coaxial powder feeding nozzle, such as powder melting and sticking to feed nozzle, oxidizing prior to deposition, poor powder focusing and poor laser energy utilization have been observed.

A co-axial nozzle was also designed, fabricated and tested at the RRCAT's LRM laboratory. A section view of the developed coaxial powder feeding nozzle is presented in Figure 1.6a.

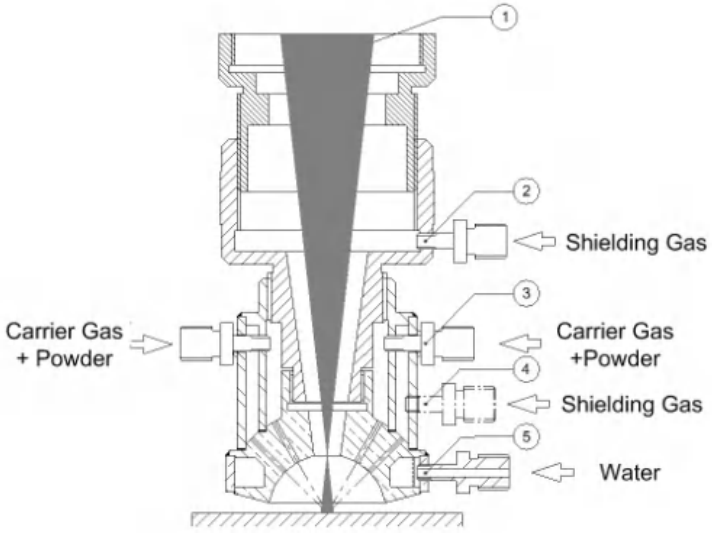

(a)

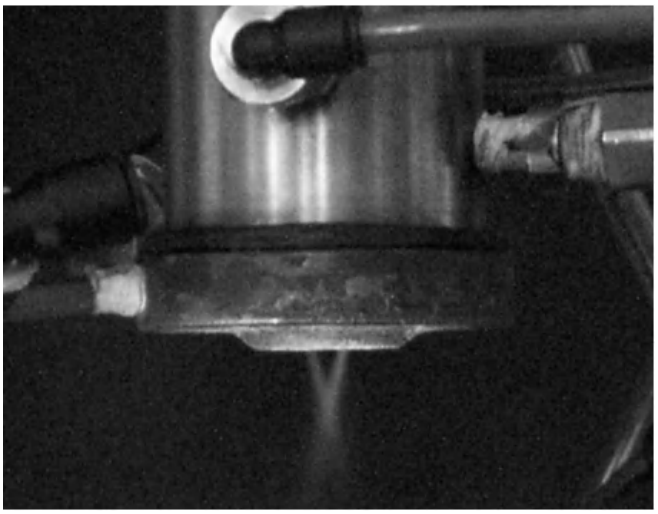

(b)

Figure 1.6. *Co-axial LRM nozzle at the RRCAT's LRM Laboratory: (a) schematic arrangement; (b) powder flow at a 6 g/min feed rate*

The co-axial nozzle consists of three concentric polar matrices of holes. The central hole is used for laser beam (1) and shielding gas (2); the next outer four holes are used to inject the powder with the carrier gas (3) in the converging cone shape

and form a co-axial laser-powder stream; the outermost eight holes are used to supply a converging conical jet of shielding gas (4). The position and diameter of the powder beam can be adjusted by changing the gas flow velocity of the shielding gases. These annular matrices of holes are fabricated in a water-cooled hemisphere (5) with a polished inner surface. The hemisphere shape enables an effective shielding against hot and molten metal at one end; it also facilitates the reutilization of the reflected laser beam the other end. The water-cooled head enables prolonged operation time. The laser beam focus is set near the exit of the central hole, so that the powder mat interacts with the expanding laser beam. The nozzle has a provision of changing the focus of the laser beam with respect to the nozzle exit. Thus the operating point for the laser rapid manufacturing can be changed without sacrificing powder catchment and laser energy utilization. The performance of the co-axial powder feeding system is mainly concerned with the ability to deliver the powder that forms a defect free metal track. Figure 1.6b shows the powder stream through a co-axial powder feeder at a 6 g/min powder feed rate.

The main criterion for evaluating the cladding performance is the powder catchment efficiency. The powder catchment efficiency is defined as the weight ratio of the metal track formed to the powder delivered during the laser rapid manufacturing. For metal track deposition before the powder particle is melted, the catchment efficiency is mainly governed by the ratio of the laser generated melt-pool to the powder impact area on the substrate. Whichever is smaller, out of the laser spot diameter and the powder stream diameter at the substrate, determines the width of the metal track. The reported catchment efficiencies of various co-axial nozzles are within the range of 30% to 95%.

1.3.3. *CNC workstation*

In a CNC workstation, three-axis interpolation (X, Y and Z) is sufficient to reach any point in the space, but two more axis (A and C) are required to orientate towards a particular direction. Therefore, a three-axis configuration is the minimum system requirement and a five-axis configuration is a universal requirement without redundancy. Apart from axes-movement, a laser workstation requires other features, such as laser on/off, gas on/off, powder feeder on/off etc., for LRM.

1.4. Various laser rapid manufacturing systems

Table 1.2 presents the configuration of various LRM systems being used at various national laboratories/universities.

Process	Laser	Material feeding	CNC workstation
Laser Engineered Net Shaping (LENS) [WEB 18]	2.4 kW CW Nd:YAG Laser	Co-axial	5-axis
Freeform Laser Consolidation (FLC) [LIU 03b]	1 kW pulsed Nd:YAG Laser	Lateral	3-axis
Directed Light Fabrication (DLF) [MIL 98]	2 kW CW Nd:YAG Laser	Co-axial	5-axis
Shape Deposition Manufacturing (SDM) [WEB 21]	2.4 kW CW Nd:YAG Laser	Lateral	5-axis CNC mill
Laser Direct Casting (LDC) [CHA 02]	2.8 kW CW Nd:YAG Laser	Co-axial	4-axis fully integrated CNC
Selective Laser Cladding (SLC) [BEN 06]	5 kW CW CO_2 Laser	Lateral	3-axis workstation
Automated Laser Fabrication (ALFa) [ALI 10]	1 kW CW Fiber Laser	Lateral	5-axis workstation

Table 1.2. *Configuration of various LRM systems*

A LRM system was integrated at the RRCAT's LRM Laboratory. The schematic arrangement of the system is shown in Figure 1.7. It consists of a 2 kW fiber laser system, a 5-axis workstation in a glove-box, a computerized numerical controller, a coaxial nozzle, a twin powder feeder, gas analyzers and cameras with image processing hardware.

A procured 2 kW fiber laser has an output power range of 50 W to 2,050 W with an emission wavelength of 1,080 nm. The system has a switching on/off time of 80 μs and an output modulation rate of 5 kHz. The laser beam is randomly polarized and has a product parameter lower than 4. The system has a delivery fiber with a core diameter of 50 μm. The overall size of the laser system is 1.2 m × 1.2 m × 0.75 m. The output laser beam is passed through refractive focusing optics and indigenously developed compact co-axial nozzle is employed for laser rapid manufacturing. The system is integrated with a 5-axis workstation for job manipulation. The five axes are X, Y, Z, V and W. The X, Y and Z axes are linear traverse axes mutually perpendicular to each other, whereas V is a tilt axis about the

Y axis, for tilting the laser head, and W is a continuous rotational axis about the Z axis. The effective stroke length of linear axes is 250 mm. The angular tilt of the V axis is ± 110°, whereas the W axis is capable of a 360° continuous rotation. The manipulator is interfaced with a standard computer numerical controller for manipulating the workstation. The laser head coupled with a manipulator is mounted in a glove-box. The glove box is essentially required for controlling atmospheric conditions during processing. Oxygen and moisture are the main impurities in atmosphere which affects the properties of the deposited bulk materials. Therefore, the system is integrated with oxygen and moisture analyzers. The desired purity levels are achieved by purging high purity grade Argon gas. In case there is an increase in the impurity level, the high purging rate is used to reinstate the indented purity level in the glove-box. The purity level of the glove-box is retained by keeping the differential pressure just above the atmospheric pressure. For online monitoring and improvement of the deposition process, the system is equipped with image capturing devices like CCD cameras with a suitable output port for storing measured data in a storage device. This facilitates process monitoring along with parametric measurements and its control. An application program is being developed for user based requirements for monitoring and process control. The comprehensive control system will work in close loop control mode for continuous feedback.

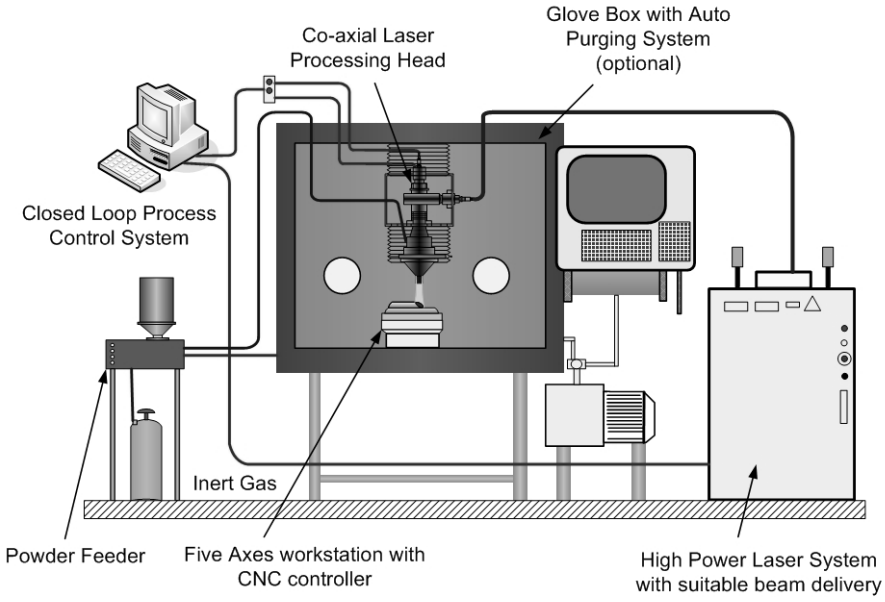

Figure 1.7. *Schematic arrangement of a LRM system at the RRCAT's LRM Laboratory*

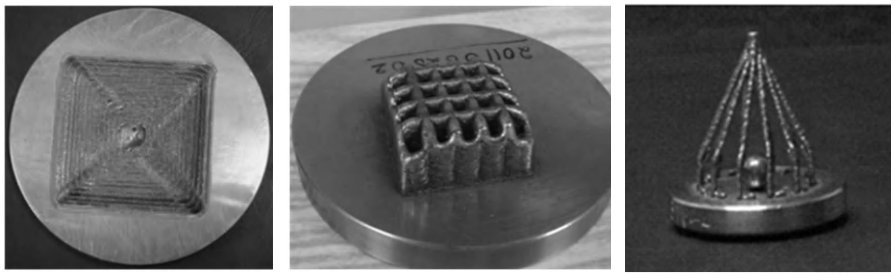

(a) (b) (c)

Figure 1.8. *Typical geometries fabricated using a LRM system at the RRCAT's LRM Laboratory*

The typical geometries fabricated using the LRM system at the RRCAT's LRM Laboratory is shown in Figure 1.8. Figure 1.8a shows the 1.5 mm thick laser clad surface of 50 mm × 50 mm with Stellite-6 on a SS316L substrate. Figure 1.8b shows a typical cross thin-walled porous structure of Inconel-625 on a substrate with a 75 mm base diameter and 12 mm height. Figure 1.8c is a simple cage of Inconel-625 (size: 40 mm base diameter × 60 mm height), laser rapid manufactured with a pulse mode operation of laser.

1.5. Relevant processing parameters

At the manufacturing end, LRM is an extension of the laser cladding process to near net shaping of the component. Hence, the reported efforts of laser cladding can be extrapolated for the development of the LRM process. Many researchers have studied laser cladding process by means of simple parameter variations for their system and selected material combinations [VET 94, KRE 95, NUR 83]. All these researches have some common observations about the variation of process parameters. These observations are summarized in Table 1.3.

Parameters	Clad height	Melt depth	Dilution	Hardness/cracking
Laser power	–	+	+	–
Scan speed	–	–	–	+
Material feed rate	+	–	–	+
Laser spot	+	–	–	+
(+ : increase; – : reduction)				

Table 1.3. *Effect of the increase of different parameters on clad layer properties*

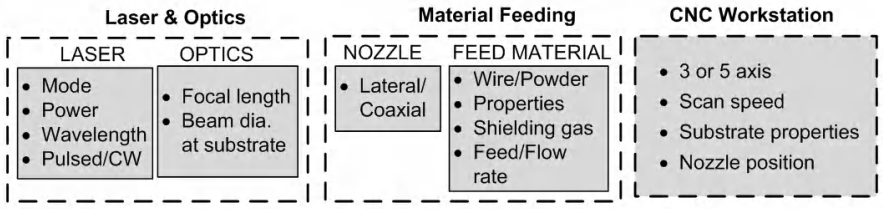

Figure 1.9. *Various LRM process parameters*

Figure 1.9 presents important LRM process parameters. The parameters can be divided into three major categories: laser and optics, material feeding and job manipulation. Among laser and optics parameters, many parameters such as mode, wavelength, type of laser operation: continuous wave/pulsed and focal length are fixed for a selected laser and beam delivery system. Among material feeding parameters, the type of feeding (lateral/co-axial) and the shape of the feed material (wire/powders) are fixed with the selection of the material feeding system. Among the parameters relevant to job manipulation, the number of axis is fixed once the configuration of the job manipulation system is selected. The shielding gas and substrate properties are governed by the application. Thus, the basic parameters that play a major role in the formation of tracks for particular system are laser power (P_L), beam diameter at the substrate (D_L), material feed/flow rate (m_p) and scan speed (V_s). However, we find the effect of these three basic parameters can be accounted for with the following two parameters:

$$Laser\ Energy\ per\ unit\ traverse\ length\ (E_l) = \frac{P_L}{V_s \times D_L} \quad [1.3]$$

$$Powder\ fed\ per\ unit\ \ traverse\ length\ (m_{p/l}) = \frac{m_p}{V_s \times D_L} \quad [1.4]$$

The parameters "laser energy per unit traverse length" and "powder fed per unit traverse length" govern the laser energy and the material available for the single track deposition respectively. At extremely high laser energy per unit traverse length and lower powder fed per unit traverse length, there may be vaporization of the feed material. As a result, there may be very thin or no track formation. On the contrary, at extremely low laser energies per unit traverse length and higher powder fed per unit traverse length, the feed material may not fuse and form a discontinuous track. Hence, there is a processing window, where there is a balance of both the parameters, resulting in uniformly fused continuous tracks. For processing Inconel 625, the optimum process window is found to be in the range of 120 kJ/m to 360 kJ/m for laser energy per unit traverse length and 10 g/m to 40 g/m for powder fed per unit traverse length [PAU 07].

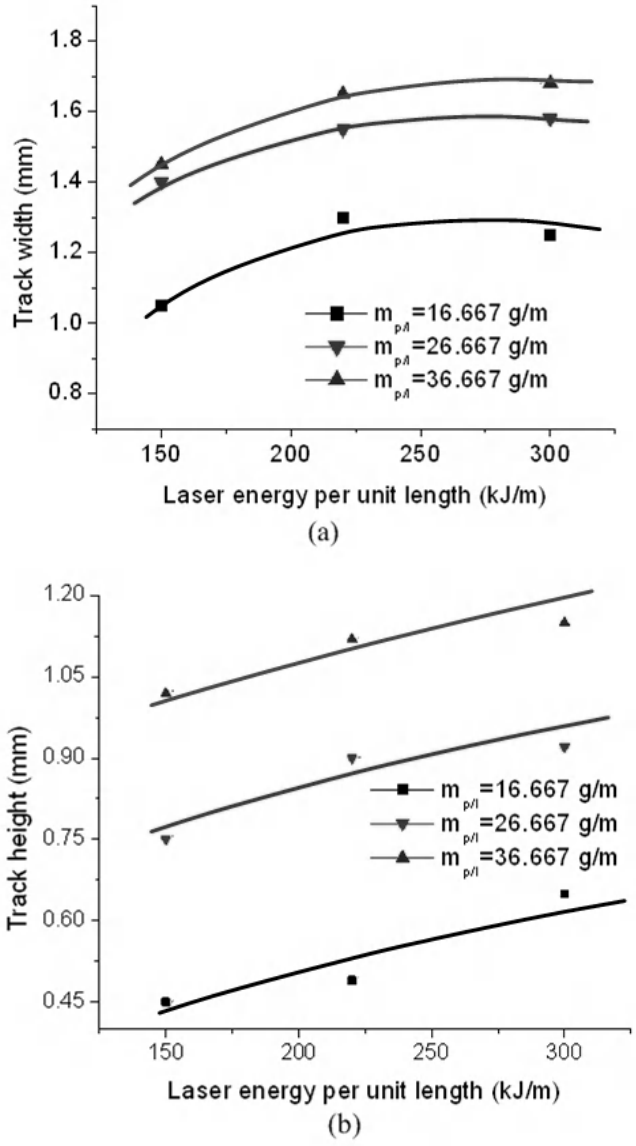

Figure 1.10. *Effect of the laser energy per unit traverse length and powder fed per unit traverse length on: (a) track width; and (b) track height*

Figures 1.10a and b present the effect of the laser energy per unit traverse length and powder fed per unit traverse length on a single track width and height

respectively. It may be observed that track width and height are primarily governed by the parameter "powder fed per unit traverse length" and they increase as this parameter is increased. The variation of 100% in "laser energy per unit traverse length" is found to result in a maximum variation of only 20% in width and height of the single track. Thus, the increase in "laser energy per unit traverse length" has little influence on the track geometry. This was also witnessed by Pinkerton *et al.* [PIN 08].

Multi-layer deposition on a single track is required to shape the single wall of the 3D porous structure fabricated using LRM. The effect of processing parameters, i.e. "laser energy per unit traverse length" and "powder fed per unit traverse length" as a function of number of layers of a single wall were investigated. Figure 1.11a and b show the material deposited per unit length and catchment efficiency, respectively, in a different number of layers for various "laser energy per unit traverse lengths" and "powder fed per unit traverse lengths". Figure 1.11a shows that the material deposited per unit traverse length increased from the first layer to the second layer, and in subsequent layers it tended to saturate. Figure 1.11b shows that the catchment efficiency enhances from the first layer to the second layer, which could be because of the enhancement of the surface area of the melt-pool when we go from the flat surface of the substrate to the convex surface of the first layer of the track. The improvement in the catchment efficiency results in the increased material deposition per unit traverse length in the second layer, as seen from Figure 1.11a. The variation of the catchment efficiency for a higher number of layers shows enhanced randomness as observed in Figure 1.11b. This might be because the catchment efficiency is based on very complex processes such as ricochet effects, adhesion and recoil of the incoming preheated powders at the molten pool and the surrounding solid surface of the substrate. Consequently, a large scatter in experimental data is obtained, as shown in Figure 1.11b.

Figure 1.11a also shows that as the laser energy per unit traverse length was increased, the track width and track height increased, leading to higher material deposition per unit traverse length. Similarly, with increased powder fed per unit traverse length, the mass deposited per unit traverse length was also observed to increase, as shown in Figure 1.11a. In contrast to this, the catchment efficiency decreased with the increase in powder fed per unit traverse length and increased with the increase in the laser energy per unit traverse length. However, the increase in the catchment efficiency with the increase in the laser energy per unit traverse length was much higher for a lower powder fed per unit traverse length compared to a higher powder fed per unit traverse length, as seen in Figure 1.11b. These results are understandable based on the consideration of the amount of powder melted by the interacting laser beam and the fraction of the mass of the powder that becomes attached to the layers in a track.

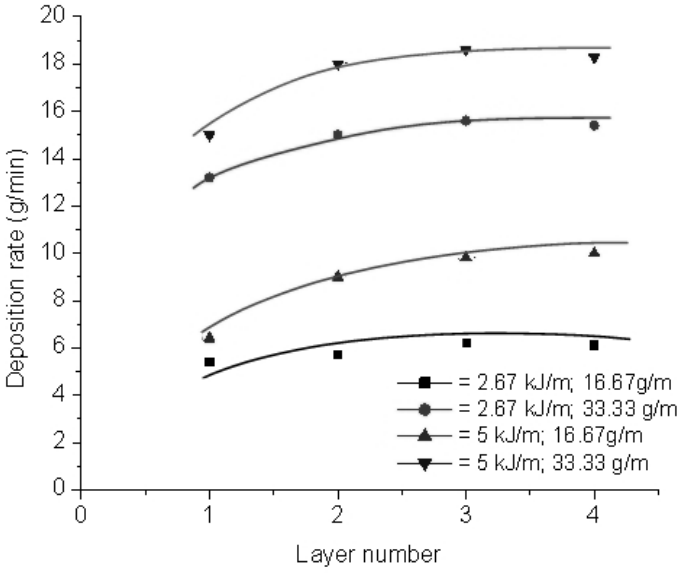

(a)

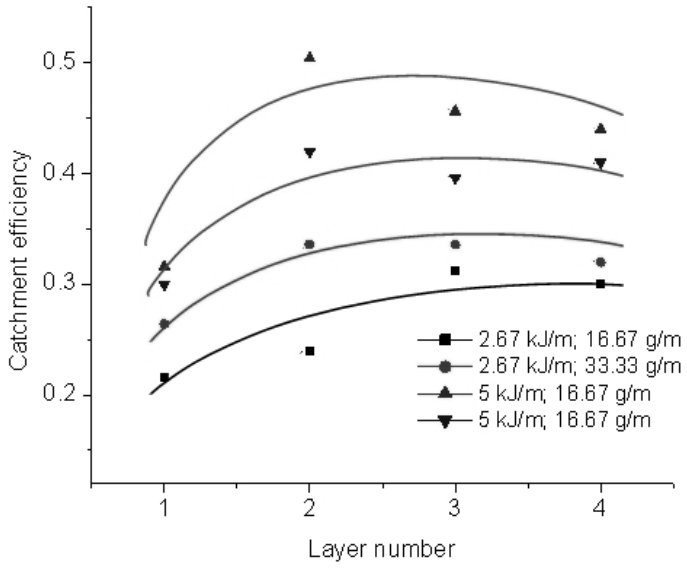

(b)

Figure 1.11. *(a) The material deposited per unit length and (b) the catchment efficiency for a different number of layers at various "laser energy per unit traverse lengths" and "powder fed per unit traverse lengths"*

When a large surface is to be covered or a porous layer is to be fabricated, a number of tracks are laid adjacent to one another with an overlap for covering large surfaces and without/limited overlap for porous layers. Hence, another parameter that plays a vital role during the formation of multi-track structures is the transverse traverse index (i). This is the ratio of the transverse traverse distance (x) to track width (W) (see Figure 1.12). Mathematically:

$$Transverse\ traverse\ index\,(i) = \frac{x}{W} \qquad [1.5]$$

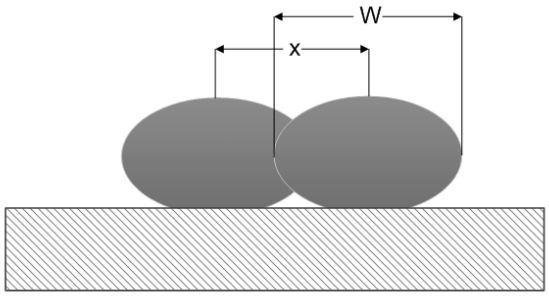

Figure 1.12. *Schematic diagram of a transverse section of a transverse traverse index*

Fully-dense structure LRM uses a transverse traverse index closer to 0.6, while a porous structure is fabricated when the transverse traverse index is greater than 0.7.

A particular combination of primary processing parameters, i.e. laser energy per unit length and powder fed per unit length creates a particular width and height. The ratio of track width to track height is known as the track aspect ratio. It plays a vital role during multi-layer overlapped track deposition. Mathematically, it is given as

$$A = \frac{W}{H} \qquad [1.6]$$

Experimentally, it was found that a minimum aspect ratio ($A \geq 5$) had to be maintained to avoid inter-run porosity, due to the lack of a fusion zone at track roots during multi-layer overlapped deposition. Figure 1.13a presents a fractograph, showing the inter-run porosity of LRM samples with an aspect ratio of ~ 3.5, while Figure 1.13b shows a sound and defect free fractography of a sample with an aspect

ratio of more than 5, i.e. around 7. In both samples, the direction of overlaying was along the tensile axis.

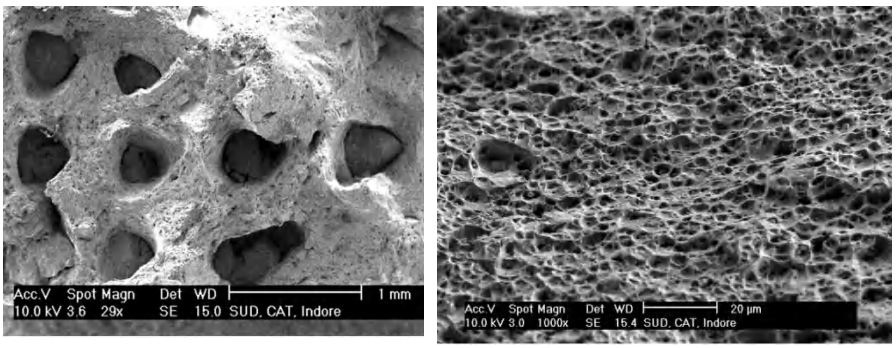

(a) (b)

Figure 1.13. *SEM fractograph of an LRM sample with an: (a) aspect ratio of ~ 3.5; and (b) aspect ratio of ~ 7*

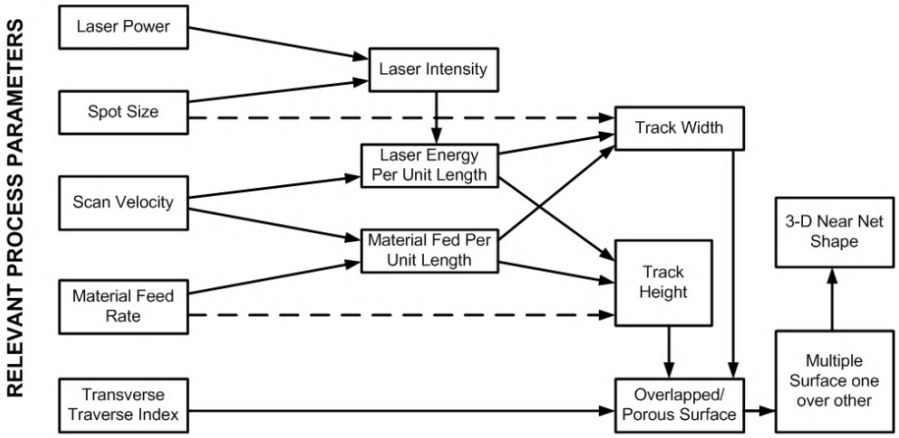

Figure 1.14. *Relevant processing parameters and their effects*

Thus, the optimum combination of the above parameters can be used to fabricate various geometries. Figure 1.14 presents the processing parameters and their effects on the fabricated geometry.

S.No.	Application description	Materials
1	High pressure gas turbine blade shroud, interlock, turbine blade	Triballoy on Nimonic
2	Parts of off-shore drilling heads	CrC, Cr, Ni on cast iron
4	Automotive parts	Stellite, Triballoy T-800
5	Turbine blade, plough blades	Stellite 6, Stellite SF
6	Diesel engine valve, deformation tool, stainless steel seal runner, camshaft, compressor blade (Ti-6Al-4V)	Stellite 6
7	Extruder screw plastic machinery	LC2.3B (Ni-base), Al-bronze
8	Deep drawing tool (cast iron GGG60)	Stellite SF6
9	Leading edge steam turbine blade	Stellite 6, Stellite 6F
10	Valve in a combustion engine (x45crsi9)	Triballoy T-800
11	Gas turbine airfoil thermal barrier	Inconel 625 + CrC
12	Valve in a combustion engine (x45crsi9)	Stellite 21
13	Extruder screw plastic machinery (14CrMoV6 9)	Ni-Cr-Al-Y
14	Molding die (45nicr6)	Co-Cr-W-C
15	Exhaust valves large diesel engines (nicr20alti ~ DIN 2.4952)	Ti-6Al-4V + cubic BN
16	Nuclear valve (AISI 304)	Ni-Cr alloy
17	Blowing mold	PWA Alloy 694
18	Die for production of glass bottles	Stellite 6, Colmonoy 5

Table 1.4. *Some typical examples of industrial applications of LRM [MAR 98]*

1.6. Typical applications of LRM

The list of applications of LRM is appending due to global research efforts. Some typical examples of industrial applications of LRM are summarized in Table 1.4. In the following section, some of the LRM applications developed at our laboratory for various in-house and industrial applications are briefly described.

1.6.1. *Colmonoy-6 bushes*

Nickel-based alloys "Colmonoy" are preferred for hardfacing applications in nuclear power plants due to their outstanding wear resistance, high hardness at elevated temperatures and low induced radioactivity [BHA 00]. Pre-fabricated Colmonoy-6 bushes are used as a substitute for local hard-facing for complicated component geometry with limited accessibility. Conventionally, these bushes are made by casting/weld deposition followed by machining [DAS 03]. However, high capital cost for the low volume of fabrication made this a prohibitive option. Therefore, these customized Colmonoy-6 bushes were fabricated by LRM at our laboratory as an alternative to conventional processing.

Type 316L stainless steel plate, 75 mm in diameter and 12 mm thick, was used as a base/substrate. Colmonoy-6 bushes, with dimensions of 20 mm outer diameter, 2.5 mm wall thickness and 40 mm length, were laser rapid manufactured by providing helical upward motion to the co-axial powder feeding nozzle.

To improve the cracking resistance of Colmonoy-6 deposits, slow cooling was achieved by placing the substrate in a special sand bath maintained at an elevated temperature of 673 K during LRM. The sand bath consisted of an electrically heated copper plate buried in the sand. The temperature of the bath was measured and automatically controlled with the help of a temperature controller.

Figure 1.15a presents the photograph of the LRM of Colmonoy-6 brushes. After LRM, the fabricated parts were left buried in the sand bath for more than 8 hours to achieve the slow rate of cooling. The resultant Colmonoy-6 bushes were crack free. The measured dimensional tolerance using a three-point method was 0.2–0.5 mm, while the surface roughness (Ra) was 25–40 μm. The desired dimensional accuracy and surface finish were achieved by a series of machining and grinding processes [PAU 06].

Figure 1.15b presents the Colmonoy bushes after the final machining and grinding.

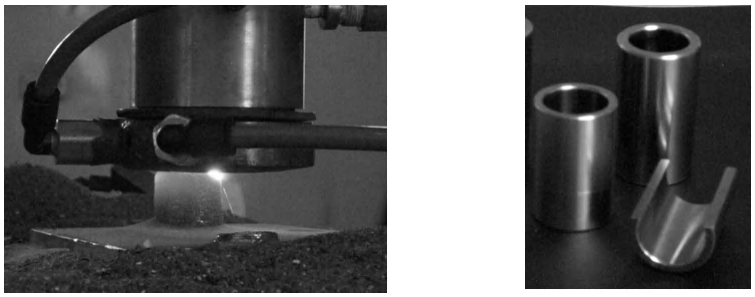

(a) (b)

Figure 1.15. *(a) LRM; and (b) finally, machined and ground Colmonoy-6 bushes*

The laser rapid manufactured Colmonoy-6 bushes were subjected to a number of tests for material characterization. Dye penetrant testing and ultrasonic testing at 10 MHz revealed no surface and internal defects respectively. The multi-layer structure of Colmonoy-6 bushes could be very clearly seen during optical microscopy (see Figure 1.16a). The microstructure of the Colmonoy-6 bush showed a uniform dendrite growth in the direction of build-up. It featured primary dendrite phases and an inter-dendrite constituent as shown in Figure 1.16b.

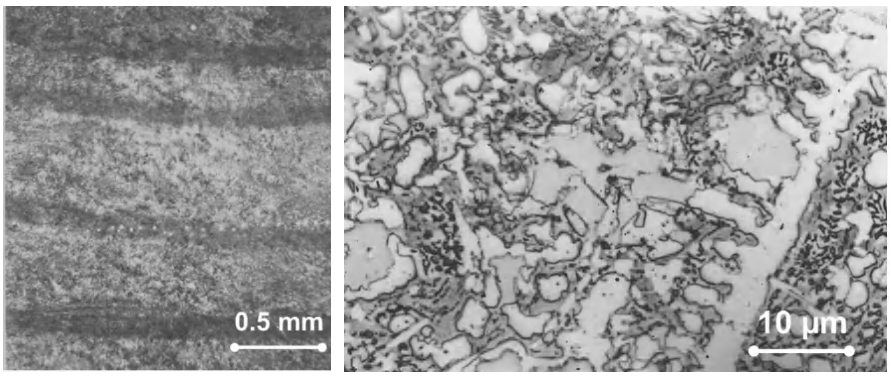

(a) (b)

Figure 1.16. *(a) Different layers of multi-layered Colmonoy-6 bush (longitudinal section); and (b) microstructure of a typical cross-section of a Colmonoy-6 bush*

The compressive testing as per the ASTM E9 standard revealed that the compressive strength of LRM fabricated Colmonoy-6 specimens are on par with their wrought counterparts (see Figure 1.17a). The microhardness profile for the

longitudinal and transverse section of LRM Colmonoy-6 is presented in Figure 1.17b.

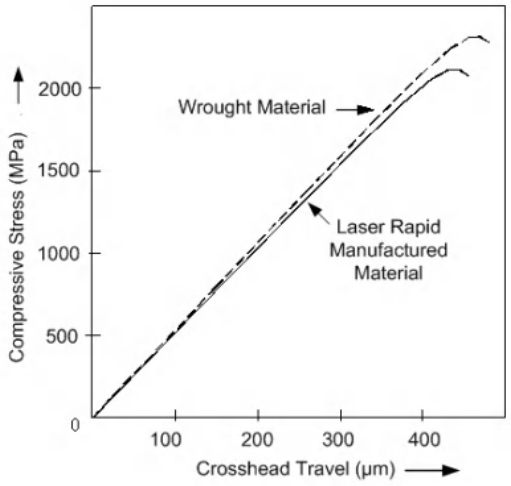

(a)

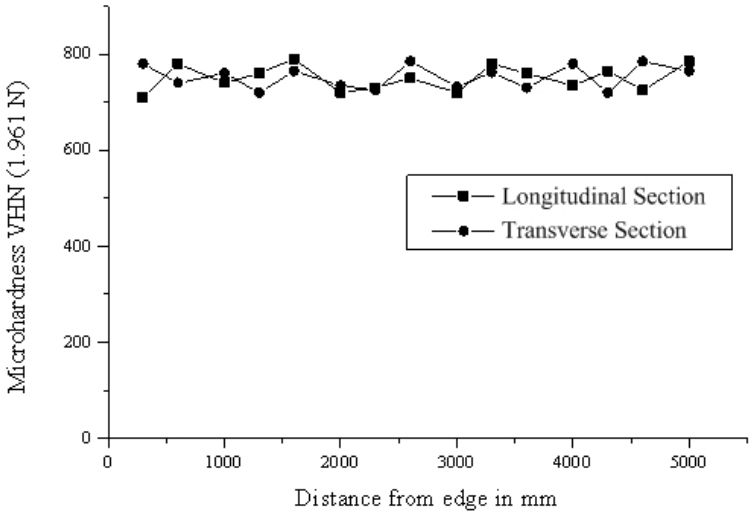

(b)

Figure 1.17. *(a) Typical compressive stress and crosshead travel curve for LRM and wrought Colmonoy-6; and (b) longitudinal and transverse micro-hardness profiles of LRM Colmonoy-6 bush*

This example demonstrated that LRM can be used as a cost effective alternative technique for the fabrication of Colmonoy-6 bushes [PAU 06]. LRM has a significant advantage over other techniques, in terms of saving on expensive Colmonoy-6 material and reduced machining of the hard material [DAS 03].

1.6.2. *Solid and porous structures of Inconel-625*

Inconel-625 is a nickel-chromium based alloy, which is widely used for various naval, aerospace and nuclear applications. It has an outstanding fatigue and thermal-fatigue strength; good oxidation and corrosion resistance; excellent resistance to stress corrosion cracking and pitting resistance at elevated temperature; and excellent characteristics for welding and brazing [SMC 11]. Considering the wide spread applications and its oxidation resistant property the studies of the LRM structures (solid and porous) were carried out at our laboratory using Inconel-625. A number of samples for various processing parameters were fabricated and their mechanical and metallurgical properties were evaluated using standard characterization techniques, such as tensile testing, Rockwell hardness testing, Charpy impact testing etc. Table 1.5 presents the comparison of some of the important mechanical properties of LRM and hot finished and annealed Inconel-625. The properties of LRM Inconel-625 were found to be on par with those of conventionally processed Inconel-625.

Properties	LRM [PAU 07]	Hot finished and annealed [SMC 11]
0.2 % yield stress	571±25 MPa	395±15 MPa
Ultimate tensile stress	915±20 MPa	824±25 MPa
Elongation	49±3 %	51±4%
Charpy V-notch impact resistance, J	102±5	110±5
Rockwell hardness	46 – 52 R_C	27 R_C

Table 1.5. *Comparison of some important mechanical properties of LRM and hot finished and annealed Inconel-625*

Figure 1.18a and b show the cross-section of a typical multilayer overlap LRM fabricated Inconel-625 deposit and its microstructure. The microstructure examinations revealed that there were finely intermixed dendritic and cellular microstructures with high dislocation density. The direction of dendrite growth was

in the direction of deposition. The fine dendrite formation was due to an inherent rapid cooling rate during LRM, while the cellular microstructure is attributed to the relatively lower cooling rate during the multi-layer deposition.

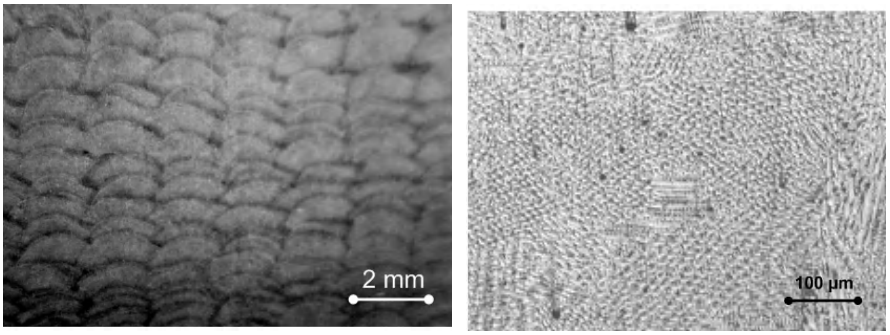

(a) (b)

Figure 1.18. *(a) Typical cross-section exhibiting multilayer overlap deposition; and (b) microstructure of LRM fabricated Inconel-625*

The fine microstructures with high dislocation density are responsible for higher mechanical strength and hardness, while formation of a cellular microstructure has helped to keep the ductility intact.

Conventional methods of fabricating porous structures, such as the furnace sintering technique, space holder technique, replication technique, combustion synthesis technique, ferromagnetic fiber arrays technique and vapor deposition technique, have limitations in the fabrication of the porous structures with engineered mechanical properties due to the inability to precisely control a number of parameters: such as pore-size, shape, volume fraction, pore-distribution, contaminations and their phases, etc. Moreover, they cannot be used for generating functionally designed porous structures with graded porosity. Such structures can potentially be fabricated using LRM. Gu *et al.* studied the processing conditions and microstructural features of porous SS316L by directed metal laser sintering [GU 08]. Li *et al.* focused on the densification behavior of metal powders and its effect on the fabrication of graded porous structures during selective laser sintering [LI 10a, LI 10b]. Krishna *et al.* employed LRM for the fabrication of porous structures of Ti with a broad range of compressive yield strengths between 21 MPa and 463 MPa and a low Young's modulus between 1.7 GPa and 28 GPa [KRI 05]. Recently, a diode laser in continuous mode and a CO_2 laser in pulsed mode were used to produce multi-layer porous structures. A comparison between them with respect to their internal geometry, pore size and part density, using a range of techniques including micro-tomography were reported by Ahsan *et al.* [AHS 11].

At our laboratory, the porous structures were laser rapid manufactured using a cross-thin-wall fabrication strategy and structures up to 60% porosity was achieved. The mechanical properties of these structures were also investigated. In a cross-thin-wall fabrication strategy, the porous material is fabricated by depositing the material in mutually orthogonal directions in successive layers. Figure 1.19a presents a schematic of the cross-thin-wall fabrication strategy.

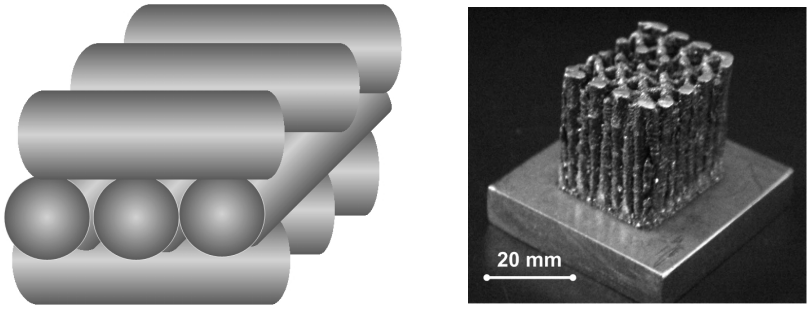

(a) (b)

Figure 1.19. *(a) Schematics of the cross-thin-wall fabrication strategy; and (b) a LRM porous structure of ~20% porosity*

The investigation indicated that the properties of LRM porous structures were governed by the major processing parameters involved, i.e. laser energy per unit transverse length, powder fed per unit transverse length and transverse traverse index [PAU 12]. The response surface method using the Box-Behken design of experiments was employed to investigate the effect that these three important processing parameters have on the porosity. The range of the parameters used in the investigation were 120 kJ/m to 360 kJ/m for laser energy per unit traverse length, 10 g/m to 40 g/m for powder fed per unit traverse length and 0.7 to 2.4 for the transverse traverse index. These parameters were selected based on the single track experiments as described in section 1.3. The investigation showed that the powder fed per unit traverse length was a predominating parameter in determining the porosity of the structures, followed by the transverse traverse index and the laser energy per unit traverse length.

While studying the combined effect of processing parameters, it was found that the laser energy per unit traverse length and transverse traverse index had a maximum impact on the porosity of the LRM structures. It is because of this fact that there is a higher material deposition for a respective rectangular cross-sectional area at the higher laser energy per unit traverse length and lower transverse traverse index, resulting in a lower porosity. Similarly, at the lower laser energy per unit

traverse length and lower transverse traverse index, there is a higher material deposition with a smaller cross-sectional area and the porosity remains lower. On the other hand, for the lower laser energy per unit traverse length and higher transverse traverse index, there is less material deposition for the same rectangular cross-sectional area and subsequently, the porosity is higher, while for the higher laser energy per unit traverse length and higher transverse traverse index, there is less material deposition with a bigger cross-sectional area and subsequently, the porosity is the highest. For the range of the parameters under investigation, the surface response of the porosity as a function of the laser energy per unit traverse length (E_l), powder fed per unit traverse length ($m_{p/l}$) and transverse traverse index (i) was calculated and presented in the following equation [PAU 12]:

$$\begin{aligned} Porosity\ (\%) = {} & 14.2843 - 0.12105\ E_l + 0.2432\ m_{p/l} - 6.9277\ i \\ & + 1.379 \times 10^{-3}\ E_l\ m_{p/l} + 0.0811\ E_l\ i - 0.2196\ m_{p/l}\ i \end{aligned} \quad [1.7]$$

Figure 1.20 presents a typical engineering stress-strain curve obtained during compressive strength testing of the LRM porous structures. The curve indicates that there is a sharp increase in stress with small compression in the beginning up to point A. This is a region of elastic and small plastic deformation. Therefore, this slope is not generally used to determine the Young's modulus of the porous structures. The associated plastic deformation in this region is responsible for mechanical damping. After the initial increase in stress, there is a change in the slope of the curve due to a regime of plastic deformation, where a small increase in stress resulted in a larger compression up to point B. The measured value of the porosity at this point is less than 10% of the initial value. After an extended plateau regime, the curve finally enters into a region of densification, when the porosity was negligible with neighboring tracks completely coalescing with each other. The measured value of porosity was negligible at this point.

The micrograph placed as an inset between O and A shows the cross-section of the laser rapid manufactured porous material at the beginning of the compression test. In this micrograph, the pores are clearly visible and the cross-sectional shape of the tracks is nearly circular. The micrograph placed between A and B shows the cross-section of the laser rapid manufactured porous material after compression near point B. In this micrograph, the pores and tracks have an elongated shape due to compression. The pores are compressed and almost filled with material flow. This flow of the material gives rise to a plateau regime in the stress strain curve. The slope and length of the curve in the plateau region depends on the rate of densification of the material, which is primarily governed by the interaction of stress fields around the pores [BAN 01]. The micrograph near point C shows the cross-section of the totally compressed porous material. The neighboring tracks are

compressed together and the completely deformed shape of the pore is clearly visible.

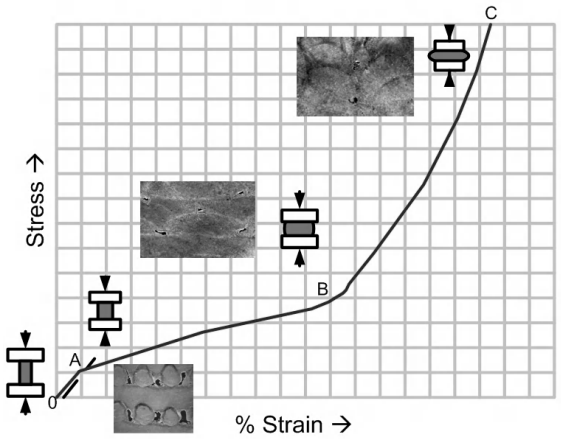

Figure 1.20. *Typical engineering stress-strain curve obtained during compressive strength testing of the LRM porous structures*

Porosity (%)	Yield strength along the laser scanning and transverse traverse direction (MPa)		Yield strength along the buildup direction (MPa)	
	Value	Standard deviation	Value	Standard deviation
0.32	526.07	11.5	494.73	6
2.63	481.2549	17.5	423.3	8
3.67	521.19	15.5	458.053	11
4.31	539.026	9.5	487.763	12
5.19	487.2365	10.5	402.8489	8
6.01	507.674	6	489.8593	7
7.68	453.4074	14	421.0413	6
8.69	433.323	8.3	413.364	9
9.8	282.2563	4.6	259.606	8.3
11.57	255.8092	8.2	226.227	6.8
14.47	223.69	6.2	202.39	5.6
16.58	175.32	2.8	167.69	4.5
19.96	147.38	5.2	122.487	3.6

Table 1.6. *Yield strength of a LRM structure for various porosities*

Table 1.6 presents the yield strength of the LRM porous structure at various porosities. It may be noted that the yield strength decreases faster with the increase in the porosity, because the mechanical properties are highly sensitive to microstructural parameters, such as pore size, shape, orientation, distribution, etc. These parameters give rise to stress concentration within the material. When the porosity is low, the pores are further away from each other, giving rise to isolated stress concentrations. At the higher porosity, these stress concentrations have interacting fields, as the distance between the pores are reduced. At a very high porosity, any small irregularities, like cracks, etc., also interacted with the pores and raised the stress concentrations multifold. The above observation is in agreement with the conventionally processed porous materials [NAK 07]. It is clear from Table 1.6 that there is anisotropy in the mechanical properties of laser rapid manufactured porous structures. The value of yield stress is 122.487±3.6 MPa along the X and Y-axis, while it is 147.36±5.2 MPa along the Z-axis for LRM samples of around 20% porosity. This difference in value is due to the LRM strategy. The reported tensile yield strength of the conventionally processed Inconel-625 is 414–758 MPa, 414–655 MPa and 290–414 MPa in rolled, annealed and solution annealed condition respectively [SMC 11].

The microstructural studies of the porous structures indicates that the resultant LRM specimens have pores, arranged in the form of regular arrays (see Figure 1.21a). The location of these pores is at the junctions of the adjacent tracks and adjoining layers, specifically in the track overlap region (see Figure 1.21b).

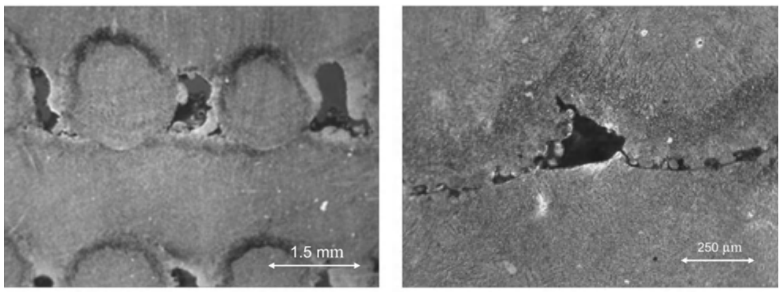

Figure 1.21. *(a)Micrograph indicating the pores; and (b) the location of pores in the LRM structure*

The previous case study demonstrates the feasibility of laser rapid manufacturing solid and porous structures of the Inconel-625 alloy. The fabrication of porous structures with control on porosities and yield strengths has vast potential in various prosthetic and engineering applications.

1.6.3. *Cemented carbide components*

In the realm of hard materials, tungsten carbide (WC) is a popular choice for tools, dies and wear prone parts and it is widely used for machining, mining, metal cutting, metal forming, construction and other applications. It has a unique combination of high strength, high hardness, high toughness and a moderate modulus of elasticity, especially with fine grained WC and finely distributed cobalt. The most commonly produced commercial straight grades of WC-Co have cobalt contents ranging from 4 to 30% by weight, with grain sizes ranging from 0.5 to 10 microns [UPA 98]. Conventionally, WC-Co is sintered at about 1,450°C to shape the components using powder metallurgy technology. In the WC-Co system, Cobalt plays the most significant role as a binder and is responsible for densification through wetting, spreading and formation of agglomerates during liquid phase sintering. A uniform distribution of metal phase in a ceramic is beneficial for improved mechanical properties of the composite. The thermo-physical and optical properties of WC-Co are listed in Table 1.7.

Properties	**Unit**	**WC**	**Co**	**Steel**
Density	kg/m^3	15,800	8,900	7,800
Melting point	Deg.C	2,687	1,495	1,435
Thermal conductivity	W/m K	84	100	68
Coeff. of thermal exp.	m/m K	4.3	14	13.7
Hardness	HRA	93	67	28
Absorption @1.06 μm	-	0.82	0.58	0.71

Table 1.7. *Thermo-physical and optical properties of WC-Co*

This indicates that the laser absorption of WC powder particles is about 1.4 times greater than that of Co for a 1.064 μm wavelength. In a WC rich powder mixture, the availability of more WC facilitates the absorption of a greater fraction of the incident laser power into WC, resulting in excessive heating and the partial melting of the WC particles. This excessive heating or partial melting of WC results in a carbon deficiency in the WC-Co alloys due to the precipitation of carbon as graphite.

$$2WC \leftrightarrow W_2C + C \qquad [1.8]$$

This graphite reacts with atmospheric oxygen and forms CO and CO_2; it often appears as gas porosity in the WC-Co system. While the carbon deficiency in the

matrix leads to the formation of a brittle ternary eutectic phase of W, Co and C (often referred to as an eta phase). An eta phase can exists in both forms, either M_6C ranging from $Co_{3.2}W_{2.8}C$ to Co_2W_4C or $M_{12}C$ for a fixed composition Co_6W_6C. In the case of laser processing, the presence of M_6C is more probable due to the rapid cooling rate. Both, graphite and eta-phase are detrimental for the mechanical properties of WC-Co deposits. Therefore, the selection of laser processing parameters and material composition play critical roles in the LRM of WC-Co.

We carried out comprehensive LRM experiments with various WC-Co compositions. We observed that WC-6 wt% Co and WC-12 wt% Co are good for uniform continuous deposit. But as the thickness increased the process became unstable, leading to a bulk-defect in the material. Therefore, WC-17 wt% Co was selected for the laser fabrication in the present study.

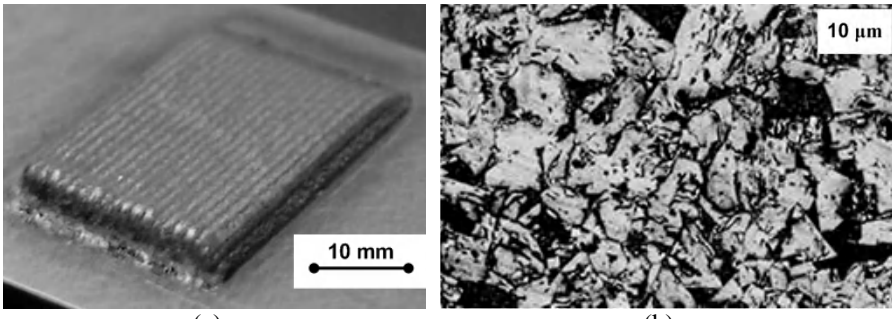

(a) (b)

Figure 1.22. *(a) Multi-layer overlapped tracks; and (b) backscattered electron image of LRM material*

Figure 1.22a shows the macro-morphology of a multi-layer overlapped LRM material. It can be seen that the multi-layer overlapped track gave a smooth rippled surface topography. It indicates that the powder particles were melted and the deposit formed was strongly bonded together. The samples were subjected to a dye-penetrant test and it confirmed that the fabricated material was mostly free from surface defects, i.e. porosity and cracks with the exception of a few samples, where micro-cracks were observed at isolated locations.

Figure 1.22b shows the backscattered electron image of the laser rapid manufactured WC-Co sample. There was a continuous film of cobalt separating the carbide particles. There was no partial or full melting of the WC particles, as the sharp edges of WC were clearly visible. The WC-Co matrix was continuous and distribution of the WC particles was uniform. The average grain size of the WC particles was about 10 microns. The microstructure observed was comparable with

that produced with the conventional sintering process [UPA 98]. It may be noted that powder particle sizes between 0.1 microns and 10 microns are used in the conventional sintering of cemented carbide and maximum transverse rupture strength is achieved when the powder particle size is in the range of 4 microns. Dynamic blowing of powder particles is very difficult, as it often results in clogging and uncontrolled flying of the metal powders. When a pre-placed bed technique, like selective laser sintering, is tried, fully dense material cannot be achieved [HUA 04, SUN 05].

The typical result of three-point flexural testing for conventionally sintered material and laser fabricated material is presented in Figure 1.23a.

In the load-displacement curve, there is a higher slope for the laser fabricated material compared to the conventionally processed material. This confirms that the laser fabricated material is stiffer than the conventionally sintered material. As per the curve, the general behavior of the laser fabricated material is more ductile, while it is brittle for the conventionally processed material. The load-displacement curve for the laser fabricated material exhibits an initial linear increase in the displacement with increasing load. As the load is further increased, the slope of the curve decreases and the material enters the plastic zone. With a further increase in the load, the slope becomes negative and leads to material failure.

During the test we observed that a crack was generated at the bottom face of the specimen and it propagated to the top, leading to complete failure. There are few valleys in the curve, specifically in plastic zone, showing propagation of cracks in the opposite direction to that of loading. It seems that these cracks are stopped by the ductile cobalt matrix, leading to recovery in loading with increasing displacement. This shows that the laser fabricated material is more resistant to abrupt loading and it is likely to get blunt, rather than break during extreme loading condition.

XRD analysis of the WC-17wt% Co laser clad sample was carried out using a CuKα source at 50 kV and 40 mA. The results of the test are presented in Figure 1.23b. The analysis confirms the presence of WC and Co phases in the laser deposited zone, while the peak for higher metallic carbides, i.e. W_3C, Co_3W_3C, Co_6W_6C, etc., is absent. In the case of conventional WC-Co sintering and continuous wave (CW) laser cladding, it is difficult to fabricate WC-Co deposits without the formation of higher carbides due to uncontrolled local heating and longer interaction time [TEC 95, CAD 97, CAY 99, HID 00]. In LRM, this could be achieved due to a very low heat input, controlled local heating and inherent rapid cooling.

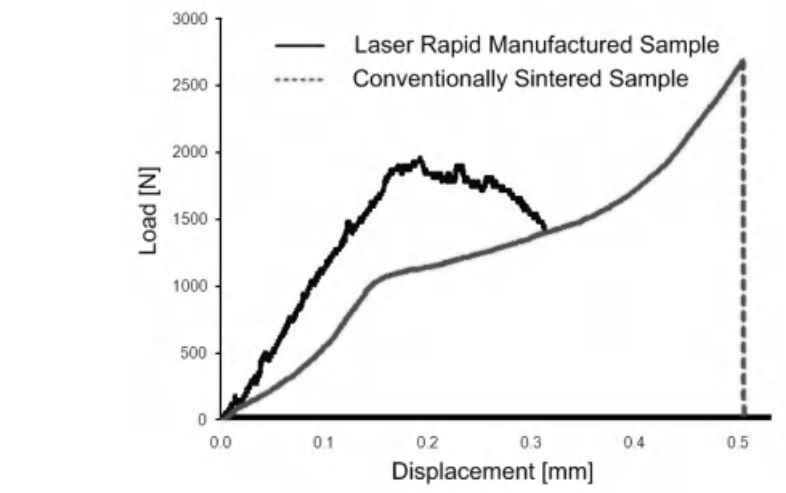

(a)

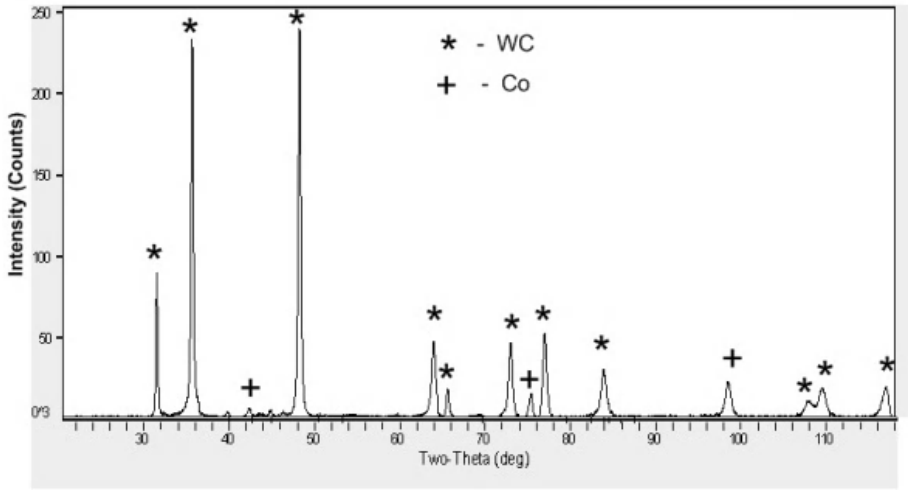

(b)

Figure 1.23. *(a) Typical load displacement curve of conventionally processed and LRM material during three-point flexural testing and (b) XRD analysis of LRM material*

LRM was deployed for the fabrication of low cost tools by depositing WC-Co on mild steel (see Figure 1.24). The performance of these tools was found to be 80% of the performance of conventionally processed tools.

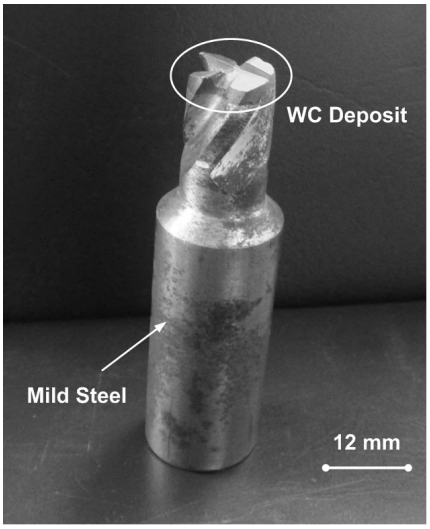

Figure 1.24. *LRM low cost cemented carbide end mill*

1.6.4. *Erosion wear resistant surfaces*

Erosion wear determines the service life of the equipment/components handling solid–liquid mixtures. Different methods like heat-treatment, surface coatings, etc., were employed to improve the surface characteristics of the target material to minimize the wear [HOL 83, LEV 85, NAI 86, BAL 91, DEU 96, IWA 01, SPE 01, TAM 02, PAU 08]. Among these methods, LRM has many advantages over conventional methods, such as good bonding between the clad layer and the substrate, low heat input and distortion of the substrate, etc. [PAU 07, KAT 00].

To reduce post-cladding machining work, the overlap between two clad layers is generally kept between 50% and 60% [BRU 88]. Further crack formation in the clad layer can be reduced by preheating the substrate [PAU 06]. The quality of the developed clad is assessed by analyzing the microstructure, crack formation, bonding between the layer and the substrate and variation of hardness along the clad depth. A number of studies were carried out in this domain relatively recently. Zhang *et al.* [ZHA 00] fabricated an Ni-alloy clad layer on martensitic stainless steel and evaluated its erosion wear with and without heat-treatment using a slurry pot tester. They found around 37% improvement in the erosion resistance of the clad surface compared to that of the substrate.

Similar improvement in the cavitation erosion resistance of an Ni–Cr–Fe–WC clad layer was observed by Tam *et al.* [TAM 02]. They attributed this improvement

to the formation of a Ni-rich matrix reinforced by precipitation of carbides and tightly bound WC particles. Iwai *et al.* [IWA 01] used TiN coating on high-speed steel by single-layered and multi-layered PVD processes. They found that the PVD coating gives 50–91% higher erosion resistance than that of the substrate material. Zhao *et al.* have applied ceramic coatings to protect the pump impeller due to slurry erosion–corrosion. The test specimens were tested in jet-in-slit rotating tester for erosion. They found that the ceramic coatings are effective in preventing the erosion damage to the pump impeller. Mann [MAN 00] fabricated a coating for the mitigation of the slit effect in the hydro-turbines of a hydropower station located in the Himalayan region. He observed a minimum volume loss for borided T410 steel followed by D-gun sprayed tungsten carbide, borided 13Cr–4Ni steel, hard chrome plating, plasma nitriding and D-gun coated chromium carbide steels. Speyer *et al.* [SPE 01] applied aluminum base coatings to AISI 1020 steel to improve erosion resistance. They observed that aluminum does not increase the erosion resistance but alloying with silicon improves its performance. They reported that erosion resistance increases with the increase in the micro-hardness, particularly at a 30º impact angle compared to a 90º impact angle. Deuis *et al.* [DEU 96] observed that the aluminum–silicon alloys and aluminum-based MMCs containing hard particles offer superior operating performance and resistance to wear.

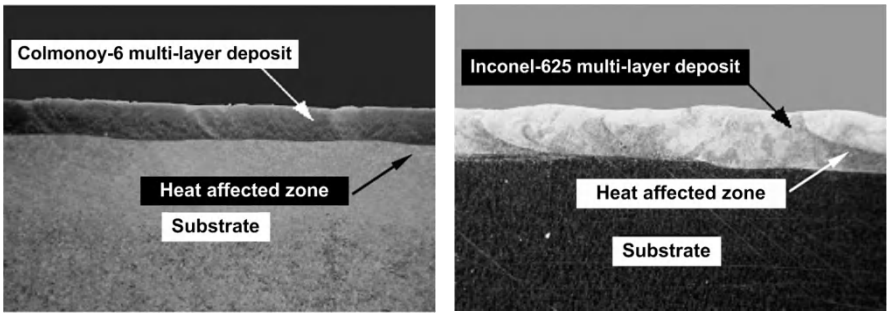

Figure 1.25. *Macrographs of a cross-section of: (a) Colmonoy-6 overlapped track on AISI 316L steel; and (b) Inconel-625 overlapped track on AISI 304L steel*

The hard-facing of an austenitic stainless steel surface, two nickel-based powders, Colmonoy-6 and Inconel-625 by LRM was investigated. Figure 1.25a and b present the macrographs of the cross-section of Colmonoy-6 overlapped track on AISI 316L steel and Inconel-625 overlapped track on AISI 304L steel respectively. The micro-hardness of the clad layer over the cross-section for Colmonoy-6 and Inconel-625 was measured. It was observed that three distinct zones appear in the micro-hardness curve corresponding to the substrate, interface region and clad layer. At the substrate, the micro-hardness is observed to be

approximately 200 VHN, which is representative of AISI 316L steel. A noticeable improvement in the surface micro-hardness was observed at the fusion line showing 354 VHN. The micro-hardness value increases very rapidly from 354 to 688 VHN in the beginning of the clad layer. The microhardness in the entire clad layer varies from 643 to 746 VHN. The variation in the micro-hardness may be attributed to the microstructural variation across the interface in the clad layer. Similarly, the micro-hardness of the Inconel-625 clad layer was determined at a 0.981 N load. It was observed that the substrate material shows a 216 VHN micro-hardness, while the interfacial region shows a slightly higher micro-hardness at 252 VHN. Increasing the distance from the fusion line towards the clad layer shows a gradual increase in the micro-hardness. The micro-hardness of whole Inconel-625 clad layer varies from 244 to 352 VHN. This shows that the micro-hardness in the clad layer is only marginally higher than the substrate (AISI 304L steel).

The schematic diagram of a slurry pot tester used for erosion wear studies as shown in Figure 1.26. The detail of this tester is described by Desale *et al.* [DES 05].

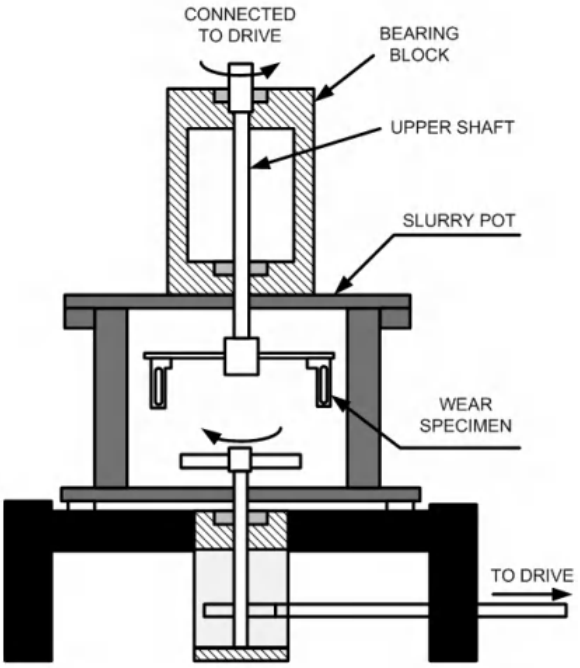

Figure 1.26. *Schematic diagram of a slurry pot tester*

The wear behavior of both the substrates and the claddings of Colmonoy-6 and Inconel-625 were evaluated using a slurry pot tester at a velocity of 3 m/s with a quartz-water particulate mixture of 550 μm sized particles. The solid concentration was kept as 10% by weight and the orientation angle was varied in the range of 15–90º. The measurement of mass loss in a known time period was used to evaluate the erosion rate in gram-per-gram (g/g) of impacting solid particles. The erosion rate of both the clad surface and the substrate materials at different impact angles is given in Figure 1.27a and b.

AISI 316L steel shows an increased erosion rate with an increase in the orientation angle, showing the maximum erosion rate as 1.73×10^{-8} g/g for a 22.5º orientation angle which decreases with a further increase in the angle till 90º; while the Colmonoy-6 clad layer shows the variation of the wear with the angle, showing the maximum wear as 0.368×10^{-8} g/g for a 45º orientation angle. It was observed that the Colmonoy-6 clad showed improvement in erosion wear resistance in the range of 41.5–77.8% compared to the substrate material, i.e. AISI 316L steel over the range of orientation angles. At a 22.5º orientation angle, the cladding shows the maximum improvement of 77.8% in erosion wear resistance, which may be due to the increase in the clad layer surface hardness (700 VHN) reducing the cutting wear contribution.

Similarly, the erosion rate (g/g) of Inconel-625 cladding and AISI 304L steel versus the orientation angle is presented graphically in Figure 1.27b. It was observed that the erosion rate of AISI 304L steel increases with an increase in the orientation angle showing a maximum erosion rate of 1.88×10−8 g/g for a 22.5º orientation angle, and then decreases with further increase in the angle until 90º. The Inconel-625 clad layer also shows a similar variation of the wear with the angle showing maximum wear at a 30º orientation angle.

It was observed that Inconel-625 clad shows around 30.6% improvement in the erosion resistance at a 15º impact angle compared to the substrate material. However, Inconel-625 clad does not show any significant improvement in the erosion wear resistance at higher impact angles compared to that of the substrate material (AISI 304L steel). A possible reason for the lack of improvement in the erosion wear resistance of the clad layer may be the higher degree of dilution and insignificant improvement in the micro-hardness of the clad layer [MAN 00].

Experimental investigations on the erosion wear behavior of the LRM surface of Colmonoy-6 and Inconel-625 on SS316L and SS304L were carried out, and showed improvement in the surface properties of engineering materials.

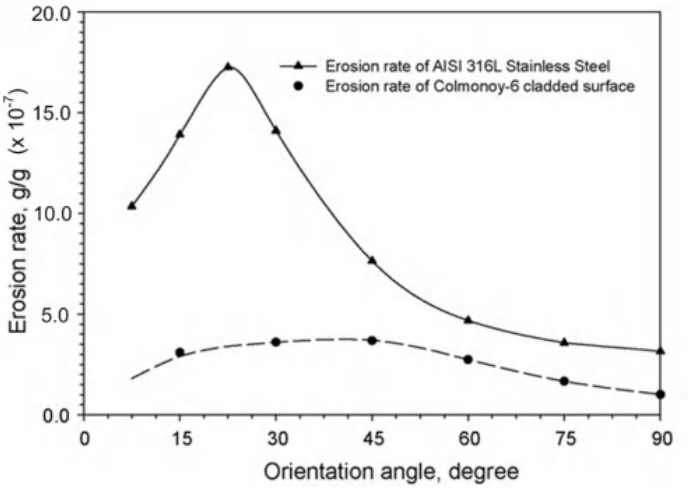

(a)

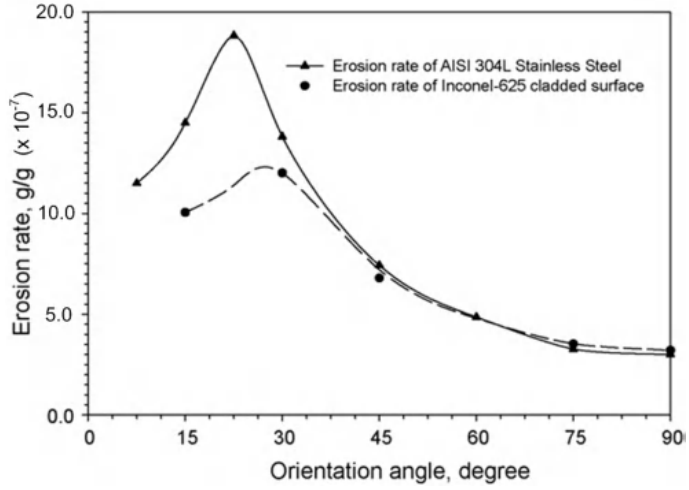

(b)

Figure 1.27. *Variation of the erosion rate of the substrate and clad layer with the orientation angle (d = 550 µm, Cw= 10 wt. %, V = 3 m/s). (a) AISI 316L steel and Colmonoy-6 clad layer and (b) AISI 304L steel and Inconel-625 clad layer*

1.7. LRM process modeling

Figure 1.28 presents the schematic arrangement of the LRM process domain. The physical domain of the LRM process consists of a substrate, deposited material,

a powder stream and a laser beam. To model the process, the laser beam specifications, material deposition, laser beam-powder interactions and heat transfer throughout the process domain should be integrated in a dynamic fashion.

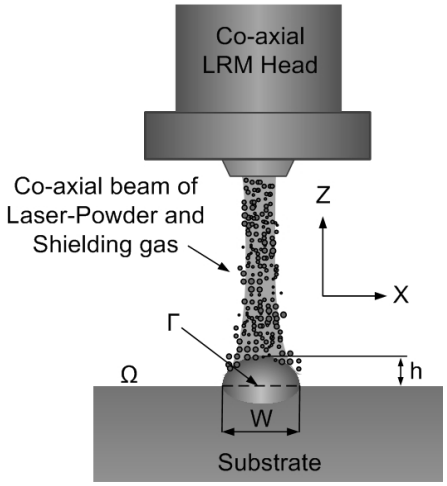

Figure 1.28. *Schematic arrangement of the LRM process domain*

Figure 1.29 presents various interaction zones (involving laser, powder, shielding gas and substrate) and their effects. The total interaction process can be divided into two interaction zones, i.e. the first interaction zone involves laser-shielding gas and powder, while the second interaction zone engages the laser, shielding gas, powder and substrate. The powder particle speed and the stand-off distance (distance between the substrate and nozzle) define the flight period and govern the interaction of the powder and laser beam for pre-heating. The local distribution of powder particles in the stream and the spatial profile of the laser beam determine the temperature of powder particles after the first interaction zone.

As a result of these interactions the laser energy is either absorbed by powder or it transmits through the powder cloud to the substrate or some of the energy is lost due to the reflection by powder particles and radiation. In the second interaction zone, the transmitted laser energy melts a thin layer of the substrate causing wetting of the substrate and the preheated powder falls, melts and forms a molten track on the substrate. The molten track undergoes self-quenching and solidifies to form a track. In this interaction zone, the laser energy is either utilized to melt the powder and substrate or lost through reflection, heat convection, conduction and radiation.

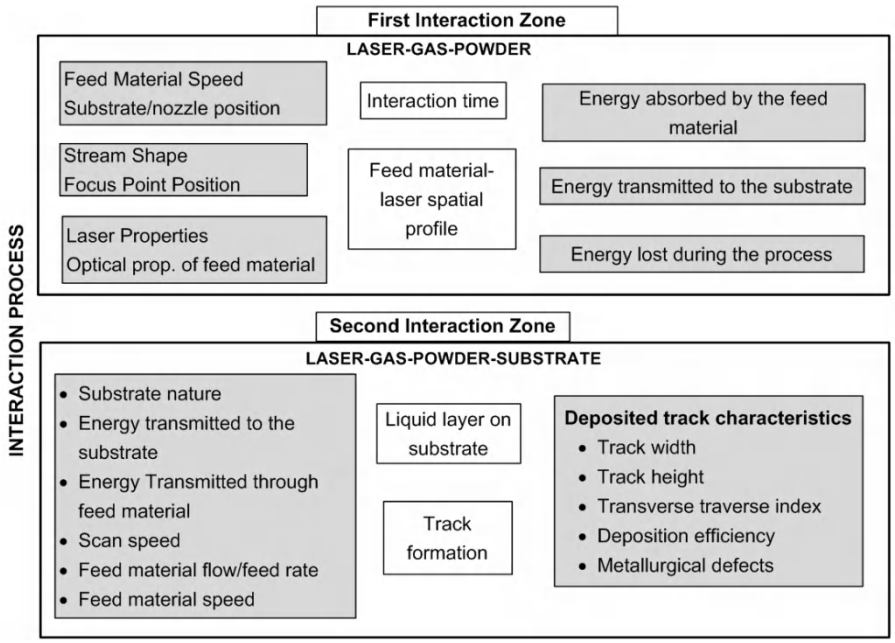

Figure 1.29. *Various interaction zones involving the laser, powder, shielding gas and substrate and their effects*

All the physical phenomena described above in the process domain can be mathematically presented by the following continuity, momentum balance and heat conduction equations:

– continuity equation:

$$\frac{\partial \rho}{\partial t} + \nabla .(\rho u) = 0 \qquad [1.9]$$

– momentum balance equation:

$$\frac{\partial (\rho u_n)}{\partial t} + \nabla \cdot (\rho U u_n) = \nabla \cdot (\mu \nabla u_n) - \frac{\partial p}{\partial n} - \frac{\mu_l}{k}\frac{\rho}{\rho_l} u_n + \rho g \qquad [1.10]$$

– heat conduction equation:

$$\nabla\left(K\,\nabla T\right)+Q=\frac{\partial\left(\rho C_p T\right)}{\partial t}+U\cdot\nabla\left(\rho C_p T\right) \qquad [1.11]$$

where ρ(kg/m^3) is the density, t (s) is time, U (m/s) is the velocity vector, p (Pa) is the pressure, μ (kg/m.s) is the viscosity, g (m/s^2) is the gravity field, K (kg/m.K) is the thermal conductivity, c_p (J/kg.K) is the specific heat capacity, Q (W/m^3) is the power generated per unit volume within the substrate, and u_n (m/s) is the liquid velocity in the n-direction, respectively. In equation [1.10], the third terms on the right side are the Darican damping terms which represent the damping force for liquid passing through a porous zone. In these terms, ρ_l (kg/m^3) is the density of liquid, μ_l (kg/m.s) is the viscosity of liquid, and k is the permeability of the porous media which can be defined by the Kozeny-Carman equation.

The above equations are solved under the following appropriate initial-essential and boundary conditions:

$$\begin{aligned} &T(x, y, z,0) = T_0 \\ &T(x, y, z,\infty) = T_0 \end{aligned} \qquad [1.12]$$

$$\begin{aligned} -K(\nabla T\cdot n)_{\Omega}| &= \left[\beta_e\, I(x,z,u)-h_c\,(T-T_0)-\varepsilon\sigma\left(T^4-T_0^4\right)\right]_{\Omega} \quad \text{if } \Omega\in\Gamma \\ &= \left[-h_c\,(T-T_0)-\varepsilon\sigma\left(T^4-T_0^4\right)\right]_{\Omega} \quad \text{if } \Omega\notin\Gamma \end{aligned} \qquad [1.13]$$

where n is the normal vector of the surface, β_e is the effective absorption factor, ε is the emissivity, σ is the Stefan-Boltzman constant; I (Wm^{-2}) is the laser energy distribution on the unit length and u (m/s) is the velocity of the laser beam normal to the cross-section of work piece; h_c is the heat convection coefficient (Wm^{-2} K), Ω (m^2) and Γ(m^2) are the area of unit length work piece surface under laser beam irradiation; and T_0 (K) is the ambient temperature.

Considering the above equations, there have been several studies using analytical and numerical tools with newer or alternative strategies for better process insight and superior understanding of the LRM process. A 2D thermal model was developed to predict the temperature distribution in the deposited metal for SS316 during the LENS process as a function of time and process parameters [WAN 06].

A three-step analytical and numerical approach was used with a finite element calculation to predict the shapes of manufactured structures and thermal loadings

[PEY 08]. The effects of heat conduction, Marangoni flow and thermal buoyancy, on melting process and the shape of molten pool were numerically analyzed [YAN 01]. An analytical model was used to predict the effect of the beam shape on the melt-pool shape and optimized the overlap required for laser surface processing applications [AHM 10]. The numerical model for a pulsed laser considered the cladding and established the correlation between the track geometry and laser pulse shaping parameters (laser pulse frequency and energy) when the other process parameters were constant [TOY 04]. A theoretical model, supported by an experiment, was investigated to optimize the process parameters for the fabrication of a less than 1 mm thin wall [LIU 06]. A self-consistent 3D model was developed for a coaxial laser powder cladding process, which simulates heat transfer, phase changes, and fluid flow in the molten pool [QI 06]. A mathematical 3D model was developed to simulate the temperature and composition distribution during the laser cladding process of the H13 tool steel for a laser beam of TEM_{00} [HE 10]. The model assumed the temperature independent thermo-physical properties and absorption coefficient of the laser and they were considered to be the same for the substrate and the powder. A comprehensive model was developed to evaluate the track geometry during LRM [ALI 07]. In addition, a FEM based model was developed for the determination of the track geometry and dilution in laser cladding [HOF 11].

An analytical approach for estimating the track characteristics (track height and width) was presented based on the mass conservation of the powder feeding stream [WAN 11]. Here, the simulation was capable of predicting the track width and height with reasonable accuracy at a medium powder feed rate. Recently, a finer 2D numerical modeling approach was developed and published by the authors to simulate the track geometry during LRM [KUM 12]. The following section presents the modeling efforts as a case study.

In the present study, the Eulerian description method is applied and a finite element method (FEM) based finer approach is used to simulate track geometry and temperature distribution in 2D during LRM [KUM 12]. The consideration of all phenomena occurring during LRM makes the problem highly complicated. Hence, the following adjustments as well as assumptions are made to reduce the complexity with a minimum compromise to the process description.

(a) To take the effect of laser-material interaction into account in the modeling, a method developed by Picasso *et al.* [PIC 94] is considered. Based on this method, the total power absorbed by the work piece P_w can be defined as:

$$P_w = P_d + P_p = \beta_e \, P_l \qquad [1.14]$$

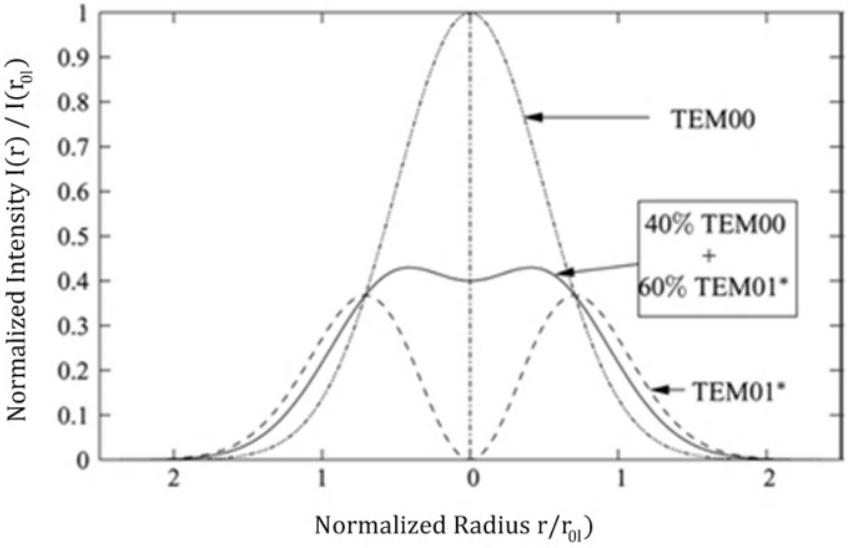

Figure 1.30. *Laser beam profiles: fundamental and mixed modes [KUM 08]*

(b) Laser energy distribution: the laser beam is assumed to be a mixture of the first two fundamental modes, 40% TEM_{00} and 60% TEM_{01}, which gives a near flat top beam profile (see Figure 1.30). The combined intensity profile for a mixed mode laser beam is given by Kumar *et al.* [KUM 08] as:

$$I_l(r) = \frac{2P_l}{\pi r_{0l}^2}\left[a + (1-a)\frac{2r^2}{r_{0l}^2}\right] exp\left[-\frac{2r^2}{r_{0l}^2}\right] \qquad [1.15]$$

(c) Powder particle distribution: a coaxial powder jet with a laser is considered in the model. The total mass of the powder has a weighted distribution factor consistent with a standard Gaussian distribution of powder particles, normal to the powder flow direction. Each vertical slice of the domain, parallel to the direction of the track deposition, limits the deposition according to the local distribution of powder particles, conforming to energy and mass balance. In this way, the local height of the track is defined considering the powder particle distribution.

(d) Latent heat of fusion: the effect of the latent heat of fusion on the temperature distribution is considered by modifying the specific heat capacity, c_p* [LEW 04]:

$$\begin{aligned} c_p^* &= c_{ps} && (T < T_s) \\ c_p^* &= \frac{L_f}{T_l - T_S} + c_{pf} && (T_s < T < T_l) \\ c_p^* &= c_{pl} && (T < T_l) \end{aligned} \qquad [1.16]$$

where, T_s and T_l are the solidus and the liquidus temperatures, respectively, for a phase change over an interval of temperatures T_s and T_l .

(e) Marangoni flow: the effect of fluid motion due to the thermo-capillary (Marangoni) phenomena is considered by modifying the thermal conductivity K*. This modification is presented as:

$$K^*(T) = \alpha\, K(T_m) \qquad if \quad T > T_m \qquad [1.17]$$

where α is the correction factor. The recommended correction factor based on the experimental work is 2.5 [LAM 97].

(f) Power attenuation: the laser beam passes through the powder cloud and falls on the work-piece. During this journey, a part of the laser power is absorbed by the powder particles, a part is absorbed by the substrate and the remainder is reflected by the powder particles/substrate. The energy added to the substrate by the laser beam is presented by the following expression:

$$Q_s = (1-\beta_p)\beta_s P_l \Delta t \qquad [1.18]$$

The interaction time can be defined as:

$$\tau = \frac{2 r_l}{u} \qquad [1.19]$$

(g) Combined heat transfer coefficient: a combined radiative and convective heat transfer coefficient (h_c^*) is considered in order to reduce the computational time [GED 04]:

$$h_c^* = 24.1 \times 10^{-4}\ \varepsilon_t\ T^{1.61} \qquad [1.20]$$

(h) Temperature dependency of material properties: in the proposed modeling approach, material properties are considered to be temperature dependent.

Using the assumptions listed above, as well as assuming a constant velocity for the moving laser beam, if equations [1.14] to [1.20] are inserted into equation [1.11], the simplified boundary condition is derived as:

$$-K(\nabla T \cdot n)|_{\Omega} = \frac{2\beta_e P_l}{\pi r_l^2}\left[a+(1-a)\frac{2(x-u_x t)^2}{r_l^2}\right] \times exp\left[-\frac{2r^2}{r_l^2}\right] - h_c^*\,(T-T_0) \quad for \quad \Omega \in \Gamma \qquad [1.21]$$
$$= -h_c\,(T-T_0) \qquad if\ \Omega \notin \Gamma$$

The above equation is solved in the process domain using the FEM method, to simulate temperature distribution, as well as the shape and size of the melt-pool. Once the melt-pool boundary is obtained, the material addition is incorporated into the model by calculating excessive enthalpies above melting point for all nodal points in the process domain and using those for the computation of local track height at every node along the track width on the substrate. The local height $h_e(x)$ of the track for each discrete location *i* is computed by considering the energy balance of the molten pool beneath it. Mathematically, it can be represented as:

$$Z_{new,e}\big|_{\Omega} = z + h_e(x)\big|_{\Omega} \qquad at \qquad (x,z) \in W_{jet}^{melt} \qquad [1.22]$$

$$W_{jet}^{melt} = \left\{\left[(x,z)\middle|T_{(x)} \geq T_m \in W_{melt}\right] \cap \left[(x,z) \in W_{jet}\right]\right\} \qquad [1.23]$$

$$h_e(x) = \frac{h_{melt}(x)\,\rho_w\ \{C_p\ (T(x)-T_m)+L_f\}_w}{\rho_{jet}\ \{C_{pp}\ (T_{mp}-T_i(x))+L_{fp}\}_{jet}} \qquad [1.24]$$

where, $T_i(x)$ and $T(x)$ are the local preheating temperature of the powder material and the local temperature of the molten pool, respectively. The effect of the powder flow rate and its local distribution is incorporated into the model by calculating the local track height $h_m(x)$ and using the conservation of mass, as represented by the following mathematical expressions:

$$h_m(x) = \frac{\eta\, m_p}{W_{jet}\ \rho_{jet}\ u} \qquad [1.25]$$

Finally,

$$h_{new} = h_e \cap h_m \qquad [1.26]$$

Actual track height h_{new} is the minimum of the two heights, i.e. h_e and h_m. It may be noted that the proposed methodology carries out the mass and energy balance at the end of each time step, and calculates the geometry of the deposited material during that time step. This deposited geometry is meshed and used for the subsequent computational steps. The temperature distribution for each discrete step for the interaction time period in the process domain was computed. Using the temperature distribution through the substrate, the melt-pool boundary was estimated using the constant enthalpy method, where a single equation is applicable for both the solid and liquid process domains. Thus, the computed cumulative enthalpy difference between the nodal enthalpy and the enthalpy at the melting point was used for the prediction of the track geometry by applying the conservation of energy. To implement this methodology recursively, a combined code was developed.

As the Eulerian method of description is used, the laser-material interaction time at the observation plane will be limited to interaction time (τ). Therefore, the interaction time is divided into finite time steps (Δt) to simulate the temporal temperature distribution and track geometry. Figure 1.31 presents the temporal track geometry and melt-pool at three discrete time steps $\Delta t = \tau/10$, $\Delta t = \tau/2$ and $\Delta t = \tau$.

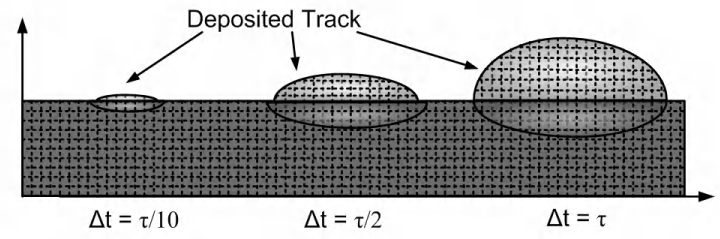

Figure 1.31. *Schematic of the temporal track geometry and melt-pool at various time steps*

The effect of the laser beam, in mixed mode at various laser scanning speeds, on track geometry was numerically simulated. Figure 1.32a presents the simulated results of the effect of the scan speed on the predicted track, i.e. scan speeds of 300, 600, 1,000 and 3,000 mm/min with a fixed laser power (P_l) of 800 W and powder feed rate (m_p) of 8 g/min. A decrease in the track height was observed with the increase in scan speed, due to the reduced powder feed per unit length when sufficient laser energy per unit length is available. Also, the track width decreased with the increase in the scan speed; this is primarily due to a reduced interaction time. The effect of the laser beam in mixed mode at various powder feed rates on track geometry was also numerically simulated. Figure 1.32b presents the simulation results of the effect of the powder feed rate on track geometry, i.e. rates of 3, 5, 8

and 12 g/min with a fixed laser power (P_l) of 800W and scan speed (u) of 300 mm/min. It was also observed that at a constant laser power, the track height increases to a certain value with the increase in the powder feed rate and thereafter saturates. This is because a minimum laser energy per unit length is required to melt the incoming powder per unit length.

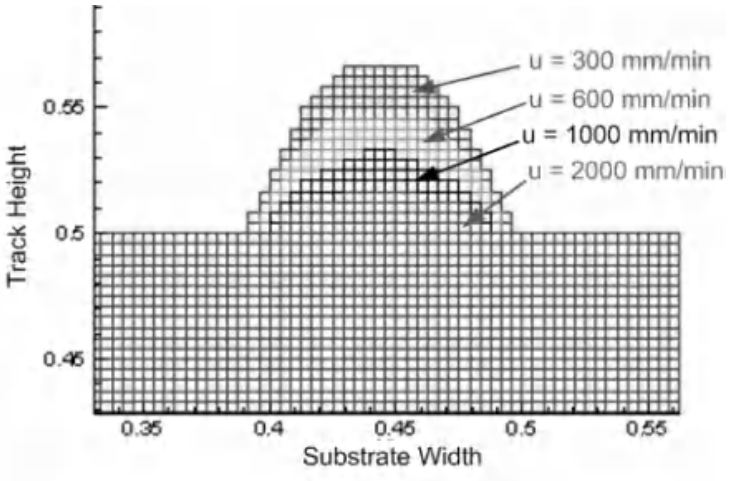

(a)

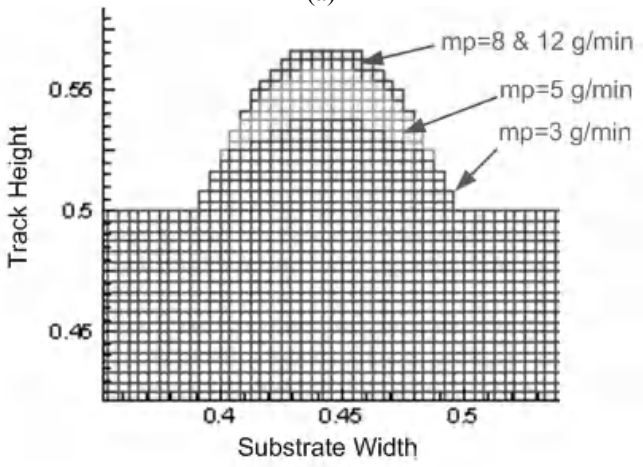

(b)

Figure 1.32. *Effect of: (a) scan speed; and (b) powder feed rate on track geometry*

A number of track geometries were simulated using the developed model with different sets of processing parameters. For the same set of processing parameters,

the tracks were laid and cut normal to the scanning direction. The track geometries were examined under the optical microscope. The experimental results for track height and width were comparable with the simulation results. The results of experiments with a mixed mode laser beam confirmed the trend for various powder feed rates. The simulation results of track geometries and its experimental verification for powder feed rates 5 g/min and 8 g/min with fixed laser power (P_l) of 800 W and a scan speed (u) of 600 mm/min are presented in Figure 1.33a and b respectively.

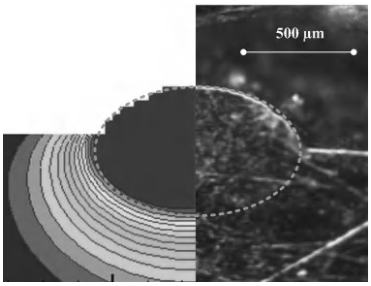

Track geometry comparison for P_l=800 W, m_p=5 gm/min, u=600 mm/min

(a)

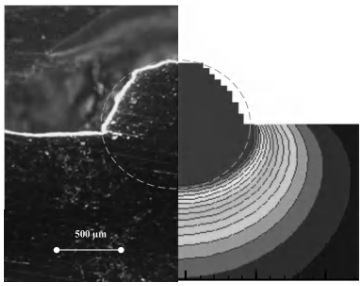

Track geometry comparison P_l =800 W, m_p=8 gm/min, u=600 mm/min

(b)

Figure 1.33. *Comparison of track geometry at P_l=800 W, u=600 mm/min at various powder feed rates: (a) m_p=5 gm/min; and (b) m_p=8 gm/min*

The above modeling approach and its experimental verification indicate that the temperature distributions and geometries of the deposited material can be predicted for various processing parameters with the above listed simplifications. Efforts are being made to model the process with more realistic conditions, by considering the various phenomena involved with a more generic approach.

1.8. LRM process control

From the above sections, it is clear that LRM is a complicated multi-parameter process. Laser power, laser beam size, scanning speed and powder flow rate plays a primary role on the quality of deposits, while the transverse traverse index, powder size, shielding gas, rastering pattern and the substrate temperature play the role of secondary important parameters [MAZ 99]. Most of the applications that have been adopted in the industries do not have a close loop control of these parameters, but still achieve good quality and reproducibility. This is just because the adopted combination of the material and processing system has a larger processing window.

In many applications, a small disturbance from one or more of these parameters causes the processing point to depart from the narrow processing window, and the application fails in quality and reproducibility. Monitoring process dynamics and online control of these primary and secondary parameters is the solution for such applications with a narrow processing window. Hence, advanced and intelligent process control is the key for the successful deployment of LRM technology for many critical applications.

The complete control of LRM requires the monitoring of many in-process signals and is challenged with simultaneous control of processing parameters. The interdependence of these processing parameters further aggravates the complexities. For example, track width, height, temperature and dilution depend on variables such as laser power, laser beam size, scan speed, powder feed rate and substrate surface conditions. The straight control loop for all these variables may serve the purpose, provided other variables do not deviate from their optimum. Hence, the control system needs to diagnose what is wrong, if anything, what to alter and by how much. Hence, it is a field of active research worldwide. Figure 1.34 presents various processing parameters, their relevance and possible control options.

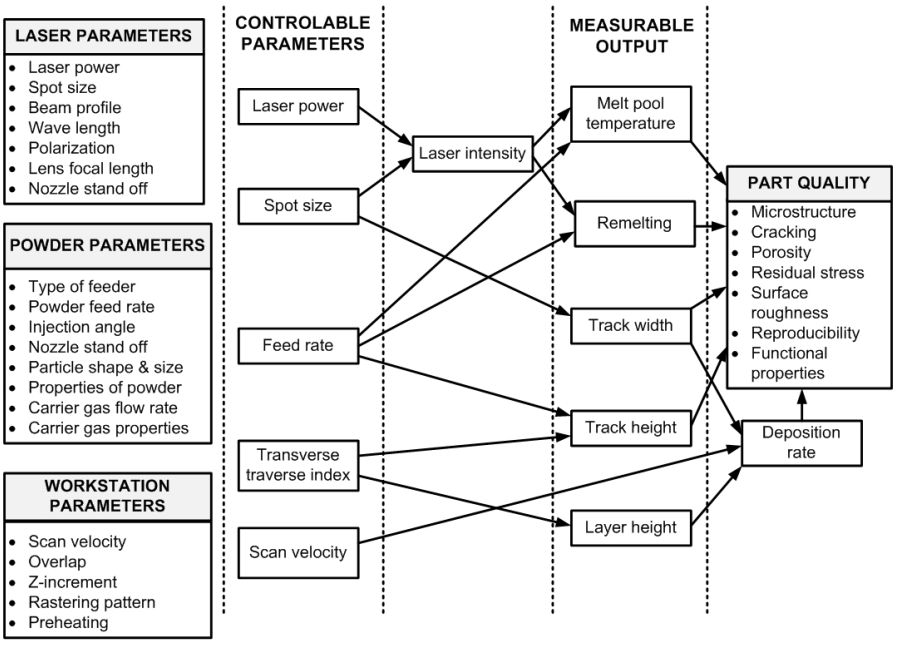

Figure 1.34. *Various processing parameters, their relevance and possible control options*

Due to the harsh environment created by high power laser and metal powders, non-contact-type sensors are preferred over contact-type sensors. Recent advances in electronics provided great benefits. Digital cameras with high resolution and speed are extensively being deployed to estimate track geometry [TYL 11, MEH 07, CRA 11, MER 96, DON 03], powder flow distribution and particle velocity [TAN 11] and melt-pool surface temperature [MER 96]. Photodiodes are also used to measure the melt-pool temperature from the infrared radiation and to monitor the melt-pool height in a triangular setup [MAZ 00]. Dual wave-length pyrometers are employed to monitor the melt-pool temperature [DON 03, SAL 06]. It is well established that the methodologies using cameras provide the most comprehensive information about the process with limited processing speed due to image processing, while the methodologies using photodiodes and pyrometers are simple and provide limited information with a faster response time. In the following section detailed information about some of the measurement methodologies of relevant LRM parameters for process control is presented.

1.8.1. *Measurement of melt-pool temperature*

The melt-pool temperature is one of the prominent parameters, which is more clearly indicative of many output-characteristics (e.g., track width, height and re-melting). The melt-pool temperature can be measured using conventional techniques (e.g. thermocouple [HU 00]), but they lag in versatility due to a contact-based approach. During LRM, the laser beam travels over the substrate and contact type sensors are mounted at a fixed location on the substrate. It is difficult to measure the local temperature of the laser–powder–substrate interaction resulting in the melt-pool using contact type sensors. In addition, the temperature of the melt-pool is very high, which necessitates the use of a non-contact type sensor. Therefore, emission based instruments are used that estimate the temperature by measuring the intensity of a particular wavelength emitted by the melt-pool. However these instruments have limitations in their usability for different materials due to different emissivities [XIN 06]. To overcome this limitation, dual-wavelength-based pyrometers are used to measure the melt-pool temperature [HUA 08, SON 11a].

Figure 1.35a shows the schematic arrangement of a temperature measurement setup as the laser beam reaches point a (i.e. at the beginning of the pulse) on the substrate and then reaches point b and c respectively, as shown in Figure 1.35a. When the laser beam passes these points, the average energy deposited at the unit width surface along the scan direction on the substrate increases resulting in an increase in the temperature (see Figure 1.36b). The temperature reaches a maximum when the laser beam is at the shortest distance from point d, i.e. point b. As the laser moved further ahead, the temperature falls due to heat loss due to conduction and convection.

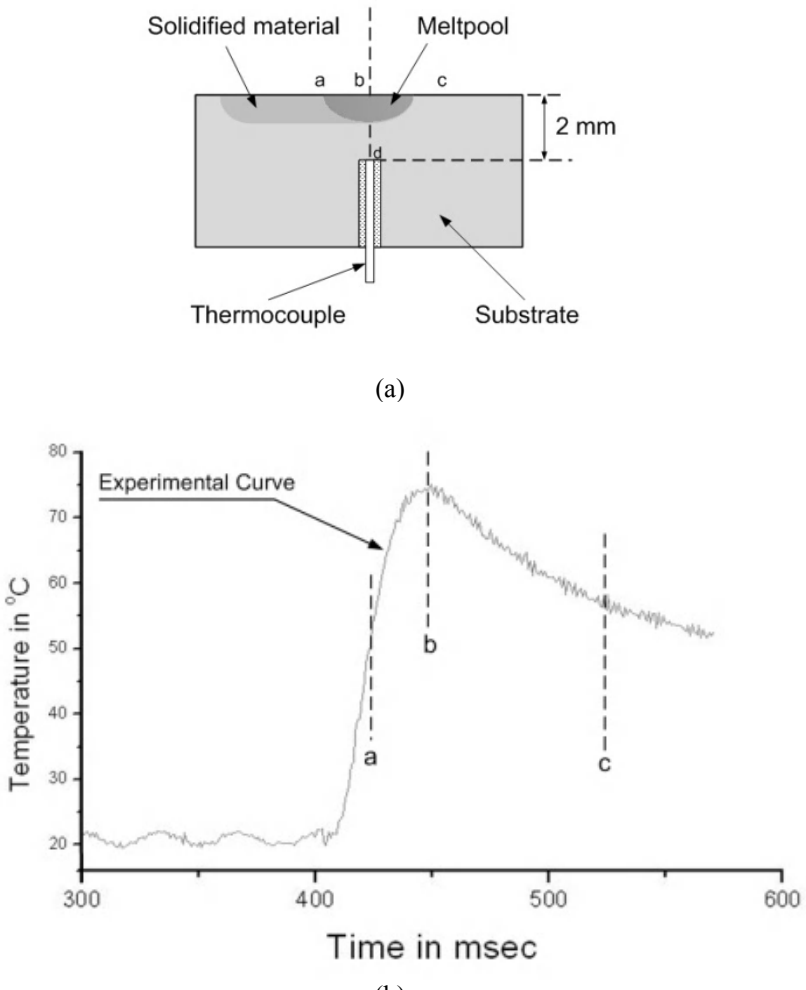

Figure 1.35. *Temperature measurement by the contact method: (a) schematic arrangement; (b) time-temperature curve*

In LRM, the melt-pool temperature depends upon laser power, beam size, scan speed and powder feed rate as controllable processing parameters. It also depends on uncontrollable parameters, i.e. surface roughness, the incident angle of the laser beam, etc. [HUA 08]. The effect of these parameters is presented in Table 1.8.

With an increase in processing parameter	Melt-pool temperature	Reason
Powder feed rate	Decreases	Laser energy is absorbed by a greater number of powder particles
Scanning velocity	Decreases	Reduction in laser energy per unit length
Laser power	Increases	Increase in laser intensity
Laser beam size	Decrease	Reduction in laser intensity
Subsequent layer	Increases	Due to the pre-heating effect
Incident angle	Decreases	Due to a lower absorption coefficient
Surface roughness	Increases	Due to a higher absorption coefficient

Table 1.8. *Effect of the LRM processing parameters on the melt-pool temperature*

1.8.2. *Measurement of track geometry*

Precise control in track geometry governs the overall shape and size of the laser rapid manufactured component, as the track is an elementary block of the fabrication. Triangulation and image processing based techniques have been tried to estimate the dimension of track geometry. The triangulation technique uses an external line laser source and camera, as presented in Figure 1.36. In this scheme, an external laser is scanned over the molten/solidified track near the molten pool and a reflected laser is collected at the camera. Then, the triangulation algorithm is employed to measure the track geometry.

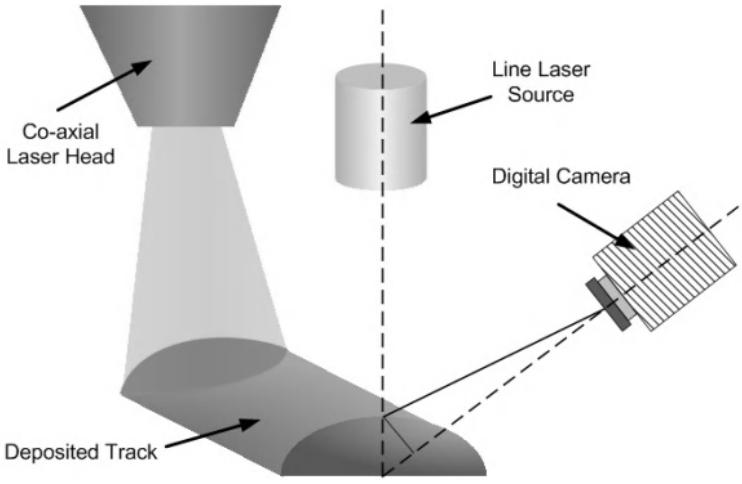

Figure 1.36. *Measurement of track geometry by the triangulation method*

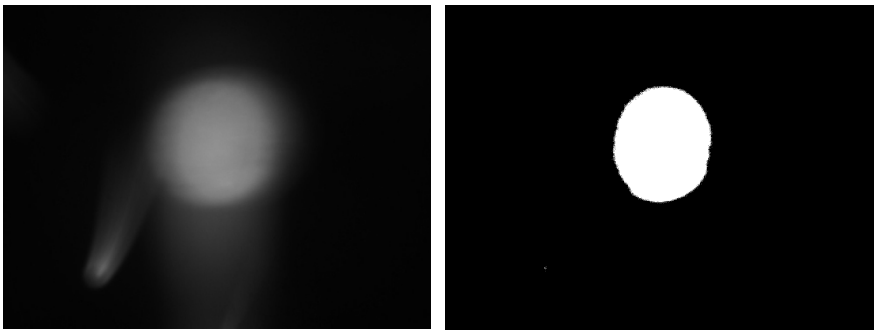

(a) (b)

Figure 1.37. *(a) Typical gray image of the molten pool; and (b) corresponding image after employing the binarization technique*

Due to its high temperature, the molten pool is an immense heat source emitting light in the broader range of wavelengths from ultraviolet to infrared. The CCD/CMOS based cameras with neutral density filter (10–20% transmission) are generally employed to capture the image of the melt-pool [HER 10, SON 11b, MEH 07, CRA 11]. The acquired gray melt-pool image is then used to estimate the actual size, shape and location of the molten pool by employing the binarization technique for a selected gray value. The selection of the gray value depends upon the LRM system configuration and geometry being fabricated. Figure 1.37a shows a typical gray image of the molten pool exhibiting a decreasing value of gray level from the center toward the outside; Figure 1.37b presents the corresponding image after employing the binarization technique. The computed binary image is compared with a reference image produced either by offline measurements or by isotherms of infrared imaging and thus, a generated error signal is sent to the process controller for remedial actions.

1.8.3. *LRM process controllers*

While considering the above discussion, it is easy to start with one control output and one measurement input to design the controller. This can be further extended to multiple outputs and multiple inputs. Temperature and geometry represent them as the obvious choice for the controller input. It is observed that a controller based on a simple on-off logic is able to give better output results [SON 11b], but using some advanced control logic output quality can be improved further. Traditional controllers, i.e. PID, are designed on the basis of system equations resulting in improved output [SAL 06, FAT 07]. However, these equations are not truly representative of the process, thus knowledge based control methodologies are

finding more recognition than traditional methodologies [DON 03]. They exploit the knowledge base generated for each possible condition during the LRM process. This knowledge is used in a neural network to make decisions. This controller can avoid the requirement for accurate modeling of the system dynamics. These knowledge based systems need time to make decisions due to their large data base. This time can be minimized by using a feed forward mechanism to assist it.

Laser power, scan speed and powder feed rate are basic control inputs. Shutter position, standoff distance, laser input current, auxiliary gas speed, etc., are degenerative controls which ultimately affect the main control input. It is observed that laser power variation is not as quick as the variation in the scan speed. So scan speed is preferred over laser power as a control input.

1.9. Future prospects

Though the LRM has many advantages in terms of quality, reproducibility and a shorter cycle time compared to conventional technologies, they are currently not being supported by industrial economics in many applications. Hence, LRM and conventional technologies are being combined together to enhance the mutual advantages and reduce the adverse effect of the individual constituent processes. This is called hybrid processing. In general, manufacturing processes can be classified into three classes: additive, subtractive and forming. Figure 1.38 presents the classification of the manufacturing processes.

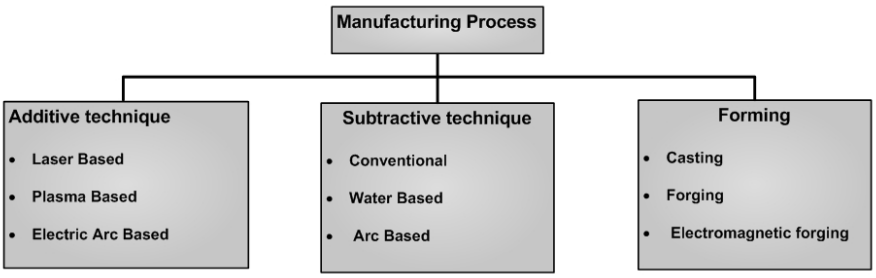

Figure 1.38. *Classification of the manufacturing processes*

In the additive manufacturing technique, the components or indented near net shape geometry is manufactured directly from a solid model by consecutive layer-by-layer deposition technique via a fusion, sintering and polymerization technique. In the subtractive processes, the final geometry is built by machining the block. All conventional manufacturing processes are subtractive processes. Forming refers to a

group of manufacturing methods by which the given material, usually shapeless or having a simple geometry, is transformed into a useful part without changing the mass or composition of the material. This part usually has a complex geometry with well-defined (a) shape, (b) size, (c) accuracy and tolerances, (d) appearance and (e) properties. The example of metal forming processes includes cold and hot forging, extrusion, rolling, bending and deep drawing. In a hybrid manufacturing process, the final geometry shape, with conditional accuracy, is achieved by combining either more than one additive process or combination an additive and a subtractive manufacturing process. Hybrid manufacturing may also have two different additive techniques. The different possible combinations of the hybrid process are present in Figure 1.39.

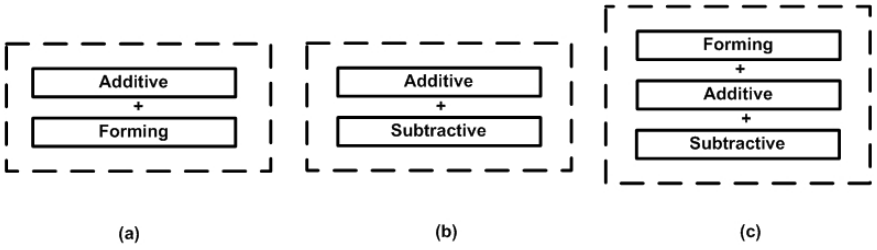

Figure 1.39. *Different combinations for hybrid manufacturing*

When LRM is combined with one of the conventional processes, it is known as hybrid laser rapid manufacturing. The hybrid process is adopted to address specific problem issues like deposition rate, geometrical precision, reduced cycle time, enhancing manufacturing volume, tumbling geometrical complexity, tailored multi-material geometry; large component size, etc. The material used for prototyping can be solid or liquid depending on the type of application and the usage. Research on hybrid processing is being pursued by different laboratories under different process nomenclatures. These are controlled metal buildup, which uses Laser cladding/welding with 2½ axis milling at the Fraunhofer Institute for Production Technology (IPT) Germany; shape deposition manufacturing, which is a combination of micro-casting and milling at Carnegie Mellon University, United States; CO_2 laser based processing and milling at the Korea Institute of Machinery and Materials, Korea; 3D welding and milling at the Korea Institute of Science and Technology, Korea [SRE 06]. The combination of process selection for hybrid manufacturing depends on materials, geometrical precision, process flexibility and cost.

1.10. Conclusion

Laser rapid manufacturing is an extremely flexible technique with applications in multiple areas from the repair of large scale components to the manufacturing of components with specific end applications. It is now crossing the barriers of conventional component fabrication and entering into a new era of "feature-based design and manufacturing". The scope of this technology is being extended to more complex multi-material and multi-functional components with a high degree of control on fabrication. The availability of compact high power lasers, advanced CAD/CAM systems with faster computing speeds, and advanced diagnostic and control systems have provided a new dimension to manufacturing and LRM is one such development. Technical factors (advancements in sub-systems) and economic factors (falling price of lasers and other sub-systems) will further increase the deployment of LRM technology in manufacturing.

The present research trend indicates that a deeper understanding of the involved phenomena is being generated through experimentation and modeling. More and more materials with potential applications are being investigated to generate a comprehensive database of LRM materials, their microstructure and mechanical and other properties through the intensive collaboration between universities, research organizations and industry. The fabrication of Colmonoy-6 bushes proves the importance of LRM for strategic applications. Manufacturing low-cost tools using LRM is another niche area with future scope for industrial applications. The mechanical and metallurgical properties of the components fabricated through LRM are somewhat poorer than, or in some cases nearly identical to, those of their wrought counterparts; however, these limitations can be suitably exploited for certain specific applications, such as fabrication of porous structures for prosthetics. Wear resistant surfaces produced by LRM are a cost-effective solution to local wear, Ni-based hard-facing on austenitic stainless steel using LRM is one such example.

With the increased interest from various industries, LRM is likely to lead in the fields of aerospace, medical devices and tooling. In combination with innovative design and planning, the capabilities of LRM have been established to fabricate complex components with delicate details that are very difficult or even impossible to make using conventional manufacturing processes. It does not mean that LRM is a threat to the existence of conventional manufacturing processes, it is simply going to augment the industries with advanced manufacturing technology to address unresolved complex geometrical and material issues. In combination with other conventional manufacturing processes, LRM is going to provide a unique cost effective solution to next generation "feature based design and manufacturing" using the strength of virtual and remote manufacturing.

1.11. Acknowledgments

The authors express their sincere gratitude to Dr P.D. Gupta, Director of RRCAT for his constant support and encouragement. Thanks are due to our collaborators Prof. A.K. Nath of the Indian Institute of Technology, Kharagpur, India and Prof. B.K. Gandhi of the Indian Institute of Technology, Roorkee, India. We thankfully acknowledge the technical support of Dr P. Ganesh, Miss A. Kumari, Mr S.K. Mishra, Mr C.H. Prem Singh, Mr M.O. Ittoop, Mr A. Varma, Mr. A. Adbol and Mr S.K. Perkar provided during the experimental work presented above. One of the authors, Dr C.P. Paul, acknowledges the enthusiastic collaboration and fruitful discussions with Prof. A. Khajepour, Prof. E. Toyserkani, Prof. S. Corbin and Dr M. Alimardani at the University of Waterloo, Canada.

1.12. Bibliography

[AHM 10] AHMED N., VOISEY K.T., MCCARTNEY D.G., "Investigation into the effect of beam shape on melt-pool characteristics using analytical modeling", *Optics and Laser Engineering*, vol. 48, pp. 548-554, 2010.

[AHS 11] AHSAN M.N., PAUL C.P., KUKREJA L.M., PINKERTON A.J., "Porous structures fabrication by continuous and pulsed laser metal deposition for biomedical applications: modeling and experimental investigation", *Journal of Materials Processing Technology*, vol. 211, pp. 602-609, 2011.

[ALI 07] ALIMARDANI M., TOYSERKANI E., HUISSOON J.P., "A 3D dynamic numerical approach for temperature and thermal stress distributions in multilayer laser solid freeform fabrication process", *Optics and Laser Engineering*, vol. 45, pp. 1115-1130, 2007.

[ALI 10] ALIMARDANI M., FALLAH V., KHAJEPOUR A., TOYSERKANI E., "The effect of localized dynamic surface preheating in laser cladding of Stellite 1", *Surface and Coatings Technology*, vol. 204, no. 23, pp. 3911-3919, 2010.

[BAL 91] BALAN K.P., REDDY A.V., JOSHI V., SUNDARARAJAN G., "The influence of microstructure on the erosion behavior of cast irons", *Wear*, vol. 145, pp. 288-296, 1991.

[BAN 01] BANHART J., "Manufacture, characterization and application of cellular metals and metal foams", *Progress in Materials Science*, vol. 46, pp. 559-632, 2001.

[BEN 06] BENDEICH P., ALAM N., BRANDT M., CARR D., SHORT K., BLEVINS R., CURFS C., KIRSTEIN O., ATKINSON G., HOLDEN T., ROGGE R., "Residual stress measurements in laser clad repaired low pressure turbine blades for the power industry", *Mater. Sci. Eng*. A, vol. 437, no. 1, pp. 70-74, 2006.

[BHA 00] BHADURI A.K., INDIRA, R. *et. al*., Recommended hard facing materials for NSSS components of PFBR, Task Force Report, no. IGC/HTF/04, March 2000.

[BRU 88] BRUCK G.J., "Fundamentals and industrial application of high power laser beam cladding", *Proceedings of Laser Beam Surface Treatment and Coating, SPIE*, vol. 957, pp. 14-28, 1988.

[CAD 97] CADNAS M., VIJANDE R., MONTES H.J., SIERRA J.M., "Wear behavior of laser cladded and plasma sprayed WC-Co coatings", *Wear*, vol. 212, pp. 244-253, 1997.

[CAY 99] MCCAY M.H., DAHOTRE J., HOPKINS A., MCCAY T.D., "The influence of metals and carbides during laser surface modification of low alloy steel", *Journal of Materials Science*, vol. 34 no. 23, pp. 5789-5802, 1999.

[CHA 02] CHAM J.G., BAILEY S.A., CLARK J.E., FULL R.J., CUTKOSKY M.R., "Fast and robust: hexapedal robots via shape deposition manufacturing", *The Int. J. Rob. Res*., vol. 21, no. 10-11, pp. 869-882, 2002.

[CHE 89] CHEN X., TAO Z., "Maximum thickness of the laser cladding", *Key Engineering Materials*, vol. 46/47, pp.381-386, 1989.

[CHI 11] DEMARTINI C., MELLA P., "Time competition. The new strategic frontier", *iBusiness*, vol. 3, pp. 136-146, 2011.

[CHU 86] HULL C.W., Apparatus for production of three-dimensional objects by stereolithography, US Patent, no. 4575330, 1986.

[CRA 11] CRAEGHS T., CLIJSTERS S., YASA E., BECHMANN F. *et. al*., "Determination of geometrical factors in layer wise laser melting using optical process monitoring", *Optics and Lasers in Engineering*, vol. 49, pp. 1440-1446, 2011.

[DAS 03] DAS C.R., ALBERT S.K., BHADURI A.K., G. KEMPULRAJ, "A novel procedure for fabrication of wear resistant bushes for high temperature application", *Journal of Materials Processing Technology*, vol. 141, pp. 60-66, 2003.

[DAV 06] DAVIS S.J., WATKINS K.G., DEARDEN G., FEARON E., ZENG J., "Optimum deposition parameters for the direct laser fabrication (DLF) of quasi-hollow structures", *Proceeding of Photon Conference Manchester, Institute of Physics*, 2006.

[DEC 89] DECKARD C., Method and apparatus for producing parts by selective sintering, US Patent, no. 4863538, 1989.

[DES 05] DESALE G.R., GANDHI B.K., JAIN S.C., "Improvement in the design of a pot tester to simulate erosion wear due to solid-liquid mixture", *Wear*, vol. 259, pp. 196-202, 2005.

[DEU 96] DEUIS R.L., SUBRAMANIAN C., YELLUP J.M., "Abrasive wear of aluminum composites: a review", *Wear*, vol. 201, pp. 132-144, 1996.

[DON 03] DONGMING H., RADOVAN K., "A Sensing, modeling and control for laser-based additive manufacturing", *International Journal of Machine Tools and Manufacture*, vol. 43, pp. 51-60, 2003.

[DRA 94] DRAUGELATES, U. *et al.*, "Corrosion and wear protection by CO_2 laser beam cladding combined with the hot wire technology", *Proceeding of ECLAT '94*, pp. 344-354, 1994.

[EBO 85] EBOO G.M., LNDEMANIS A.E., "Advances in laser cladding technology", *Proceeding of Applications of High Power Lasers, SPIE*, vol. 527, pp. 86-94, 1985.

[EVA 04] EVANS H., BUCKLER G., LEFER D., *They Made America: from the Steam Engine to the Search Engine: Two Centuries of Innovators*, 1st edition, Little, Brown and Company, New York, USA, pp. 11, 2004.

[FAT 07] FATHI A., KHAJEPOUR A., TOYSERKANI E., "Clad height control in laser solid freeform fabrication using a feed forward PID controller", *International Journal of Advanced Manufacturing Technology*, vol. 35, pp.280-292, 2007.

[FOL 83] FOLEY T., LEVY A., "The erosion of heat-treated steels", *Wear*, vol. 91, pp. 45-64, 1983.

[GED 02] GEDDA H., POWELL J., WAHISTROM G., LI W.B., ENGSTROM H., MAGNUSSON C., "Energy redistribution during CO_2 laser cladding", *Journal of Laser Applications*, vol.14, no.2, pp.78-82, 2002.

[GED 04] GEDDA H., Laser cladding: an experimental and theoretical investigation, PhD Thesis, Lulea University of Technology, Sweden, pp. 38, 2004.

[GU 08] GU D., SHEN Y., "Processing conditions and micro structural features of porous 316L stainless steel components by DMLS", *Applied Surface Science*, vol. 255, pp. 1880-1887, 2008.

[HE 10] HE X., YU G., MAZUMDER J., "Temperature and composition profile during double-track laser cladding of H13 tool steel", *Journal of Physics D: Applied Physics*, vol. 43, pp. 015502, 2010.

[HEN 92] HENSEL F., BINROTH C., SEPOLD G., "A comparison of powder and wire-fed laser beam cladding", *Proceeding of ECLAT '92*, pp. 39-44, 1992.

[HER 10] HERALIC A., CHRISTIANSSON A.K. *et al*., "Increased stability in laser metal wire deposition through feedback from optical measurements", *Optics and Lasers in Engineering*, vol. 48, pp. 478-485, 2010.

[HID 00] HIDOUCI A., PELLTIER J.M., DUCOIN F., DEZERT D., GUERJOUMA R.EI, "Microstructural and mechanical characteristics of laser coatings", *Surface and Coating Technology*, vol. 123, pp. 17-23, 2000.

[HOF 11] HOFMAN J.T., LANGE D.FDE, PATHIRAJ B., MEIJER J., "FEM modeling and experimental verification for dilution control in laser cladding", *Journal of Material Processing Technology*, vol. 211, pp. 187-196, 2011.

[HU 00] HU Y.P., CHEN C.W., MUKHERJEE K., "Measurement of temperature distribution during laser cladding process", *Journal of Laser Application*, vol. 12, no. 3, pp.126-130, 2000.

[HUA 08] HUA T., JING C., XIN L. *et. al*., "Research on molten pool temperature in the process of laser rapid forming", *Journal of Material Processing Technology*, vol. 198, pp. 454-462, 2008.

[HUA 04] HUANG S.W., SAMANDI M., BRANDT M., "Abrasive wear performance and microstructure of laser clad WC/Ni layers", *Wear*, vol. 256, pp. 1095-1105, 2004.

[IWA 01] IWAI Y., HONDA T., YAMADA H., MATSUBARA T., LARSSON M., HOGMARK S., "Evaluation of wear resistance of thin hard coatings by a new solid particle impact test", *Wear*, vol. 251, pp. 861-867, 2001.

[KAT 00] KATHURIA Y.P., "Some aspects of laser surface cladding in the turbine industry", *Surface and Coatings Technology*, vol. 13, pp. 262-2692, 2000.

[KRE 95] KREUTZ E., BACKES G., GASSER A., WISSENBACH K., "Rapid Prototyping with CO_2 laser radiation", *Applied Surface Science*, vol. 86, pp. 310-316, 1995.

[KRI 07] KRISHNA B.V., BOSE S., BANDYOPADHYAY A., "Low stiffness porous Ti structures for load bearing implants", *Acta Biomater*, vol. 3, pp. 997-1006, 2007.

[KUM 08] KUMAR S., ROY S., PAUL C.P., NATH A.K., "Three-dimensional conduction heat transfer Model for laser cladding process", *Numerical Heat Transfer B*, vol. 53, pp. 271-287, 2008.

[KUM 12] KUMAR A., PAUL C.P., PATHAK A.K., BHARGAVA P., KUKREJA L.M., "A finer modeling approach for numerically predicting single track geometry in two dimensions during Laser Rapid Manufacturing", *Optics and Laser Technology*, vol. 44 no. 3, pp. 555-564, 2012.

[LAM 97] LAMPA C., KAPLAN A.F.H., POWELL J., MAGNUSSON C., "Analytical thermodynamic model of laser welding", *Journal of Physics D: Applied Physics*, vol. 30, pp. 1293-1299, 1997.

[LEV 85] LEVY A.V., YAN J., ARORA V.D., "Sand-water slurry erosion of carburized AISI 8620 steel", *Wear*, vol. 101, pp. 117-126, 1985.

[LEW 04] LEWIS R.W., NITHIARASU P., SEETHARAMU K.N., *Fundamentals of the Finite Element Method for Heat and Fluid Flow*, John Wiley & Sons Ltd, pp. 164-166, 2004.

[LI 85] LI L.J., MAJUMDAR J., "A study of mechanism of laser cladding process", *Proceedings of Laser Processing of Materials*, pp. 35-50, Metallurgical Society of America, America Institute of Metallurgical Engineers, Warrendale, PA, 1985.

[LI 10a] LI R., SHI Y., WANG Z., WANG L., LIU J., JIANG W., "Densification behavior of gas and water atomized 316L stainless steel powder during selective laser melting", *Applied Surface Science*, vol. 256, pp. 4350-4356, 2010.

[LI 10b] LI R., LIU J., SHI Y., DU M., Xie Z., "316L stainless steel with gradient porosity fabricated by selective laser melting", *Journal of Materials Engineering and Performance*, vol. 19, pp. 666-671, 2010.

[LIN 98] LIN J., STEEN W.M., "Design characteristics and development of a nozzle for co-axial laser cladding", *Journal of Laser Application*, vol.10, pp. 55-63, 1998.

[LIN 99a] LIN J., "A simple model of powder catchment in coaxial laser cladding", *Optics and Laser Technology*, vol. 33, pp. 233-238, 1999.

[LIN 99b] LIN J., "Concentration mode of powder stream in coaxial laser cladding", *Optics and Laser Technology*, vol. 33, pp.251-257, 1999.

[LIN 99c] LIN J., HWANG B., "Coaxial laser cladding on an inclined substrate", *Optics and Laser Technology*, vol. 31, pp. 571-578, 1999.

[LIU 03a] LIU C., LIN J., "Thermal processes of a powder particle in coaxial laser cladding", *Optics and Laser Technology*, vol. 35, pp. 81-86, 2003.

[LIU 03b] LIU W, DUPONT J.N., "Fabrication of functionally graded TiC/Ti composites by Laser Engineered Net Shaping", *Scr. Mater*., vol. 48, no. 9, pp. 1337-1342, 2003.

[LIU 06] LIU J., LI L., "Direct Fabrication of Thin-Wall Parts by Laser Cladding", *Journal of Manufacturing Processe*s, vol. 8, pp. 1-7, 2006.

[MAN 00] MANN B.S., "High energy particle impact wear resistance of hard coatings and application in hydro turbines", *Wear*, vol. 237, pp. 140–146, 2000.

[MAR 98] MARCEL S., Laser cladding with powder, PhD Thesis, University of Twente, Enschede, Netherlands, 1998.

[MAR 90] MARSDEN C.F., HOUDLEY A.F.A., WAGNIERE J.D., "Characterization of laser cladding process", *Proceeding of ECLAT'90*, pp. 543-553, 1990.

[MAZ 99] MAZUMDER J., SCHIFFERER A., CHOI J., "Direct materials deposition: designed macro and microstructure", *Materials Research Innovations*, vol. 3, pp. 118-131, 1999.

[MAZ 00] MAZUMDER J., DUTTA D., KIKUCHI N., GHOSH A., "Closed loop direct metal deposition: art to part", *Optics and Lasers Engineering*, vol. 34, pp. 397-414, 2000.

[MEH 07] MEHRDAD I.-T., TOSERKANI E., "An image-based feature tracking algorithm for real-time measurement of clad height", *Machine Vision and Applications*, vol.18, pp. 343-354, 2007.

[MER 96] MERIAUDEAU F, TRUCHETET F., "Control and optimization of the laser cladding process using matrix cameras and image processing", *Journal of Laser Applications*, vol. 8, no. 6, pp. 317-324, 1996.

[MIL 98] MILEWSKI J.O., LEWIS G.K., THOMA D.J., KEEL G.I., NEMEC R.B., REINERT R.A., "Directed light fabrication of a solid metal hemisphere using 5-axis powder deposition", *Journal of Materials Processing Technology*, vol. 75, pp. 165-172, 1998.

[MOA 09] MOAT R.J., PINKERTON A., LI L., WITHERS P.J., PREUSS M., "Crystallographic texture and microstructure of pulsed diode laser-deposited Waspaloy", *Acta Materialia*, vol. 5, pp. 1220-1229, 2009.

[NAI 86] NAIM M., BAHADUR S., "Effect of microstructure and mechanical properties on the erosion of 18 Ni (250) maraging steel", *Wear*, vol. 112, no. 2, pp. 217-234, 1986.

[NAK 07] NAKAJIMA H., "Fabrication, properties and application of porous metals with directional pores", *Progress in Materials Science*, vol. 52, pp. 1091-1173, 2007.

[NUR 83] NURMINEN J.I., SMITH J.E., "Parametric evaluation of laser/clad interactions for hardfacing applications", *Lasers in Materials Processing*, pp. 94-107, 1983.

[PAU 97] PAUL C.P., KUMAR H., THAKUR S., NATH A.K., "Development of mechanically vibrated gas assisted powder feeder for laser cladding", *National Laser Symposium, PRL*, Ahmedabad, December 1997.

[PAU 06] PAUL C.P., JAIN A., GANESH P., NEGI J., NATH A.K., "Laser rapid manufacturing of colmonoy-6 components", *Optics and Lasers in Engineering*, vol. 44, pp. 1096-1109, 2006.

[PAU 07] PAUL C.P., GANESH P., MISHRA S.K., BHARGAVA P., NEGI J., NATH A.K., "Investigating laser rapid manufacturing for Inconel-625 components", *Optics and Laser Technology*, vol. 39, ppp. 800-805, 2007.

[PAU 08] PAUL C.P., KHAJEPOUR A., "Automated laser fabrication of cemented carbide components", *Optics and Laser Technology*, vol. 40, pp. 735-741, 2008.

[PAU 12] PAUL C.P., MISHRA S.K., PREMSINGH C.H., BHARGAVA P., TIWARI P., KUKREJA L.M., "Studies on laser rapid manufacturing of cross-thin-walled porous structures of Inconel 625", *International Journal of Advanced Manufacturing Technology*, 2012.

[PEY 08] PEYRE P., AUBRY P., FABBRO R., NEVEU R., LONGUET A., "Analytical and numerical modeling of the direct metal deposition laser process", *Journal of Physics D: Applied Physics*, vol. 41, pp. 025403, 2008.

[PIC 94] PICASSO M., MARSDEN C.F., WAGNIERE J.D., FREND A., RAPPAZ M., "A simple but realistic model for laser cladding", *Journal of Metallurgical and Materials Transactions B*, vol. 25, pp. 281-291, 1994.

[PIN 08] PINKERTON A., WAN W., LI L., "Component repair using laser direct metal deposition", *Proceedings of the Institution of Mechanical Engineers Part B: Journal of Engineering Manufacture*, vol. 222, pp. 827-836, 2008.

[POW 88] POWELL J., HENRY P.S., STEEN W.M., "Laser cladding with pre-placed powder–analysis of thermal cycling and dilution effects", *Surface Engineering*, vol. 4, no. 2, pp. 141-9, 1988.

[QI 06] QI H., MAZUMDER J., KI H., "Numerical simulation of heat transfer and fluid flow in coaxial laser cladding process for direct metal deposition", *Journal of Applied Physics*, vol. 100, pp. 024903, 2006.

[SAL 06] SALEHI D., BRANDT M., "Melt-pool temperature control using Lab VIEW in Nd:YAG laser blown powder cladding process", *International Journal of Advanced Manufacturing Technology*, vol. 29, pp. 273-278, 2006.

[SAN 10] SANDIA NATIONAL LABORATORIES, http://www.sandia.gov/mst/pdf /LENS.pdf, visited on June 29, 2010.

[SMC 11] SPECIAL METALS CORPORATION, "ICONEL® alloy 625", *Special Metals*, no. SMC-063, January 2006, available online at: http://www.specialmetals.com/documents /Inconel%20alloy%20625.pdf.

[SON 11a] SONG L., MAZUMDER J., "Feedback control of melt-pool temperature during laser cladding process", *IEEE Transactions on Control Systems Technology*, vol. 19, no. 6, pp. 1349-1356, 2011.

[SON 11b] SONG L., MAZUMDER J., "Control of melt-pool temperature and deposition height during direct metal deposition process", *International Journal of Advanced Manufacturing Technology*, pp. 1-10, 26 May 2011.

[SPE 01] SPEYER A.J., WOOD R.J.K., STOKES K.R., "Erosion of aluminum-based claddings on steel by sand in water", *Wear*, vol. 250, pp. 802-808, 2001.

[SRE 06] SREENATHBABU A., KARUNAKARAN K.P., "Hybrid adaptive layer manufacturing: an Intelligent art of direct metal rapid tooling process", *Robotics and Computer-Integrated Manufacturing*, vol. 22, pp. 113–123, 2006.

[SUN 05] SUN S., DURANDET Y., BRANDT M., "Parametric investigation of pulsed Nd:YAG laser cladding of Stellite 6 on stainless steel", *Surface and Coatings Technology*, vol. 194, pp. 225-231, 2005.

[TAM 02] TAM K.F., CHENG F.T., MAN H.C., "Cavitations erosion behavior of laser-clad Ni–Cr–Fe–WC on brass", *Materials Research Bulletin*, vol. 37, pp. 1341-1351, 2002.

[TEC 95] TECHEL A., LUFT A., MULLER A., NOWOTNY A., "Production of hard metal-like wear protection coatings by C02 laser cladding", *Optical and Quantum Electronics*, vol. 27, pp. 1313-1318, 1995.

[TOY 04] TOYSERKANI E., KHAJEPOUR A., CORBIN S.F., "3-D finite element modeling of laser cladding by powder injection: effects of laser pulse shaping on the process", *Optics and Laser Engineering*, vol. 41, pp. 849-867, 2004.

[TOY 06] TOYSERKANI E., KHAJEPOUR A., "A mechatronics approach to laser powder deposition process", *Mechatronics*, vol. 16, no.10, pp. 631-641, 2006.

[TYL 11] TYLER A.D., YUNG C. S., "Vision-based clad height measurement", *Machine Vision and Applications*, vol.22, pp.129-136, 2011.

[UPA 98] UPADHYAYA G.S., *Cemented Tungsten Carbides Production, Properties and Testing*, Noyes Publications, New Jersey, 1998.

[VAL 10] VALSECCHI B., PREVITALI B., VEDANI M., VIMERCATI G., "Fiber laser cladding with high content of Wc-Co based powder*", International Journal of Material Forming*, vol. 3, Supplement 1, pp. 1127-30, 2010.

[VET 94] VETTER P.A., ENGEL T.H., FONTAINE J., "Laser cladding: the relevant parameters for process control", *Proceeding of SPIE*, vol. 2207, pp. 452-562, 1994.

[WAN 06] WANG L., FELICELLI S., "Analysis of thermal phenomena in LENSTM deposition", *Material Science and Engineering*, vol. A 435-436, pp. 625-631, 2006.

[WAN 11] WANG Z., DONG S., XU B., XIA W., "Laser clad geometry: experimental observation and geometric modeling", *Advance Material Research*, vol. 148-149, pp. 628-632, 2011.

[XIN 06] XING F., LIU W., WANG T., "Real time sensing and control of metal powder laser forming", *Proceedings of the 6th world congress on Intelligent Control and Automation*, pp. 6661-6665, June 21-23 2006.

[XUE 00] XUE L., ISLAM M.U., "Freeform laser consolidation for producing metallurgically sound and functional components", *Journal of Laser Application*, vol. 12 no. 4, pp. 160-165, 2000.

[XUE 01] XUE L., ISLAM M.U., THERIAULT A., "Laser consolidation process for the manufacturing of structural components for advanced robotic mechatronic system – a state of art review", *Proceeding of 6th International Symposium on Artificial Intelligence and Robotics & Automation in Space (i-SAIRAS 2001)*, Canadian Space Agency, St-Hubert, Quebec, Canada, June 18-22, 2001.

[YAN 01] YANG L.X., PENG X.F., WANG B.X., "Numerical modeling and experimental investigation on the characteristics of molten pool during laser processing", *International Journal of Heat and Mass Transfer*, vol. 44, pp. 4465-4473, 2001.

[YUS 08] YUSOFF W.A.Y, THOMAS A.J, "The effect of employing an effective laser sintering scanning strategy and energy density value on eliminating "orange peel" on a selective laser sintered part", *Proc. International Association for Management of Technology (IAMOT)*, 2008.

[ZHA 00] ZHANG D.-W., LEI T.C., ZHANG J.-G., OUYANG J.-H., "The effects of heat treatment on microstructure and erosion properties of laser surface-clad Ni-base alloy", *Surface and Coatings Technology*, vol. 115, 176–183, 2000.

[ZHA 99] ZHAO H.X., GOTO H., MATSUMURA M., TAKAHASHI T., YAMAMOTO M., "Slurry erosion of plasma-sprayed ceramic coatings", *Surface and Coatings Technology*, vol. 115, 123–131, 1999.

[ZHO 10] ZHONG M., LIU W., "Laser surface cladding: the state of the art and challenges", *Proceedings of the Institution of Mechanical Engineers*, vol. 224, Part C: *Journal of Mechanical Engineering Science*, pp. 1041-60, 2010.

Chapter 2

Lasers in Metal Forming Applications

This chapter reports on current knowledge in the field of laser beam forming, including some recent research advances and applications. In addition this chapter also presents the results of a laser beam forming (LBF) a mild steel plate. The experiments were conducted using the classical Taguchi experimental design. Analysis of variance (ANOVA) was employed to establish the parameter effect on the curvature of LBF plates. The laser formed mild steel samples were characterized through microstructural analysis and mechanical testing to establish the effect of the process on the formed components.

2.1. Introduction

Worldwide the manufacturing industry is a major contributor to any nation's gross domestic product (GDP). In South Africa it contributes over 18.5% of the national GDP. In recognition of the importance of manufacturing industry to the economy, governments come out with various development strategies. The South African Government recently developed two strategies to boost the success of the manufacturing sector in the new millennium. These are the National Research and Development Strategy (NRDS) and the Integrated Manufacturing Strategy (IMS).

The NRDS is aimed at ensuring that technology resources are better developed, focused and utilized while the IMS aims to ensure a paradigm shift toward the

---

Chapter written by Stephen A. AKINLABI, Mukul SHUKLA, Esther T. AKINLABI and Tshilidzi MARWALA.

Lasers in Manufacturing Edited by J. Paulo Davim

optimization of the existing raw material into intensive goods and services [THE 11b]. To this effect, many new processes are being developed and investigated with the aim of improving the manufacturing process. One of these modern processes is the LBF process.

2.2. Laser

The term LASER is an acronym for light amplification by stimulated emission of radiation. Albert Einstein first predicted that the laser effect existed; however, it was not until 1960 that Theodore Maiman, a physicist at Hughes Research Laboratories, constructed the first laser that emitted light in the visible range. A laser beam like all other light waves is a form of electromagnetic radiation. Light may be simply defined as the electromagnetic radiation that is visible to the human eye (wavelength range 0.37–0.75 μm but often of 0.55 μm with a frequency of 10^{15} Hz and lying in between the ultraviolet and infrared radiation) [KAN 09]. However, lasers may have a wavelength ranging from 0.2 to 500 μm, for example, X-ray through ultra violet and visible to infrared radiation. A typical illustration of an electromagnetic spectrum is shown in Figure 2.1.

Laser generation is the result of energy emission associated with the transition of an electron from a higher energy to a lower energy level, or orbit, within an atom [KAN 09]. A laser beam is the heat or energy source in laser material processing. It is often considered as a useful source of intense heat for various applications. Generation of very high energy concentration becomes possible with lasers because of their unique properties when compared to a normal light source: some of these properties include low divergence, monochromatism, coherence and stability. As such, energy generated from lasers can be employed to heat, melt and vaporize most materials. Laser related applications include surface modification – heat treatment, welding, cutting, forming, etc. The application of lasers can be broadly divided into low power and high power as illustrated in Figure 2.2.

There are various types of lasers with different characteristics depending, to a large extent, on the active medium used for the laser action. The principal laser categories include solid state lasers, gas lasers, liquid dye lasers, semiconductor (diode) lasers and free electron lasers. Ruby and Nd:YAG are examples of solid state lasers. Both are extensively employed in manufacturing applications. The Nd:YAG laser is capable of transmission using a fiber cable, and can be used in either the pulsed or CW mode (with power levels up to 6 kW).

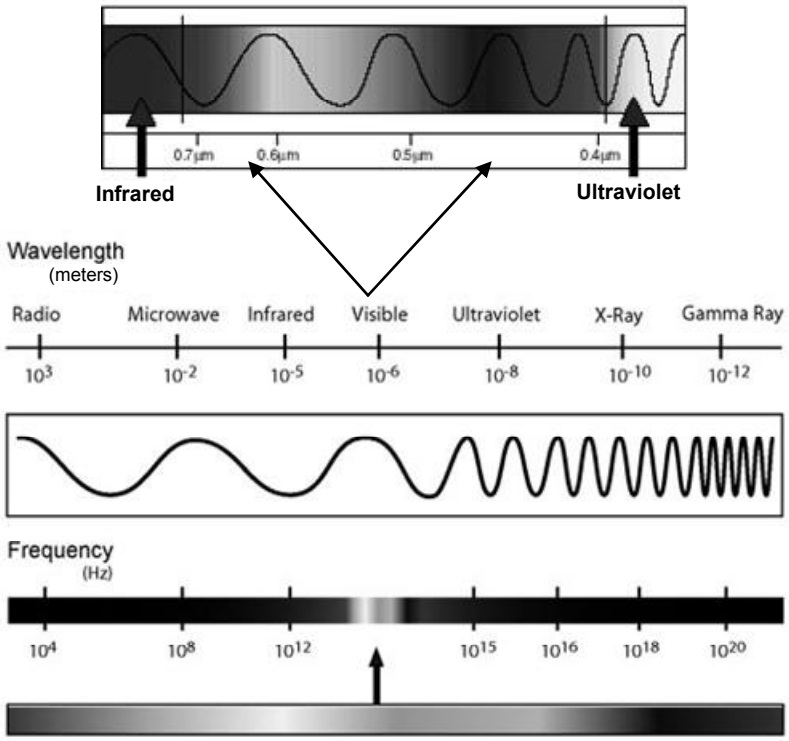

Figure 2.1. *The electromagnetic spectrum [THE 11a]*

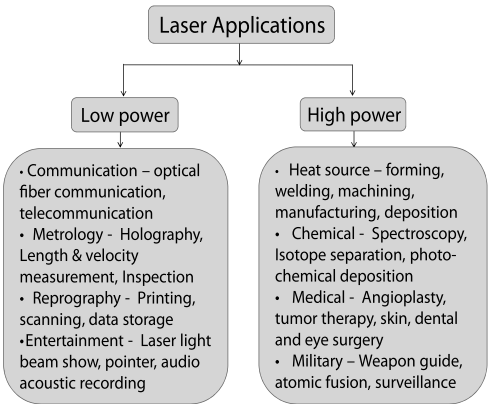

Figure 2.2. *Classification of laser applications*

The properties of a laser beam that have significant influence on material processing include, low divergence, monochromaticity, coherence, brightness, stability, size and mode. A diffraction limited beam is proportional to the beam wavelength and inversely proportional to the diameter of the aperture from which the beam emerges. Lasers are generally considered to be monochromatic. The intensity of a laser beam is the power per unit area (P/A). The high directionality or low divergence of a laser beam tends to concentrate all the available energy into a very small region, resulting in a very high intensity [KAN 05, ION 09].

2.3. Metal forming – introduction

Forming is the manufacturing process by which the size or shape of a part is changed by application of forces or heat or both, thereby inducing stresses on the part which are greater than the yield strength but less than the fracture strength of the material [KAN 09]. Various traditional forming methods such as mechanical press forming, hot break forming, roll forming, deep drawing, etc., have been employed for specific manufacturing applications for many years.

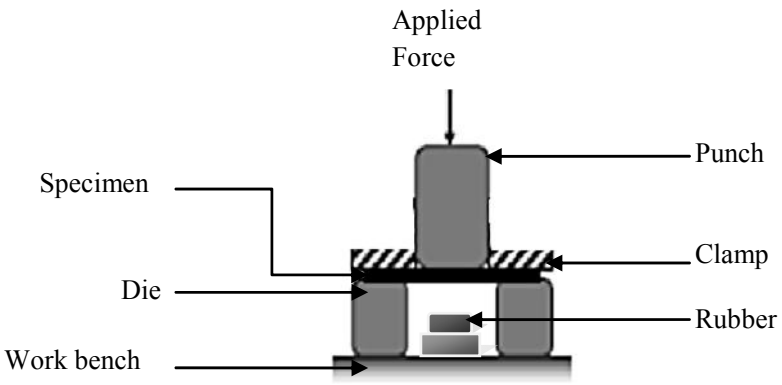

Figure 2.3. *Schematic diagram of the mechanical forming process [ZHA 04]*

The mechanical bending process is one of the most common techniques of bending or forming metals for various industrial applications, such as door panels in cars, ribs, stringers and wing panels of aircraft, etc. A simplified schematic diagram of the mechanical forming process is shown in Figure 2.3. However, mechanical bending processes are often characterized with springback. Springback is the amount of deformation strain recovered by elastic unloading when the component is

removed from the press. Springback and surface residual stresses can be regarded as an after effect of the forming process [WAT 01, WAL 00].

LBF on the other hand is a flexible and promising manufacturing process for sheet metal forming. It is considered as a novel manufacturing method for the bending/forming and shaping of metallic components. It is a thermo-mechanical forming process that enables parts (sheet metals, rods and pipes) to be formed without external forces and does not require the use of expensive dies and presses, which are required in the majority of traditional forming methods [YAN 10, DUT 04, MCG 01]. The process is achieved by irradiating the surface of the material with a laser beam, thereby inducing rapid localized heating followed by cooling, as the laser energy is either moved to the adjacent area or switched-off. As a consequence of the thermally induced forming process, minimal springback occurs in the cooling phase after the laser is switched-off [YAN 10].

2.4. Laser beam forming

LBF is a relatively new technique developed in the mid-1980s for the shaping of metallic components. It originates from a similar oxy-acetylene-based flame bending process also called line heating. Oxy-acetylene flame has been extensively used for shaping heavy metal components, such as beams for construction purposes and decking and hull plates for the ship building industry [MOS 87, ARA 73, ROT 74]. However, the divergent nature of the oxy-acetylene flame during forming often leads to significant reliance on the operator's skill. One of the tough tasks is to establish a steep thermal gradient during the process for thin materials with high thermal conductivity. This consequently led to the operator spending more time perfecting the process, and such trial and error may plague the task until completion.

In contrast to flame bending technique, LBF supplies high energy intensity resulting in the steep thermal gradient required for bending to take place. In addition, LBF can be localized to a region because of its coherent and monochromatic characteristics. The process is achieved by introducing thermal stresses to the surface of the sheet material through controlled irradiation with a defocused laser beam [NAM 85]. The resultant shape and bend are determined by governing process parameters, such as the beam power and size, scanning velocity and the number of scan irradiations [SCU 87]. In the traditional forming process, the formed components depend on specialized heavy tools like dies and punches and the application of external forces to impact the bend into the flat sheet metal. A flow diagram of the LBF process is shown in Figure 2.4.

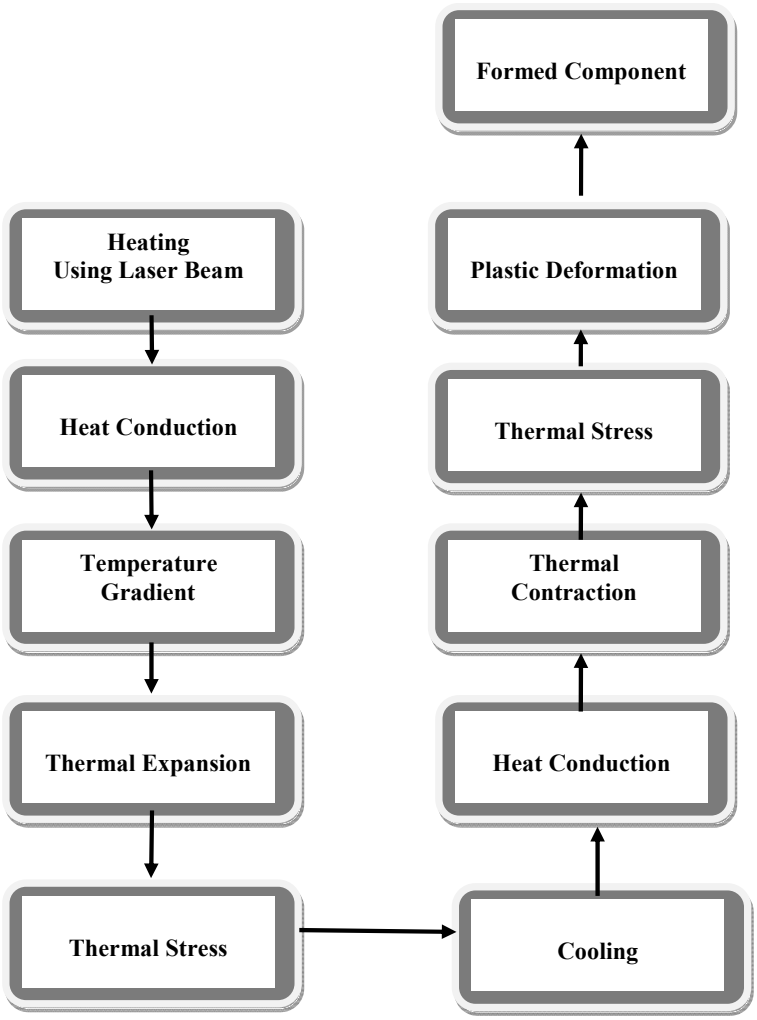

Figure 2.4. *Typical flow diagram of the LBF process*

2.4.1. *Principles of LBF*

LBF is a material processing technique very similar to that of the laser surface heat treatment. It involves the scanning of a defocused beam over the surface of the metallic sheet to be formed [KAN 09, ION 05]. The laser beam moving along a straight line without interruption causes the sheet to bend along the line of motion. The basic components of a LBF system include:

– a laser source with a beam delivery system;

– a motion unit on which the work piece is mounted or a robot for holding a fiber optic system;

– a cooling system;

– a temperature monitoring system;

– a shape monitoring system;

– a computer control system.

It was developed from the line heating process to form reproducible and precise shapes, these were met by the ability to control the transverse speed of the laser beam, the beam spot size and the induced temperature gradient. The potential of fully automating a laser forming process with the aid of a computer numeric control system is a unique advantage that has positioned the process [DUT 04, SHE 09a].

2.4.2. *Parameters influencing the LBF process*

A schematic diagram of the LBF process and parameters is shown in Figure 2.5.

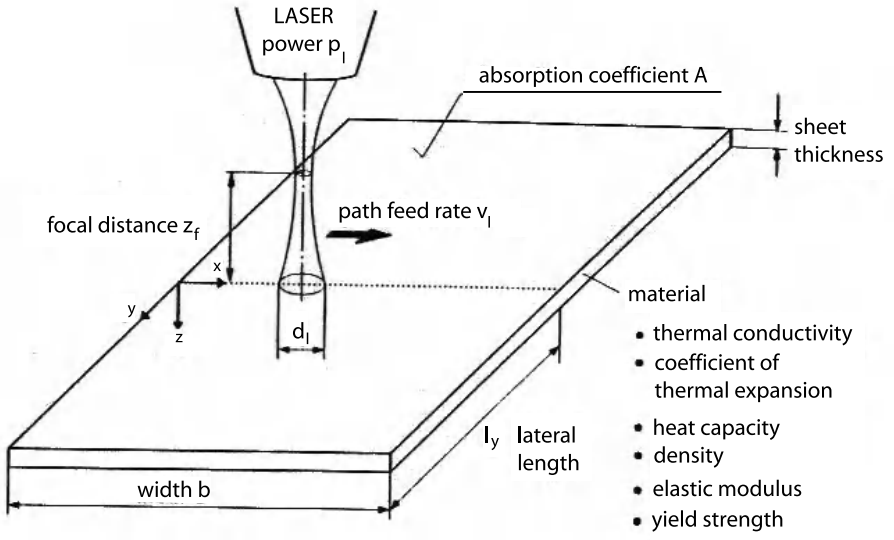

Figure 2.5. *Schematic of the LBF process and parameters [THE 11a]*

In the drive to fully harness the potential of the LBF process, it has become very important to identify the effect of the process parameters on the structural integrity and physical properties of formed materials. In this context, concerted efforts have been applied both experimentally and numerically or analytically in order to establish the effects of influencing factors during the LBF process.

LBF has been investigated in the applications of many materials, such as low or mild steel [LAW 01, THO 01], stainless steel [DUT 04], aluminum and its alloys [MER 01], titanium and its alloys [WAL 00, MAR 98], etc., which have a high thermal expansion coefficient and are currently used because of their technical benefits. In particular, the effect of the rapid and repeated heating and cooling associated with the LBF process makes investigations into it more critical. Shi *et al.* [SHI 06] conducted a comprehensive study on the mechanisms of LBF for metal plates. Based on the study of thermal transfer and elastic–plastic deformation, further explanation was given with respect to a new mechanism referred to as the coupling mechanism. Shi *et al.* used a 3D, nonlinear, indirectly coupled thermal–structural model to investigate laser forming with two laser beams scanning simultaneously along two parallel lines. They made these numerical investigations to study the difference in temperature and plastic deformations between the two simultaneous laser scans and the single sequential scan along the same lines. They found that the plastic deformation of simultaneous laser scans is larger if the distance between the two scanning lines is smaller than the size of the plastic zone of a single laser scan. Liu *et al.* [LIU 08] conducted one of the first investigations on the laser forming of a composite material. They investigated the deformation mechanism of an aluminum matrix composite during laser forming with different volume fractions of particle reinforcement. Further investigations were conducted by using a microstructure-integrated finite element method and found that the bending angle of the composite increased with an increase in the volume fraction of particles [LIU 07].

Furthermore, Thompson and Pridham's [THO 01] investigation of laser formed mild steel showed, from the mechanical and metallurgical characterization, that the laser beam formed component can also perform like any other component manufactured from the conventional process. It was also reported that the LBF process increases the yield strength of the irradiated surface of the formed component. Cheng and Yao [CHE 03] reported their investigation on the effect of material anisotropy on the laser forming process. The study covers both numerical and experimental work. Cold rolled sheet metal exhibited anisotropy mostly caused by preferred orientations of grains developed during rolling reductions. The anisotropy index, or R value, of a material in a particular orientation was determined using an ASTM standard tensile test. The grain textures in the formed samples were determined using an electron back-scatter diffraction method (EBSD). It was found that there was a significant difference in the laser forming properties of the rolled

AISI 1010 mild steel depending on the orientation of the scan line to the rolling direction in the part. It was also found that the anisotropic effect increases with increased rolling reductions, i.e. thinner materials. It was concluded that the higher the temperature achieved in the component the less the materials' anisotropy has an effect.

The last two decades have experienced tremendous advances in the modeling [SHE 06, YAN 10, NAM 87, VOL 94a] of the LBF process. The modeling process became a very important analytical technique that helped to provide a basis for determining the heating pattern required and a better understanding of the thermo-mechanical behavior of the LBF process. Consequently it made the application of LBF feasible and profitable to the industry. According to Shen and Vollertsen [SHE 09b], the development of laser beam models have metamorphosed from analytical temperature gradient mechanism (TGM) models to empirical models. The transformation and the development of LBF models are illustrated in Figure 2.6.

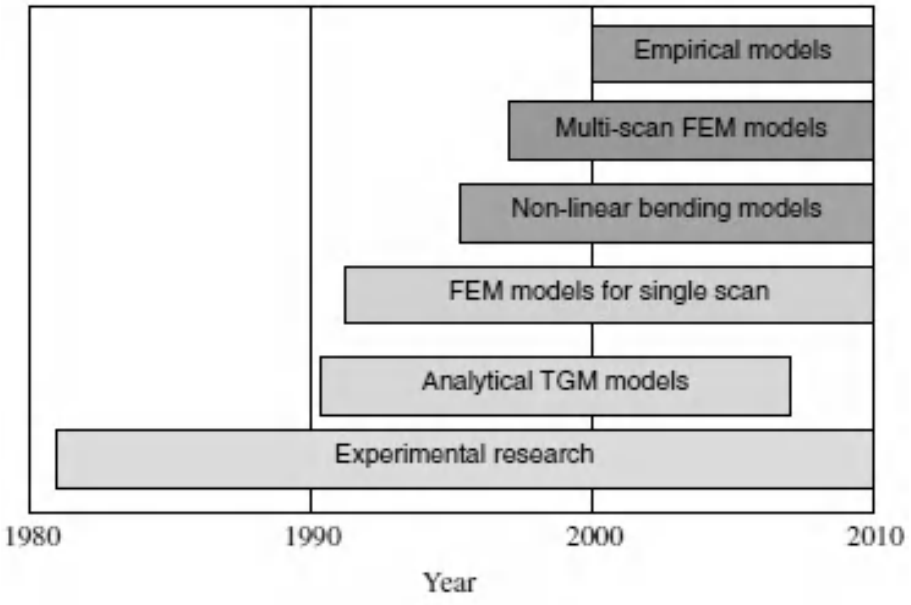

Figure 2.6. *Summary of the development of LBF models [SHE 09b]*

Experimental research has primarily been the most popular approach in LBF research, but improvement over the years has led to the development of the laser beam models. An analytical model was developed initially from the elastic bending theory but with increasing understanding of the LBF mechanism, more thermal and

mechanical factors were included in the analytical models for more precise predictions. The empirical models were based on the vast experimental data without taking into consideration the mechanism and the LBF process. But with the development of artificial intelligence algorithms, the performance prediction improved further [SHE 09b, VOL 94b].

The process of determining the effect of process parameters such as laser power, beam diameter, scan velocity, number of irradiation etc., during LBF is considered as a major problem in order to form the plate to the desired curvature [GEI 93a, YAN 10]. Furthermore, it is known that the LBF process is a complex thermal mechanical process because of factors that could influence the forming process. These factors include energy factors (laser power, laser scan velocity, absorption coefficient, etc.), geometrical factors (sheet thickness and sheet width) and material factors (thermal, physical and mechanical properties) and lack of a good understanding of the process.

From the above, the influencing factors in the LBF process can be broadly classified into three groups: energy factors, material properties and plate geometry, this is illustrated in Figure 2.7.

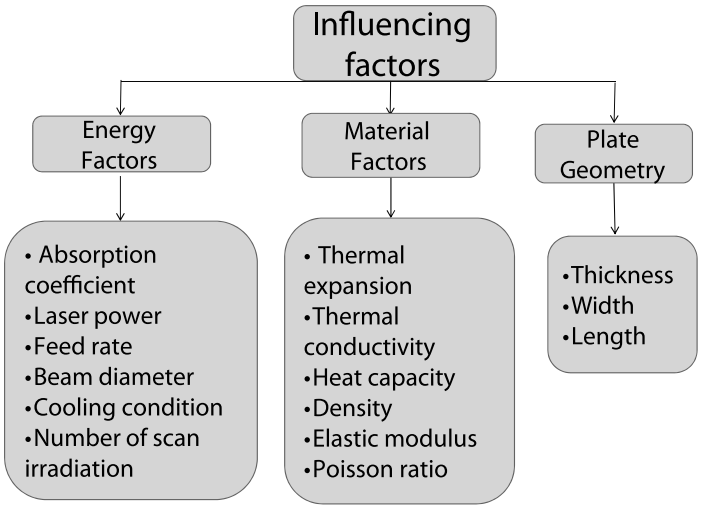

Figure 2.7. *Classification of factors influencing the LBF process*

2.4.2.1. *Energy factors*

Holzer *et al.* [HOL 94], from their investigation, reported that LBF is related to the energy absorption into the metal sheet because of the rapid heating of the metal surface with the laser beam and cooling. This process thereby setup a temperature gradient across the thickness of the material. The heat flux density developed on the surface of the material follows the normal distribution and may be expressed as a function of variables: such as the laser power, beam radius, heat flux density absorption coefficient of the material and the distance from the center of the laser beam. Equation [2.1] gives the formula for calculating the heat influx density during a LBF process.

$$Q(r) = \frac{2\eta P}{\pi R^2} \exp\left(-\frac{2r^2}{R^2}\right) \qquad [2.1]$$

where:

Q = heat flux density;

η = absorption coefficient of the sheet material;

P = laser beam power;

R = beam radius;

r = distance from the center of the laser beam.

Vollertsen [VOL 98] reported that the primary factors involved in the energy absorption include the surface material property, laser beam power and scanning speed. While Scully [SCU 87] considered beam diameter and cooling effect as less important than the primary factors in the LBF process. The variables of energy factors are hereby discussed.

Surface material property

LBF being a thermomechanical process induces thermal stresses in the material, thereby creating an interaction between the beam and the material. These material interactions demonstrated by the absorption behavior and the processing parameters are complex phenomenon. However, Vollertsen [VOL 98] demonstrated that laser intensity has a strong influence on the absorption behavior. This best explains the reason why the absorption rate of the carbon dioxide (CO_2) laser (wavelength is 10.6μm) on an uncoated metal surface is low when compared to YAG lasers with a wavelength of 1.06 μm. As such, the rate of absorption is often improved by coating the surface of the metal, a graphite coating is suggested for the LBF process because of its high absorption coefficient which may be in the range of 50–80%. Hence, the

rate of absorption is strongly dependent on the material property, material surface condition and wave length of the source of heat. The only drawback identified with the use of graphite coatings is the difficulty of automating the coating process and the challenges the coating thickness process possess during multiple irradiations, making the absorption behavior complex to manage [STE 90].

Laser power

The work of several researchers, based on statistical analyses of parameter effects in laser bending, established a linear relationship between the laser power and the bend angle and an inverse relationship with the radius of curvature [VOL 98, CHA 00, HOS 08]. It was found that as the power increases, the bend angle increases to a point before it starts decreasing, while the radius of curvatures decreases in a similar manner. It shows that an optimal laser power will yield a maximum bend angle. This implies therefore that when the laser power is effectively controlled, a desired bending angle and curvature are obtained. One of the few exceptions was recorded for an aluminum alloy whose bending angle was found to be smaller than the expected value based on the linear relationship [PAU 08].

Scanning velocity

This is the variable that measures and controls the energy absorption in the LBF process. It has also been reported by researchers that a relationship exists between the scan velocity and the bending angle [WAL 00, VOL 94b]. As the scan velocity is increased there is a decrease in the bending angle formed. The explanation for this can be attributed to a small interaction time between the laser beam and the material. This means that the little heat energy developed was insufficient to bring about enough deformation. In addition, it is believed that different scan velocities change the temperature profile at this instance. In the instance of a low scan velocity, the temperature field is more homogeneous because of more interaction time for heat conduction across the cross-section of the sheet material, thereby developing plastic strain. In the instance of fast scan velocity, a steep temperature gradient is developed in the plate thereby creating a plastic compression.

Beam diameter

This is also known as the spot size of the beam. Vollertsen [VOL 94a] reported that the effect of the beam diameter on the outcome of a forming process is smaller to the laser power or scan velocity but it is strongly related to the LBF mechanism because it can be related by the energy density. The effect of the spot size on the resulting bending angle is the same as that of the increasing scan velocity, the bend angle decreases [WAL 00]. Hence, the energy density of the laser spot is reduced when the beam diameter is increased. This may be the reason for the decreasing bending angle during LBF.

Number of scan irradiations

This is one of the important parameters in the LBF process as it forms the pattern of the desired shape, i.e. straight and circular scan irradiation patterns. An increase in the scan irradiations also increases the bending angles to an optimum level after which it will no longer have any significant effect on the bending angle. A bending angle of a few degrees can only be achieved with a single scan irradiation but in order to produce desired deformations of a larger bending angle, multiple scan irradiation might be required [VOL 94b, WAL 00]. The decrease in the bending angle with the increasing number of scan irradiations, as reported by Hennige [HEN 97], may be attributed to the strain hardening of the material, which was a result of the induced deformation during the process and saturation in absorption of the material with an increase in number of scan irradiations [MAR 00].

Cooling effect

Reported literature on temperature gradient measurement show that the temperature difference between the top irradiated surface and the bottom is strongly responsible for the development of the bending angle [CHE 01]. Following this, some researchers [CHE 01, CHE 11] have studied the effect of cooling to improve the LBF process efficiency. Scully [SCU 87] found that the effort of cooling has no significant effect on the change in bending angle during LBF. In his investigation, different cooling mediums were employed to establish the effect of cooling on the resulting change in bending angle, this is summarized in Table 2.1.

Cooling Medium	**Bending Angle (°)**
Water bath, natural convection with steel support	1.16
Water bath, natural convection with no steel support	1.08
Dry ice, entire plate rested on a block of dry ice	1.11
Forced air convection, plate suspended by clamp on one edge	1.13
Natural air convection, plate rested on an aluminum table	1.28

Table 2.1. *Effect of cooling on bending angle [SCU 87]*

Line energy

This is the applied laser energy that generates thermal stresses during the LBF process and can be defined as the ratio between the laser power *P*, and the laser scan velocity *V*. A line energy threshold must be exceeded to initiate a permanent deformation by the temperature gradient mechanism during the LBF process (equation [2.2]). The relative contribution of the forming mechanism for a given line energy depends on the thermal gradient generated through the thickness of the material [CHE 11].

$$LE = \frac{P}{v} \qquad [2.2]$$

where:

P = laser power (Watt);

V = scan velocity (mm/sec).

The key parameters responsible for energy absorption into the material during the LBF process are the laser power, scan velocity and the absorption factor of the material. According to Yau *et al.* [YAU 98] the bend angle can best be controlled by adjusting the laser power and the scan velocity within the range of the linear relationship between the bend angle and the line energy. Geiger *et al.* [GEI 93b] further found that a relationship with the bending angle exists between laser power, plate thickness and scan velocity (equation [2.3]). If these three parameters are known, the bending angle can be estimated.

$$Ba = \frac{P}{t\sqrt{v}} \qquad [2.3]$$

where:

B_a = bending angle;

t = plate thickness (mm).

2.4.2.2. *Material properties*

The properties of the material play a unique role in the LBF process because the process involves rapid heating and cooling which in turn induces thermal stress and strain into the material. Some of these thermal properties include the density, thermal conductivity of the material, heat capacity, and the coefficient of thermal expansion. The thermal conductivity of the material is the the material's ability to

conduct heat, while the density is a physical property defined as the measure of the relative heaviness of the object with a constant volume $\delta = \frac{m}{v}$. Thermal conductivity determines the magnitude of the temperature gradient along the cross-section of the sheet plate and the temperature field; consequently, contributing to the process in which the temperature gradient mechanism is involved.

Heat capacity is the amount of heat required to change the temperature of an object by a given amount. The coefficient of thermal expansion describes how much a material will expand for each degree of temperature increase. This may be expressed mathematically using equation [2.4];

$$\alpha = \frac{dl}{lxdT} \qquad [2.4]$$

where:

dl = change in length of the material in the direction being measured;

L = overall length of the material;

dT = change in temperature over which dl is measured.

Geiger *et al.* [GEI 94] reported that a linear relationship exists between the bend angle and the ratio of the coefficient of thermal expansion to the volumetric heat capacity (equation [2.5]). Investigating the effect of material properties during the LBF process by an experimental approach may be very expensive, time consuming and error prone. As such, the effect of the process parameter in LBF may be best identified through numerical analysis:

$$Ba = \frac{t_c}{h_v} \qquad [2.5]$$

where:

t_c = coefficient of thermal expansion;

h_v = volumetric heat capacity.

2.4.2.3. *Plate geometry*

The plate geometry includes sheet thickness, length and width. These strongly influence the development of the bending angles during the LBF process. According

to Shi and Jin [SHI 01], sheet thickness is the most important of the three parameters. Geiger *et al.* also reported that a linear relationship exists between the bending angle and the sheet thickness of the material. The length and width may be considered when small components are being formed even though the effect is significantly small.

2.5. LBF mechanisms

The LBF process is realized by introducing thermal stresses into the surface of a work piece with a high power laser beam. These internal stresses induce plastic strains that bend the material or result in local elastic/plastic buckling. The process is principally used at the macro level to form metallic sheet material. The principle behind the sheet material process uses a laser beam that is guided across the sheet surface. The path of the laser is dependent on the desired forming result. In the simplest case, it may be a point and in another case it may be a straight line, rotating and wavering beam across the whole part [DEA 03].

The study and modification of laser beam geometry or orientation become essential in the LBF process because it is one possible method of varying the temperature distribution without changing the input power or scanning speed. Some researchers have investigated the effect of beam geometry on laser bending; the result from the investigation suggests that beam geometry plays an important role in the resulting temperature distributions on the work piece. Longer beam dimension in the scanning direction produces higher temperatures due to longer beam-material interaction time. As a result, it is implied therefore that higher temperatures produce more plastic strains and hence higher deformation. Mucha *et al.* [MUC 97] further confirmed this stand from the investigation of the effect of beam geometry on the deformation of plates. Their analytical and experimental work found that the bending angle obtained with the use of the rectangular laser beams is higher than with a circular beam.

There are several distinct mechanisms of laser forming to date [LI 01, HU 02, CHE 03, CHE 11]. The most extensively studied and reported mechanisms are the temperature gradient mechanism (TGM) and buckling mechanism (BM), which depend on the process setup. The significant process variables that determine the active mechanism are the transverse speed, laser spot diameter, incident laser power and absorption coefficient. These variables fall into two broad categories. The first are those that involve “out-of-plane” deformation, i.e. laser bending, induced by introducing a steep thermal gradient into the surface. The second are those involving “in-plane” shrinkage resulting from full penetration of the laser beam, the latter gives rise to an overall shortening in length and increase in thickness of the

irradiated zones [KAN 09]. The various LBF mechanisms can be summarized as shown in Table 2.2.

Laser Beam Forming Mechanisms			
Principle	**Process variables**	**Applications**	**Formed curvature**
TGM	– Rapid scan velocity – Small beam diameter or the same as the plate thickness – Plate thickness: thick	Form thick plates	Curvature is towards the beam
BM	– Slow scan velocity – Plate thickness: thin – Large beam diameter	Form thin plates	Depend on boundary conditions
UPM	– Slow scan velocity – Large beam diameter or the same as the plate thickness – Thick and stiff plates	Alignment and adjustment	Thickening of the curvature
PM	– Moderate scan velocity – Thin plate – Small beam diameter	Form micro-components	Form spot rather than line pattern

Table 2.2. *Summary of LBF mechanisms*

Thus, LBF is a term used to encompass both laser bending and planar or spatial transformation [DEA 03]. They identified three key mechanisms to explain the thermo-mechanical behavior in laser forming, each associated with specific combinations of component geometries and laser process conditions. These are comprised of the TGM, the BM and the shortening or planar upsetting mechanism (UM). The single point source is also considered and discussed as a LBF mechanism. In addition, Yong *et al.* [YON 06] recently conducted a comprehensive study of the mechanisms of laser forming for the metal plate. Based on the study of thermal transfer and elastic-plastic deformation, they further investigated the mechanisms of the LBF process and came up with a new mechanism called the coupled mechanism.

2.5.1. *Temperature gradient mechanism (TGM)*

This mechanism is widely reported [HU 02, YON 06, KAN 09] and can be used to form sheet material out of plane towards the laser beam. The temperature gradient mechanism develops from processing conditions, one of which is the rapid heating of the work piece surface in order to generate high temperature gradients in the work piece. The conditions of the TGM are energy parameters which lead to the development of a steep temperature gradient across the cross-section of the sheet thickness. The selection of the spot size during the temperature gradient condition is usually the same as the thickness of the material or less, and the scan velocity is high so as to develop a steep temperature gradient.

The thermal expansion of the heated surface brings about the initial bending of the sheet away from the heat source or towards the cold side of the work piece during the heating process. The bend angle at this stage is very small (about 0.05º); this is often regarded as counter bending. The counter bending phenomenon developed by the small spot size is also regarded as being detrimental to the development of a plastic bending angle towards the laser beam. This is because the phenomenon is similar to the relaxation of the surface stresses at the heated surface. As such, the thermal expansion leads to reduced surface stresses and therefore, the fraction of the thermal strain which is converted into plastic strain is less than without counter bending.

Furthermore, as the heated surface tries to expand, the constraint of the surrounding material, which is at a lower temperature restricts its free expansion. This results in compressive thermal stresses that induce plastic compressive strain in the heated layer. On cooling, the heated surface layer contracts more than the lower layers, which are not heated as much as the surface layers, resulting in the bending of the sheet toward the heat source. The conditions for the temperature gradient mechanism are energy parameters that lead to a steep temperature gradient across the sheet thickness. This results in a different thermal expansion through the sheet thickness.

To summarize, the TGM is comprised of the following steps:

– heating the surface of the material and resulting in the initial thermal expansion towards the cold region;

– further heating and plastic compression of the surface;

– cooling of the heated surface and thermal contraction;

– development of bending angles.

A schematic illustration of the TGM is presented in Figure 2.8.

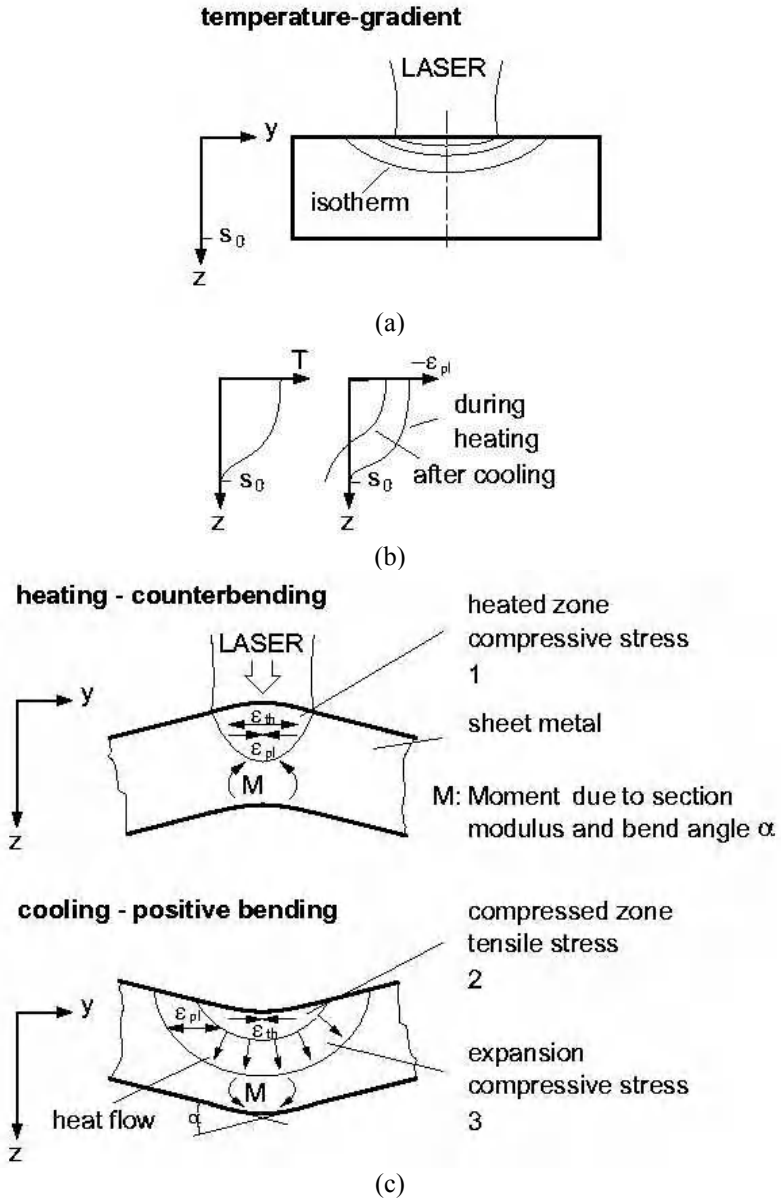

Figure 2.8. *Schematic illustration of the TGM: (a) beginning of heating; (b) temperature and strain variation in thickness direction; and (c) development of the bend angle during heating and cooling*

2.5.2. *Buckling mechanism*

The BM occurs in relatively thin sheets where the ratio of the diameter of the heated area to the sheet thickness is relatively high i.e. in the order of 10. This is if the laser beam diameter is large compared to the sheet thickness and the processing speed is low resulting in a small, or no, temperature gradient across the sheet thickness. The following summarizes the steps in BM operation:

– heating a large area of the sheet metal to develop a compressive stresses;

– the onset of buckling;

– growth of buckling;

– shifting the buckle through the whole sheet;

– relaxation of the elastic stresses.

The material is heated almost uniformly across the thickness since the developed temperature gradient is small. The heated region tends to expand, however the expansion is hindered by the unheated surrounding material. The restraint leads to the development of thermal compressive stresses in the sheet, which in turn forms a very thin material that may lead to the material buckling when under a critical stress.

Bending of the material close to the center of the heat source occurs plastically due to the high temperatures in the region. Close to the root of the buckle, the material is subjected to elastic bending because of the lower temperatures in that region [KAN 09].

The direction of the bending that results from the buckling mechanism can be unpredictable; it could be either towards or away from the heat source. This is because of a number of factors such as the boundary conditions, the pre-bending of the sheet, residual stresses and other external forces. However, it has been noted that for relatively high scan rates, i.e. 15 mm/s, depending on the process conditions, bending is always towards the laser beam. It is unpredictable at lower speed. The area of applications is in bending the sheet along straight lines and in tube forming. This mechanism can be used for the out-of-plane bending of sheet material; it may be accompanied by some in-plane shrinkage as well.

The schematic diagram of the BM is presented in Figure 2.9.

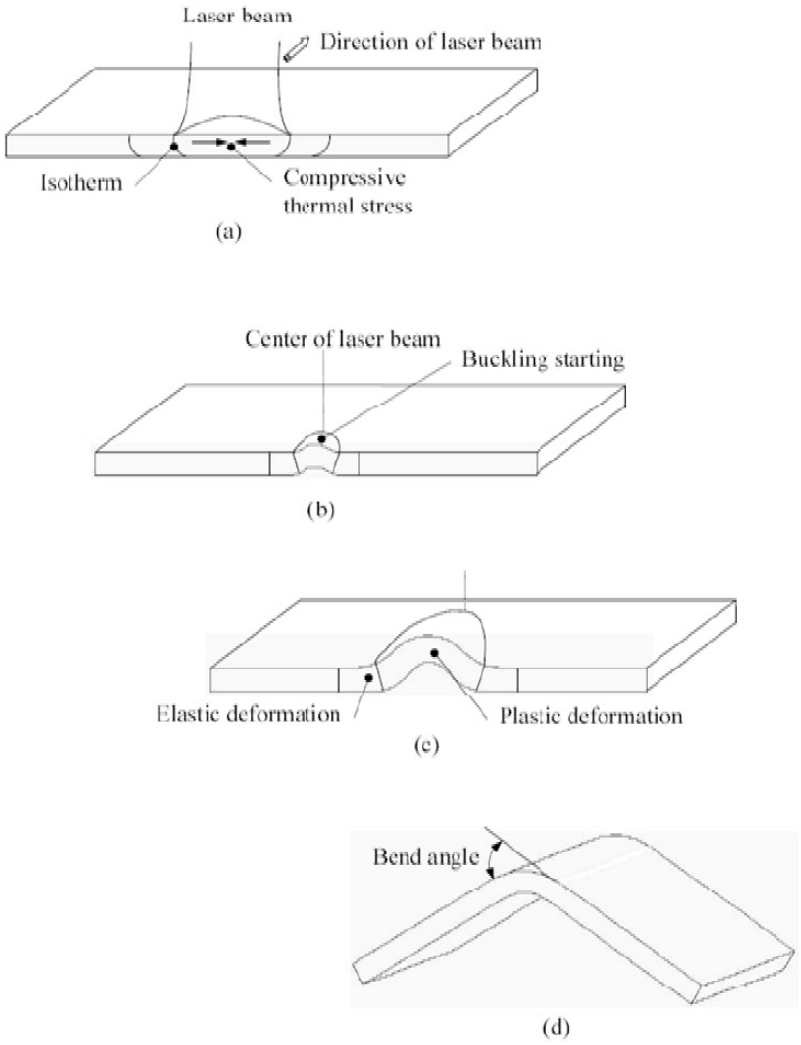

Figure 2.9. *Schematic illustration of the LBF stages using BM – sequence of steps leading to the bending of a plate [VOL 94]: (a) generation of thermal compressive stresses by laser beam; (b) development of buckling by thermal stresses; (c) development of elastic and plastic deformation; and (d) development of bend*

2.5.3. *Point mechanism*

This is the dividing line between the two previously discussed mechanisms, i.e. TGM and BM. The point source mechanism creates a heated zone in the shape of a

spot rather than a line. Using short pulses of the laser introduces a thermal gradient, yet the mechanism remains a point source since the beam is stationary when heating the component. Longer pulses enable heating through thicker materials, and may be mistaken for another type of mechanism for instance buckling, however the beam and work piece are also stationary when in contact. Micro-components may be formed with the point source mechanism.

2.5.4. *Shortening or upsetting mechanism*

The upsetting mechanism, shown in Figure 2.10, develops when uniform heating of a localized zone is achieved through the thickness of the sheet metal. The process parameters may be similar to the buckling mechanism, except that the diameter of the heat source is the same as plate thickness, or larger than it, and the scan velocity is low, as such the thermal conductivity of the material is moderately high. As a result of the near homogenous heating of the sheet in the localized zone, and prevention of thermal expansion by the surrounding material, the sheet is subjected to near uniform compressive strain through the thickness of the material.

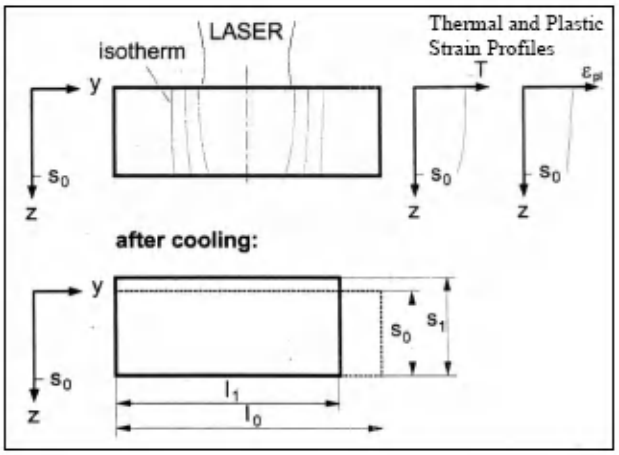

Figure 2.10. *Schematic illustration of the upsetting mechanism [VOL 98]*

During cooling, the region contracts and deformation occurs in the sheet. This mechanism finds applications in spatial sheet metal forming and profile forming, aligning operations in micro parts production and a wide range of forming results: such as the bending of extrusions and tubes. The three mechanisms to some extent accompany each other because of the distinct transition region of processing

parameters and geometries, wherein one mechanism leads to another during the process.

The upsetting mechanism may follow these steps:

– heating across the material and resultant thermal expansion;

– more thermal expansion that exceeds the elastic strain, result in developing plastic compression across the cross-section;

– finally, cooling of the material.

2.6. Advantages and disadvantages of LBF

The LBF process, being a thermal process, does not require any external force to bring about the deformation in the flat plates in comparison to the convectional forming process. The deformations are achieved by scanning the laser beam on the sample surface, whereby thermal stresses are induced. The following are the advantages of the LBF process compared to the convectional forming process [WAL 00]:

– the ability to form thick, brittle and hard materials;

– the ability to form a wide variety of complex shaped components through the development of new irradiation patterns;

– the ability to achieve precise deformation because spring back behavior is eliminated.

– the non-contact nature makes the process flexible; that is it can be automated, and as such saves some time associated with producing tooling and is free from tool inaccuracies that might result from wear and defection since no dies and presses are required for a LBF process;

– forming in inaccessible areas can be achieved because the process is non-contact;

– the energy source is better controlled, hence so is the process when compared to flame bending and mechanical forming process;

– minimal heat affected zone and material degradation when compared to the flame bending process where the heat source is more scattered.

In spite of the above listed merits of the LBF process, some drawbacks have also been identified. These include:

– a high investment cost in the laser facility makes it more expensive in comparison to convectional forming process, i.e. flame bending;

– the process is comparatively slow by a factor of 5-20;

– the process consumes high energy because of its low efficiency;

– safety precautions and protective wear are absolutely essential because of the likely multidirectional reflection characteristic of the intense laser beam.

The basic theoretical background to the LBF process has been presented so far. The next section will focus on the results of the LBF study of a steel plate.

2.7. LBF of a steel plate

2.7.1. *Introduction*

A large number of items used on a daily basis require different metal components, such as steel. Steel is an alloy consisting mostly of iron, with a carbon content between 0.02–2.1% by weight, depending on the grade. Carbon is considered to be one of the most cost effective alloying elements for iron but various other alloying elements are used and these include manganese, chromium, vanadium and tungsten. Carbon and other elements act as a hardening agent, preventing dislocations in the iron crystal lattice from sliding past one another, thereby strengthening the steel.

Today, steel is one of the most common materials in the world with more than 1,300 million tons produced annually. This high production rate might be a result of its inexpensive mass production process. It is also a major component in construction, infrastructure, manufacturing tools, ships, automobiles, machines, domestic appliances and weapons. Modern steel is generally identified by various grades defined by various standards. Despite the growth of aluminum and its alloys, steel still makes up the largest percentage of the metal composition used for car bodies.
[MOS 87].

2.7.2. *Material*

The material investigated in this research is a low carbon steel AISI 1008, supplied in the hot rolled condition. This is a formable steel used for industrial applications, but mostly used in the automotive industry because of its ability to be formed to desired shapes. The composition of the hot rolled formable steel has a maximum carbon content of 0.29 wt%. This material finds applications in automotive components, ship building, construction, domestic and agricultural machinery. A rectangular test sample size of 200 × 50 × 3.0 mm^3 was cut from the

steel plates and laser beam formed. The chemical composition of the parent material is presented in Table 2.3.

Element	**C**	**Si**	**Mn**	**P**	**S**
% by wt	0.072	0.068	0.321	0.0098	0.0091
Element	**Cr**	**Mo**	**Ni**	**Al**	**Fe**
% by wt	0.042	<0.005	0.0064	0.042	99.4347

Table 2.3. *Chemical composition of the parent material*

2.7.3. *Laser system*

The laser system employed to form the mild steel plates (AISI 1008) was a 4.4 kW Nd:YAG laser system (Rofin DY 044) from the Council of Science and Industrial Research – National Laser Centre (NLC), Pretoria, South Africa. The laser components include a fast axial gas flow, radio frequency excitation and stable optical cavity. An infrared light produced by the Nd:YAG laser has a wavelength of 1.06 μm which enables more efficient beam absorption in the work piece and a TEM_{00} mode. In addition, the delivery head of the laser beam is equipped with a 315 mm focal length mirror. Argon gas was used for shielding and cooling and the gas flow rate through the laser head was 10 *l*/min. This unit is classified as a class 1 laser system and has a maximum output power of 4.4 kW. The laser system used for the experiments is shown in Figure 2.11.

Figure 2.11. *Rofin DY 044 laser system*

2.7.4. *Experimental LBF setup*

The LBF were conducted with the following parameter range; laser power range between 1,800-3,600 W, beam diameter 12-18 mm and scan velocity of 0.04-0.08 m/sec. A varied number of scan tracks per irradiation were considered for the purpose of studying the effect on the process and response. Pure argon gas at a flow rate of between 5-15 *l*/min was used for cooling the irradiated surface and shrouding the environment to avoid oxidation. The generated curvatures were measured using a coordinate measuring machine, at three different points on the curvatures. The average of the measurement was then recorded.

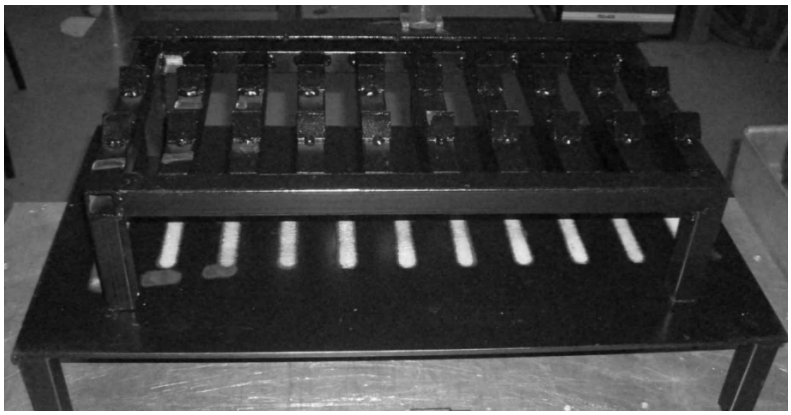

(a)

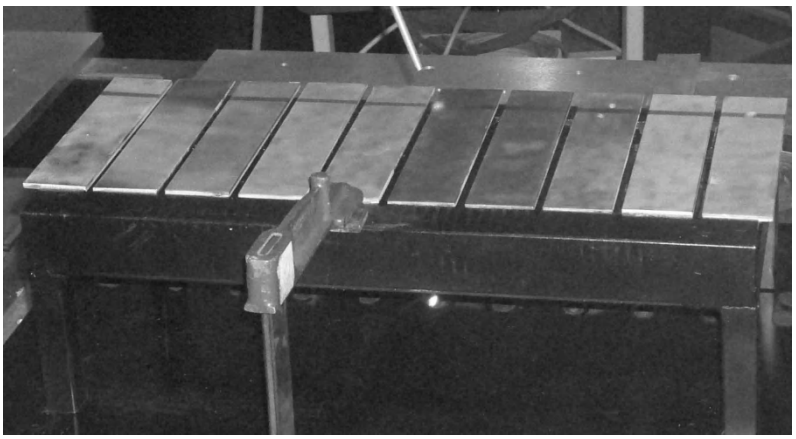

(b)

Figure 2.12. *Experimental setup showing the open mold and placed samples*

The experimental setup for the laser forming is shown in Figures 2.12a and b. A customized open mold was fabricated as a fixture for the samples. The mold provides a stable platform for positioning the samples and also ensures alignment of the samples in the direction of the laser beam (Figure 2.12a).

The open mold was considered for the experimental setup following preliminary studies whereby both open and cantilever type molds were employed. The choice for an open mold was based on the opportunity for maximum deformation of the sample and production of multiple formed samples. This also facilitates the scanning of samples from either ends of the mold. The test samples were all arranged and aligned on the mold for the beam irradiation (Figure 2.12b). The laser head was positioned to a specific height of about 315 mm for irradiation, this offset enables a defocused beam of 12 mm diameter to impinge on the target surface of the samples. With an open mold, multiple samples were formed at an instance, this effectively reduced the setup time for each process. After completing a run, the samples were irradiated with a different type of laser power, scanning speed, beam size, etc. [AKI 11c]. Typical laser formed steel samples are shown in Figure 2.13.

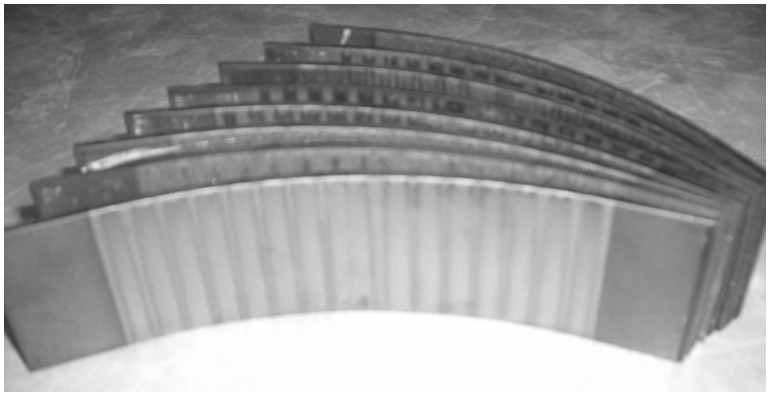

Figure 2.13. *Typical laser formed samples*

2.8. Design of experiments

Design of experiment (DOE) is a systematic approach to solving engineering problems by applying a set principles and techniques at the data collection stage to ensure that the generated results are reliable, valid, and can substantially support a technical conclusion. A classically designed experiment will ultimately save time, cost of experiments, and reduce errors in results if not completely eliminate them. Furthermore, designed experiments are aimed at reducing the effect of sources of variation in the output of experiments. This has been successfully applied to various

industrial applications such as quality control, manufacturing processes, material testing, process design and systems, greatly reducing the time and cost of experiments. Some of the DOE types that have been successfully employed are full factorial, fractional factorial, Taguchi designs, central composite design (CCD) and response surface methodology (RSM) [ROS 96, MON 06, XIA 11].

2.8.1. *Taguchi design*

The Taguchi design is a DOE technique with special application of principles and techniques that was employed in this study. It is used to identify variables that mostly influence the outcome of an experiment; under Taguchi DOE, the number of experiments is often limited and consequently reduces the overall cost. A set of experiments were performed to produce different curvatures from the laser beam formed steel component. The effect of the process parameters were investigated on the forming of the curvatures. To achieve this, an L_{27} Taguchi array with five experimental factors at three levels each was employed (Tables 2.4 and 2.5) [AKI 11a]. The levels of factors contained in Table 2.4 represent the variation in parameters for the experiment. For example, there are three levels of laser power, 1,800, 2,400 and 3,000 W. The experiments were repeated three times for improved accuracy making a total of $27 \times 3 = 81$ experiments.

Factors	Description	Levels		
		1	2	3
P	Laser power (W)	1,800	2,400	3,000
B	Beam diameter (mm)	12	15	18
V	Scan velocity(m/sec)	0.04	0.06	0.08
N	Number of scan tracks	1	3	5
C	Cooling rate (l/min)	5	10	15

Table 2.4. *LBF factors and their corresponding levels*

Taguchi designs have successfully been used to carry out the robust design of processes and products to solve several optimal problems in the manufacturing industries. It has also developed a methodology for finding the optimal settings of control parameters and making a product or process insensitive to the noise factor (7-8). In contrast to other optimal analytical methods, the experiments are planned according to the optimized problems.

Run	Factors					Measured Curvatures			
	P	B	V	N	C	Replicate 1	Replicate 2	Replicate 3	Mean Curv.
1	1	1	1	1	1	1,647.7	1,642.4	1,660.9	1,150.3
2	1	1	1	1	1	1,516.9	1,514	1,520.2	1,517.0
3	1	1	1	1	3	1,430.8	1,418	1,452.8	1,437.2
4	1	2	2	2	1	930	930	920	926.7
5	1	2	2	2	2	915	915	915	915.0
6	1	2	2	2	3	900	900	900	900.0
7	1	3	3	3	1	731.4	728	738.8	732.7
8	1	3	3	3	2	703.7	700.2	708	703.9
9	1	3	3	3	3	738.7	737	738.7	738.1
10	2	1	2	3	1	1,002.5	1,000	1,000	1,000.8
11	2	1	2	3	2	1,113.4	1,114.8	1,113	1,113.7
12	2	1	2	3	3	1,002.5	1,002	1,000.5	1,001.7
13	2	2	3	1	1	800	800	800	800.0

Table 2.5. *L_{27} Taguchi orthogonal array and measured curvatures*

Run	P	B	V	N	C	Repl. 1	Repl. 2	Repl. 3	Mean Curv.
14	2	2	3	1	2	806	806	802.6	804.9
15	2	2	3	1	3	818	815.6	820	817.9
16	2	3	1	2	1	306.1	309.7	301	305.6
17	2	3	1	2	2	293.1	292.4	293.8	293.1
18	2	3	1	2	3	312.2	311.7	309.9	311.3
19	3	1	3	2	1	920	920.9	919.2	920.0
20	3	1	3	2	2	905	908	908	907.9
21	3	1	3	2	3	945	947	945.8	945.9
22	3	2	1	3	1	239.3	238.5	240.2	239.3
23	3	2	1	3	2	275.8	274.2	274	274.7
24	3	2	1	3	3	262.3	260.8	262.4	261.8
25	3	3	2	1	1	450	451.6	450.3	450.6
26	3	3	2	1	2	450.2	448	450	449.4
27	3	3	2	1	3	450.6	450	452	450.9

Table 2.5. *(continued)* $\boldsymbol{L_{27}}$ *Taguchi orthogonal array and measured curvatures*

Firstly, the upper and lower limits for the control parameters and the orthogonal array test and data analysis method are selected. Secondly, the experiments are carried out as the designed orthogonal array, taking note of all the influencing parameters. Thirdly, the best level for the control parameters will be established after analyzing the data. The quality characteristics can then be predicted on the optimized levels of the control parameters. Lastly, the optimized results will be verified through tests and the best setting chosen for the application purposes.

2.8.2. *Effect of LBF factors on the resulting curvature*

The main effect plot of factors on the average bending angle is shown in Figure 2.14. This can be used to derive valid conclusions about the effect of various factors. Plots of factors P, B and N implies that an increase in the laser power, beam diameter, and number of scan irradiation respectively, impact the bending angle positively. On the other hand, an increase in the scan velocity increases the bending angle slightly while the cooling rate does not have a significant effect on the bending angle.

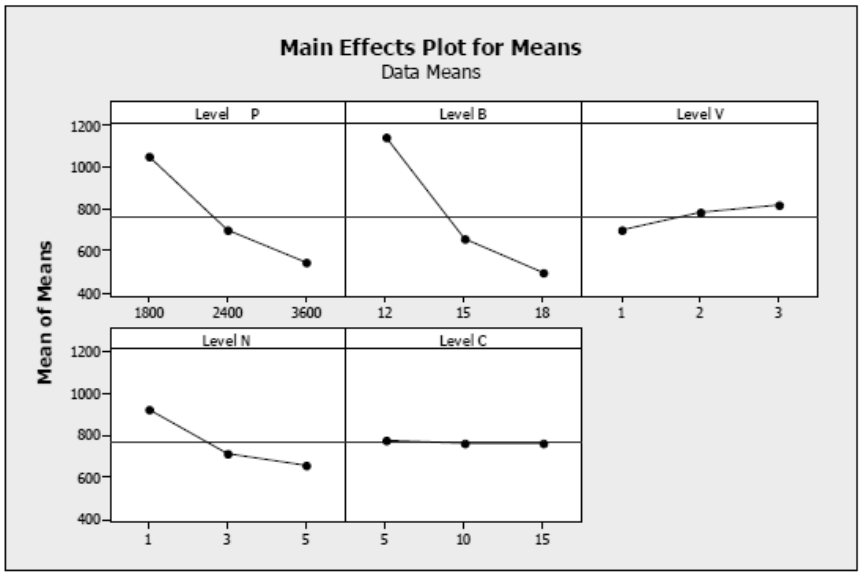

Figure 2.14. *Main effects plot on the mean radius of curvature*

The response table based on the Delta statistic for the effect of five LBF process parameters on the bending angle or radius of curvature is presented in Table 2.6.

Level	Laser power (kW)	Beam diameter (mm)	Scan velocity (mm/sec)	Number of scan tracks	Cooling rate (l/min)
1	2.889	3.022	8.444	4.856	5.711
2	5.511	6.6278	6.200	5.378	5.422
3	8.244	7.344	2.000	6.411	5.511
Delta	5.356	4.322	6.444	1.556	0.289
Rank	2	3	1	4	5

Table 2.6. *Response table of LBF factors on the radius of curvature*

2.9. Sample characterization

The laser formed samples and the parent material were characterized by both mechanical testing methods and microstructural evaluation in order to determine the structural integrity of the formed components, and also to establish a relationship (if one exists) that exists between the mechanical properties of the formed component [AKI 11b]. The evaluations conducted include the following.

2.9.1. *Optical microscopy*

All the specimens for analysis were taken 100 mm from the end of the samples. The polished specimens were etched with Nital solution (2%) by submerging them in the solution for 20 seconds. The microstructure was observed under an Olympus PMG3 optical microscope. The micrograph for both the parent material and the laser beam formed component is shown in Figures 2.15a and b respectively.

The evolution of the microstructures of the parent material was conducted to establish the structural configuration of the grains before producing the formed components. This gives a good baseline for comparison and also determines the effect of the beam on the structure of the materials. It was observed that the microstructure of the steel plates consists of fine grains of ferrite and a small amount of pearlite as shown in Figure 2.15a of parent material.

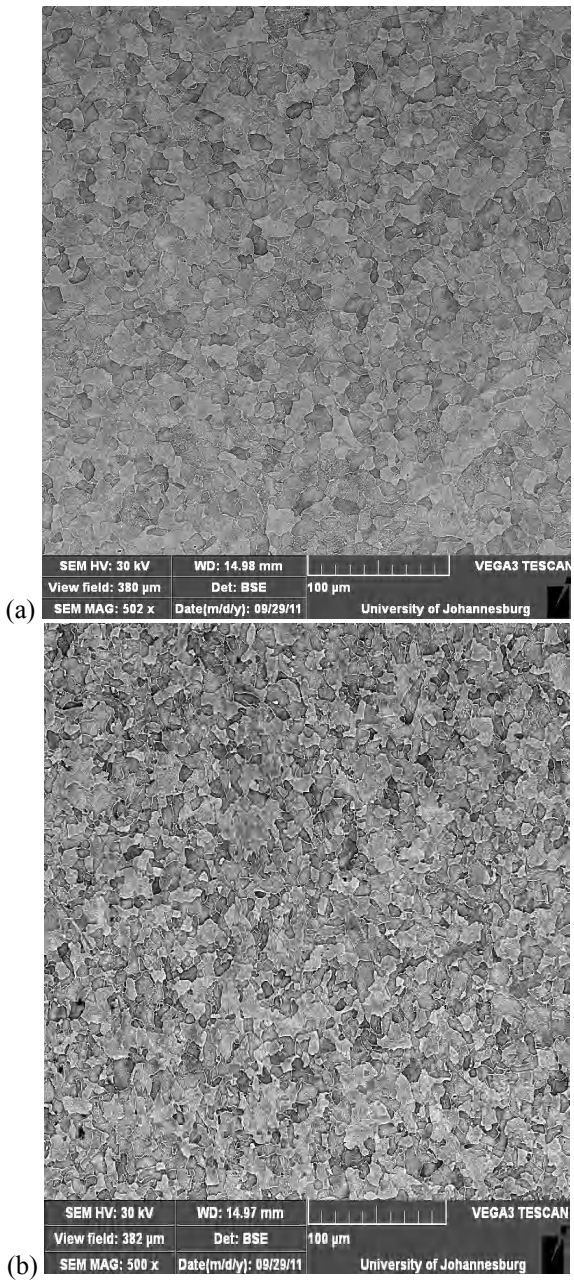

Figure 2.15. *Micrograph for: a) a parent material; and b) a laser beam formed component*

The micrograph of the bent component is a representative sample of the microstructure of the different curvatures produced. It is evident from the observation of the elongated grains in the microstructures of the laser formed sample that the sample has gone through a significant structural change when compared with the microstructure of the received material. These microstructural changes may be explained by the process of heating the material above its upper transformation temperature whereby the ferrite grain re-crystallizes. As such, the microstructure was transformed from the equiaxed ferrite matrix, recognized in the received material, to an elongated grain structure shown in Figure 2.15b. The development of this elongated grain structure can also be regarded as grain growth.

2.9.2. *Microhardness*

The Vickers microhardness profiles were measured using the FM-ARS 9000 automatic indenter according to the ASTM 384 standard. The measurements were made along the cross-section of both the parent materials and formed samples at the center of the sample thickness with a load of 300 g and a dwelling time of 15 seconds. The indentations were taken at 0.3 mm intervals and all indentations were manually focused and read. All the measurements were taken in the polished condition. The Vickers microhardness profile for both the parent material and formed component is shown in Figure 2.16.

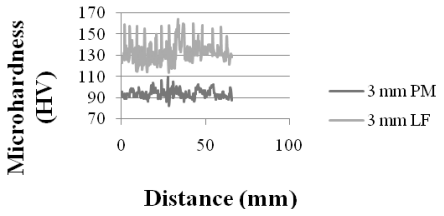

Figure 2.16. *Microhardness profile of the parent material and the laser formed sample*

The average Vickers microhardness values measured for the parent material and the laser formed component are 98 HV and 140 HV respectively. It was observed that the Vickers microhardness values measured in the formed samples are higher compared to the parent material. The high microhardness values can be attributed to grain refinement associated with rapid cooling during the laser forming process.

2.9.3. *Tensile test*

The tensile samples were prepared from the parent material and tested in accordance with the ASTM E-8 standard. A servo-hydraulic Instron 8801 tensile

testing machine was used to conduct the tests. An extension rate of 5 mm/min and a gauge length of 50 mm were used. The tensile test was carried out both on 3 and 4 mm steel plates. The ultimate tensile strength (UTS), yield strength and elongation percent of three samples of the 3 mm parent steel material tested are presented in Table 2.7.

	T_1	T_2	T_3	T_{mean}
UTS (MPa)	320.9	324.4	326.9	324.1
Yield Strength (MPa)	282.1	269.5	252.1	268
% Elongation	46.9	46.0	45.3	46.1

Table 2.7. *Tensile test results for a 3 mm parent material*

The tensile properties of the formed components were established through the relationship that exists between hardness and yield strength, shown in equation [2.6]. This became necessary because the experimental testing process of tensile testing for curve formed components is still under development. The estimated values of UTS for the parent material show a close correlation with experimental values as presented in Table 2.8.

$$UTS = 9.81\left[\frac{H}{2.9}\right]\left[\frac{n}{0.217}\right]^n \qquad [2.6]$$

where:

UTS = ultimate tensile strength;

H = hardness value;

n = strain index.

Estimated UTS (MPa)	
Parent Material (PM)	316
Laser Beam Formed Component (LBF)	432

Table 2.8. *Estimated UTS for a PM and LBF component*

The tensile results show a 38% increase in the UTS of the LBF component compared to the parent material. This can be attributed to the strain hardening resulting from the laser forming process.

2.10. Conclusion

The mild steel plates were successfully laser formed and the influence of the process parameters was studied. The Taguchi method of designing experiments was employed. Analysis of variance (ANOVA) was used for analysis of experimental results. From the main effect plots and statistical analysis the following factors were established to have a more significant effect on the bending angle:

– laser power;

– number of scan irradiation;

– scan velocity;

– beam diameter.

In this chapter, a fundamental understanding of the LBF process and the related literature has been presented. Experimental methodology, results and discussion on a study conducted on the LBF of AISI 1008 steel plates were also reported. It was found that the LBF process improves the hardness value and the grain structure of the formed component.

2.11. Bibliography

[AKI 11a] AKINLABI S.A., SHUKLA M., AKINLABI E.T., MARWALA T., "Laser beam forming of 3 mm steel plate and the evolving properties", *Journal of World Academy of Science, Engineering and Technology*, vol. 59, pp. 2279-2283, 2011.

[AKI 11b] AKINLABI S.A., AKINLABI E.T., SHUKLA M., "Effect of laser beam forming on microstructure and mechanical properties of AISI 1008 steel", *ASME McMat 2011 Conference*, Chicago, USA, May–June, 2011.

[AKI 11c] AKINLABI S.A., MARWALA T., AKINLABI E.T., SHUKLA M., "Effect of scan velocity on resulting curvatures during laser beam bending of AISI 1008 steel plates", *Journal of Advanced Materials Research*, vol. 299-300, pp. 1151-1156, 2011.

[ARA 73] ARAKI M., INOUE N., HORIOKA M., ANDO M., "On angular distortion of hull steel plates by line heating methods", *Journal of the Society of Naval Architects of Japan*, vol. 133, pp. 343, 1973.

[CHA 00] CHAN K.C., YAU C.L., LEE W.B., "Laser bending of thin stainless steel sheets", *Journal of Laser Applications*, vol. 12 no. 1, pp. 34-40, 2000.

[CHE 11] CHE JAMIL M.S., SHEIKH M.A., LI L.,"A study of the effect of laser beam geometries on laser bending sheet metal by buckling mechanism", *Journal of Optics and Laser Technology*, vol. 43, pp. 183-193, 2011.

[CHE 01] CHENG J., YAO Y.L., "Cooling effects in multiscan laser forming", *Journal of Manufacturing Processes*, vol. 3 no. 1, pp. 60-72, 2001.

[CHE 03] CHENG P., YAO Y.L., "The influence of sheet metal anisotropy on laser forming process", *Proceedings of ICALEO 2003*, no. 101, Jacksonville, Florida, 2003.

[CHE 05] CHENG P., YAO Y.L., LIU C., PRATT D., FAN Y., "Analysis and prediction of size effect on laser forming of sheet metal", *Journal of Manufacturing Process*, vol. 7, no. 1, pp.28-41, 2005.

[DEA 03] DEARDEN G., EDWARDSON S.P., "Some recent development in 2 and 3 dimensional laser forming for macro and micro applications", *Journal of Optics A: Pure and Applied Optics*, vol. 5, S8-S15, 2003.

[DUT 04] DUTTA M.J., NATH A.K., MANNA I., "Studies on laser bending of stainless steel", *Material Science and Engineering A*, vol. 385, pp. 113-122, 2004.

[EDW 07] EDWARDSON S.P., ABED E., CAREY C., EDWARDS K.G., DEARDEN WATKINS K.G., "Key factors influencing the bend per pass in laser forming", *Proceedings of ICALEO*, no. P506, pp. 508-514, 2007.

[GEI 93a] GEIGER M., HOFFMAN P., HUTFLESS J., "Laser material processing in synergy to metal forming", *Production Engineering (Annals of the German Academic Society for Production Engineering)*, vol. 1, pp. 37, 1993.

[GEI 93b] GEIGER M., VOLLERTSEN F., DEINZER G., "Flexible straightening of car body shells by laser forming", *International Congress and Exposition*, Detroit, MI, USA, 1993.

[GEI 94] GEIGER M., ARNET H., VOLLERTSEN F., "Laser forming", *Proceedings of the LANE*, pp. 81-92, 1994.

[HEN 97] HENNIGE T. "Laser forming of spatially curved parts", *Proceedings of the LANE*, pp. 409-420, 1997.

[HOL 94] HOLZER S., ARNET H., GEIGER M., "Physical and numerical modeling of the buckling mechanism", *Proceedings of the LANE*, pp. 379-386, 1994.

[HOS 08] HOSEINPOUR G.M., MOSLEMI N.H., LIAGHAT G.H., TORKAMANY M.J., JELVANI S., PANAHIZADE V., "An experimental study of sheet metal bending by pulsed Nd:YAG laser with DOE method", *International Journal of Material Forming*, vol. 1, pp. 137-140, 2008.

[HU 02] HU Z., KOVACEVIC R., LABUDOVIC M., "Experimental and numerical modeling of buckling instability of laser sheet forming", *International Journal of Machine Tools and Manufacture*, vol. 42 no. 13, pp. 1427-1439, 2002.

[ION 05] ION J.C., *Laser Processing of Engineering Materials*, Elsevier Butterworth Heinemann, 2005.

[KAN 09] KANNATEY-ASIBU E., *Principles of Laser Materials Processing*: John Wiley & Sons Inc., New York, 2009.

[KNU 08] KNUPFER S.M., MOORE A.J., "The effects of laser forming on the mechanical and metallurgical properties of low carbon steel and aluminium alloy samples", *Materials Science and Engineering A*, 2008.

[LAW 01] LAWRENCE J., SCHMIDT M.J.J., LI L., "The forming of mild steel plates with 2.5 kW high power diode laser", *International Journal of Machine Tools & Manufacture*, vol. 41, pp. 967-977, 2001.

[LI 01] LI W., YAO Y.L., "Laser bending of tubes: mechanisms, analysis and prediction", *Transactions of the ASME*, vol. 123, November 2001.

[LIU 08] LIU F.R., CHAN K.C., TANG C.Y., "Numerical modeling of the thermo-mechanical behaviour of particle reinforced metal matrix composites in laser by using a multi-particle cell model", *Composites Science and Technology*, vol. 68, pp. 1943-1953, 2008.

[LIU 07] LIU F.R., CHAN K.C., TANG C.Y., "Numerical simulation of laser forming of aluminium matrix composites with different volume fractions of reinforcement", *Materials Science and Engineering A*, vol. 458, pp. 48-57, 2007.

[MAG 98] MAGEE J., WATKINS K.G., STEEN W.M., "Advances in laser forming", *Journal of Laser Applications*, vol. 10, no. 6, 1998.

[MAR 98] MARYA M., EDWARDS G.R., "The laser forming of titanium alloys", *5th International Conference on Trends in Welding Research*, ASM International, Georgia, USA, pp. 1-6, 1998.

[MAR 00] MARYA M., EDWARDS G.R., "Factors affecting the laser bending of Ti-6Al-2Sn-4Zr-2Mo", *Journal of Laser Applications*, vol. 12, no. 4, pp. 149-159, 2000.

[MCG 01] McGRATH P., An investigation of residual stresses induced by forming processes on the fatigue resistance of automotive wheels, Doctoral dissertation, University of Plymouth, United Kingdom, 2001.

[MER 01] MERKLEIN M., HENNIGE T., GEIGER M., "Laser forming of aluminium and aluminium alloys – Microstructural investigation", *Journal of Materials Processing Technology*, vol. 115, pp. 159-165, 2001.

[MON 06] MONTGOMERY D.C., *Design and Analysis of Experiments*, John Wiley & Sons Inc., New York, 2006.

[MOS 87] MOSHAIOV A., VORUS W., "The mechanics of the flame bending process, theory and applications", *Journal of Ship Research*, vol. 31, no. 4, December, pp. 269-281, 1987.

[MUC 97] MUCHA Z., HOFFMAN J., KALITA W., MUCHA S., "Laser forming of thick free plates", *Proceedings of the LANE'97*, vol. 2, pp. 383-392, Meisenbach Bamberg, Germany, 1997.

[NAM 85] NAMBA Y., "Laser forming in space", *Proceedings of International Conference on Lasers*, Las Vegas, pp. 403-407, 1985.

[NAM 87] NAMBA Y., "Laser forming of metals and alloys", *Proceedings of LAMP*, pp. 37-44, 1987.

[PAU 08] PAUNOIU V., SQUEO E.A., QUANDRINI F., GHEORGHIES C., NICOARA D., *International Journal of Material Forming*, vol. 1, pp. 1371-1374, 2008.

[ROS 96] ROSS P.J., *Taguchi Techniques for Quality Engineering*, Tata McGraw Hill, New York, 1996.

[ROT 74] ROTHMAN R.L., Flame Straightening Quenched-and-Tempered Steels in Ship Construction, SSC247, Ship Structure Committee, 1974.

[SCH 11] Schematic diagram of Laser forming process, available from: www.liv.ac.uk/~me0u5040/forminf1.htm1, accessed 12 October 2011.

[SCU 87] SCULLY K., "Laser line heating", *Journal of Ship Production*, vol. 3 no. 4, pp. 237-246, 1987.

[SHE 06] SHEN H., YAO Z., HU J., "An analytical formula for estimating the bending angle by laser forming", *Journal of Mechanical Engineering Science*, vol. 220, 2006.

[SHE 09a] SHEN H., YAO Z., "Study on mechanical properties after laser forming", *Optics and Lasers in Engineering*, vol. 47, pp. 111–117, 2009.

[SHE 09b] SHEN H., VOLLERTSEN F., "Modelling of laser forming – an overview", *Computational Material Science*, vol. 46, pp. 834-840, 2009.

[SHI 06] SHI Y., YAO Z., SHEN H., HU J., "Research on the mechanisms of laser forming for the metal plate", *International Journal of Machine Tools & Manufacture*, vol. 46, pp. 1689-1687, 2006.

[SHI 01] SHICHUN W., JINSONG Z., "An experimental study of laser bending for sheet metals", *Journal of Materials Processing Technology*, vol. 110, pp. 160-163, 2001.

[STE 90] STERN G., "Absorptivity of cw CO_2, CO and YAG-laser beams by different metallic alloys", *ECLAT'90*, pp. 25-35, 1990.

[THE 11a] The Electromagnetic Spectrum, available at: http://www.google.co.za/images?hl=en&q=The+electromagnetic+spectrum&um=1&ie=UTF-8&source=univ&ei=HThuTJnGO8LMswbtwsTtBQ&sa=X&oi=image_result_group&ct=title&resnum=1&ved=0CCMQsAQwAA&biw=779&bih=440, accessed 12 October, 2011.

[THE 11b] The South African National Research Strategy, available from: http://www.naci.org.za/pdfs/sa_rd_strat_2002.pdf, accessed 12 October, 2011.

[THO 01] THOMPSON C., PRIDHAM M., "Material property changes associated with laser forming of mild steel component", *Journal of Materials Processing Technology*, vol. 118, pp. 40-44, 2001.

[VOL 94a] VOLLERTSEN F., "Mechanisms and models for laser forming", *Laser Assisted Net Shape Engineering, Proceedings of the LANE*, vol. 1, Meisenbach Bamberg, pp. 345–360, 1994.

[VOL 94b] VOLLERTSEN F., "An analytical model for laser bending", *Lasers in Engineering*, vol. 2, pp. 261-276, 1994.

[VOL 98] VOLLERTSEN F., "Forming and rapid prototyping", in SCHUOCKER D. (ed.) *Handbook of the Euro Laser Academy*, Chapman & Hall, Vienna, 1998.

[WAL 00] WALCZYK D.F., VITTAL S., "Bending of titanium sheet using laser forming", *Journal of Manufacturing Processes*, vol. 2, no. 4, pp. 258-269, 2000.

[WAT 01] WATKINS K.G., EDWARDSON S.P., MAGEE J., DEARDEN G., FRENCH P., *Laser Forming of Aerospace Alloys*, Society of Automotive Engineers, pp. 2610 2001.

[WEG 02] WEGENER K., ADELHARDT M., "Ship building experiences a revolution", *Industrial Laser Solutions*, vol. 17 no. 12, pp. 9-12, 2002.

[XIA 11] XIAN S.N., ZHENG G.S., XIONG W.W., LU M.L., "The use of Taguchi method to optimize the laser welding of sealing neuro-stimulator", *Optics and Lasers in Engineering*, vol. 49, pp. 297-304, 2011.

[YAN 10] YANG L.J., TANG J., WANG M.L., WANG Y., CHEN Y.B., "Surface characteristic of stainless steel after pulsed laser forming", *Applied Surface Science*, vol. 256, pp. 7018-7026, 2010.

[YAU 98] YAU C.L., CHAN K.C., LEE W.B., "Laser bending of lead frame materials", *Journal of Materials Processing Technology*, vol. 82, no. 1-3, pp. 117-121, 1998.

[YON 06] YONG J.S., ZHEN Q.Y., HO I.S., JUN H., "Research on the mechanisms of laser forming for the metal plates", *International Journal of Machine Tools and Manufacture*, vol. 46, pp. 1689-1697, 2006.

[ZHA 04] ZHANG W., LAWRENCE YAO Y., *Laser Material Processing Manufacturing Engineering Handbook*, Hwaiyu Geng, vol. 34, pp. 1-22, 2004.

Chapter 3

Laser Forming of Metal Foams

The current chapter shows that laser forming is able to produce large deformations of foams without affecting their structural integrity. The proposed technology is innovative as similar results were never obtained for open- or closed-cell aluminum foams by any other forming technique. Experimental results show that a very good formability was obtained by laser forming of several commercial foams.

3.1. Introduction

Aluminum alloy foams and sponges (Figure 3.1) are cellular materials with a unique combination of physical properties, which are useful for many applications, from energy absorption to thermal management. They can be produced by means of several techniques, which lead to specific characteristics in terms of foam structure and pore distribution. Unfortunately, these materials are typically brittle under mechanical forming, and this fact strongly limits their use. In a general manufacturing process, compression can be used to reduce the cell size and to increase the foam density but it is not possible to give curvature to a flat panel as the panel bending would result in the foam's failure.

Recent studies have shown that laser forming is able to produce large deformations of foams without affecting their structural integrity. This technology is

---

Chapter written by Fabrizio QUADRINI, Denise BELLISARIO, Erica A. SQUEO and Loredana SANTO.

Lasers in Manufacturing Edited by J. Paulo Davim

innovative as similar results have never been obtained for open- or closed-cell aluminum foams by any other forming technique.

Laser forming is a no-contact technique which presents many advantages as it requires no external forces or dies, it can shape complex curved surfaces and the springback is negligible. This technology seems to be very promising for industrial applications, as highly automated manufacturing processes can be defined. Moreover, it is possible to reduce tooling costs for rapid prototyping. The process offers great flexibility as a lot of other applications, such as soldering, brazing, and hardening can be performed by means of the same apparatus. The number of industrial applications of laser forming is continuously increasing, due to the possibility of forming highly accurate sheet metal products in a cost effective way.

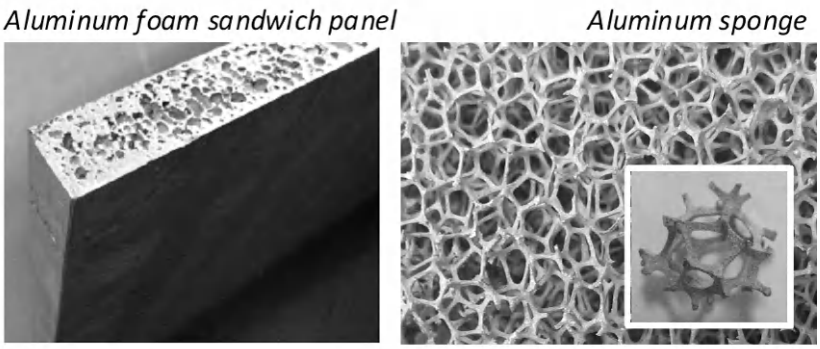

Figure 3.1. *Aluminum foams*

3.2. Scientific background

In the last 50 years porous metals and metal foams gained a growing interest in the scientific and industrial world because of their various potential applications; numerous studies were carried out to investigate the different ways to produce metal foams [LEF 08], [BAN 06]. Open-cell and closed aluminum foams cannot be formed by conventional mechanical processes because of the occurrence of failure during deformation. In order to produce complex shape parts, only two solutions are available: near net shaping or non-conventional technologies.

3.2.1. *Aluminum foam sandwich panels*

The efforts made to optimize compressive, tensional, torsional, and flexural properties of the foam structure have led to the development of aluminum foam

sandwich (AFS) panels, which are composites comprising an aluminum (alloy) foam core and two dense metallic face sheets firmly attached to the core. AFS structures can be produced by means of different technologies. In particular, the face sheet, or skin, can be bonded to the metal foam by means of *ex situ* or *in situ* bonding methods [BAN 08].

One of the main issues in metal foam production is in relation to the possibility of producing near net shape aluminum foam parts for large-scale production; few methods have been proposed to that end. The main method consists of mixing aluminum powder with the foaming agent; this powder is then compacted by a cold isostatic press to get billets for the extrusion process. The billet is the precursor material necessary for the foaming process, which is carried out in a shaped steel mold. Obviously this technique requires front-end investments in foaming molds and tools to shape the liquid foam but reduces post processing time [SCH 04]. An alternative process to produce near net shaped aluminum foam parts is based on the advanced pore morphology (APM) approach [STO 05], which consists of small-volume foam elements joined to each other in a separate process step. Using the APM process, pure foam parts, foam-filled hybrid structures and sandwich structures with a cellular core layer can be produced. A few attempts have been made to form metal foams in the desired shape by means of secondary forming processes, die-stamping [CON 06], forging [GAG 08] or incremental forming [JAC 08]. In these studies, great attention was given to the failure occurring during forming, and this topic was also discussed in other works, regarding the AFS panel failure mechanisms under bending tests [TAG 04, CRU 07, LEH 08].

3.2.2. *Open-cell aluminum foams*

Stochastic open-cell foams (or sponges) can be produced using open cell polymer foam templates to create a mold for investment or pressure casting. Polymer templates are inexpensive and available with a wide range of average cell sizes. The relative density and cell size of the cast foams is strictly dependent on those of the templates. Open-cell, stochastic nickel foams are used to produce electrodes and current collectors of metal-metal hydride batteries [WAD 02]. Instead, open-cell aluminum foams can be efficiently used to build compact heat exchangers for convective cooling [LU 98]. It was observed that compressed open-cell aluminum foam heat exchangers can generate thermal resistances that are two or three times lower than the best commercially available heat exchangers, while requiring the same pumping power [BOO 03]. However, in these studies, heat exchangers were produced by cutting open-cell aluminum foam panels into the desired shape, with the result of very simple flat geometries for the exchangers. On the contrary, complex shape structures are often necessary for an optimized design of heat exchangers. In this case, the final shape should be directly cast because of the

very low formability of this class of materials. Open-cell aluminum foams are quite often brittle materials, and show good deformation only by compression. In order to improve their formability, it is important to investigate new technological solutions, which could give any shape to the initial foam panel without affecting the functional properties of the foam.

Studying the formability of aluminum open-cell foams is a very hard task. Generally compression tests are performed to study the deformation mechanism of the foams during loading. The most deeply investigated material is an AA6101-T6 aluminum alloy (Al-Mg-Si) foam, Duocel®, which is produced by Erg. The foaming technology consists of infiltrating polymeric open cell foams (such as polyurethane foams) with a heat resistant material, removing the polymer by heating, casting liquid metal into the resulting form and then removing the heat resistant material.

Andrews *et al.* [AND 99] studied the compressive and tensile behavior of Duocel® to compare experimental results with models of cellular solids. They observed that the foam failed under compression by the formation of plastic hinges within the edges, because of the ductile nature of the AA6101-T6 alloy. The compressive plateau stress was roughly constant with increasing strain until densification occurred (above 50% of the strain), but the maximum tensile strain was lower than 1.5%. Therefore, a very poor formability could be expected, and further studies confirmed this statement.

Harte *et al.* [HAR 99], in their study on the fatigue failure of open and closed-cell aluminum alloy foams, discussed that the closed-cell foam Alporas® was significantly stronger in tension and in compression monotonic tests than the open-cell foam Duocel®, despite the fact that the open-cell foam consisted of the stronger cell wall material, and had a more uniform microstructure. By characterizing, in compression, several Duocel® panels with different densities and morphologies, Nieh *et al.* [NIE 00] also observed that the density is the primary variable controlling the foam modulus and yield strength. Furthermore, the cell size appeared to have a negligible effect on the foam strength, whereas the cell shape had a stronger effect.

The mechanisms and mechanics of compressive deformation were still further investigated by Zhou *et al.* [ZHO 04a] who concluded that the plastic bending of struts was the dominant deformation mechanism. Zhou and Soboyejo [ZHO 04b] also observed that annealing significantly reduces the absolute strength of the foam, but the ratio of the fatigue endurance limit to the foam strength increases with decreasing strength. More recently, Jang and Kyriakides [JAN 09] studied the evolution of crushing open-cell foams by compression at slow rates using X-ray tomography. They observed that the foam response is initially nearly linear, terminating in a limit load that is followed by an extensive plateau. At high strains

(about 55%), the load increases again due to densification. Beyond this point, cells start to buckle and collapse locally, forming bands that cover the full cross-section of the specimens.

3.2.3. *Laser forming*

The mechanism of laser forming metals is based on laser-induced thermal stresses. When considering metal plates, there are three main laser forming mechanisms: the temperature gradient mechanism (TGM), the buckling mechanism (BM) and the upsetting mechanism (UM). The TGM is present if the laser beam diameter is in the order of the sheet metal thickness. In the TGM, a fast laser scan along a line forms a steep thermal gradient across the thickness that produces differential thermal expansion, which in turn generates compressive stresses on the laser-processed surface. When these stresses reach the temperature-dependent flow-stress, plastic deformation occurs because of the restriction of the surrounding material. After laser passing, the material starts to cool and contracts, but the plastic deformation cannot recover, therefore the plate bends around the laser scanned line towards to the laser beam. In the BM, the spot diameter is greater than the plate thickness and the heated zone takes up the entire thickness. The expansion of the heated area is hindered by the surrounding material, and buckling of the irradiated material occurs. As a result, the plate starts to bend either away from or towards the laser beam. The UM uses process parameters similar to BM, but the heated area is much smaller than the plate thickness. The geometry of the plate prevents buckling due to the increased moment of inertia. In this case, the non-processed zone restricts the thermal expansion of the heated zone, which exhibits a nearly constant strain along the thickness. The material of the heated area shortens and increases its thickness during cooling; moreover, the material on the side of the laser beam starts to contract earlier than the opposite side and the plate starts to bend toward the laser beam. Finally, a combination of TGM and UM is known as the coupling mechanism (CM) [GEI 93, HEN 97, SHI 89]

3.3. Materials and experimental methods

Conventional mechanical bending processes seriously affect the mechanical performances of processed foam panels, and the challenge of forming complex shape parts is still open. In fact, metal foams show a ductile behavior only under compression and the related deformation mechanisms have been deeply investigated. However, in a manufacturing process, compression can be used only to reduce the cell size and increase the foam density. Instead, bending would be necessary to give curvature to a flat panel, but the panel bending would result in the foam failure because of the tensile stresses at the extrados.

In order to show the typical brittle behavior of the metal foams during conventional forming, mechanical bending was performed on an open-cell aluminum alloy foam. The test was carried out on a foam specimen to evaluate the maximum bending angle that can be reached before cracking. A universal material testing machine (MTS Alliance RT/50) was used, equipped with a 3 point bending fixture. The upper ram was a steel cylinder with a large diameter (60 mm), in order to better distribute the bending pressure on the specimen surface, avoiding the localized collapse of the cells. A speed of 1 mm/min was used with a span distance of 80 mm. As Figure 3.2 shows, a bending angle of about 23º was measured: after the maximum, as the upper ram kept on moving, a transversal crack propagated on the lower surface of the specimen.

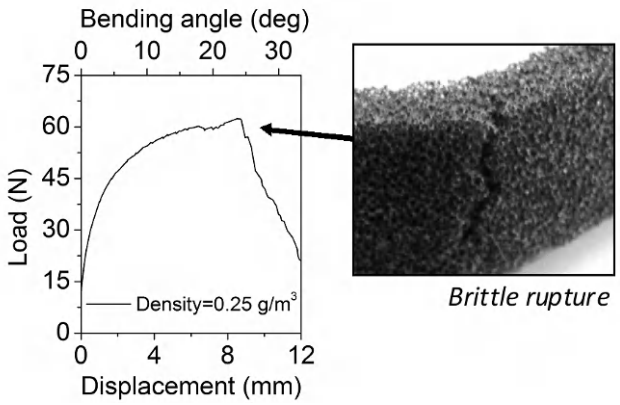

Figure 3.2. *Mechanical bending of an open-cell aluminum foam*

The ability to use a laser source to bend AFS and open-cell panels is shown in this chapter. Up until now, the laser bending technique has been used only to form sheet metals, but for the present study a diode laser was successfully used. In this way, the application of laser sources in the metal foam field was extended; in fact, they have, so far, only been used for welding or assisted foaming [KAT 03].

Due to the brittle behavior of the metal foams under tensile stress, the formability of this class of materials was rarely investigated. Nevertheless, mechanical stresses are not the only way to produce material deformation, thermal stresses can be used as well. That is the case for laser forming: rapid nonlinear thermal cycles produce thermal stresses, and thus, plastic deformation [SHE 09]. Contrary to mechanical forming, hard tooling or external forces are not present and brittle materials can be processed as well.

3.3.1. *Materials*

Three open-cell AlSi7Mg aluminum foam panels (by m-pore GmbH) and an aluminum sandwich panel (Alulight®) were used in the experimentation. The open-cell foams developed by m-pore GmbH are structurally similar to Duocell®: the compressive plateau stress and its strain rate dependency are substantially influenced by the alloy elements [GAS 01]. In the case of the (AlSi7Mg), the quasi-static plateau stress increases by a factor of 3, compared to pure aluminum (AA 1000 series). Therefore, a very poor formability was expected for the supplied foams. The three foam panels were 10 mm thick, and were different in density: (a) a foam with a pore diameter of about 6 mm and an apparent density of 0.19 g/cm^3; (b) a foam with a pore diameter about 2 mm and an apparent density of 0.21 g/cm^3; (c) a foam with a pore diameter about 1 mm and an apparent density of 0.25˚g/cm^3.

Figure 3.1 shows the structure of an acquired foam panel, type (a), with the detail of a single pore structure. As reported by the manufacturer, the metal foam structure consists of ligaments forming a network of interconnected dodecahedral like cells. The cells are randomly orientated and mostly homogeneous in size and shape. The triangular-cylindrical shaped edges of each cell are filled with metal, which is a result of the manufacturing process. Unfortunately, the foam structure of a single panel is not rigorously homogeneous in terms of its cell structure, and several cells with different size or number of ligaments can be observed.

The Alulight® AFS panel consisted of two Al 6082 cover sheets 0.65 mm thick, and a foam core made of AlSiMg. Observing the Alulight® foam panels, a difference between the two skins is visible to the naked eye. In particular, one of them is nearly smooth, whereas the other shows regular marks.

3.3.2. *Laser bending tests*

Rectangular specimens, of the size 100×35×10 mm^3, were cut from the foam panels and used for laser bending tests. The equipment used consisted of a 1.5 kW diode laser (Rofin-Sinar, DL 015) and a computer controlled motion table. The laser beam had a wavelength of 940 nm and a rectangular spot (in focalization 3.8×1.2 mm^2), which depended on the superposition of two different rays, each one coming from a 750 W emitter diode. A 63 mm long focus lens was used to maximize the depth of field. This laser source was particularly suitable because of the better absorption for aluminum alloys compared to the conventional Nd-YAG or CO_2-lasers.

A schematic view of the laser bending setup is shown in Figure 3.3. During bending, the laser beam was focused on the upper side of the specimen. For the

fabrication of each bent specimen, the sheet was fixed on a CNC motion table along the 35 mm edge. The specimens were laser scanned in the middle by moving them in a single direction under the motionless laser source. Each laser scan was 45 mm long, i.e. 10 mm longer than the specimen width. In this way the ramp effect at laser turn-on was avoided. Therefore, it is possible to assume that the laser power was constant during the bending process. During the laser scan, a flow of protective gas (nitrogen) was provided at the processed zone so as to maximize the bending efficiency. A sum of 100 or 150 passes were performed on each specimen, in sets of 10 consecutive passes. After each set, the specimen was left to cool in air for 2 min and the bending angle was evaluated by measuring the vertical displacement of the specimen's free end in the middle width by means of a centesimal comparator.

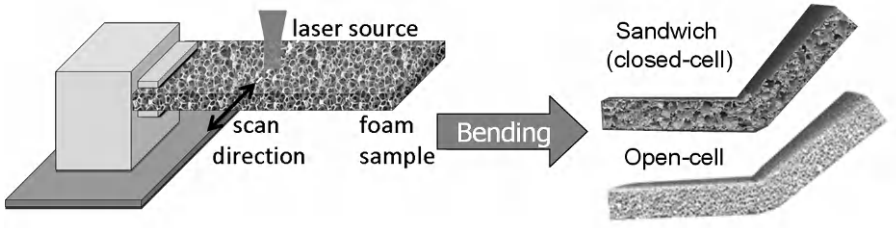

Figure 3.3. *Setup for the laser bending test and some bent samples*

The laser spot minor axis was aligned with the scan direction to increase the width of the laser heated zone. In this way the input energy per area was reduced. In fact the input energy $E = P/vt$, where P is the laser beam power [W], v is the laser scan velocity [mm/s], and t is the laser spot dimension normal to the scan velocity direction.

Four values of laser power were used (from 100 to 250 W with 50 W increments), and the scan velocities were 4, 5, 6 and 8 mm/s. Not all the combinations of laser power and scan velocity were used, because of some negative occurrences: melting of the foam (in the case of high power and low scan rate); poor bending efficiencies (in the case of low power and high scan rate); foam degradation (depending on the foam typology). One specimen was bent for all the other combinations of the process parameters.

Preliminary tests were performed to evaluate the best process conditions for each foam typology. For example, in the case of the foam sandwich panel, owing to the absence of nitrogen flow, melting occurred prematurely, therefore only 80 passes were performed at the laser power of 250 W and the scan rate of 6 mm/s.

3.3.3. *Material analyses*

Mechanical and microscopic analyses were carried out to increase the behavior of metal foams during processing. Cubic specimens were cut from open-cell panels for compression tests: the sample edge was 24 mm. Two compression tests were performed for each foam by means of a universal testing machine (MTS Insight 5) at a test rate of 1 mm/min, with a 5 N preload, and up to a maximum strain of 80% when densification occurred. Micro-structural analysis was also performed to evaluate the effect of the laser processing on the alloy structure.

3.4. Experimental results and discussion

Figures 3.4, 3.5, 3.6 and 3.7 show the bending angle as a function of the number of passes at different laser power and scan velocity values for the open-cell foam type (a), (b), (c) and the AFS panel, respectively.

The laser beam's ability to form metal foam panels was studied by the authors for the first time. Probably, in the past, the highly porous nature of the AFS panels led researchers to think that laser bending could not be applied. Instead, a very good formability was experimentally observed and the final structure of the formed panels did not show the cell collapse or cracks, which are typical of mechanical bending. Dealing with the forming mechanism, TGM was expected to be (like the laser beam spot) in the order of the thickness of the panel skin. Even if a good thermal conduction is present on the panel skin which is continuous, the apparent thermal diffusivity of the panel along the thickness is strongly affected by the foam porosity. BM has to be excluded because of the high panel stiffness. Moreover UM needs the formation of a uniform temperature gradient along the panel thickness, which is not possible considering the skin-core structure of the panel.

3.4.1. *Open-cell foams*

Figure 3.4 shows the bending curve for the open-cell foam with the lowest density (i.e. the higher pore size). The bending angle can be increased by increasing the number of passes, as well as by increasing the laser power. However, at 100 W, the energy input is too low and very low bending angles are observed for a high number of passes. Instead, at 250 W, the laser power is high to produce material melting also for a low number of passes. As a consequence, lower bending angles are measured in comparison with 200 W. However, beyond 120 passes, bending angles at 250 W become higher than the values at 200 W. This occurrence is due to the foam collapsing under heating, which strongly affects the foam geometry.

By increasing the scan velocity, the bending angle decreases because of the lowering of the energy input. In the experimented range for the type (a) foam, the best results were obtained with the lower value of the scan velocity (4 mm/s). Lower powers led to higher processing times, but they reduce sample distortions during forming. By increasing the power over 200 W, not only distortion but also material melting occurs.

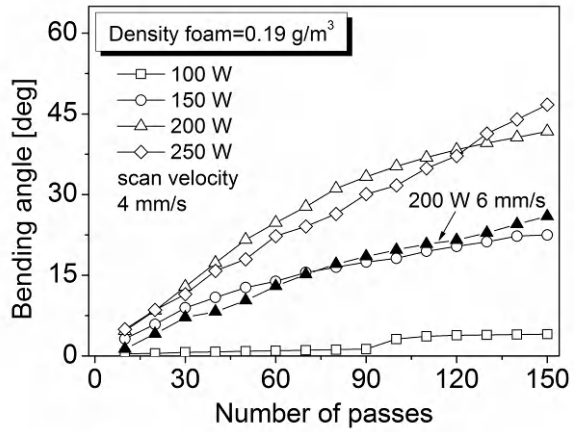

Figure 3.4. *Laser bending tests for the open-cell aluminum foam with the lowest density*

Similar results were obtained for the other two open-cell foams (Figures 3.5 and 3.6). In any case, by increasing the number of passes at a fixed laser power and scan velocity, the bending angle increases. The effect of the laser power and scan rate is the same. Higher bending angles were obtained for higher laser powers and lower scan velocities. However, these conditions led to a localized melting on the specimen laser processed line, near the end of the laser path; at this position, a very high conduction pre-heating effect was present (the material at the end of the laser path is already hot when the laser beam arrives in this zone, because of the high material conductivity). Nevertheless the melting occurrence was so limited as not to affect the bending efficiency. Another phenomenon that slightly affects the quality of the bent specimen is the occurrence of foam densification in the bending line zone, on the laser processed side. These two phenomena, melting and densification, can be overcome by sharing out the total angle on more bending lines, thus giving a foam specimen bent with a higher bend radius.

By choosing the proper combination of the process parameters, a bending angle over 50º was reached for such foams with 150 scans (Figure 3.5 and 3.6), without the occurrence of any cracks. At lower laser powers, lower bending angles are reached but this process condition could be preferred for the lower provided heat

which affects the aspect of the specimen surface. Similar bending angles cannot be obtained by means of mechanical bending because of the occurrence of the specimen failure. However, also before the failure, the cell collapse by mechanical bending is always excessive in the proximity of the upper ram.

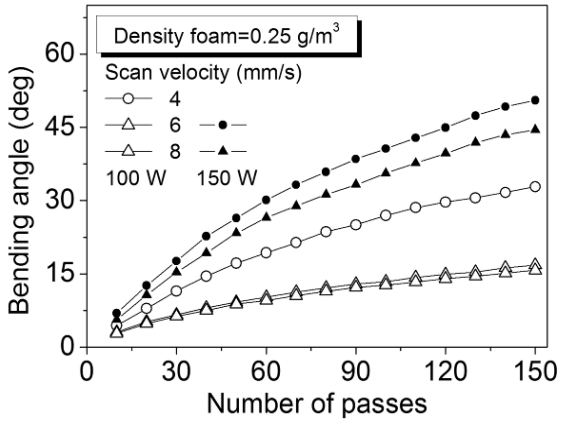

Figure 3.5. *Laser bending tests for the open-cell aluminum foam with the intermediate density*

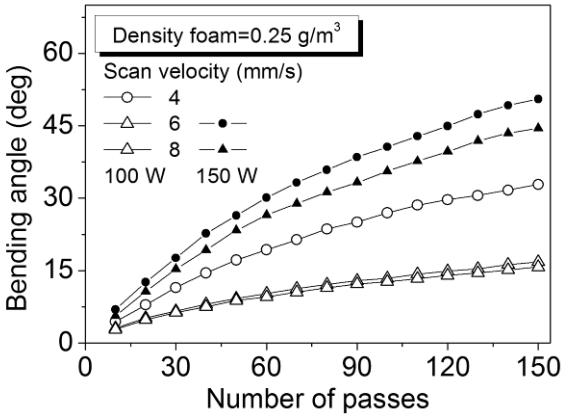

Figure 3.6. *Laser bending tests for the open-cell aluminum foam with the highest density*

Due to the high porosity of the open-cell foams, the laser deeply penetrates into the specimen, increasing the amount of the laser processed material. The reported

results are unique for this class of materials, which are generally considered not formable.

3.4.2. *Closed-cell foams (AFS panels)*

Very good results were also obtained for aluminum sandwich panels (Figure 3.7) even if a continuous skin is present on the laser heated surfaces. In this case a bending mechanism similar to the case of sheet metals probably occurs. Due to the presence of the skins, bending on a single line up to high angles inevitably leads to a crack formation on the skin not exposed to the laser beam. The effect of the laser power and the scan velocity on the bending angle is plain for the experimented ranges of the process parameters: also for AFS panels, the bending angle increases by increasing the laser power and decreasing the scan speed, as more heat is transferred to the specimen. A localized melting was observed for the highest power value, on the specimen skin, near the end of the laser path. At this position, in fact, a very high conduction pre-heating effect was present (the material at the end of the laser path is already hot when the laser beam arrives in this zone, because of the high material conductivity). However the melting occurrence was still limited so as not to affect the bending efficiency.

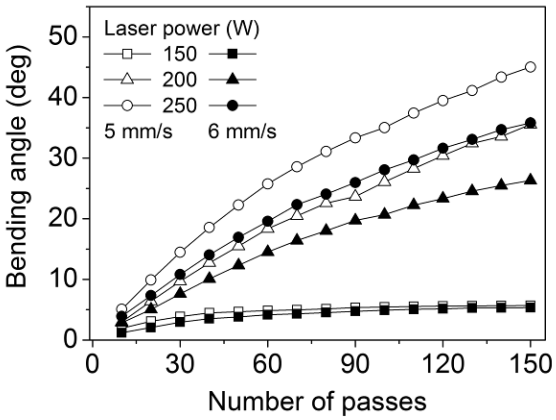

Figure 3.7. *Laser bending tests for the AFS panel*

Regarding the bending angle, it seems to reach a plateau value (a little less than 6º) for a laser power of 150 W, at both scan velocities. For higher laser powers the bending angle rises following a different trend, and no asymptotical values are visible. A maximum bending angle of about 45º was achieved after 150 passes at the laser power of 250 W and the scan speed of 5 mm/s. However, small cracks were

observed on the lower skin of the specimens which exhibited a bending angle higher than 30º (200 W, 5 mm/s; 250 W, 5 and 6 mm/s), due to the high stresses rising in that area. During laser bending of a sandwich specimen, the upper skin allows for better absorption of the laser beam, which would be nearly dispersed and not focalized on a foam structure, but contemporarily prevents the laser penetration. During processing, the lower skin is cold because it is not exposed to the laser beam, therefore it stiffens the specimen as it acts as a constraint that opposes to bending. The stiffening owing to the lower skin seems to heavily affect laser bending efficiency, as was observed by performing laser bending tests on a skin and a foam core as separate specimens. These tests were carried out at 150 W and 6 mm/s to avoid melting as the skin specimen was very thin. Owing to its low thickness, the skin specimen reached about 70º. The foam core specimen reached 18º, whereas the 10 mm thick sandwich specimen bent in the same conditions reached about 5º after 100 passes. The measured difference in the bending angle between the core and the panel sample probably depends on many effects: the discussed increase of the laser exposed surface of the core sample; the constraining effect of the lower skin of the panel sample; the slight difference between the thicknesses of the samples.

3.4.3. *The comparison*

By observing Figures 3.3, it is possible to notice a variation of the bending angle along the laser scanning path for all the foam typologies; this occurrence is known as the edge effect. For metal plates it was discussed that the irregularity caused by the edge effect could be reduced by precisely controlling the process parameters [JHA 08], for example, by varying the scan velocity in a proper way [SHE 07].

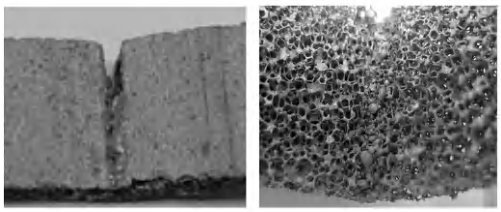

Figure 3.8. *Foam degradation due to bad processing*

During laser forming, some defects can be observed because of the laser-foam interaction (Figure 3.8, above), for a high number of passes. In such conditions, laser processing led to a localized melting on the specimen laser processed line but other visible effects are related to oxidation, densification (for open-cell foams), cracks (for AFS panels) or cutting.

For a better comparison between the different process conditions and foam typologies, the bending efficiency can be evaluated in terms of angle increase for a single pass. Apart from the initial stage, all the bending curves (Figures 3.4–3.7) show a linear trend in the bending angle, as a function of the number of passes. Therefore, a bending angle increase can be extracted from linear regression of these data, at fixed laser power and scan rate values. Results from this operation are reported in Figure 3.9. Open-cell foams show a higher bendability in comparison with sandwich panels probably due to the difference in the strengths of the foam panels. Moreover, the effect of the laser penetration in the open-cell foam is expected to be very effective, more than the spot localizing effect of the skin of the AFS panels.

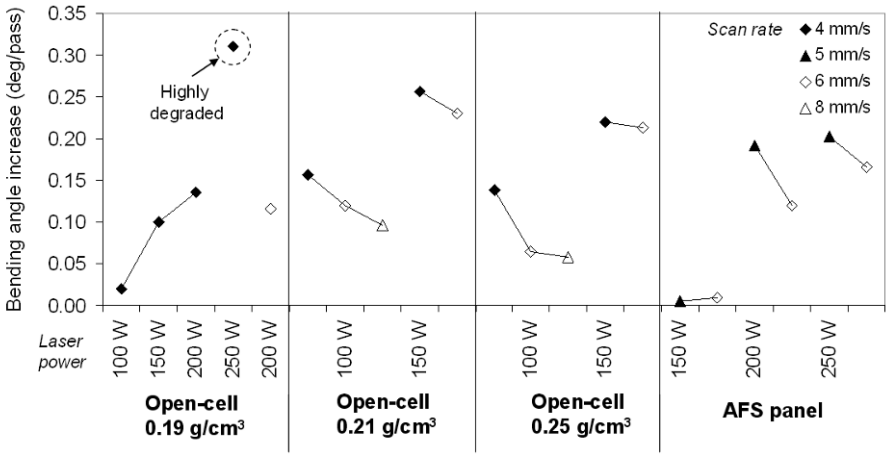

Figure 3.9. *Bending efficiency for all the foam typologies*

A complex trend of the bending efficiency on the density of the open-cell aluminum foam was measured. At low laser powers (100 W, 150 W) a better formability was observed for the foam panel with the intermediate density (0.21 g/cm^3). This kind of open-cell foam seems to be a good compromise between low strength, low density and high size of the irradiated surface. However, it is not possible to increase the laser power over 150 W – apart from in the case of the lowest foam density (0.19 g/cm^3), due to the occurrence of foam degradation. A time of 2 minutes every 10 scans is not sufficient to cool the foam down to room temperature, and the higher the foam density, the higher its temperature at the beginning of the successive set of laser scans. Instead, for the lowest density, higher laser powers can be applied, resulting in higher bendability. It should be easier to increase the bending angles in foams with big cells even when only using higher powers. In fact, due to the presence of wider spaces in the foam structure, the cells

can deform more easily in a less compact structure. However, experimental results show that the best results were obtained with higher density foams at lower laser power values.

On the experimented range, the best results were generally obtained by using low fluences (i.e. low ratios between the laser power and the scan velocity). In open-cell foams, at fluence values over 50 J/mm, material degradation rapidly occurs due to melting. In order to show the effect of the foam structure on the laser formability, Figure 3.5 reported a comparison between different foam samples which were bent under similar process conditions. It is evident that the cell structure strongly influences the foam behavior under laser heating. Actually, it is very difficult to make a comparison in terms of foam formability as the process windows are very narrow for all the foams: at 100 W the laser power was sufficient to produce a large bending in the foams with smaller cells, but not sufficient for the foams with bigger cells.

3.4.4. *Obtaining high bending angles*

Material melting of the upper skin and cracks on the lower skin are the problems that can occur during laser bending process of APS panels. Degradation and excess in cell collapse are visible in open-cell foams as well. As a consequence, very high bending angles cannot be reached. To overcome this problem the desired total angle can be shared out on more bending lines, as shown in Figure 3.10.

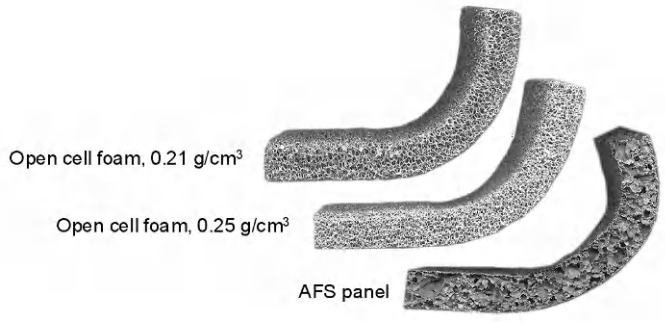

Figure 3.10. *Foam bending with high bending angles*

In particular, after 5 sets of 10 scans, the laser spot was moved 4 mm along the specimen length; this operation was repeated 15 times, therefore the total processed length of the specimen was 60 mm. Each scan was performed with a laser power of 200 W and a scan velocity of 5 mm/s for the APS panel, and 100 W and 4 mm/s for

the open-cell foams; this process parameter combination was chosen as a compromise between obtaining high bending angles for a low number of passes and avoiding material melting. As a result, a foam sandwich panel and two foam samples were bent more than 90º without any damage.

For the APS panel, no cracks were observed and the foam material in the thickness of the AFS panel remained nearly unaltered and, at the same time, a regular curvature of the panel was obtained. For open-cell foams, the proposed solution of sharing out the total angle on a higher specimen length, leads to a further advantage. Figure 3.9 reports the bending angle increase which can be interpreted as a bending efficiency which is actually strongly dependent on the number of passes; in particular, it was experimentally observed that the efficiency decreases by increasing the number of passes. Therefore, performing more contiguous bending operations with a maximum of 10 scans per line maximizes the final angle.

3.4.5. *Mechanical testing*

Results of compression tests are reported in Figure 3.11 for two open-cell foams. All the compression curves show the typical behavior of foams, with the initial pseudo-elastic range, a stress plateau due to the cell collapse, and a final stress increase because of densification. Oscillations are visible in the plateau region because of the irregular structure of the foam and the occurrence of ligament buckling during loading. Geometric irregularities are probably also responsible for the difference between curves in the initial pseudo-elastic part.

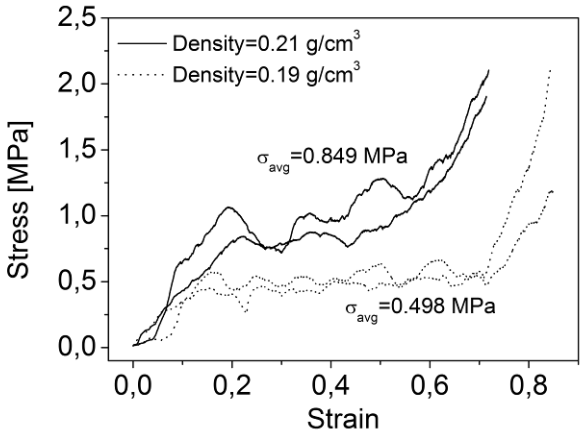

Figure 3.11. *Compression tests on open-cell foam samples*

Due to the curve oscillations in the initial part of the curve, the extraction of the material yield strength is not possible. The plateau stress can be used for a better comparison between foams and its average is reported in Figure 3.11. The plateau stress for the higher density foam is almost doubled in comparison with the lower density foam. Even if this result was expected, it was not possible to separate the effect of the foam structure (cell wall thickness and ligament length) from the effect of the base alloy mechanical properties.

In order to identify a pure elastic range, loading curves at small strains were also carried out on a low density foam sample. Successive loading curves were acquired and their superposition showed that the elastic range was correctly identified even if no information was given about the yield strength. A very low apparent elastic modulus was measured (13.6 MPa): scaling the alloy elastic modulus by the relative density of the foam (7.1%) results in an elastic modulus of about 5 GPa. This datum is two orders of magnitude higher than the measured value: evidently for small strains the elastic behavior of the foam is strongly dependent on the local deformation of ligaments. During compression, a complex combination of ligament buckling, yielding and elastic deformation occurs and experimental tests are not able to separate all these contributions from one another.

3.4.6. *Micro-structural analysis*

Studying the correlation between laser processing conditions and the microstructure of laser formed materials is a fundamental task to improve the laser formability of structures and the performances of processed parts. In the case of the diode laser forming of stainless steel, the thermal effect of the laser heating on the material annealing is clearly shown by the microstructure analysis, as annealing twins are observed in the processed zones of the samples [PAU 08]. The evaluation of the microstructure change is also important for other alloys [MER 01] or new laser forming methods [CHE 07]. In this study, the micro-structural analysis was hindered by the complex shape of the open-cell foam, but the transition between the heat affected zone (HAZ) and the un-processed area has been clearly identified.

Even when material melting does not occur, heat affected zones are always present (at least in terms of surface oxidation). Therefore, micro-structural analysis was performed to evaluate the effect of the laser processing on the alloy structure. Results for this analysis are reported in Figure 3.12 for an open-cell foam. Images were kept in three different parts of the sample: near the free end (“external part”) so as to evaluate the initial alloy microstructure, in the laser processing area where the HAZ was clearly visible, and in the middle between the free end and the HAZ. In the external part of the sample, the typical eutectic structure of the aluminum alloy is characterized by a coarse grain size probably due to a low cooling rate from the melt

during the foam production. In the middle zone the same microstructure is visible to indicate that no effect of the laser heating is present. Instead, in the laser processing area, the alloy microstructure strongly changes, with a fine and homogeneous eutectic phase because of the fast cooling after laser heating.

It was also possible to find some transition zones from the un-affected and the heat-affected part of the foam (Figure 3.13). Actually, in the entire bending zone, similar structures were observed, therefore the laser-material interaction always led to a strong change of the microstructure.

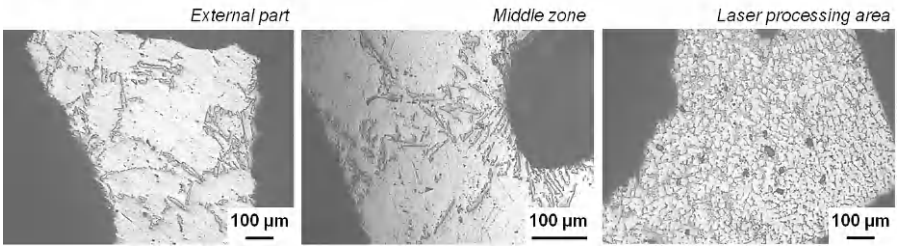

Figure 3.12. *Micro-structural analysis for a bent open-cell sample (density 0.21 g/cm^3, laser power 150 W, scan rate 4 mm/s)*

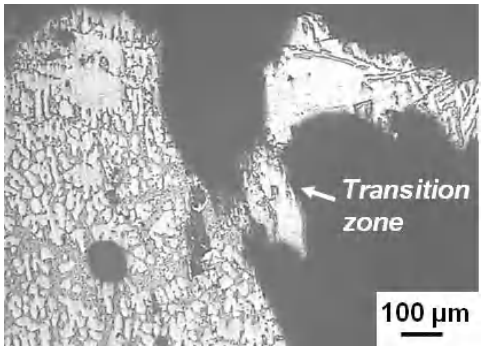

Figure 3.13. *Transition zone (density 0.21 g/cm^3, laser power 150 W, scan rate 4 mm/s)*

A last datum was obtained by analyzing the digital images of the foam cross-sections after bending in order to extract the amount of melted material. As a result, 40% of the melted material was measured, almost independently from the laser scan velocity or foam density.

3.5. Numerical modeling

The process setup of laser forming is quite complex as many geometrical and process parameters have to be considered; moreover the process window is very narrow and it is very easy to produce foam degradation during forming. In order to solve this problem, numerical simulation can be used for the definition of new laser forming processes, being able to reproduce the involved physical mechanisms. However, it is very difficult to build a valid model for the prediction of the laser-foam interaction during forming because of the foam structure complexity and the high number of parameters which have to be taken into account.

3.5.1. *The finite element model*

A 3D finite element model was implemented by Ansys rel.9.0 to investigate the forming mechanism of open-cell foams during laser exposure. Ansys Parametric Design Language (APDL) was used to easily change all the main geometric and process variables during modeling, and to reduce the computational time for model building. A batch procedure was defined to model the single cell structure depending on several geometric variables (such as the internal pore diameter and the number of structure faces). By changing these parameters, it was possible to build some cell models reproducing the commercial open-cell Al foams. Due to the difference in the apparent density of open-cell foams, a different relative density is present between them, from 7.1% to 9.3%. The proposed numerical approach was able to take into account this difference, at least in terms of solid models (Figure 3.14). In fact, mesh strategy depended on many factors (the available time for simulation, solution convergence, the accuracy of the solution) and it could affect the quality of the initial solid model. All the cell structures were free meshed and Figure 3.14 shows the appearance of the cell meshes in the case of a coarse approach. However, in order to simulate the laser bending of a foam sample, many cells have to be assembled and the final number of nodes could increase excessively.

The cell assembly procedure to form a foam structure was also modeled by APDL. Figure 3.14 reports a comparison between two different foam samples with the same apparent size.

3.5.2. *Laser processing simulation*

Numerical simulations were performed only by using the cell structure of the lowest density foam (i.e. the highest pore size). Moreover, only a small portion of the foam was modeled so as to reduce computational times. Therefore, it was not possible to make a quantitative comparison between experimental and numerical

data. Numerical results were primarily used to understand what physical mechanisms were involved during the forming of metal foams.

A 3D thermo-mechanical finite element model was implemented: the temperature-dependent material properties of AlSi7Mg were extracted by references [LED 82]. A bilinear isotropic hardening was assumed to simulate the material behavior during plastic deformation. The foam solid model is depicted in Figure 3.15 with a detail of the free mesh: the number of the cells was limited to 64 to reduce the computational time. Laser heating was modeled by means of a thermal load in terms of the heat flux over a 3.8×1.2 mm^2 rectangular spot. In order to simulate the effect of the porosity, the thermal load was also applied to the faces of inner elements up to a distance of 3.8 mm from the focalization surface. The laser scan was modeled by performing a spot translation on the focalization surface. A multi-step analysis was implemented: a laser power of 150 W and a scan velocity of 6 mm/s were fixed. A single laser scan was simulated together with a 10 s cooling phase. The heating phase was divided into 25 steps; at each time step a 1 mm spot motion was applied and therefore each time step was 1/6 s long. During cooling, the heat flux was removed and 1 s time steps were used.

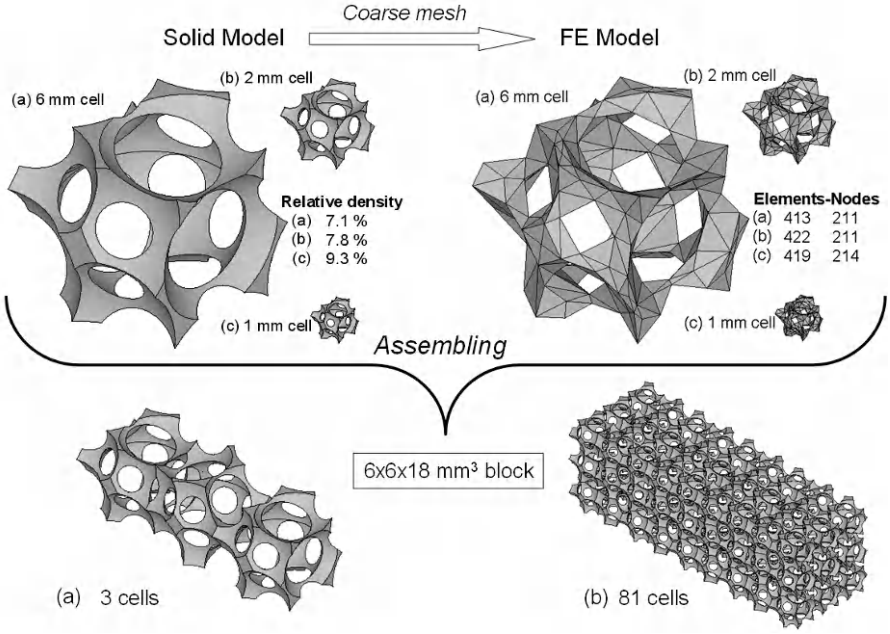

Figure 3.14. *Foam modeling*

Initially, a thermal analysis was carried out using SOLID70 thermal elements. After obtaining the thermal solution, the thermal elements were converted into SOLID45 structural elements and the thermal solution was used to define the thermal loads; subsequently, the nonlinear structural analysis was performed.

In the thermal analysis, the absorption coefficient was set to 0.2 to compensate for all the energy dissipations during laser heating. The heat transfer coefficient was 20 W/m^2 K and the room temperature was set to 25°C.

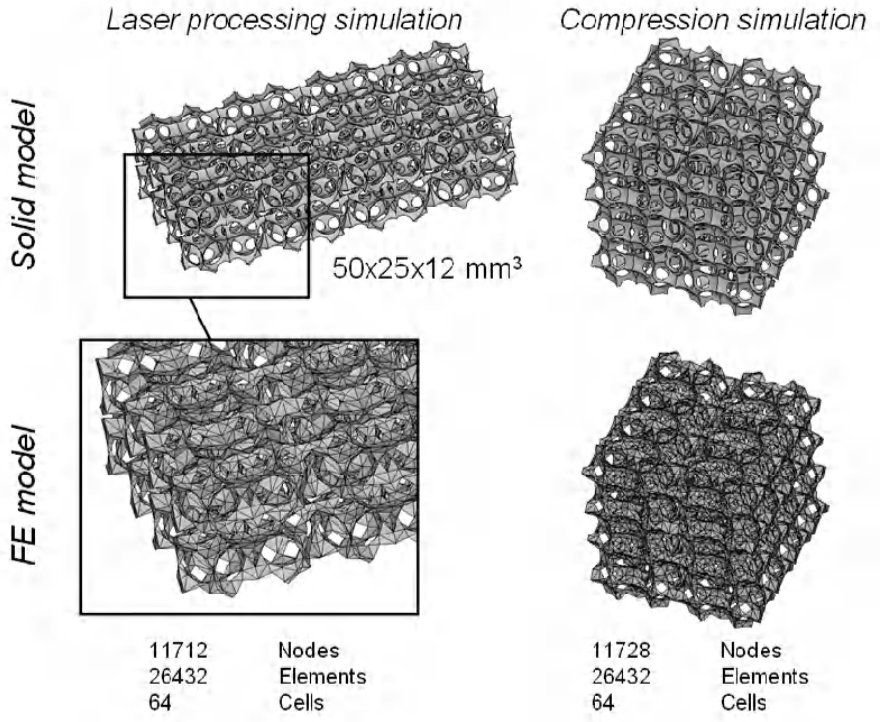

Figure 3.15. *Models for laser processing and compression test simulation*

3.5.3. *Compression test simulation*

In order to improve the predictability of the numerical model, several enhancements are necessary in terms of material behavior modeling. In the laser processing simulation, general mechanical properties of the foam base alloy have been used, but it is well known that the mechanical properties of aluminum alloys strongly depend on the process conditions, from casting to solidification. The

combination of the foam structure with the mechanical behavior of the base alloy determines the material response under mechanical loading: generally compression tests are used to study this kind of material both experimentally and by numerical modeling. Unfortunately cellular aluminum is highly porous and is characterized by an irregular geometry: the boundaries of the pores are made from the aluminum matrix, whereas the internal regions are air cavities. In order to have a precise geometrical model, recent studies have proposed generating FE models with computer tomography images as a basis. These models have been used to simulate the foams thermal [FIE 09] and mechanical behavior [VEY 11]. The serial sectioning method can also be used for the FE model generation [MIC 11]. However, because of the geometric accuracy and complexity of these methods, only small foam volumes can be modeled. Moreover, large differences are present in the adopted mechanical properties of the base alloy: the elastic modulus is always the same (about 70 GPa) but the yield strength can range from 20 MPa [MIC 11] to 130 MPa [VEY 11], depending on the foam typology.

The FE model building can be simplified by using regular shape unit cells: in the simplest case cubic unit cells can be used for open-cell foams [KON 10] but Kelvin cells [TAK 10] behave better because of the 14 sides and 36 ligaments. Large foam structures are built by repeating the same unit cell: the main problem with this kind of modeling relates to the strong final symmetry of the model, whereas the behavior of the foam is also anisotropic in the elastic range [VEY 11]. A way to solve this problem is to change the section properties of the ligaments in the Kelvin cell [JAN 10] or adopt an ellipsoidal unit cell for the foam assembly [GIO 10].

In this study, the proposed modeling method has the advantage of carefully considering the real structure of the foam in terms of relative density and pore size. The main goal is to understand the correct way to simulate the material behavior under forming: compression simulation can at least provide information about the suitability of adopting a bilinear isotropic hardening behavior. The best material model coefficients could be extracted as well.

The foam geometry was built by repeating the same unit cell: the open-cell foam with a pore diameter of about 6 mm and an apparent density of 0.19 g/cm^3 was taken as a reference (as for the laser processing simulation). The compression test of section 1.4.4 was simulated. Figure 3.15 shows the solid and FE model of a cubic sample. The 24 × 24 × 24 mm^3 block was modeled by assembling 4 × 4 × 4 unit cells. A bilinear isotropic hardening behavior was implemented for the Al alloy, fixing the elastic modulus to 70 GPa and changing the yield strength and the tangent modulus after yielding to match experimental results. The structural elements SOLID45 were used for the model discretization, and simulations were made with the large displacement option.

3.5.4. *Numerical results*

In order to obtain the numerical solution, many assumptions were made both for the foam geometry and the material behavior. Moreover, typical values for convection and heat flux were used to define the thermal loads. However, the numerical results are very interesting as they are able to simulate the foam deformation under laser exposure and compression.

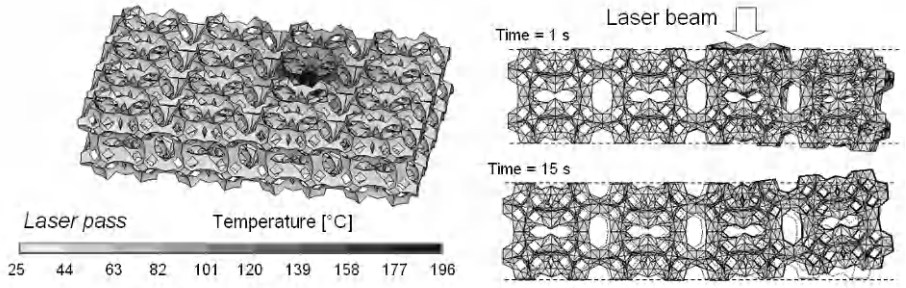

Figure 3.16. *Temperature map and foam deformation during laser forming*

A typical result is shown in Figure 3.16, which depicts the foam temperature map during the laser path together with the foam deformation. The effect of the laser motion on the temperature isotherms is visible with the typical "slipstream". The foam deformation is reported in two different process conditions: at the beginning of the laser exposure and at the end of the cooling phase (after 15 s). During the laser scan, the sample tends to bend away from the laser source because of the extension of the material under laser heating. In this stage, plastic deformation occurs, therefore, during the cooling phase, the contraction of the laser treated and yielded material causes foam bending toward the laser source. This effect is typical for laser bending and it is represented in Figure 3.17a, where the vertical displacements of two nodes on the edge of the foam-free end are reported over time. The first node was selected in correspondence with the start of the laser path (indicated as "start") and the second node in the edge middle width (indicated as middle). Generally the vertical displacements change their sign under cooling. For the node in the "start" position, that occurrence is anticipated due to foam rapid cooling after laser passing.

Figure 3.17b shows the temperature profiles during the entire simulation for two different points: at the start and the end of the laser path, from the side of the exposed surface. A temperature peak is observed when the laser passes over the point: the difference in the peak value depends on the different geometry surrounding the reference points. However, the material rapidly cools after the laser

passes because of the high specific surface of the foam and the thermal conduction in its bulk.

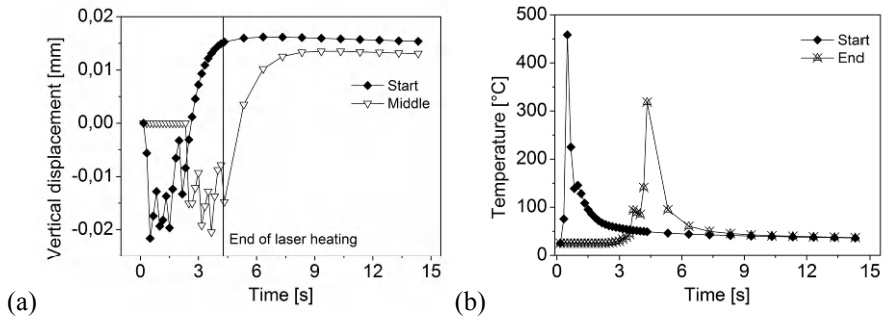

Figure 3.17. *Vertical displacement of the foam end (a) and temperature evolution (b) over time*

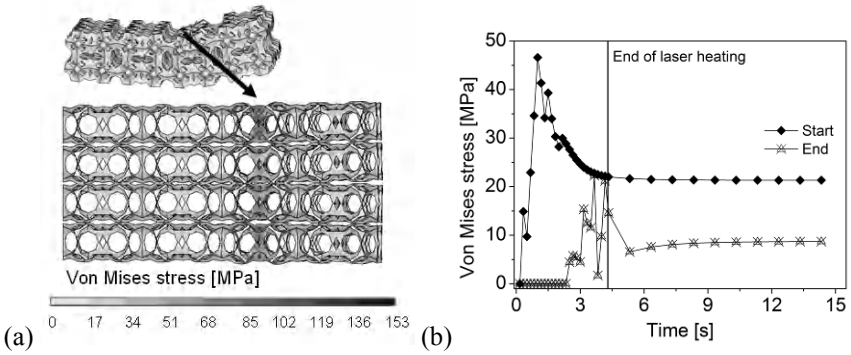

Figure 3.18. *Von Mises stress map (a) and its evolution over time (b)*

Figure 3.18 shows a stress map (von Mises stress) at the end of the cooling phase (Figure 3.18a) together with the von Mises stress evolution over time for the same nodes in Figure 3.15b (Figure 3.18b). The stress distribution is quite complex and a strong variation is calculated inside a single cell. As expected, plastic deformation occurs in all the cells during laser heating: the entity of the peak stress depends on the structure of the surrounding foam, as well as on the overall thermo-mechanical history.

Numerical results show that the mechanism at the basis of the laser forming of foams is the same for sheet metals. A temperature gradient mechanism is active but

the homogeneity of temperature and stress maps is affected by the non-homogeneity of the foam structure. However, a simulation of the full laser process (in terms of the sample geometry and process times) was not performed. Therefore, in order to provide information about the quantitative predictability of the adopted modeling strategy, mechanical testing was also simulated. For this aim, numerical analysis was carried out to simulate a compression test up to a displacement of 10 mm (40%). Low yield stress (10 MPa) and tangent modulus (1 MPa) values were used for bilinear isotropic material modeling. The model was able to accurately describe the foam deformation during compression (Figure 3.19): the model also reproduced the high cell distortion which was experimentally observed.

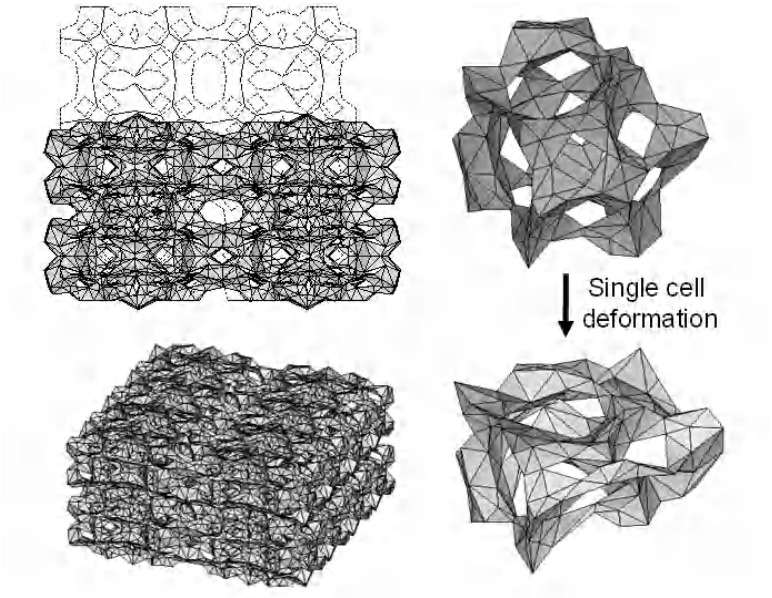

Figure 3.19. *Foam deformation during compression*

Figure 3.20 reports the von Mises stress map at different strain percentages: it is evident that plastic deformation already occurs at low displacements and propagates in the entire structure by increasing the strain. Figure 3.21 reports the comparison between numerical and experimental data in terms of the stress-strain curve: the average of the compression test was considered for the experimental curve to compensate data scattering. A preload of 0.3 MPa was applied to compensate for the differences in the first curve stage. The comparison shows that the model can predict the material response during the foam compression by applying a simple two-parameter hardening behavior.

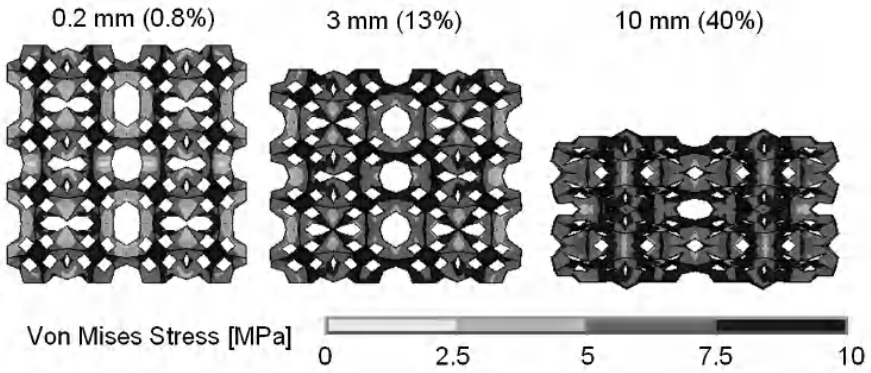

Figure 3.20. *Von Mises stress maps for different compressive strains*

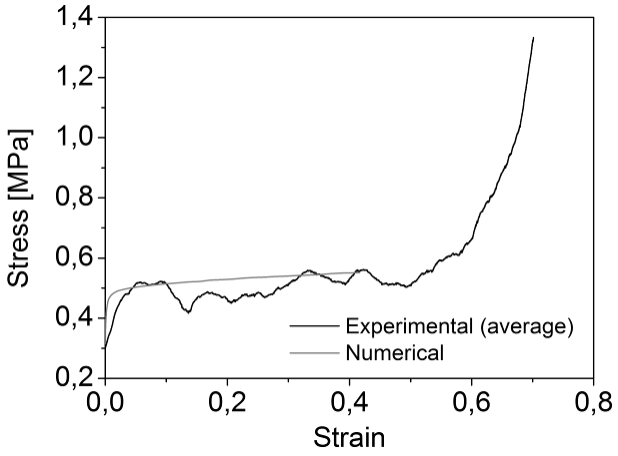

Figure 3.21. *Comparison between experimental and numerical data for the compression test*

3.6. Conclusions

Under conventional forming operations, apart from compression, open-cell foams exhibit very poor formability which strongly limits the application of this class of materials in many fields. In fact, in a general manufacturing process, compression can be used only to reduce the cell size and to increase the foam density. It is not possible to give curvature to a flat panel as the panel bending would result in the foam's failure.

The reported study shows that laser forming is able to produce large deformations in foams without affecting their structural integrity. The proposed technology is innovative as similar results were never obtained for open- or closed-cell aluminum foams by any other forming technique. Experimental results show that a very good formability was obtained by the laser forming of several commercial foams. The foams used in the present work are strongly different in terms of panel structure, pore structure, pore shape, distribution and density (in the range 0.21–0.25 g/cm^3 for open-cell foams, about 0.3 g/cm^3 for AFS panels). Therefore, different process parameter values were set (scan rates and laser powers).

A higher formability was measured for the open-cell foam panels because of several factors: the APS foam structure is coarse with large and irregular pores; the skin of the APS panel produces a constraining effect during laser forming; the strength of the open-cell foam is lower; the effect of the protective gas is more efficient in the open-cell structure.

It was shown that the process setup may significantly affect the bending efficiency, e.g. the use of a protective gas seems to be particularly important for avoiding the material melting during laser heating. The laser-foam interaction is responsible for the material degradation in such process conditions. Apart from melting or oxidation, by increasing the number of passes on a single line, the foam cells keep on collapsing with the consequence of strongly reducing the foam porosity. Even if these defects can be strongly reduced by fine tuning the process conditions, laser heating always affects the microstructure of the material directly exposed to the laser source. A fine and homogeneous structure is generated by a laser but, at a small distance from the laser processed area, the initial alloy microstructure is already visible.

Complex structures could also be obtained by laser forming if a proper scan strategy were to be designed. For example, the desired total angle can be shared out on more bending lines.

The main disadvantage of the proposed technique is related to the high cycle time as many laser scans are necessary to reach high bending angles. Nevertheless, improving material cooling between subsequent scans could lead to a high reduction of the processing time. Numerical simulation can be a useful tool for reducing the setup time and cost, but a complex calibration procedure is necessary.

3.7. Bibliography

[AND 99] ANDREWS E., SANDERS W., GIBSON L.J., “Compressive and tensile behaviour of aluminium foams”, *Materials Science and Engineering A*, vol. 270, pp. 113-124, 1999.

[BAN 06] BANHART J., "Metal Foams: Production and Stability", *Advanced Engineering Materials*, vol. 8, no. 9, pp. 781-794, 2006.

[BAN 08] BANHART J., SEELIGER H.W., "Aluminium foam sandwich panels: manufacture, metallurgy and applications", *Advanced Engineering Materials*, vol. 10, no. 9, pp. 793-802, 2008.

[BOO 03] BOOMSMA K., POULIKAKOS D., ZWICK F., "Metal foams as compact high performance heat exchangers", *Mechanics of Materials*, vol. 35, pp. 1161-1176, 2003.

[CHE 07] CHENG G.J., PIRZADA D., MING Z., "Microstructure and mechanical property characterizations of metal foil after microscale laser dynamic forming", *Journal of Applied Physics*, vol. 101, pp. 63108-1-7, 2007.

[CON 06] CONTORNO D., FILICE L., FRATINI L., MICARI F., "Forming of aluminum foam sandwich panels: Numerical simulations and experimental tests", *Journal of Materials Processing Technology*, vol. 177, pp. 364-367, 2006.

[CRU 07] CRUPI V., MONTANINI R., "Aluminium foam sandwiches collapse modes under static and dynamic three-point bending", *International Journal of Impact Engineering*, vol. 34, pp. 509-521, 2007.

[DEG 10] DE GIORGI M., CAROFALO A., DATTOMA V., NOBILE R., PALANO F., "Aluminium foams structural modelling", *Computers and Structures*, vol. 88, pp. 25-35, 2010.

[FIE 09] FIEDLER T., SOLORZANO E., GARCIA-MORENO F., OCHSNER A., BELOVA I.V., MURCH G.E., "Computed tomography based finite element analysis of the thermal properties of cellular aluminium", *Materialwissenschaft und Werkstofftechnik*, vol. 40, pp. 139-143, 2009.

[GAG 08] GAGLIARDI F., FILICE L., UMBRELLO D., SHIVPURI R., "Numerical simulation of foam forging to reproduce biomechanical components", *Materials Science and Technology*, vol. 480, pp. 510-516, 2008.

[GAS 01] GASSAN J., HARWICK W., GIRLICH D., "Behavior of aluminum foams under quasi-static and crash loadings", *Journal of Materials Science Letters*, vol. 20, pp. 1047-1048, 2001.

[GEI 93] GEIGER M., VOLLERTSEN F., "Fundamentals on the Manufacturing of Sheet Metal Microparts", *CIRP Annals*, vol. 42, pp. 301-304, 1993.

[HAR 99] HARTE A.M., FLECK N.A., ASHBY M.F., "Fatigue failure of an open cell and a closed cell aluminium alloy foam", *Acta Materialia*, vol. 47, no. 8, pp. 2511-1524, 1999.

[HEN 97] HENNIGE T., HOLZER S., GEIGER M., VOLLERTSEN F., "On the working accuracy of laser bending", *Journal of Materials Processing Technology*, vol. 71, pp. 422-432, 1997.

[LEF 08] LEFEBVRE L.P., BANHART J., DUNAND D.C., "Porous Metals and Metallic Foams: Current Status and Recent Developments", *Advanced Engineering Materials*, vol. 10, no. 9, pp. 775-787, 2008.

[JAK 08] JACKSON K.P., ALLWOOD J.M., LANDERT M., "Incremental forming of sandwich panels", *Journal of Materials Processing Technology*, vol. 204, pp. 290-303, 2008.

[JAN 09] JANG W.Y., KYRIAKIDES S., "On the crushing of aluminium open-cell foams: Part I. Experimental", *International Journal of Solids and Structures*, vol. 46, pp. 617-634, 2009.

[JAN 10] JANG W.Y., KYRIAKIDES S., KRAYNIK A.M., "On the compressive strength of open-cell metal foams with Kelvin and random cell structures", *International Journal of Solids and Structures*, vol. 47, pp. 2872-2883, 2010.

[JHA 08] JHA G.C., NATH A.K., ROY S.K., "Study of edge effect and multi-curvature in laser bending of AISI304 stainless steel", *Journal of Materials Processing Technology*, vol. 197, pp. 434-438, 2008.

[KAT 03] KATHURIA Y.P., "Nd-YAG laser assisted aluminum foaming", *Journal of Materials Processing Technology*, vol. 142, pp. 466-470, 2003.

[KON 10] KONSTANTINIDIS I.C., TSIPAS S.A., "Symmetry effects and their influence on the mechanical behavior of open and closed cell Al foams", *Materials and Design*, vol. 31, pp. 4490-4495, 2010.

[LED 82] LEDBETTER H.M., "Temperature behaviour of Young's moduli of forty engineering alloys", *Cryogenics*, vol. 22, pp. 653-656, 1982.

[LEH 08] LEHMHUS D., BUSSE M., CHEN Y., BOMAS H., ZOCH H.W., "Influence of core and face sheet materials on quasi-static mechanical properties and failure in aluminium foam sandwich", *Advanced Engineering Materials*, vol. 10, pp. 863-867, 2008.

[LU 98] LU T.J., STONE H.A., ASHBY M.F., "Heat transfer in open-cell metal foams", *Acta Materialia*, vol. 46, no. 10, pp. 3619-3635, 1998.

[MER 01] MERKLEIN M., HENNIGE T., GEIGER M., "Laser forming of aluminium and aluminium alloys – microstructural investigation", *Journal of Materials Processing Technology*, vol. 115, pp. 159-165, 2001.

[MIC 11] MICHAILIDIS N., STERGIOUDI F., OMAR H., PAPADOPOULOS D., TSIPAS D.N., "Experimental and FEM analysis of the material response of porous metals imposed to mechanical loading", *Colloids and Surfaces A*, vol. 382, pp. 124-131, 2011.

[NIE 00] NIEH T.G., HIGASHI K., WADSWORTH J., "Effect of cell morphology on the compressive properties of open-cell aluminium foams", *Materials Science and Engineering A*, vol. 283, pp. 105-110, 2000.

[PAU 08] PAUNOIU V., SQUEO E.A., QUADRINI F., GHEORGHIES C., NICOARA D., "Laser bending of stainless steel sheet metals", *International Journal of Material Forming*, vol. 1, pp. 1371-1374, 2008.

[SCH 04] SCHÄFFLER P., RAJNER W., "Process stability in serial production of aluminium foam panels and 3D parts", *Advanced Engineering Materials*, vol. 6, no. 6, pp. 452-453, 2004.

[SHE 07] SHEN H., ZHOU J., SHI Y.J., YAO Z.Q., HU J., "Varying velocity scan in laser forming of plates", *Materials Science and Technology*, vol. 23, pp. 483-486, 2007.

[SHE 09] SHEN H., VOLLERTSEN F., "Modelling of laser forming – a review", *Computational Materials Science*, vol. 46, pp. 834-840, 2009.

[SHI 06] SHI Y., YAO Z., SHEN H., HU J., "Research on the mechanisms of laser forming for the metal plate", *International Journal of Machine Tools and Manufacture*, vol. 46, pp. 1689-1697, 2006.

[STÖ 05] STÖBENER K., BAUMEISTER J., RAUSCH G., BUSSE M., "Forming metal foams by simpler methods for cheaper solutions", *Metal Powder Report*, vol. 60, no. 1, pp. 12-14, 2005.

[TAG 04] TAGARIELLI V.L., FLECK N.A., DESHPANDE V.S., "The collapse response of sandwich beams with aluminium face sheets and a metal foam core", *Advanced Engineering Materials*, vol. 6, pp. 440-443, 2004.

[TAK 10] TAKAHASHI Y., OKUMURA D., OHNO N., "Yield and buckling behaviour of Kelvin open-cell foams subjected to uniaxial compression", *International Journal of Mechanical Sciences*, vol. 52, pp. 377-385, 2010.

[VEY 11] VEYHL C., BELOVA I.V., MURCH, G.E. FIEDLER T., "Finite element analysis of the mechanical properties of cellular aluminium based on micro-computed tomography", *Materials Science and Engineering A*, vol. 528, pp. 4550-4555, 2011.

[WAD 02] WADLEY H.N.G., "Cellular metals manufacturing", *Materials Science and Engineering A*, vol. 4, no. 10, pp. 726-733, 2002.

[ZHO 04a] ZHOU J., SHROTRIYA P., SOBOYEJO W.O., "Mechanisms and mechanics of compressive deformation in open-cell Al foams", *Mechanics of Materials*, vol. 36, pp. 781-797, 2004.

[ZHO 04b] ZHOU J., SOBOYEJO W.O., "Compression-compression fatigue of open cell aluminum foams: macro-/micro- mechanisms and the effects of heat treatment", *Materials Science and Engineering A*, vol. 369, pp. 23-35, 2004.

Chapter 4

Mathematical Modeling of Laser Drilling

This chapter incorporates a review of the previously discussed mathematical modeling of laser drilling and develops a new model of laser percussion drilling. Formulation of the model is divided into three stages: solid heating, melting (and solidification), and vaporization. The governing equations are from heat conduction in a solid and liquid, and the appropriate initial and boundary equations at the solid-liquid and liquid-vapor interfaces. The newly developed model enables the prediction of the hole depth, hole profile and recast layer thickness.

4.1. Introduction

Laser drilling is one of the most extensively used applications of lasers in material processing. Its ability to produce small diameter and high aspect ratio holes in a wide variety of materials, including difficult-to-machine materials such as superalloys, ceramics and composites, make laser drilling an attractive option for modern industries. One of the most important applications is the laser drilling of a large number of closely spaced cooling holes in the turbine blades of aerospace engines. These tiny holes (ranging from 0.25 to 1 mm in diameter [LEI 09]) are required to provide sufficient cooling without reducing the structural integrity of the blade. The conventional method used for producing such holes is the electro-discharge machining (EDM), which although it gives excellent hole quality, the process is comparatively slow and expensive compared with laser drilling. Laser percussion drilling is an alternative drilling technique to the EDM due to its high production rate. It employs a series of short laser pulses to produce a hole on the

---

Chapter written by Maturose SUCHATAWAT and Mohammad SHEIKH.

Lasers in Manufacturing Edited by J. Paulo Davim

work piece. Despite being continuously improved over the years, laser percussion drilling still suffers from some defects including hole taper, splatter (re-solidified material at the hole entrance) and dross (re-solidified material at the hole exit). Therefore, it is essential to conduct further studies in order to precisely define the optimum setting of the laser parameters which produce the desired hole with the least defects.

Laser drilling is a complex process accompanied by various laser beam material interactions. When the laser beam impinges onto the work piece, it is absorbed and conducted into the work piece. Solid substrate is then heated to melting or boiling temperature depending on the laser intensity. This leads to changes of phase from solid to liquid, liquid to vapor or solid to vapor. The hole is subsequently formed by melt ejection and/or vaporization. The ejected melt may oxidize with oxygen and add more heat to the process. In some cases, plasma may be formed in the process, which traps part of the laser energy resulting in less energy delivered to the work piece. Moreover, the laser beam targeting the hole bottom may reflect repeatedly along the hole wall leading to variation of laser intensity inside the hole.

Mathematical modeling has long been recognized as an effective tool for studying various phenomena involved in laser material processing. Over the past few decades, modeling of laser drilling has continuously improved. The available models range from simple ones through to the most sophisticated model depending on the assumptions, problem setting and solving approaches. Nevertheless, similar to other mathematical models for laser processing, the governing equations for laser drilling models are typically established from heat conduction in a solid and liquid, conservation of mass and energy, as well as the boundary conditions at the interfaces.

Development of the laser drilling model is normally divided into three stages: solid heating, melting, and vaporization. During solid heating, the laser beam interacts with the solid substrate and raises the solid temperature to melting point. The modeling of this stage is typically focused on determining the temperature profile in the solid substrate [CAR 59, SAL 07, ZHA 99, SHE 01a]. Once melting begins, the solid-liquid interface is formed and propagates into the solid. Modeling of this stage is normally aimed at finding the solid-liquid interface location, its propagating speed, and the melt layer thickness [ELA 86, SHE 01b, XIE 97]. Further irradiation of the laser beam not only leads to more melting at the solid-liquid interface, it also raises the surface temperature of the liquid layer. If laser energy is sufficiently high, vaporization takes place and the liquid-vapor interface is formed. The vapor generated inside the cavity also exerts a recoil pressure on the liquid surface resulting in melt expulsion. The analysis of this stage is generally focused on determining the solid-liquid and liquid-vapor interface locations, drilling speed, and the hole profiles [SMU 91, ZHA 06, ZHA 99, SOL 99].

4.2. Solid heating

During laser heating, laser energy heats up the solid substrate from room temperature to the melting point. To determine the temperature profile in the solid and the time required to initiate melting, one-dimensional transient heat conduction in a semi-infinite solid has often been applied to the analytical modeling [CAR 59, HOL 02, ZHA 99, OBE 68]. Consider a solid plate subjected to a laser heat beam at the surface ($z = 0$) as illustrated in Figure 4.1, the heat conduction equation can be written as:

$$\frac{\partial^2 T_s}{\partial z^2} = \frac{1}{\alpha_s}\frac{\partial T_s}{\partial t} \qquad [4.1]$$

where T_s, t, z and α_s are the temperature in solid, time, vertical distance, and thermal diffusivity of the solid, respectively.

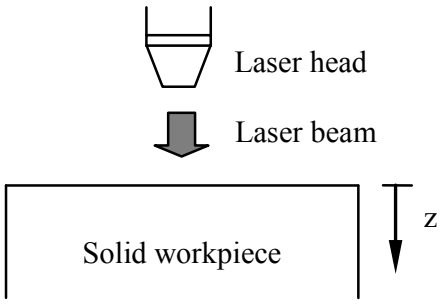

Figure 4.1. *Schematic diagram of stage 1: solid heating*

The boundary and initial conditions are

$$T_s(z,0) = T_0 \qquad [4.2]$$

$$I_{abs} = -k_s \frac{\partial T_s}{\partial z}\Big]_{z=0} \qquad [4.3]$$

where k_s is the thermal conductivity of the solid work piece, T_0 is the ambient temperature, and I_{abs} is the absorbed laser intensity defined by:

$$I_{abs} = (1-R_f)I_0 = A_s I_0 \quad [4.4]$$

where I_0, A_s, and R_f are the incident laser intensity, absorptivity, and reflectivity of the solid, respectively.

Carslaw and Jaeger [CAR 59] assumed that there would be solutions to the above system of equations if the laser intensity profile was in the form:

$$I(z,t) = I_{abs}\, erfc \frac{z}{2\sqrt{\alpha_s t}} \quad [4.5]$$

where $erfc$ is the complimentary error function and is defined by [KRE 06]:

$$erfc(x) = 1 - erf(x) = \frac{2}{\sqrt{\pi}} \int_x^{\infty} e^{-u^2} du$$

where $erf(x)$ is the error function defined by $erf(x) = \frac{2}{\sqrt{\pi}} \int_0^x e^{-u^2} du$ and u is a temporal variable defined here for integrating.

The temperature profile in a solid is then found to be:

$$T_s(z,t) = T_0 + \frac{2I_{abs}}{k_s}\left[\left(\frac{\alpha_s t}{\pi}\right)^{1/2} e^{-z^2/4\alpha_s t} - \frac{z}{2} erfc \frac{z}{2\sqrt{\alpha_s t}}\right] \quad [4.6]$$

The temperature at the surface is of particular interest, in order to estimate the time required to initiate the melting. According to equation [4.6], for a single laser pulse heating, the temperature at the surface $(z = 0)$ can now be determined from [CAR 59]:

$$T_s(0,t) = T_0 + \frac{2I_{abs}}{k_s}\left(\frac{\alpha_s t}{\pi}\right)^{1/2} \quad [4.7]$$

In the case of laser percussion drilling, a series of multiple pulses are employed. As shown in Figure 4.2, each successive laser pulse is separated by a pulse-off time where there is no laser beam-substrate interaction. The temperature drop takes place during this pulse-off duration.

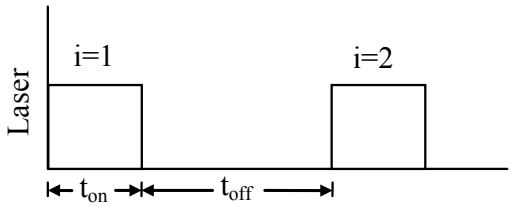

Figure 4.2. *Time step in laser percussion drilling*

The rise and drop of the surface temperature during the *i*th cycle can be estimated from [CAR 59, BAS 92]:

$$T_{on,i}(0,t) = T_{(i-1)/f} + \frac{2I_{abs}}{k_s}\sqrt{\frac{\alpha_s(t-(i-1)/f)}{\pi}}\ ;$$

$$\text{for}\ \ \frac{i-1}{f} \le t \le \left(\frac{i-1}{f} + t_{on}\right) \qquad [4.8]$$

$$T_{off,i}(0,t) = T_{(i-1)/f} + \frac{2I_{abs}}{k_s}\left[\sqrt{\frac{\alpha_s(t-(i-1)/f)}{\pi}} - \sqrt{\frac{\alpha_s(t-t_{on}-(i-1)/f)}{\pi}}\right] \text{for}$$

$$\left(\frac{i-1}{f} + t_{on}\right) \le t \le \frac{i}{f} \qquad [4.9]$$

where $T_{on,i}(0,t)$ and $T_{off,i}(0,t)$ are the surface temperatures during heating and pulse-off duration, respectively.

It is worth noting that in equation [4.9], the effect of convective heat transfer between the heated surface and the surrounding gas is not included. Therefore, some errors can be expected. Moreover, not only for solid heating, equations [4.8] and [4.9] can also be applied to laser heating of the liquid.

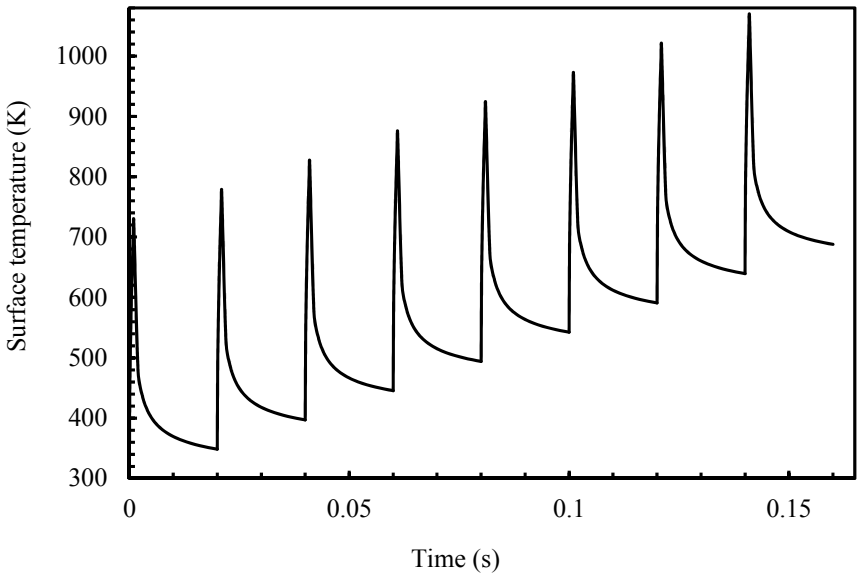

Figure 4.3. *Temporal evolution of the surface temperature of a mild steel plate subjected to pulsed irradiation*

Figure 4.3 shows the temporal characteristics of the surface temperature of a mild steel plate subjected to a laser beam at the surface. It can be seen that the surface temperature rises sharply during laser heating and decays dramatically during the pulse-off time.

Holman [HOL 02] derived an expression to predict the temperature change of a plate subjected to heat convection at the surface. By applying this equation to the case of cooling during laser pulse-off, the change in surface temperature can be written as [SAL 07]:

$$T_{off,i}(0,t) = T_{on,i} + (T_0 - T_{on,i})\left\{1 - \left[\exp\frac{h_g^2 \alpha_s t_{off}}{k_s^2}\right]\left[1 - erf\left(\frac{h_g\sqrt{\alpha_s t_{off}}}{k_s}\right)\right]\right\} \quad [4.10]$$

By using equation [4.7] to estimate the surface temperature during laser heating and equation [4.10] for cooling during the pulse-off interval, Salonitis *et al.* [SAL 07] has shown that during laser beam-material interaction, the surface temperature rises sharply while the temperature drops very slightly during the pulse-off duration.

4.3. Melting

If the energy of the laser beam incident on the solid surface is sufficiently high, melting begins and the solid-liquid interface is formed and propagates into the solid. Analysis of the melting can be described as the Stefan problem in which the phase boundary moves with time [ALE 93].

Extensive works have been carried out to study the laser-induced melting of a material, including analytical models [XIE 97, TOK 99, SHE 01b, ELA 86, LIN 90] and numerical simulations [KAR 90, BAS 88, VER 03, SHI 09]. Consider a plate irradiated with the laser beam at the surface where a thin layer of molten liquid is formed, as shown in Figure 4.4. Due to the melt pool diameter being much larger than the melt thickness, and because the melting predominantly occurs in the vertical direction, a 1D approach may be assumed [SHE 01b, CHE 00].

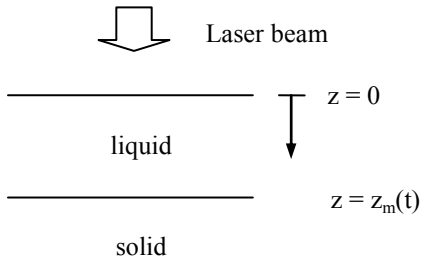

Figure 4.4. *Schematic diagram of stage 2: melting*

The heat conduction equations in the liquid and solid can be described as [SHE 01, XIE 97]:

$$\frac{\partial^2 T_l(z,t)}{\partial z^2} = \frac{1}{\alpha_l}\frac{\partial T_l(z,t)}{\partial t}; \quad 0 \le z < z_m \qquad [4.11]$$

$$\frac{\partial^2 T_s(z,t)}{\partial z^2} = \frac{1}{\alpha_s}\frac{\partial T_s(z,t)}{\partial t}; \quad z_m \le z < \infty \qquad [4.12]$$

with boundary and initial conditions:

$$-k_l \frac{\partial T_l(z,t)}{\partial z} = A_l I_0; \quad z = 0 \qquad [4.13]$$

$$T_s(z,t) = T_l(z,t) = T_m; \quad z = z_m(t) \tag{4.14}$$

$$\rho_s L_m \frac{dz_m(t)}{dt} = k_s \frac{\partial T_s(z,t)}{\partial z} - k_l \frac{\partial T_l(z,t)}{\partial z}; \quad z = z_m(t) \tag{4.15}$$

$$T_s(z,t) = T_0; \quad z \to \infty \tag{4.16}$$

$$z_m(t_m) = 0; \quad t = t_m \tag{4.17}$$

where $T_l(z,t)$ and $T_s(z,t)$ are the temperature profiles in a liquid and solid, k_l, ρ_s, and α_l are the thermal conductivity, density, and thermal diffusivity of the liquid, L_m, t_m, and $z_m(t)$ are the latent heat of melting, the time required to initiate melting, and the melting front location, respectively.

Today, solutions to the above set of nonlinear partial differential equations have been proposed by several authors [CAR 59, TOK 99, XIE 97, SHE 01b, COH 68, DOW 01]. Carslaw and Jaeger [CAR 59] reported an approximated series solution for the solidification of a semi-infinite large liquid mass. It must be noted that the proposed series solution is valid only for the case of low intensity laser irradiation. Cohen and Epperson [COH 68] assumed the same thermal conductivity and diffusivity values in the solid and liquid, and obtained the melting front location as:

$$z_m(t) = \frac{0.16 I_0}{\rho_s L_m}(t - t_m) \tag{4.18}$$

where the time to start melting, t_m, is given by [COH 68]:

$$t_m = \frac{\pi k_s^2 T_m^2}{4\alpha_s I_0^2} \tag{4.19}$$

Some researchers have developed the analytical models of laser melting by firstly assuming the temperature profiles in solid and liquid phases, which satisfy the boundary and initial conditions, and heat conduction equations at some points, i.e. at $z = 0$, $z = z_m(t)$, and $z \to \infty$ [XIE 97, SHE 01b, DOW 01]. Xie and Kar [XIE 97] assumed the temperature profile in the liquid layer to be:

$$T_l(z,t) = T_m - \frac{A_l I_0}{k_l}[z - z_m(t)] + f(t)[z^2 - z_m^2(t)] \tag{4.20}$$

where:

$$f(t) = \frac{A_l I_0}{2\alpha_l k_l \left(1 + \frac{z_m(t)}{\alpha_l}\frac{dz_m(t)}{dt}\right)}\frac{dz_m(t)}{dt}.$$

In the solid, an exponential function was assumed for the temperature profile, i.e.:

$$T_s(z,t) = T_m - (T_m - T_0)\{1 - \exp[-b(t)(z - z_m(t))]\} \quad [4.21]$$

where:

$$b(t) = \frac{1}{\alpha_s}\frac{dz_m(t)}{dt}.$$

By substituting the assumed temperature profiles into the heat conduction equations, expressions for the melt depth and the melting front velocity were derived.

In addition to the profiles assumed by Xie and Kar [XIE 97], it is generally accepted that exponential forms can be approximated for the temperature profiles in the solid and liquid [SHE 01b, ZEN 05, DOW 01]. Shen *et al.* [SHE 01b] assumed the following exponential temperature profiles in their laser melting model:

$$T_l(z,t) = T_{l0}(t)\exp\left[\frac{-z}{\delta_l(t)}\right] \quad [4.22]$$

$$T_s(z,t) = T_m \exp\left[\frac{-(z - z_m(t))}{\delta_s(t)}\right] \quad [4.23]$$

where $T_{l0}(t)$ is the melt surface temperature, and $\delta_l(t)$, and $\delta_s(t)$ are two temporal functions indicating the temperature penetration depth in a liquid and solid, respectively. By substituting equations [4.22] and [4.23] into the heat conduction and boundary equations, these two temporal functions were determined simultaneously with the melt layer thickness, and the temperature profiles in solid and liquid.

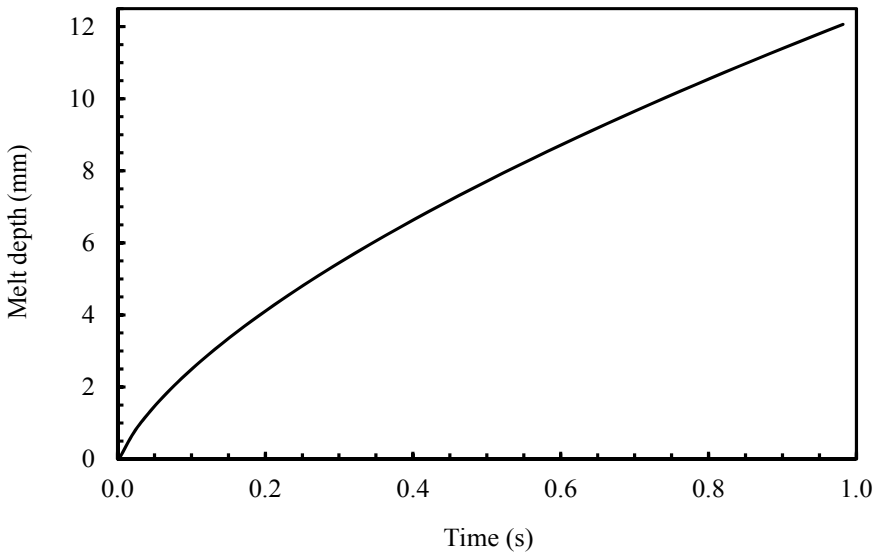

Figure 4.5. *Melt depth evolution*

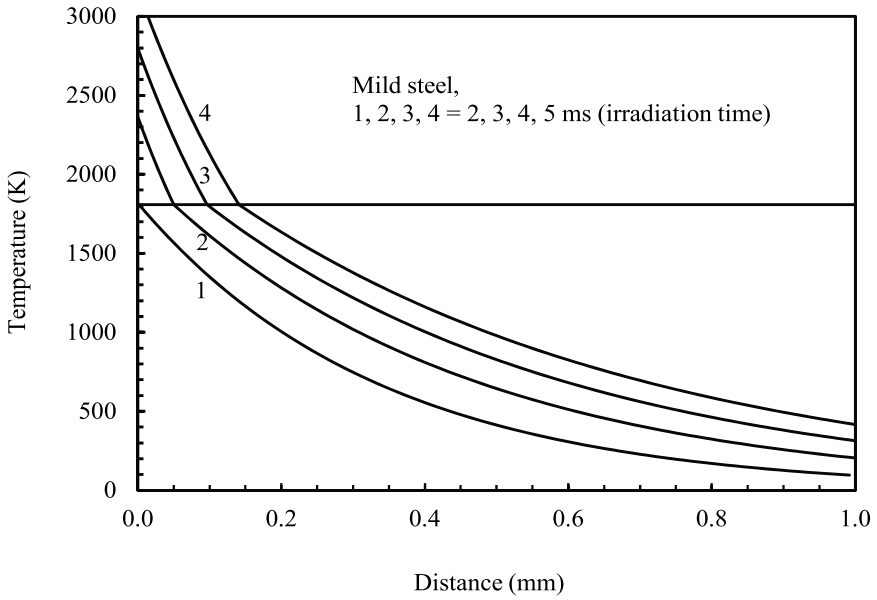

Figure 4.6. *Temperature profiles in a solid and liquid at different irradiation times*

Figure 4.5 illustrates the melt depth evolution of mild steel melting calculated using Shen *et al.* [SHE 01b]'s model. It can be seen that the melt depth rises sharply at the beginning and becomes slower as time proceeds. Shen *et al.* [SHE 01b] compared the predicted melt depth of fuse quartz melting to those measured experimentally and found that the model over-predicted the melt depth as the irradiation time increased. This is because during the experiment, plasma and vapor may be formed with increasing irradiation time and results in less laser beam energy being delivered to the surface, and hence smaller predicted melt depth. Temperature profiles in the solid and liquid are also plotted as shown in Figure 4.6 for 2, 3, 4, and 5 ms irradiation times.

An expression for the melt surface temperature $T_{l0}(t)$, was also reported as [SHE 01b]:

$$T_{l0}(t) = \left[\frac{2\alpha_l A_l^2 I_0^2}{k_l^2} t + C_0 \right]^{1/2} \qquad [4.24]$$

where:

$$C_0 = T_m^2 - \frac{\alpha_l k_s^2 A_l^2}{\alpha_s k_l^2 A_s^2} (T_m - T_0)^2 .$$

As the irradiation proceeds, the temperature of the melt rises until the melt surface temperature reaches boiling point and vaporization begins. Therefore, equation [4.24] can be used as the criteria for the transition from the melting to vaporization stages.

In laser percussion drilling, melting occurs during the "pulse-on" duration while the solidification takes place during "pulse-off". Basically, the melting model, addressed above, can also be applied to solidification; however, particular analysis for solidification has also been reported [DOW 01, ALE 93].

Development of the solidification model is widely based on Neumann's solution (given by F. Neumann in his lectures in the 1860s, see Dowden [DOW 01], p.146), in which the error function is employed to solve the Stefan problem. Figure 4.7 illustrates the schematic diagram generally considered for the solidification model.

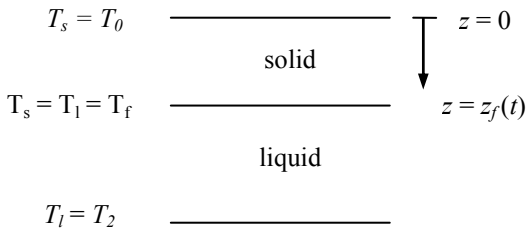

Figure 4.7. *Schematic diagram for solidification used in Dowden's model*

The boundary conditions at $z = 0$ and at $z = zf(t)$ can be written as:

$$T_s(0,t) = T_0; \quad \text{at } z = 0 \qquad [4.25]$$

$$T_s(z_f(t),t) = T_l(z_f(t),t) = T_f; \quad \text{at } z = z_f(t) \qquad [4.26]$$

$$\rho L_f \frac{dz_m(t)}{dt} = k_s \frac{\partial T_s(z,t)}{\partial z} - k_l \frac{\partial T_l(z,t)}{\partial z}; \quad \text{at } z = z_f(t) \qquad [4.27]$$

The asymptotic condition is given by:

$$T_l \to T_2; \quad \text{as } z \to \infty \qquad [4.28]$$

$$\text{with } z_f(0) = 0, \text{ and } T_l(z,0) = 0. \qquad [4.29]$$

Temperature profiles in the solid and liquid are typically assumed to be [ALE 93, DOW 01]:

$$T_s(z,t) = T_0 + a_1 erf \frac{z}{\sqrt{4\alpha_s t}} \qquad [4.30]$$

$$T_l(z,t) = T_2 - a_2 erfc \frac{z}{\sqrt{4\alpha_l t}} \qquad [4.31]$$

which satisfy the boundary conditions at $z = 0$ and at $z \to \infty$, respectively.

The assumed temperature profiles [4.30] and [4.31] will be valid at $z = z_f(t)$ only when $z_f(t)$ is proportional to $\sqrt{t}$. This is written as:

$$z_f(t) = \xi\sqrt{4t\sqrt{\alpha_l \alpha_s}} \qquad [4.32]$$

Therefore, a_1 and a_2 are obtained as:

$$a_1 = \frac{T_f - T_0}{erf\left[\xi(\alpha_l / \alpha_s)^{1/4}\right]} \quad \text{and} \quad a_2 = \frac{T_2 - T_f}{erfc\left[\xi(\alpha_s / \alpha_l)^{1/4}\right]}$$

By substituting equations [4.30] and [4.31] into the interface condition [4.27], ξ is determined.

By plotting the temperature distributions in a solid and liquid at various intervals of elapsed time, Dowden [DOW 01] found that the moving speed of the freezing front decreases as time increases.

4.4. Vaporization

Vaporization takes place when the temperature of the liquid layer reaches the boiling point. Consequently, the liquid-vapor interface is formed and propagates into the liquid layer whereas the solid-liquid interface created due to melting propagates into the solid. The cavity is then formed due to the combined effects of the vaporization and liquid expulsion. Due to the various complex mechanisms that are associated, models of the vaporization vary extensively. Theses may range from the 1D steady-state model; where analytical solutions are possible [YIL 95, ALL 76, MAZ 07], to the more sophisticated 2D transient models; where numerical methods are preferred [KAR 90, YIL 08, GAN 96, SMI 02]. The numerical approach is beyond the scope of this work and a review of the previous vaporization models emphasized here is based on the analytical approach.

Laser induced vaporization modeling is generally aimed at predicting the melt and vaporization front locations and speeds [CHE 00, SHI 09, SEM 06], hole shape and recast layer thickness [KAR 90, ZEN 05, YIL 08], and temperature distribution in the liquid and solid [ABD 06, PAT 91]. Similar to the case of laser induced melting, a vaporization model is normally established from the heat conduction equations with Stefan conditions at the solid-liquid and liquid-vapor interfaces. A

schematic diagram of the basic 1D model of laser induced vaporization is illustrated in Figure 4.8. The two moving boundaries; the solid-liquid and liquid-vapor interfaces, are formed at $z = z_m(t)$ and $z = z_v(t)$, respectively.

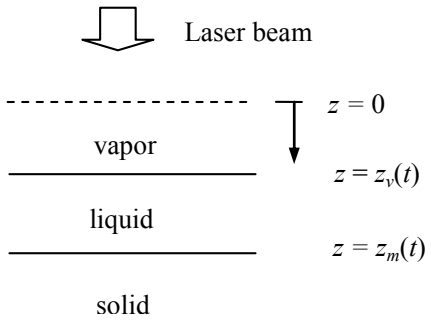

Figure 4.8. *Schematic diagram of stage 3: vaporization*

Heat conduction equations in the solid and liquid are given by:

$$\frac{\partial^2 T_l(z,t)}{\partial z^2} = \frac{1}{\alpha_l}\frac{\partial T_l(z,t)}{\partial t}; \quad 0 \le z < z_m(t) \qquad [4.33]$$

$$\frac{\partial^2 T_s(z,t)}{\partial z^2} = \frac{1}{\alpha_s}\frac{\partial T_s(z,t)}{\partial t}; \quad z_m(t) \le z < \infty \qquad [4.34]$$

Boundary conditions at the solid-liquid and liquid-vapor interfaces can be written as [CHE 00, ZHA 99, SMU 91]:

$$\rho_s L_m \frac{dz_m(t)}{dt} = k_s \frac{\partial T_s(z,t)}{\partial z} - k_l \frac{\partial T_l(z,t)}{\partial z}; \quad \text{at } z = z_m(t) \qquad [4.35]$$

$$T_s\,(z_m(t),t) = T_l\,(z_m(t),t) = T_m; \quad \text{at } z = z_f(t) \qquad [4.36]$$

$$\rho_l L_v \frac{dz_v(t)}{dt} = I_{abs} + k_l \frac{\partial T_l(z,t)}{\partial z}; \quad \text{at } z = z_f(t) \qquad [4.37]$$

$$T_l(z_v(t),t) = T_{l0}\ ;\ \text{at}\ \ z = z_v(t) \qquad [4.38]$$

where L_v is the latent heat of vaporization and T_{l0} is the melt surface temperature.

It is generally accepted that the melt surface temperature T_{l0} is a function of the vapor pressure. This vapor pressure can be estimated from the well-known Clasius-Clapeyron equation [MCQ 97, ATK 02]:

$$p_{vap} = p_0 \exp\left[\frac{L_v}{R}\left(\frac{1}{T_b} - \frac{1}{T_{l0}}\right)\right] \qquad [4.39]$$

where p_0 and T_b are atmospheric pressure and boiling point, and R is the specific gas constant. Therefore, if p_{vap} is known, T_{l0} can be calculated.

In addition to equation [4.39], the melt surface temperature may also be determined from [SAN 99]:

$$T_{l0} = I_{abs}\sqrt{\frac{4t}{\pi\rho_l c_{eff} k_l}} \qquad [4.40]$$

where c_{eff} is the effective heat capacity and is defined as:

$$c_{eff} = c_{ps} + \frac{L_m}{T_m} \qquad [4.41]$$

where c_{ps}, L_m and T_m are the specific heat of a solid, the latent heat of melting, and the melting temperature of the material.

However, it is worth mentioning that the melt surface temperature in equation [4.40] is not a function of the vapor pressure, but is a function of the laser intensity and the irradiation time only. Moreover, only the latent heat of melting is included (see equation [4.41]) and the latent heat of vaporization is not accounted for. Therefore, when using equation [4.40] to estimate the melt surface temperature some errors can be expected.

Although equations [4.33]–[4.38] are the most basic equations for this type of problem, solving these nonlinear differential equations simultaneously is complex. Therefore, in order to simplify the equations, researchers have made further assumptions in their models. These assumptions are, for example:

1) Linear temperature distribution in the liquid layer [ZHA 99, KAR 92]:

$$\frac{\partial T_l(z,t)}{\partial z} = \frac{T_m - T_{l0}}{z_m(t) - z_v(t)}, \qquad [4.42]$$

2) Linear temperature distribution in the solid, starting from t^r [ZHA 06]. Hence, the 1D heat conduction equations in solid and liquid are commonly accepted for this type of problem [ZHA 99, ZEN 05].

Following the above description, the liquid-vapor and solid-liquid interfaces are formed respectively at z :

$$z = z_v(r,t) \qquad [4.43]$$

$$z = z_m(r,t) \qquad [4.44]$$

The interface equations are now given by

$$I_{abs} + k_l \frac{\partial T_l(z,t)}{\partial z}\left[1+\left(\frac{\partial z_v(r,t)}{\partial r}\right)^2\right] = \rho_l L_v \frac{\partial z_v(r,t)}{\partial t}; \quad \text{at } z = z_v(r,t) \qquad [4.45]$$

$$\rho_s L_m \frac{\partial z_m(r,t)}{\partial t} = k_s \frac{\partial T_s(z,t)}{\partial z}\left[1+\left(\frac{\partial z_m(r,t)}{\partial r}\right)^2\right] - k_l \frac{\partial T_l(z,t)}{\partial z}\left[1+\left(\frac{\partial z_m(r,t)}{\partial r}\right)^2\right];$$
$$\text{at } z = z_m(r,t) \qquad [4.46]$$

Most of the previously developed models required additional auxiliary equations to enable the solving of the equations. These auxiliary equations are generally established from the conservation of mass and momentum. The mass balance is of particular interest. If the melt ejection is taken into consideration, the mass balance can be written as [SEM 97, NG 06, LOW 02]:

$$\dot{m}_s = \dot{m}_m + \dot{m}_v \qquad [4.47]$$

where $\dot{m}_s$, $\dot{m}_m$, and $\dot{m}_v$ are the solid melting rate, molten liquid ejection rate, and vaporization rate, respectively.

In order to reduce a variable in the previously defined equations, specified profiles were assigned to $z = z_m(r,t)$ and $z = z_v(r,t)$. For example, Collins and Gremaud [COL 11] used conical and parabolic profiles (Figure 4.9a), Cheng *et al.* [CHE 00] used a conical profile with a cut-off bottom (Figure 4.9b), and Kar and Mazumder [KAR 90] employed a combined profile consisting of a parabolic profile at the hole bottom and a conical profile for the cavity side (Figure 4.9c). By using this technique, the mathematical complexity of the problem is greatly reduced.

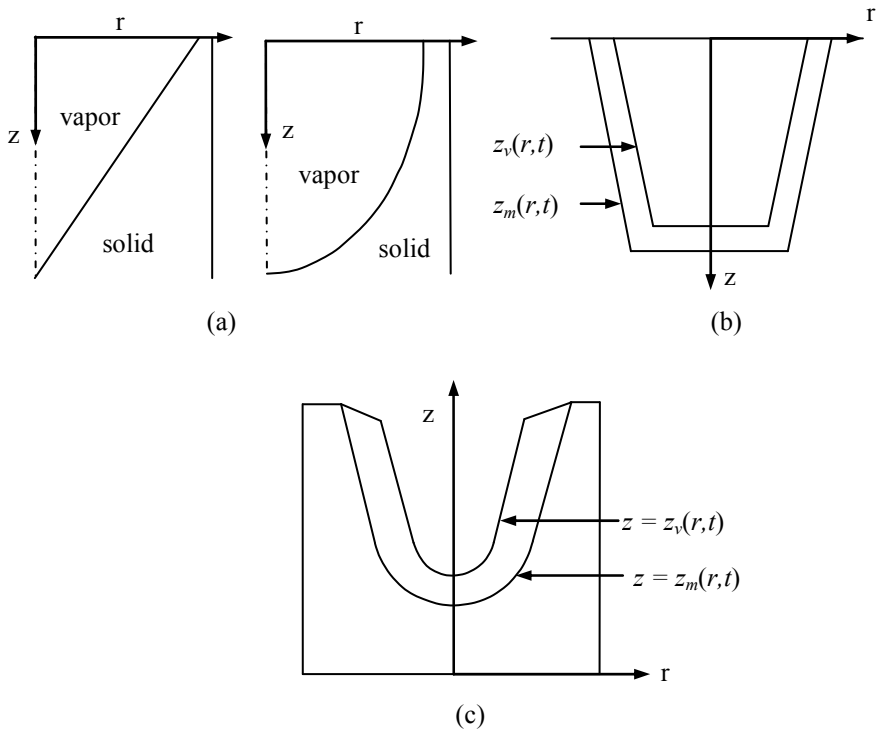

Figure 4.9. *Hole profiles used in laser drilling models:(a) conical and parabolic profiles; (b) conical with cut-off bottom;(c) conical and parabolic combined profile*

4.5. Mathematical model of laser percussion drilling incorporating the effects of the exothermic reaction

In addition to the basic laser induced mechanisms, i.e. heating, melting, and vaporization, modeling of laser drilling has been continuously improved by incorporating other related mechanisms into the models. These consist of heat convection and radiation at the surface, multiple reflections along the hole wall, absorption of laser energy in the vapor and/or plasma, recoil pressure, assist gas pressure, and oxidation energy, etc. Including these factors into the model would improve the accuracy of the model; however, solving the problem becomes more difficult due to complexity of the equations.

In this section, a new mathematical model of laser percussion drilling is developed. The model is divided into two stages: pulse-on and pulse-off durations. During the pulse-on period, the model accounts for the recoil pressure, additional heat generated due to oxidation of metal with oxygen assist gas (exothermic reaction), and assist gas pressure. The newly developed model enables the prediction of the hole depth, hole profiles and recast layer thickness.

4.5.1. *Modeling the pulse-on heating process*

A schematic diagram of the currently developed model is illustrated in Figure 4.10. A laser beam with intensity I_0 irradiates the substrate surface, which is initially at temperature T_0. The solid substrate is then heated, melted and vaporized. Once the vapor is formed, it exerts recoil pressure on the molten liquid as it leaves the cavity, and pushes the melt away radially. The material removal therefore consists of two mechanisms; vaporization and melt ejection. Oxygen assist gas also plays a role in the process. The oxidation reaction between oxygen and metal provides the additional energy, called exothermic energy, to the laser beam-material interaction. The assist gas also enhances the melt ejection mechanism by adding more pressure to the recoil pressure. Moreover, the assist gas also promotes the heat convection rate at the surface of the liquid layer.

The following assumptions are made for the model:

1) The absorbed laser intensity distribution over the work piece surface is assumed to be uniform. This assumption is reasonable because the laser beam considered is produced by the Nd:YAG laser and is delivered through a fiber with an approximately top-hat profile [LOW 02].

2) Plasma generation is neglected in the model. It is valid to assume so because, unlike the CO_2 laser, in the case of an Nd:YAG laser operating at 1.06 μm, plasma may not be formed during the drilling process [LAC 97, LOW 02, DOW 96]. Only solid, molten liquid and vapor are accounted for.

3) There is no interaction between the laser beam and the vapor. It is considered here that the vapor is optically thin, hence no laser power is absorbed. Moreover, assist gas is also employed to help remove the vapor from the cavity.

4) No laser power is absorbed by the ejected melt.

5) The generation of shock waves is ignored.

6) The changes in surface absorptivity, melting point, and boiling point due to the formed oxide layer are neglected. The competing effects between the possible change in the absorptivity and the difference in the melting and boiling points of the oxide and parent material are assumed to cancel each other out.

7) Not all of the metal oxidizes with the O_2 assist gas. The oxidation efficiency is introduced in the model.

8) The discontinuity between the vapor directly above the liquid surface and the liquid is negligible. That is, the vapor and liquid at the surface is in thermodynamic equilibrium.

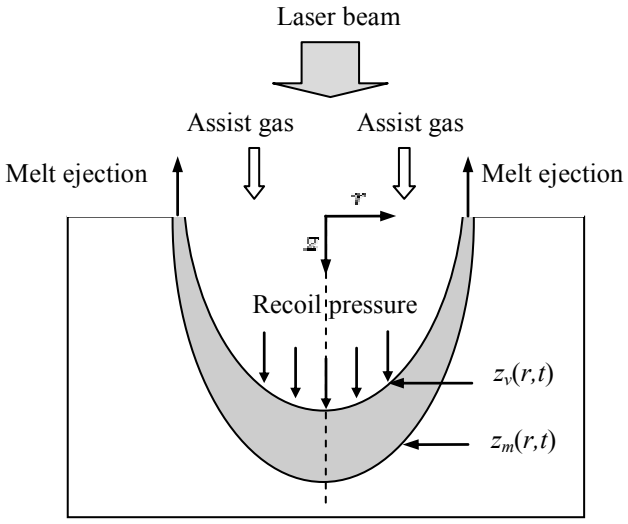

Figure 4.10. *Schematic diagram of the model*

Energy balance

Once vaporization has started, the liquid-vapor and solid-liquid interfaces are formed, respectively, at

$$z = z_v(r,t) \qquad [4.48]$$

$$z = z_m(r,t) \qquad [4.49]$$

where $z_v(r,t)$ and $z_m(r,t)$ are the depth of vaporization and melting fronts, r and t are radial distance and time. Figure 4.11 illustrates the variables defined in the model.

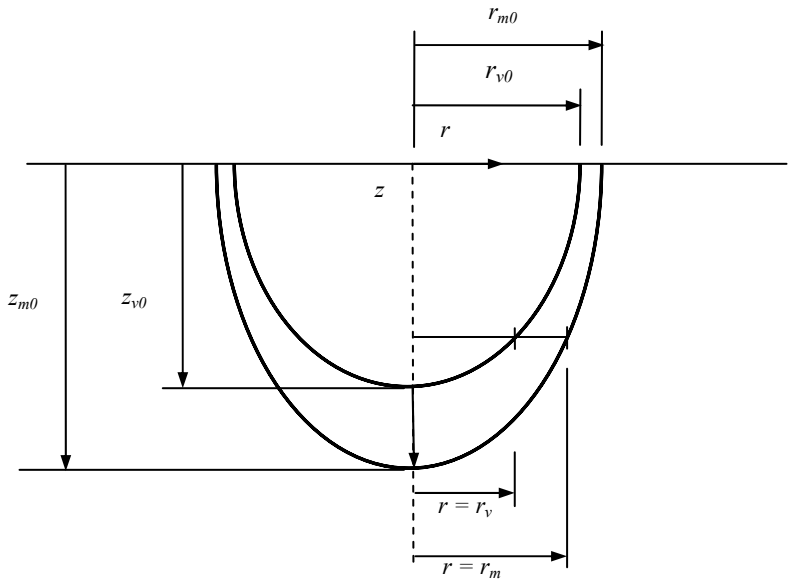

Figure 4.11. *Schematic diagram of the variables defined in the model*

At the liquid-vapor interface, Stefan's equation can be written as:

$$\rho_l L_v \frac{\partial z_v}{\partial t} - k_l \frac{\partial T_l}{\partial z}\left[1+\left(\frac{\partial z_v}{\partial r}\right)^2\right] = I_{abs} + \rho_l H_{ox}\eta_{ox}\frac{\partial z_m}{\partial t} - h_g(T_{l0} - T_g) \qquad [4.50]$$

where H_{ox}, η_{ox}, and h_g are the enthalpy of oxidation, oxidation efficiency, and heat transfer coefficient of the assist gas; T_l, T_g and T_{l0} are the melt temperature, assist gas temperature, and melt surface temperature, respectively. The oxidation efficiency η_{ox} defines the percentage of the melt that actually oxidizes with the O_2 assist gas. It was determined experimentally by Ng *et al.* [NG 06] and the value $\eta_{ox} = 0.26$ is used in the present model.

$z_m(r,t)$ and $z_v(r,t)$ may be assumed to have parabolic profiles, i.e.:

$$z_m(r,t) = z_{m0}(t) - \frac{r^2}{r_{m0}^2} z_{m0}(t) \qquad [4.51]$$

$$z_v(r,t) = z_{v0}(t) - \frac{r^2}{r_{v0}^2} z_{v0}(t) \qquad [4.52]$$

At the symmetry axis, $\frac{\partial z_m}{\partial r} = 0$ and $\frac{\partial z_v}{\partial r} = 0$, Stefan's equations at the two interfaces can now be expressed as:

$$\rho_l L_v \frac{dz_{v0}(t)}{dt} - k_l \frac{T_m - T_{l0}}{z_{m0}(t) - z_{v0}(t)} = I_{abs} + \rho_l H_{ox} \eta_{ox} \frac{dz_{m0}(t)}{dt} - h_g (T_{l0} - T_g) \qquad [4.53]$$

$$\rho_s L_m \frac{dz_{m0}(t)}{dt} = k_s \frac{T_0 - T_m}{2\sqrt{\alpha_s t}} - k_l \frac{T_m - T_{l0}}{z_{m0}(t) - z_{v0}(t)} \qquad [4.54]$$

Combining equations [4.53] and [4.54] gives:

$$\rho_s L_m \frac{dz_{m0}(t)}{dt} + \rho_l L_v \frac{dz_{v0}(t)}{dt} = k_s \frac{T_0 - T_m}{2\sqrt{\alpha_s t}} + I_{abs} + \rho_l H_{ox} \eta_{ox} \frac{dz_{m0}(t)}{dt} - h_g (T_{l0} - T_g) \qquad [4.55]$$

which can also be written as:

$$z'_{v0}(t) = \frac{1}{\rho_l L_v}[I_{abs} + h_g(T_g - T_{l0}) + \frac{k_s(T_0 - T_m)}{2\sqrt{\alpha_s t}} + \rho_l H_{ox}\eta_{ox} z'_{m0}(t) + \rho_s L_m z'_{m0}(t)] \quad [4.56]$$

where $z'_{v0}(t) = \frac{dz_{v0}(t)}{dt}$ and $z'_{m0}(t) = \frac{dz_{m0}(t)}{dt}$.

Mass balance

In laser drilling, a hole is formed by material removal from the cavity in the form of melt ejection and vaporization. Thus, it can be written that the mass of the solid melt at the solid-liquid interface is equal to the total mass removed due to melt ejection and vaporization, i.e.:

$$\dot{m}_s = \dot{m}_m + \dot{m}_v$$

$$S_{sl}\rho_s \frac{\partial z_m}{\partial t} = S_m \rho_l V_m + S_{lv}\rho_l \frac{\partial z_v}{\partial t} \quad [4.57]$$

where S_{sl}, S_{lv}, S_m, and V_m are the solid-liquid interface area, liquid-vapor interface area, melt ejection area, and the melt ejection velocity, respectively. These parameters are given by:

$$S_m = \pi(r_{m0}^2 - r_{v0}^2) \quad [4.58]$$

$$S_{sl} = \frac{\pi r_{m0}}{6z_{m0}^2(t)}[(r_{m0}^2 + 4z_{m0}^2(t))^{3/2} - r_{m0}^3] \quad [4.59]$$

$$S_{lv} = \frac{\pi r_{v0}}{6z_{v0}^2(t)}[(r_{v0}^2 + 4z_{v0}^2(t))^{3/2} - r_{v0}^3] \quad [4.60]$$

As $r \to 0$, the mass equation becomes:

$$\frac{\pi r_{m0}}{6z_{m0}^2(t)}[(r_{m0}^2 + 4z_{m0}^2(t))^{3/2} - r_{m0}^3]\rho_s z'_{m0}(t)$$

$$= \pi(r_{m0}^2 - r_{v0}^2)\rho_l V_m + \frac{\pi r_{v0}}{6z_{v0}^2(t)}[(r_{v0}^2 + 4z_{v0}^2(t))^{3/2} - r_{v0}^3]\rho_l z'_{v0}(t) \qquad [4.61]$$

In order to obtain a solution for the problem, the energy equation [4.56] and the mass equation [4.61] must be solved simultaneously. However, because equation [4.61] is quite complex, solving the system of equations analytically would be a time consuming process. Therefore, for the sake of simplicity, the paraboloid surface area is approximated here by the conical surface area, which can be formulated in a much simpler form. Collins [COL 11] has also developed a model using both conical and parabolic profiles. The results confirm that there is no significant difference in the hole depth prediction.

To apply a conical surface area instead of a poraboloid, a surface area correction factor is needed. Comparison between a paraboloid and a conical surface shows that the difference in the surface area of the two profiles is smaller for the shallow hole and tends to approach a constant value – around 25%, as the hole gets deeper. Therefore, a surface area correction factor, defined here as *sc*, is estimated to be between 1.20–1.24. In this present model, $sc = 1.23$ is selected.

The mass balance can now be expressed in terms of the conical surface area as:

$$sc\, r_{m0}\rho_s z'_{m0}(t)\sqrt{r_{m0}^2 + t^2(z'_{m0}(t))^2} = (r_{m0}^2 - r_{v0}^2)\rho_l V_m + sc\, r_{v0}\rho_l z'_{v0}(t)\sqrt{r_{v0}^2 + t^2(z'_{v0}(t))^2} \qquad [4.62]$$

which may be rearranged as:

$$z'_{v0}(t) = \frac{1}{\sqrt{2}}\sqrt{\frac{-r_{v0}^4 sc^2\rho_l^2 + \sqrt{r_{v0}^2 sc^2\rho_l^2(a_1 + a_2 + a_3)}}{r_{v0}^2 sc^2 t^2\rho_l^2}} \qquad [4.63]$$

where:

$$a_1 = (r_{v0}^6 sc^2 + 4r_{m0}^4 t^2 V_m^2 - 8r_{m0}^2 r_{v0}^2 t^2 V_m^2 + 4r_{v0}^2 t^2 V_m^2)\rho_l^2,$$

$$a_2 = 4r_{m0}^4 sc^2 t^2 \rho_s^2 (z'_{m0}(t))^2 + 4r_{m0}^2 sc^2 t^4 \rho_s^2 (z'_{m0}(t))^4,$$

$$a_3 = 8r_{m0}(-r_{m0}^2 + r_{v0}^2) sc\, t^2 V_m \rho_l \rho_s z'_{m0}(t) \sqrt{r_{m0}^2 + t^2 (z'_{m0}(t))^2}$$

The propagating speed of the solid-liquid and liquid-vapor interfaces can be determined by solving energy equation [4.56] and mass equation [4.63] simultaneously.

The positions of the solid-liquid and liquid-vapor interfaces at $r = 0$ can be estimated from:

$$z_{m0}(t) = \int_0^t z'_{m0}(t)dt \qquad [4.64]$$

$$z_{v0}(t) = \int_0^t z'_{v0}(t)dt \qquad [4.65]$$

Melt front radius at the hole entrance (r_{m0})

In the previously developed laser drilling models, it is often assumed that the hole entrance diameter does not exceed the beam spot diameter [KAR 92, LOW 02, KAR 90, COL 11]. In fact, especially in the case of metals, the hole entrance diameter is usually larger than the theoretical beam spot diameter due to radial heat diffusion. Hence, to improve upon the previous models, the hole entrance diameter is estimated from the spatial temperature distribution due to an instantaneous point source, which is written as [CAR 59]:

$$T_r(r,t) = \frac{P_P}{2\pi\alpha_l \rho c_{pl} t} \exp\left(\frac{-r^2}{4\alpha_l t}\right) \qquad [4.66]$$

where $T_r(r,t)$ and P_P are the temperature distribution in the radial direction and laser peak power.

The melt front radius at the hole entrance (T_{l0}) is hence approximate by a radial distance at which $T_r(r,t)=T_m$.

Melt ejection velocity (V_m)

Melt ejection velocity is another variable required in the model. It can be determined from Bernoulli's equation:

$$p_{vap} + p_{eff} = \frac{\rho_l V_m^2}{2} + \rho_l g z_{m0}(t) + \frac{\sigma}{r_{v0}} \qquad [4.67]$$

where p_{vap}, p_{eff}, g and σ are the vapor pressure (recoil pressure), effective assist gas pressure, gravitational acceleration and surface tension, respectively. The hydrostatic and surface tension terms on the right-hand side are negligible compared to other terms. Therefore, the expression for melt ejection velocity can be written as:

$$V_m = \sqrt{\frac{2\,(p_{vap} + p_{eff})}{2\,\rho_l}} \qquad [4.68]$$

It can be seen from equation [4.68] that in order to calculate the melt ejection velocity, the values of the vapor pressure p_{vap}, and the effective gas pressure p_{eff}, are essential.

Vapor pressure (p_{vap})

Vapor pressure exerted on the melt surface can be estimated from the Clausius-Clapeyron equation [MCQ 97, ATK 02]:

$$p_{vap} = p_0 \exp\left[\frac{L_v}{R}\left(\frac{1}{T_b} - \frac{1}{T_{l0}}\right)\right] \qquad [4.69]$$

where p_0 and T_b are atmospheric pressure and boiling temperature, R is the specific gas constant, which is 149.13 J/kg.K for steel.

Effective assist gas pressure (p_{eff})

In addition to supplying exothermic energy to the process, the process gas also assists the melt ejection mechanism. By adding the assist gas pressure to the recoil pressure exerted on the molten liquid surface, more liquid can be removed, thus producing a higher penetration rate.

For isentropic gas flow, total pressure, which consists of static and dynamic pressure terms, is constant along the gas stream. However, in the case of laser drilling, where the hole bottom is perpendicular to the gas axis, and if a uniform gas pressure profile is assumed within the laser beam, the dynamic gas pressure may be negligible. Due to adiabatic expansion of the assist gas at the nozzle exit, the gas is accelerated up to the local speed of sound leading to the critical state [LOW 02, NG 06]. The critical assist gas pressure at the nozzle exit, p_c, can be defined as:

$$p_c = \left(\frac{2}{\gamma+1}\right)^{\frac{\gamma}{\gamma-1}} p_g \qquad [4.70]$$

where p_g is the pressure inside the nozzle, γ is the specific heat ratio which is taken to be 1.4 for oxygen assist gas.

At the hole entrance, assist gas pressure is reduced from p_c to the effective assist gas pressure, p_{eff}, due to pressure loss between the gas nozzle exit and the hole entrance.

$$p_{eff} = p_c \frac{A_{eff}}{A_{eff} + A_{rl}} \qquad [4.71]$$

where A_{eff} is the effective area of gas entering the hole, A_{rl} is the cylindrical area of the radial loss of assist gas pressure defined by the nozzle exit diameter, d_n, and the nozzle-work piece distance, z_n:

$$A_{eff} = \pi r_{v0}^2 \qquad [4.72]$$

$$A_{rl} = \pi d_n z_n \qquad [4.73]$$

4.5.2. *Solidification during pulse-off*

In laser percussion drilling, each laser pulse is separated by a pulse-off time interval. During the pulse-off duration, the molten liquid layer is cooled down and solidification of the molten liquid layer occurs. To model the freezing problem, Dowden [DOW 01] exploited Neumann's solution, in which the error function is used for solving the 1D transient heat conduction problem. By assuming that the

solidification takes place mainly in a vertical direction, the schematic diagram of the pulse-off model is shown in Figure 4.12.

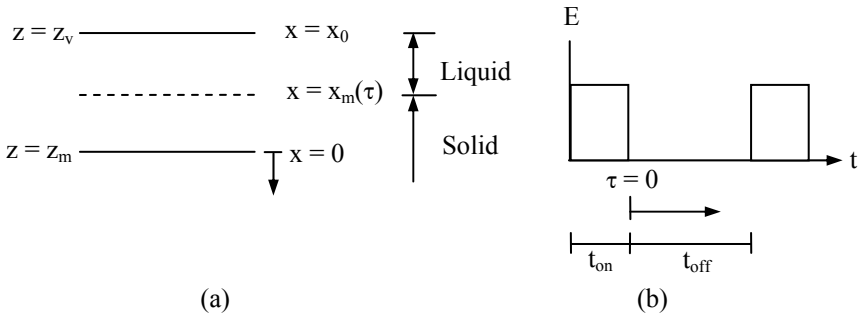

Figure 4.12. *(a) Schematic diagram of the solidification model, (b) time scale of the solidification model*

At the end of the pulse-on period $(\tau = 0)$, the solid-liquid interface is at $x = 0$ and the liquid is at $x < 0$. During the pulse-off duration (from $\tau = 0$ to $\tau = t_{off} = \frac{1}{f} - t_{on}$, where f is the frequency) a thin layer of the liquid is solidified and the solid-liquid interface is moved to $x = x_m(\tau)$. The initial and boundary conditions for this case are:

$$T_l(x_m(\tau),\tau) = T_m \qquad [4.74]$$

$$T_l(x_0,\tau) = T_{l0,off}(\tau) \qquad [4.75]$$

$$T_l(x_m(\tau),\tau) = T_s(x_m(\tau),\tau) = T_m \qquad [4.76]$$

$$k_s \frac{\partial T_s(x,\tau)}{\partial x} - k_l \frac{\partial T_l(x,\tau)}{\partial x} = \rho_s L_m \frac{dx_m(\tau)}{d\tau} \qquad [4.77]$$

$$T_s(\infty,\tau) = T_0 \qquad [4.78]$$

$$\text{and } x_m(0) = 0 \qquad [4.79]$$

where $T_{l0,off}(\tau)$, x_0 and $x_m(\tau)$ are the melt surface temperature during pulse-off, the liquid-vapor interface location, and the solid-liquid interface location, respectively.

The temperature drop of the melt surface subjected to heat convection cooling may be estimated from [HOL 02]:

$$T_{l0,off}(\tau) = T_{l0} + (T_g - T_{l0})\left\{1 - \left[\exp\frac{h_g^2\alpha_l\tau}{k_l^2}\right]\left[1 - erf\left(\frac{h_g\sqrt{\alpha_l\tau}}{k_l}\right)\right]\right\} \quad [4.80]$$

The temperature profiles in solid and liquid that satisfy the boundary conditions may be assumed in the forms:

$$T_l(x,\tau) = T_{l0,off}(\tau) - B_1\ Erf\left(\frac{x - x_0}{2\sqrt{\alpha_l\tau}}\right) \quad [4.81]$$

$$T_s(x,\tau) = T_0 + B_2\ Erfc\left(\frac{x}{2\sqrt{\alpha_s\tau}}\right) \quad [4.82]$$

To seek solutions in these forms, $x_m(\tau)$ must be proportional to $\sqrt{\tau}$ [DOW 01] i.e.:

$$x_m(\tau) = \xi\sqrt{4\tau\sqrt{\alpha_l\alpha_s}} \quad [4.83]$$

where ξ is a constant.

At $x = x_m(\tau)$, B_1 and B_2 in equations [4.81] and [4.82] become:

$$B_1 = \frac{T_{l0,off}(\tau) - T_m}{erf\left[\dfrac{-x_0 + 2\sqrt{\tau\sqrt{\alpha_l\alpha_s}}\,\xi}{2\sqrt{\alpha_l\tau}}\right]} \quad [4.84]$$

$$B_2 = \frac{T_m - T_0}{erfc\left[\left(\dfrac{\alpha_l}{\alpha_s}\right)^{1/4}\xi\right]} \quad [4.85]$$

Finally, ξ can be determined by solving the interface condition in equation [4.84]. By substituting ξ into equation [4.90], the location of the solidification front $x_m(\tau)$ is obtained.

In summary, each cycle of the multiple pulsed drilling passes through one step of drilling during the pulse heating (where the pulse width defines the interaction time), and one step of solidification during pulse-off (where the pulse frequency defines the pulse-off duration). The calculation is then repeated one pulse at a time until the given constraints, i.e. material thickness, number of pulses etc., are met.

4.6. Experimental procedures for model verification

To validate the model, a laser drilling test was performed on 2.4 mm thick mild steel sheets using a GSI-JK300D pulsed Nd:YAG fiber laser with a 1.06 μm wavelength. Oxygen was used as the assist gas throughout the experiments. Figure 4.13 illustrates the schematic diagram of the experimental setup.

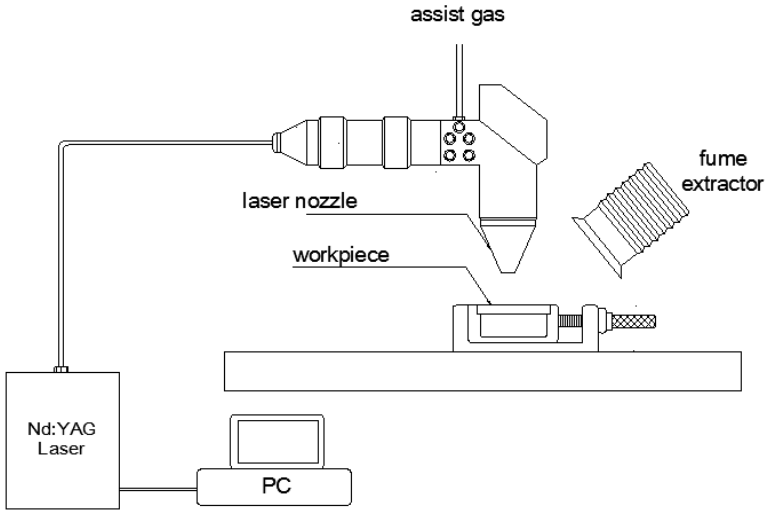

Figure 4.13. *Schematic diagram of the experimental setup*

Flat mild steel work piece was placed at the focal distance below the laser head. Holes were drilled with successive pulses until a through hole was achieved. Each hole was sectioned from the original work piece using a precision fine cutter,

mounted into polymer resin, and then ground until the center of the hole was reached. Finally, the hole depth and recast layer thickness were measured.

4.7. Results and discussion

Figures 4.14–4.16 compare the predicted hole depth values with those obtained experimentally. The melt surface temperature is assumed to be from slightly above boiling point up to some point around 5,000 K. It is found that the melt surface temperature ranging between 3,900 and 4,300 K gives reasonable predictions compared to the experimental data. Variation of the melt surface temperature within this range would cause a slight deviation in the predicted hole depth. To generalize the model for other ranges of operating parameters, $T_{l0} = 4,000$ K seems to be the most compromising option for mild steel. Therefore, this value is used throughout the modeling work presented here.

It can be seen from Figures 4.14 and 4.15 that the current model provides good agreement compared to the experimental data, whilst in Figure 4.16 the model gives a good prediction of the hole depth for the first 4 pulses and slightly under-predicts the hole depth for the last two pulses.

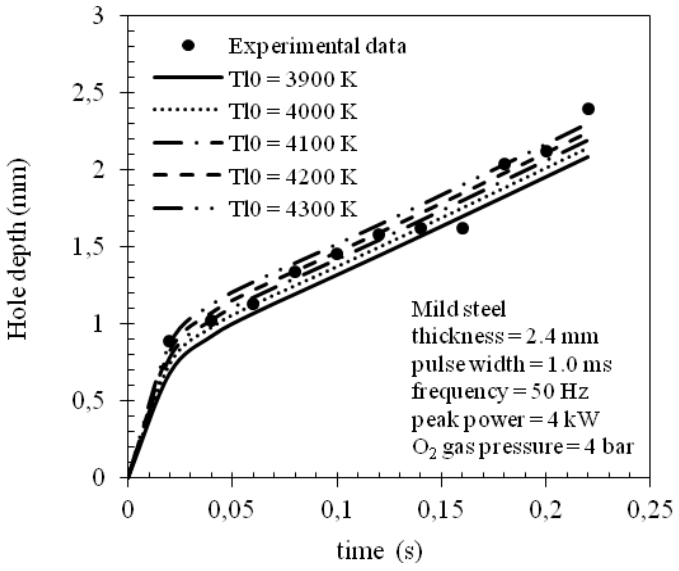

Figure 4.14. *Comparison between the predicted and measured hole depth, t_{on} = 1.0 ms, T_{l0} from 3,900 – 4,300 K*

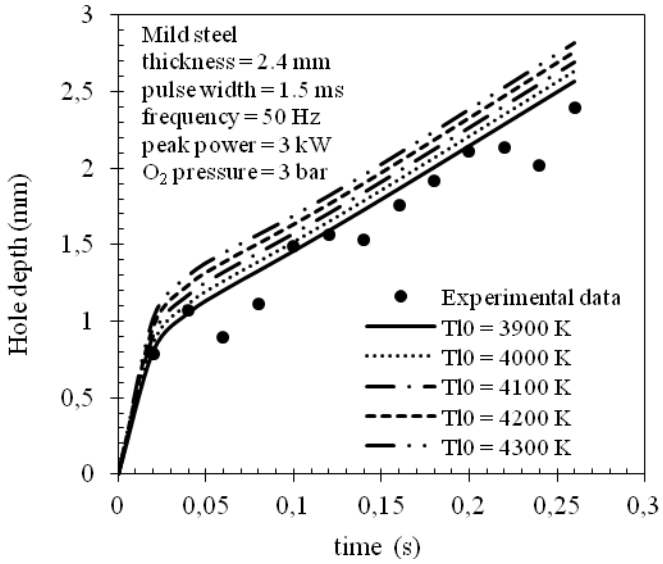

Figure 4.15. *Comparison between the predicted and measured hole depth, t_{on} = 1.5 ms, T_{l0} from 3,900 – 4,300 K*

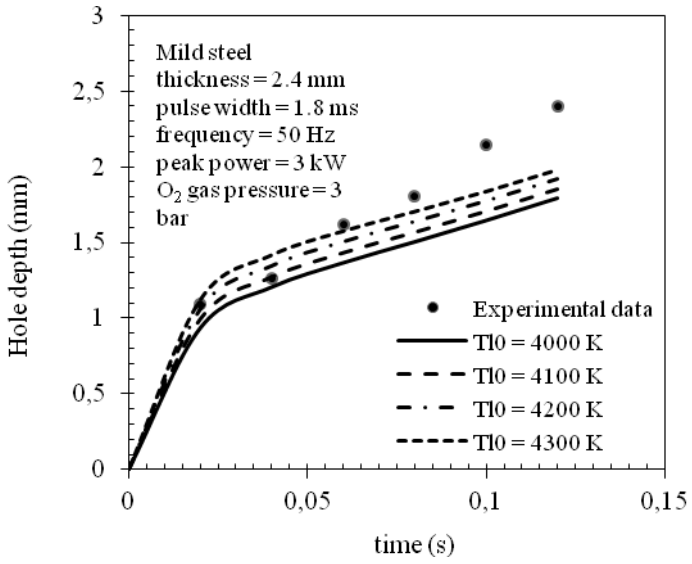

Figure 4.16. *Comparison between the predicted and measured hole depth, t_{on} = 1.0 ms, T_{l0} from 4,000 – 4,300 K*

Figure 4.17 compares the predicted breakthrough pulses to those required experimentally for 0.5, 1.0, 1.5, and 1.8 ms pulse widths. It is obvious that as the pulse width increases, fewer pulses are required to generate a through hole. This is due to the fact that, for a longer pulse width, higher laser energy per pulse irradiates the work piece surface. This consequently leads to more heating, melting, and vaporization of the material. In other words, longer pulse width gives deeper holes. Similar trends have also been reported in the literature [WEB 04, HAN 04, LOW 00, WAN 07]. It should be noted from Figure 4.17 that the current model gives a fair prediction for the cases of 1.0, 1.5, and 1.8 ms pulse width, whilst the model underestimates the breakthrough pulse for the 0.5 ms pulse width. This discrepancy could possibly be attributed to the difference in the actual melt surface temperature and the melt surface temperature assumed in the model. For actual laser drilling with a short laser-material interaction time, a lower melt surface temperature, and hence a lower recoil pressure can be expected. However, because the current model assumes the same value of the melt surface temperature for all ranges of the pulse width, the same value of the recoil pressure is applied. In this case, it could possibly be because the assumed melt surface temperature is higher than the actual melt surface temperature; hence, the higher predicted recoil pressure and the higher drilling rate.

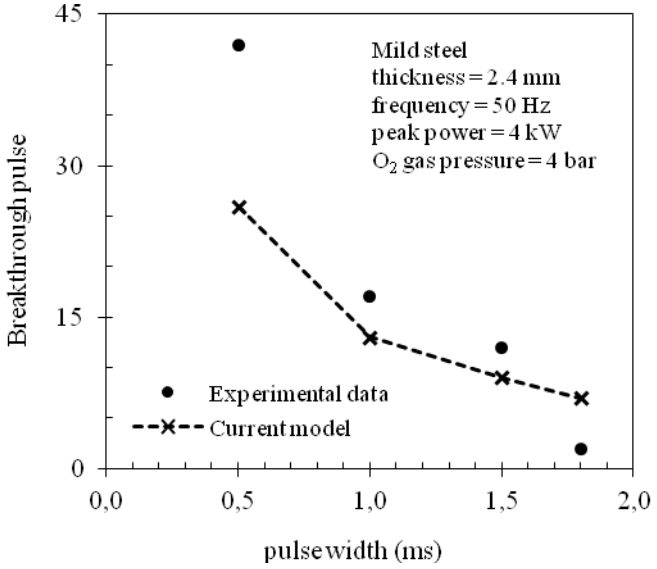

Figure 4.17. *Effect of pulse width on the breakthrough pulse*

In Figure 4.18, the predicted hole profile is plotted against the profile obtained experimentally. It can be seen that the model gives excellent prediction for the melt

front; however, a discrepancy between the predicted and experimentally obtained vapor front can be observed. This is probably due to two main reasons. Firstly, there is multiple-reflection of the laser beam inside the cavity during actual drilling, whereas the current model ignores this effect. Modest [MOD 06] has revealed that multiple reflections inside the cavity raise the laser intensity in the cavity to some extent especially at the hole center. With higher laser intensity in the cavity, more melt can be removed, which in turn results in a smaller recast layer thickness. Secondly, it could possibly be due to the difference in the actual drilled hole geometry and the parabolic profile assumed in the model. From Figure 4.18, it is quite clear that the actual drilled hole profile is not a perfect parabola but an "inlet cone" at the hole entrance. Because the current model assumes a hole to be parabolic with a fixed diameter, the volume of the material to be melted, vaporized, and removed is greater, and hence at the end of the laser irradiation a thicker recast layer is predicted.

Figure 4.19 shows the predicted hole taper and exit diameter after irradiating with 20 to 24 pulses. Here, the hole taper is calculated from the solidification front. It can be seen that the hole taper decreases as more pulses irradiate. Once a through hole has been produced, subsequent laser pulses enlarge the hole wall, resulting in a smaller hole taper.

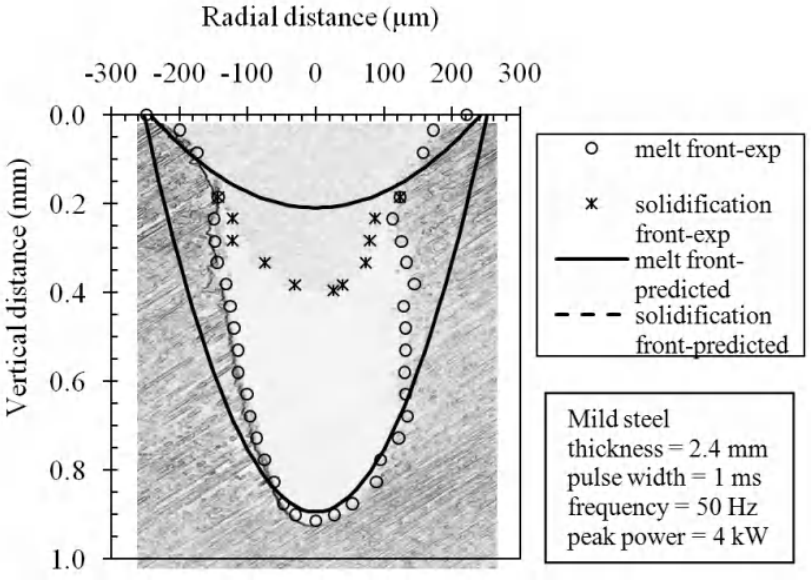

Figure 4.18. *Comparison of the laser drilled hole profile*

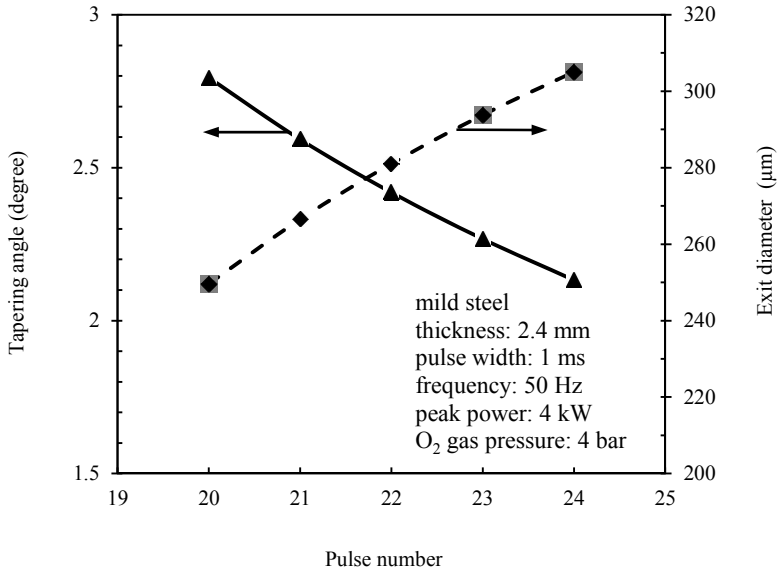

Figure 4.19. *Predicted hole exit diameter and hole taper*

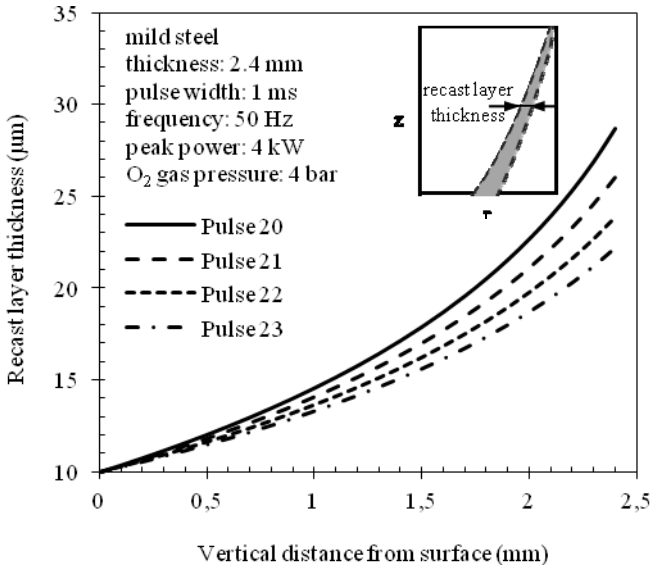

Figure 4.20. *Variation of the recast layer thickness for 17-20 laser pulses*

Figure 4.20 illustrates the variation of the wall recast layer thickness with the vertical distance from the work piece surface for 20-23 laser pulses. It can be seen that the recast layer thickness is largest at the hole bottom (z = 2.4 mm) and becomes smaller as it approaches the hole entrance (z = 0 mm). In the case of drilling, melting mainly proceeds in the z-direction. The liquid is therefore accumulated at the hole bottom before it is expelled radially along the hole wall. During pulse-off duration, the remaining liquid in the cavity is solidified, hence a thicker recast layer at the hole bottom. In the case of a through hole, it can be expected that once the through hole has been achieved, the recast layer thickness would be significantly reduced. This is because the molten liquid accumulated at the hole bottom is flushed down the hole exit. Therefore, only a wall recast layer is formed. The number of pulses employed also influences the recast layer thickness. It can be seen from Figure 4.18 that the recast layer thickness decreases as the number of pulses increases.

4.8. Conclusion

In this chapter, mathematical modeling of laser drilling is reviewed and a new mathematical model of multiple pulsed laser percussion drilling is developed. The new model accounts for the recoil pressure, exothermic reaction, melt ejection, O_2 assist gas effect and solidification of the melt during the laser pulse-off period. The governing equations are derived and solved by treating the laser drilling process, like the Stefan problem, at the solid-liquid and liquid-vapor interfaces.

The newly developed model enables the prediction of the hole depth, number of pulses required to initiate breakthrough, hole profile, hole taper and recast layer thickness. Comparisons with the experimental data show good agreement for the prediction of the hole depth, and not as good but acceptable predictions for the hole profile and recast layer thickness.

4.9. Bibliography

[ABD 06] ABD EL-GHANY S.E.-S., "On the evaporation of a semi-infinite target induced by a pulsed laser", *Optics & Laser Technology*, vol. 38, pp. 77-86, 2006.

[ALE 93] ALEXIADES V., SOLOMON A.D., *Mathematical Modeling of Melting and Freezing Processes*, Hemisphere Publishing Corporation, Washington, 1993.

[ALL 76] ALLMEN M.V., "Laser drilling velocity in metals", *Journal of Applied Physics*, vol. 47, pp. 5460-5463, 1976.

[ATK 02] ATKINS P.W., *Physical Chemistry*, Oxford University Press, Oxford, 2002.

[BAS 88] BASU B., SRINIVASAN J., "Numerical study of steady-state laser melting problem", *International Journal of Heat and Mass Transfer*, vol. 31, pp. 2331-2338, 1988.

[BAS 92] BASU S., DEBROY T., "Liquid metal expulsion during laser irradiation", *Journal of Applied Physics*, vol. 72, pp. 3317-3322, 1992.

[CAR 59] CARSLAW H.S., JAEGER J.C., *Conduction of Heat in Solids*, Oxford University Press, New York, 1959.

[CHE 00] CHEN J., KAHLEN F.J., KAR A., "Effects of intrapulse structure on hole geometry in laser drilling", *Journal of Laser Applications*, vol. 12, pp. 232-238, 2000.

[COH 68] COHEN M.I., EPPERSON J.P., "Application of lasers to microelectronic fabrication", *Advances in Electronics and Electron Physics*, suppl. .4, pp. 139-186, 1968.

[COL 11] COLLINS J., GREMAUD P., "A simple model for laser drilling", *Mathematics and Computers in Simulation*, vol. 81, pp. 1541-1552, 2011.

[DOW 96] DOWDEN J., KAPADIA P., "The penetration depth in keyhole welding with pseudo-continuous Nd-YAG and CO lasers investigated mathematically", *Applied Surface Science*, vol. 106, pp. 235-239, 1996.

[DOW 01] DOWDEN J.M., *The Mathematics of Thermal Modeling: An Introduction to the Theory of Laser Material Processing*, Chapman & Hall/CRC, Florida, 2001.

[ELA 86] EL-ADAWI M.K., "Laser melting of solids-an exact solution for time intervals less or equal to the transit time", *Journal of Applied Physics*, vol. 60, pp. 2256-2259, 1986.

[GAN 96] GANESH R.K., BOWLEY W.W., BELLANTONE R.R., HAHN Y., "A model for laser hole drilling in metals", *Journal of Computational Physics*, vol. 125, pp. 161-176, 1996.

[HAN 04] HAN W., PRYPUTNIEWICZ R.J., "Investigations of laser percussion drilling of small holes on thin sheet metals", *Proceedings of SPIE*, vol. 5525, pp. 31-40, 2004.

[HOL 02] HOLMAN J.P., *Heat Transfer*, McGraw-Hill, Boston, 2002.

[KAR 90] KAR A., MAZUMDER J., "Two-dimensional model for material damage due to melting and vaporization during laser irradiation", *Journal of Applied Physics*, vol. 68, pp. 3884-3891, 1990.

[KAR 92] KAR A., ROCKSTROH T., MAZUMDER J., "Two-dimensional model for laser-induced materials damage: effects of assist gas and multiple reflections inside the cavity", *Journal of Applied Physics*, vol. 71, pp. 2560-2569, 1992.

[KRE 06] KREYSZIG E., *Advanced Engineering Mathematics*, Wiley, New York, 2006.

[LAC 97] LACROIX D., JEANDEL A.G., BOUDOT C., "Spectroscopic characterization of laser-induced plasma created during welding with a pulsed Nd:YAG laser", *Journal of Applied Physics*, vol. 81, pp. 6599-6606, 1997.

[LEI 09] LEIGH S., SEZER K., LI L., GRAFTON-REED C., CUTTELL M., "Statistical analysis of recast formation in laser drilled acute blind holes in CMSX-4 Nickel superalloy", *International Journal of Advanced Manufacturing Technology*, vol. 43, pp. 1094-1105, 2009.

[LIN 90] LING Z., ZHI-RONG Z., JIANGLONG L., "Heat and mass transfer model during melting of metal induced by cw CO_2 laser irradiation", *Key Engineering Materials*, vol. 46-47, pp. 497-504, 1990.

[LOW 00] LOW D.K.Y., LI L., BYRD P.J., "The effects of process parameters on spatter deposition in laser percussion drilling", *Optics and Laser Technology*, vol. 32, pp. 347-354, 2000.

[LOW 02] LOW D.K.Y., LI L., BYRD P.J., "Hydrodynamic physical modeling of laser drilling", *Transactions of the ASME*, vol. 124, pp. 852-862, 2002.

[MAZ 07] MAZHUKIN V.I., LOBOK M.G., SMUROV I., "Transient effects in pulsed laser irradiation", *Applied Surface Science*, vol. 253, pp. 7744-7748, 2007.

[MCQ 97] MCQUARRIE D.A.; SIMON J.D., *Physical Chemistry – A Molecular Approach*, University Science Books, Sausalito, California, 1997.

[MOD 06] MODEST M.F., "Effects of multiple reflections on hole formation during short-pulsed laser drilling", *Journal of Heat Transfer*, vol. 128, pp. 653-661, 2006.

[NG 06] NG G.K.L., CROUSE P.L., LI L., "An analytical model for laser drilling incorporating effects of exothermic reaction, pulse width and hole geometry", *International Journal of Heat and Mass Transfer*, vol. 49, pp. 1358-1374, 2006.

[OBE 68] OBERT E.F., *Boundary Value Problems of Heat Conduction*, International Textbook Company, Scranton, 1968.

[PAT 91] PATEL R.S., BREWSTER M.Q., "Gas-assisted laser-metal drilling: theoretical model", *Journal of Thermophysics and Heat Transfer*, vol. 5, pp. 32-39, 1991.

[REA 65] READY J.F., "Effects due to absorption of laser radiation", *Journal of Applied Physics*, vol. 36, pp. 462-468, 1965.

[SAL 07] SALONITIS K., STOURNARA A., TSOUKANTAS G., STAVROPOULOS P., CHRYSSOLOURIS G., "A theoretical and experimental investigation on limitations of pulsed laser drilling", *Journal of Materials Processing Technology*, vol. 183, pp. 96-103, 2007.

[SAN 99] SANKARANARAYANAN S., EMMINGER H., KAR A., "Energy loss in the plasma during laser drilling", *Journal of Physics D: Applied Physics*, vol. 32, pp. 1605-1611, 1999.

[SEM 97] SEMAK V., MATSUNAWA A., "The role of recoil pressure in energy balance during laser materials processing", *Journal of Physics D: Applied Physics*, vol. 30, pp. 2541-2552, 1997.

[SEM 06] SEMAK V.V., CAMPBELL B.R., THOMAS J.G., "On the possible effect of pedestal pulse-on material removal by ultrahigh intensity laser pulses", *Journal of Physics D: Applied Physics*, vol. 39, pp. 3440-3449, 2006.

[SMI 02] SMITH W.R., "Models for solidification and splashing in laser percussion drilling", *SIAM Journal on Applied Mathematics*, vol. 62, pp. 1899-1923, 2002.

[SHE 01a] SHEN Z.H., ZHANG S.Y., "Laser heating of thin plate with time-dependent absorptance", *Microwave and Optical Technology Letters*, vol. 28, pp. 364-367, 2001.

[SHE 01b] SHEN Z.H., ZHANG S.Y., LU J., NI X.W., "Mathematical modeling of laser induced heating and melting in solids", *Optics and Laser Technology*, vol. 33, pp. 533-537, 2001.

[SHI 09] SHIN S., CHUNG H., "Modeling of melting, evaporating, and resolidifying procedure in laser-induced metal processing", *Transactions of the ASME*, vol. 131, pp. 024501-1-024501-5, 2009.

[SMU 91] SMUROV I.YU., UGLOV A.A., LASHIN A.M., MATTEAZZI P., TAGLIAFERRI V., COVELLI L., "Movement of phase boundaries of metals subjected to surface periodic energy pulses", *Journal of Applied Physics*, vol. 69, pp. 8031-8036, 1991.

[SOL 99] SOLANA P., KAPADIA P., DOWDEN J.M., MARSDEN P.J., "An analytical model for the laser drilling of metals with absorption within the vapour", *Journal of Physics D: Applied Physics*, vol. 32, pp. 942-952, 1999.

[TOK 99] TOKAREV V.N., KAPLAN A.F.H., "An analytical modeling of time dependent pulsed laser melting", *Journal of Applied Physics*, vol. 86, pp. 2836-2847, 1999.

[VER 03] VERHOEVEN J.C.J., JANSEN J.K.M., MATTHEIJ R.M.M., "Modelling laser induced melting", *Mathematical and Computer Modelling*, vol. 37, pp. 419-437, 2003.

[WAG 74] WAGNER R.E., "Laser drilling mechanics", *Journal of Applied Physics*, vol. 45, pp. 4631-4637, 1974.

[WAN 07] WANG A.H., WANG W.Y., BAI Z.K., XIE C.S., ZENG D.W., SONG W.L., "YAG laser percussion drilling of a functional multi-layer thin plate", *Optics and Laser Technology*, vol. 39, pp. 840-845, 2007.

[WEB 04] WEBB C.E.; JONES J.D.C., *Handbook of Laser Technology and Applications: Volume III-Applications*, Institute of Physics, 2004.

[XIE 97] XIE J., KAR A., "Mathematical modeling of melting during laser materials processing", *Journal of Applied Physics*, vol. 81, pp. 3015-3022, 1997.

[YIL 95] YILBAS B.S., SAHIN A.Z., DAVIES R., "Laser heating mechanism including evaporation process initiating laser drilling", *International Journal of Machine Tools and Manufacture*, vol. 35, pp. 1047-1062, 1995.

[YIL 08] YILBAS B.S., MANSOOR S.B., SHUJA S.Z., ABUALHAMAYEL H., "Laser pulse heating and vapor front generation", *AIChE Journal*, vol. 54, pp. 627-638, 2008.

[ZEN 05] ZENG D., LATHAM W.P., KAR A., "Two-dimensional model for melting and vaporization during optical trepanning", *Journal of Applied Physics*, vol. 97, pp. 104912-1-7, 2005.

[ZHA 99] ZHANG Y., FAGHRI A., "Vaporization, melting and heat conduction in the laser drilling process", *International Journal of Heat and Mass Transfer*, vol. 42, pp. 1775-1790, 1999.

[ZHA 06] ZHANG C., SALAMA I.S., QUICK N.R., KAR A., "One-dimensional transient analysis of volumetric heating for laser drilling", *Journal of Applied Physics*, vol. 99, pp. 113530-1-113530-10, 2006.

Chapter 5

Laser Cutting a Small Diameter Hole: Thermal Stress Analysis

Laser cutting of a small diameter hole in titanium alloy is carried out. The temperature and stress fields developed around the hole circumference are modeled and predicted incorporating the ABAQUS finite element code. The morphological and microstructural changes around the cutting section are examined using optical and scanning electron microscopes. The residual stress developed in the vicinity of the cut surface is measured using the XRD technique. It is found that the maximum stress occurs at the mid-thickness of the work piece in the cut section. The predicted residual stress agrees well with the XRD data. Irregular striation patterns are found at the kerf surface.

5.1. Introduction

Laser cutting of metal sheets finds applications in industry due to its precision of operation, low cost, and short processing time. Laser cutting of metal sheets involves assisting gas processing to protect the cutting section from the oxidation reactions. Moreover, oxidation reactions increase the temperature in the cutting section, while causing sideways burning around the cut edges. This becomes one of the important concerns for the laser cutting of metal sheets with high oxygen affinity, such as titanium and its alloys. The attainment of high temperature in the cutting section causes the development of high temperature gradients in the vicinity of cut edges. This, in turn, results in high thermal stress formation in the cutting

Chapter written by Bekir S. YILBAS, Syed S. AKHTAR and Omer KELES.

Lasers in Manufacturing Edited by J. Paulo Davim

section. In addition, thermal expansion and contraction in the cutting section have a significant effect on the residual stress formation in this region. This is particularly true for laser cutting of small diameter holes, such as 2 mm. Consequently, investigation into thermal stress development during laser cutting of small diameter holes into titanium alloy sheets becomes essential.

Considerable research studies were carried out to examine the laser cutting of titanium alloys. Nd:YAG laser cutting of a titanium alloy sheet was studied by Qi *et al.* [QI 04]. Their findings revealed that compressed air was suitable for the laser cutting of titanium alloy; however use of argon as an assisting gas resulted in improved cut quality. Laser cutting of titanium with a pulsed and modulated pulsed Nd:YAG laser was carried out by Maher and Tong [MAH 98]. They indicated that the use of argon as an assisting gas eliminated rear surface dross on the edge of the kerf. Pulsed laser cutting of the nickel-titanium alloy was investigated by Pfeifer *et al.* [PFE 10]. They showed that due to the local energy input only a small heat-affected zone was formed and alloy properties were retained in the cutting section. The multi-objective optimization of the Nd:YAG laser cutting of a nickel-based superalloy sheet was studied by Dubey and Yadava [DUB 08]. They assessed the influence of laser cutting parameters on the multiple quality characteristics of the cut section. Optimization study for the laser cutting of titanium sheet was carried out by Almeida *et al.* [ALM 06]. They used a factorial analysis and evaluated the affecting parameters on the end product quality. Laser cutting of titanium sheet was examined by Shanjin and Yang [SHA 06]. They indicated that argon and nitrogen could be used as assisting gases when cutting titanium alloys. Laser cutting of titanium sheet with a pulsed mode CO_2 laser was carried out by Rao *et al.* [RAO 05]. They used helium as an assisting gas, which resulted in laser cuts with narrow heat affected zone and low dross. Laser cutting of nickel based super alloys was investigated by Thawari *et al.* [THA 05]. They showed that laser cutting quality improves by using an assisting gas in the cutting section. Laser cutting of holes into titanium alloy was investigated by Yilbas *et al.* [YIL 11]. They showed that the use of nitrogen, as an assisting gas, resulted in minimum dross attachment at the rear surface of the cut edges.

Although laser cutting of holes into titanium alloy was investigated previously [YIL 11], the cut hole diameter was limited to only 4 mm and small diameter hole cutting and stress analysis remained obscure. Therefore, in the present study, the laser cutting of a 2 mm diameter hole into titanium alloy is carried out. Temperature and stress fields developed around the cut section are examined numerically incorporating the ABAQUS code. The metallurgical and morphological changes in the cutting section are examined using the optical and scanning electron microscopes. The residual stress formed at the vicinity of the kerf surface is measured using the XRD technique.

5.2. Modeling heating and thermal stress

5.2.1. *Heating analysis*

In the heating analysis, the solid body heat conduction with temperature-dependent conductivity, internal energy (including latent heat effects), and convection and radiation boundary conditions are considered. The Fourier heat transfer equation for the laser heating process can be written as:

$$\rho \frac{DE}{Dt} = \left(\nabla(k\nabla T)\right) + S_o \qquad [5.1]$$

where E is the energy gain per unit mass of the substrate material, k is the thermal conductivity, and S_o is the heat source term resembling the laser beam, i.e.:

$$S_o = I_o \delta e^{-\delta z}(1-r_f) e^{\left(-\frac{(x-rSinwt)^2+(y-rCoswt)^2}{a^2}\right)} \qquad [5.2]$$

I_o is the laser power peak density, δ is the absorption coefficient, *a* is the Gaussian parameter of the laser beam, r_f is the surface reflectivity, ρ is the density, and x and y are the axes while the laser beam scans the surface along the circumference of the cut hole, then, $r = \sqrt{x^2 + y^2}$, i.e. circular cutting is carried out and the laser beam motion follows the circumference of the laser cut hole with a constant angular velocity, ω. The effective penetration depth of the laser beam after the key-hole formation is estimated by considering the multiple reflections from the cut edges and incorporating the exponential decay of incident laser intensity along the absorption depth. This can be simplified as:

$$\delta = \frac{1}{L}\ln\left(\frac{I_o}{I_L}\right) \qquad [5.3]$$

where L is the thickness of the work piece, I_o is the peak power intensity at the work piece surface, I_L is the depth below the surface where the laser power intensity reduces 1/e value. It should be noted that the absorption of the incident beam by the substrate material is assumed to behave similarly to the Lambert-Beer law, i.e. exponential decay of the intensity along the work piece thickness. The laser beam axis is parallel to the z-axis (Figure 5.1). It should be noted that the laser beam intensity distribution is assumed to be Gaussian at the irradiated surface. It is considered that once the temperature in the irradiated region exceeds the melting temperature of the substrate material, superheating in the liquid phase occurs. In this case, the pressure in the liquid phase may rise. Since the irradiated surface is freely exposed to the atmosphere, the liquid phase expands freely in the melted zone.

Therefore, the pressure increase in the liquid phase can be neglected. In addition, the specific heat capacity of the liquid phase is kept the same in the simulation during superheating in the liquid phase. However, the evaporation at the surface does not take place during the heating cycle, since the surface temperature remains below the boiling temperature of the substrate material in the present study.

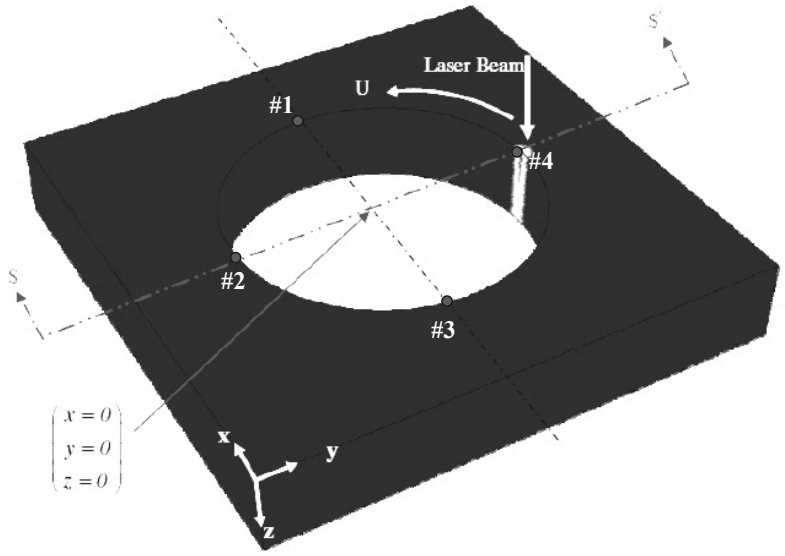

Figure 5.1. *A schematic view of laser cutting and locations around the circumference of the cut hole*

The convective and radiation boundary conditions are considered at the free surface of the work piece. Therefore, the corresponding boundary condition is:

– at the irradiated surface:

$$\frac{\partial T}{\partial z} = \frac{h}{k}(T_s - T_{amb}) + \frac{\varepsilon\sigma}{k}(T_s^4 - T_{amb}^4) \qquad [5.4]$$

– at the rear side of the surface:

$$\frac{\partial T}{\partial y} = \frac{h}{k}(T_s - T_{amb}) + \frac{\varepsilon\sigma}{k}(T_s^4 - T_{amb}^4) : \frac{\partial T}{\partial z} = \frac{h}{k}(T_s - T_{amb}) \qquad [5.5]$$

where h (= 20 W/m^2) is the heat transfer coefficient due to natural convection, and T_s and T_{amb} are the surface and ambient temperature, respectively, ε is the emissivity (ε = 0.9 is considered), σ is the Stefan-Boltzmann constant (σ = 5.67 × 10^{-8} W/m^{2}K^4). At a distant boundary (at edges of the solution domain) a constant temperature boundary is assumed (T = 293 K), i.e.:

$$x = \infty;\quad y = \infty;\quad z = \infty \quad \rightarrow \quad T = 293 \text{ K}$$

Initially (prior to laser cutting), the substrate material is assumed to be at a constant ambient temperature, i.e. $T = T_{amb}$, which is considered to be (T_{amb} = 293 K).

Equation [5.1] is solved numerically with the appropriate boundary conditions to predict the temperature field in the substrate material. Table 5.1 gives the data used in the simulations in line with the experimental conditions. However, the enthalpy method is used to analyze the phase change problem, [ABA 09]. The specific heat capacity is associated with the internal energy gain of the substrate material, i.e.:

$$Cp(T) = \frac{\partial U}{\partial T}$$

However, the internal energy gain during the phase change is associated with the latent heat of fusion, which is given separately in terms of solidus and liquidus temperatures (the lower and upper temperature bounds of the phase change range) and the total internal energy associated with the phase change, called the latent heat [ABA 09]. Since the primary interest is the stress field developed in the cutting section, the flow field generated in the liquid phase at the kerf surface during the laser cutting process is omitted.

5.2.2. *Thermal stress analysis*

The elastic strain increment vector, $\{\Delta\boldsymbol{\varepsilon}^{\mathbf{el}}\}$ is related to the stress increment vector, $\{\Delta\boldsymbol{\sigma}\}$ by Hook's law:

$$\{\Delta\boldsymbol{\sigma}\} = [\mathbf{D}]\ \{\Delta\boldsymbol{\varepsilon}^{\mathbf{el}}\} \qquad [5.6]$$

where [**D**] contains the elastic constants related to the temperature-dependent elastic modulus, E and Poisson's ratio, ν. The total strain vector, $\{\Delta\boldsymbol{\varepsilon}\}$, may be expressed as follows:

$$\{\Delta\boldsymbol{\varepsilon}\} = \{\Delta\boldsymbol{\varepsilon}^{\mathbf{el}}\} + \{\Delta\boldsymbol{\varepsilon}^{\mathbf{th}}\} + \{\Delta\boldsymbol{\varepsilon}^{\mathbf{pl}}\} \qquad [5.7]$$

where $\{\Delta\varepsilon^{el}\}$ is the elastic strain increment vector, $\{\Delta\varepsilon^{th}\}$ is the thermal strain increment vector, $\{\Delta\varepsilon^{pl}\}$ is the plastic strain increment vector. The incremental thermal strain vector, $\{\Delta\varepsilon^{th}\}$ arises from the volume changes that accompany the temperature increment, ΔT, which is calculated by the thermal analysis. It is normally accounted for in the stress analyses through a temperature-dependent differential thermal expansion coefficient, $\alpha(T)$. In ABAQUS/Standard analysis, a spatially varying thermal expansion can be defined for homogeneous solid continuum elements by using a distribution, which includes the tabulated values for the thermal expansion [ABA 09]. ABAQUS uses an implicit backward-difference scheme for time integration of both temperature and displacements at every material integration point [ABA 09].

Density kg/m^3	Latent heat of melting (J/kg)	Solidus temperature (K)	Liquidus temperature (K)
4,430	4.2 x 10^5	1,878	1,933

(a) Density and melting properties of the Ti-6Al-4V alloy

Temperature (K)	*Cp* (J/kgK)	*k* (W/mK)
300	403	6.5
573	505	7
673	520	9
773	530	11
873	545	12
1,073	620	17

(b) Thermal properties of the Ti-6Al-4V alloy

Table 5.1. *Thermal properties of Ti-6Al-4V alloy used in the simulations [CRS 11]*

5.3. Numerical simulation

Finite element discretization was carried out using the ABAQUS software [ABA 09]. The simulation is performed using the ABAQUS/Standard and consists of a sequential thermal-stress analysis. In the sequential thermal-stress analysis, 91,572 elements are used to create the model using two element types; for the heat transfer analysis, the mesh used elements of type DC3D4 (4-node linear heat transfer tetrahedron) and the stress analysis used C3D4 (4-node linear 3D stress tetrahedron). The fixed boundary conditions are applied on both ends of the work piece, resembling the experimental laser cutting situation.

In the stress analysis, displacements are stored by ABAQUS at the nodal positions as a solution variable, and loads are defined as prescribed displacements and forces. Employing the interpolation functions, it is possible to calculate the strain and stress increments at any point within the element using the compatibility and constitutive equations. ABAQUS transforms the mechanical equilibrium equations into a set of simultaneous equations, such that the nodal displacements and forces are related to each other through the elemental stiffness matrix.

Laser heat flux with a Gaussian distribution and prescribed velocity of 20 cm/s along the hole circumference through user subroutine DFLUX is applied to the thermal model. The Gaussian parameter "a" is a = 0.0002 m, in accordance with the experimental power intensity distribution. The peak laser intensity is 0.5×10^{11} W/m^2 and the reflectivity is 0.65 set in the simulations in accordance with the experimental tests. The temperature-time history resulting from the thermal analysis is used as an input to the thermal stress analysis. The work piece is considered to be an elastic body, which is modeled as von Mises elastic-plastic material with isotropic hardening and with a yield stress that changes with the temperature. The mechanical properties bronze used in the simulations are given in Table 5.2.

5.4. Experimental

The CO_2 laser (LC-ALPHAIII) delivers a nominal peak output power of 2 kW in pulse mode, with different frequencies, and is used to irradiate the work piece surface. The nominal focal length of the focusing lens is 127 mm. The laser beam diameter focused at the work piece surface is 0.3 mm. Nitrogen assisting gas emerges from the conical nozzle and is directed co-axially with the laser beam. The initial cutting tests are carried out to identify the laser cutting parameters resulting in the quality cutting. This is believed to be necessary to save computational time and effort in determining the thermal stress levels in the cut edges resulting from the optimal laser cutting parameters. The laser cutting parameters are given in Table 5.3.

The laser cutting is carried out on the ti-6Al-4V sheets of 3 mm thickness. The laser cut hole diameter is 0.002 m. An optical microscope is used to photograph the hole sections. The JEOL JDX- 3530 scanning electron microscope (SEM) is used to obtain photomicrographs of the cross-section and surface of the work pieces after the tests. Energy dispersive spectroscopy (EDS) is carried out for the elemental analysis in the cut section. The XRD analysis was carried out incorporating the Bruker D8 Advanced XRD unit with MoKα radiation. A typical XRD setting was 40 kV and 30 mA. The parabolically-shaped Göbel Mirror was used in Bruker D8 Advanced, which provided the highly-parallel x-ray beams. The parallel beams from it removed the traditional limitations of the Bragg-Brentano geometry for powder diffraction and thin film investigations.

Temperature (K)	Elastic modulus (GPa)	Poisson's ratio	Expansion coefficient $\times 10^6$(1/K)	Yield stress (MPa)
300	113	0.34	8	14.37
373	108	0.34	8.6	12.81
473	103	0.34	9	11.2
589	95	0.34	9.2	10.5
698	85	0.34	9.4	7
803	70	0.34	9.7	5
973	50	0.34	1.05	2.25

(a) Mechanical properties

Gaussian Parameter (m)	Hole Radius (m)	Angular Velocity (rad/s)	Tangential Velocity (m/s)	Power Intensity W/m^2
0.0003	0.006	25	0.15	2.8×10^{12}

(b) Laser cutting parameters

Table 5.2. *Mechanical properties of the Ti-6Al-4V alloy [CRS 11] and cutting parameters used in the simulations*

5.5. Results and discussion

The laser cutting of a small diameter hole in a titanium sheet is carried out. Temperature and thermal stress fields developed in the cutting section are predicted using the ABAQUS code. Metallurgical and morphological changes in the cutting region are examined in detail. Residual stress formed at the surface vicinity of the cut edge is measured incorporating the XRD technique.

Figure 5.2 shows the temperature distribution along the top and bottom circumferences of the hole for different time periods, while Figures 5.3 and 5.4 show the temperature contours in the cutting section.

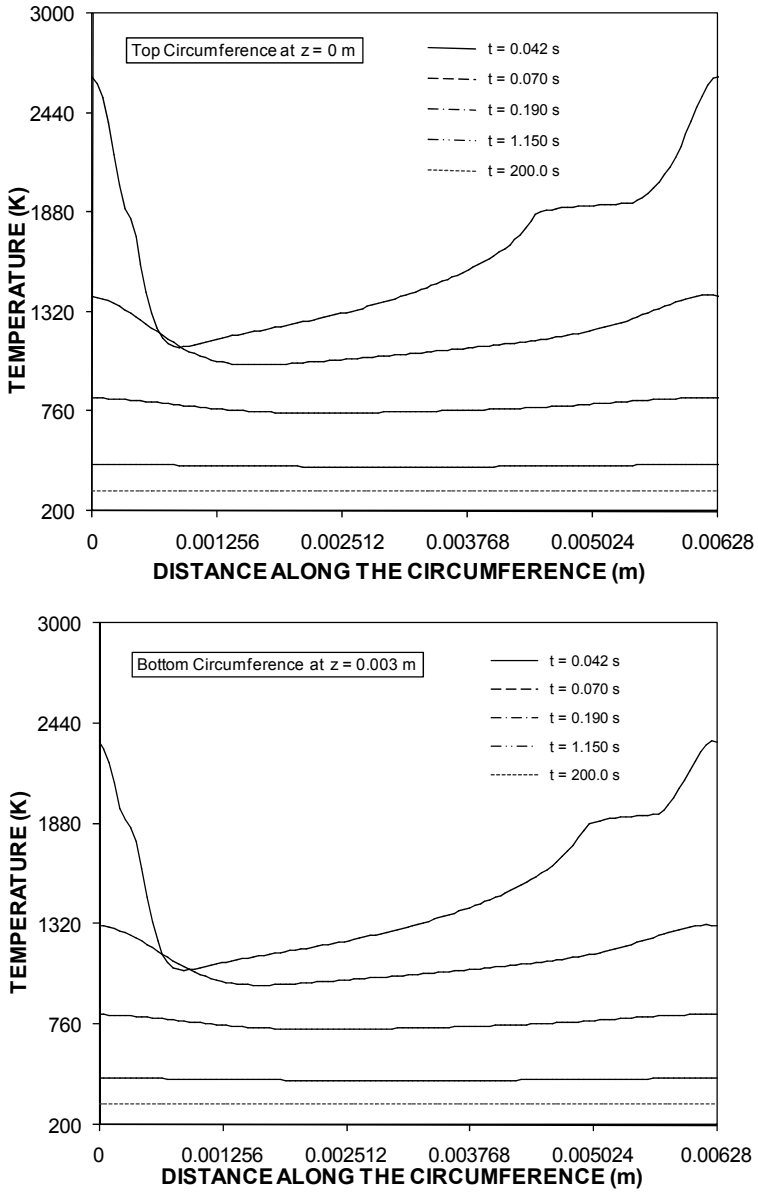

Figure 5.2. *Temperature distribution around the top and bottom circumference of the hole*

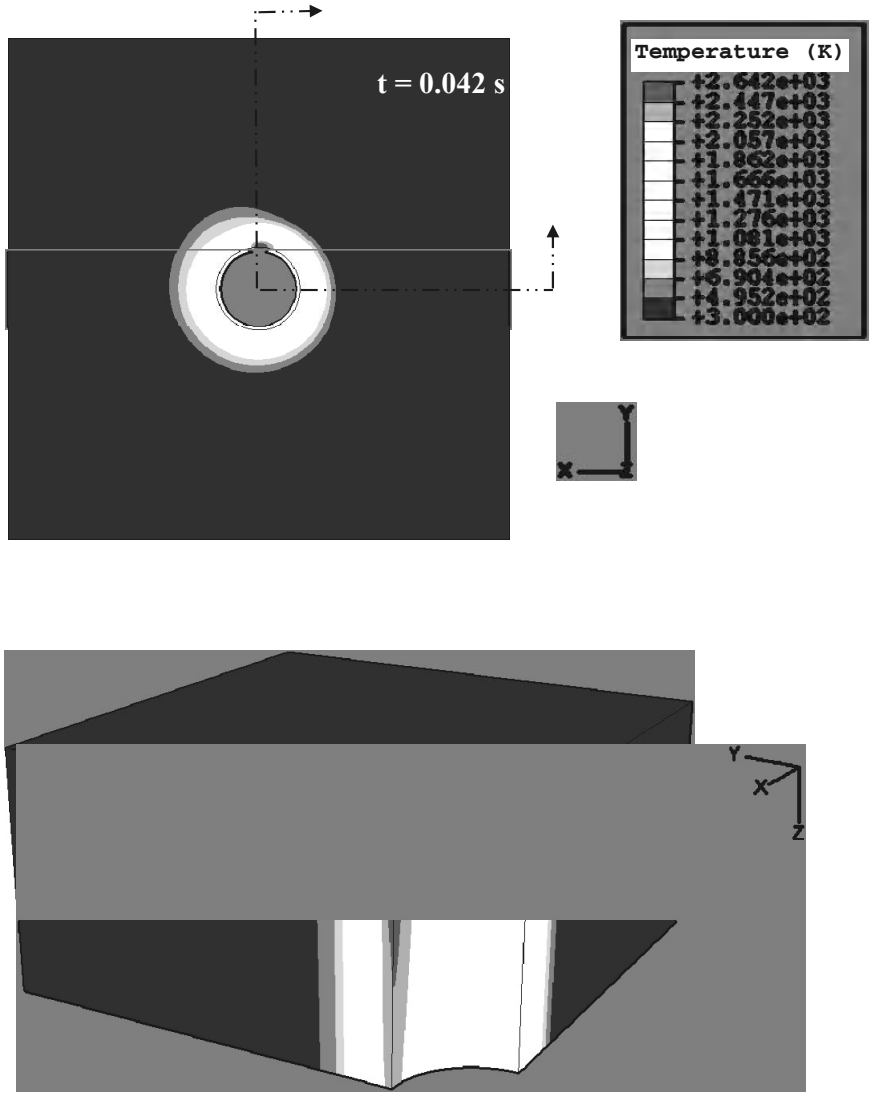

Figure 5.3. *Temperature contours in the cutting section at t = 0.042 s*

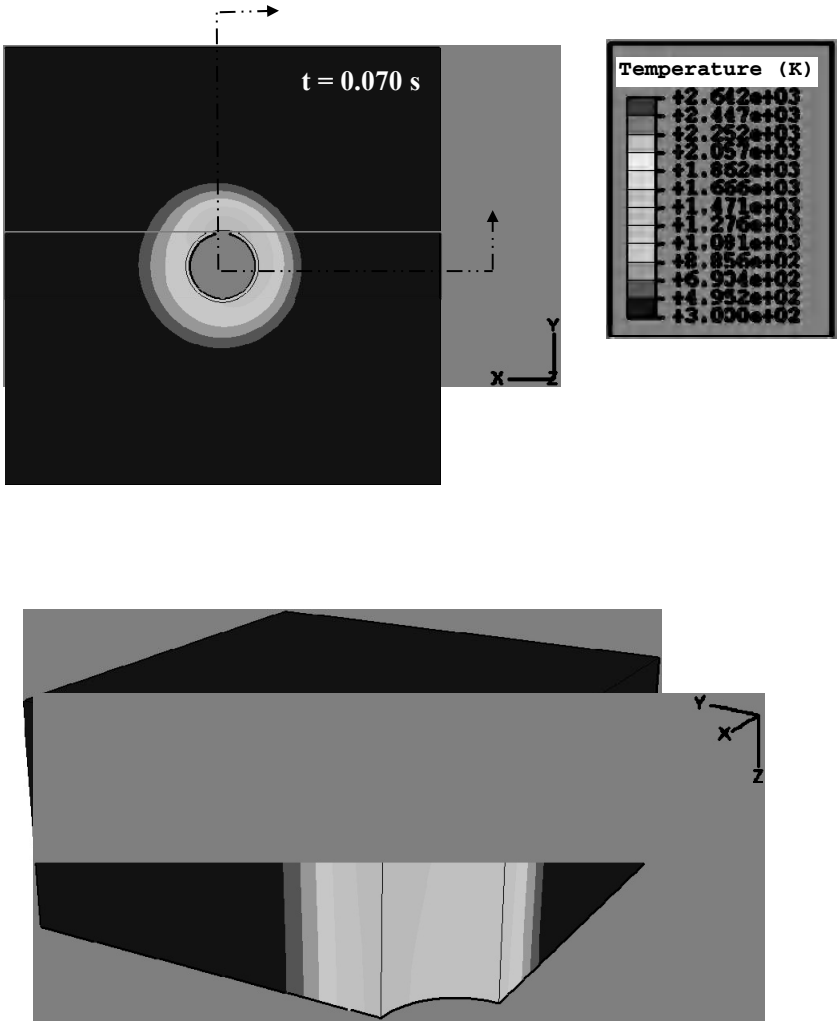

Figure 5.4. *Temperature contours in the cutting section at t = 0.07 s in the cooling cycle*

The temperature attains high values in the early heating period and reaches its maximum where the laser beam axis is located. Superheating of the liquid phase is evident at the location of the laser beam around the hole circumference, since temperature exceeds the melting temperature of the substrate material. The presence

of a "mushy" zone around the melted section is also visible from the temperature curve; in which case the temperature remains almost the same at the melting temperature in this region. Temperature decays sharply from the maximum temperature in the region next to the laser beam position. However, temperature decays around the hole circumference is gradual in the region away from the laser beam location. As time progresses, the temperature around the hole circumference reduces notably. This corresponds to the time at which the cutting is completed. As the cooling period progresses further, temperature reduces to the initial temperature and the cooling of the hole circumference is completed. When comparing temperature distribution along the top and bottom circumferences of the hole, it can be observed that the behavior of temperature is the same; however temperature attains a slightly higher value at the top circumference of the hole compared to that at the bottom circumference. This may be associated with the intensity of the laser beam upon penetration into the hole bottom. In this case, laser beam peak intensity reduces exponentially along the hole depth so that the peak intensity reduces at the bottom circumference of the hole.

Figure 5.5 shows the temperature distribution along the z-axis at different locations along the hole circumference (Figure 5.1) and two cutting periods. It should be noted that the laser beam location is at point #1 when t = 0.042 s. The temperature at the laser beam location is well above the liquidus temperature of the substrate material. This indicates the superheating of the liquid phase at location #1 and the temperature gradient developed in the vicinity of location #1 should be significantly high. Moreover, due to the conduction heating, from the region where the laser beam is located, the temperature increases at the other locations around the hole circumference. This is attributed to the small hole diameter; in this case, the small size of the hole enables a high rate of heat conduction around the hole circumference and results in a high temperature in this region.

Temperature variation along the z-axis is notable at location # 1 for t = 0.042 s. However, at locations #2 and #4, temperature variation is not notable. This is associated with the heat transfer; in which case, conduction heat transfer around the hole circumference does not result in a notable temperature variation along the z-axis at locations #2 and #4. In the case of cutting time t = 0.19 s, temperature reduces below the liquidus temperature of the substrate material. This is because of the completion of cutting and ceasing of the laser power. Although cutting is completed, temperature at locations #2 and #4 still remains high and reduction in temperature occurs at location #3 and #1. This is attributed to the absorption of the laser beam at location #1, which diminishes after the completion of the cutting process. Consequently, the energy gain of the substrate material at location #1 from the irradiated laser field ceases and is replaced with conduction heat transfer. This sharply lowers the temperature at location #1. Temperature variation along the z-axis for t = 0.19 s is visible at location #1 where the cutting ends. However, at

other locations around the hole circumference, temperature variation along the z-axis is notable.

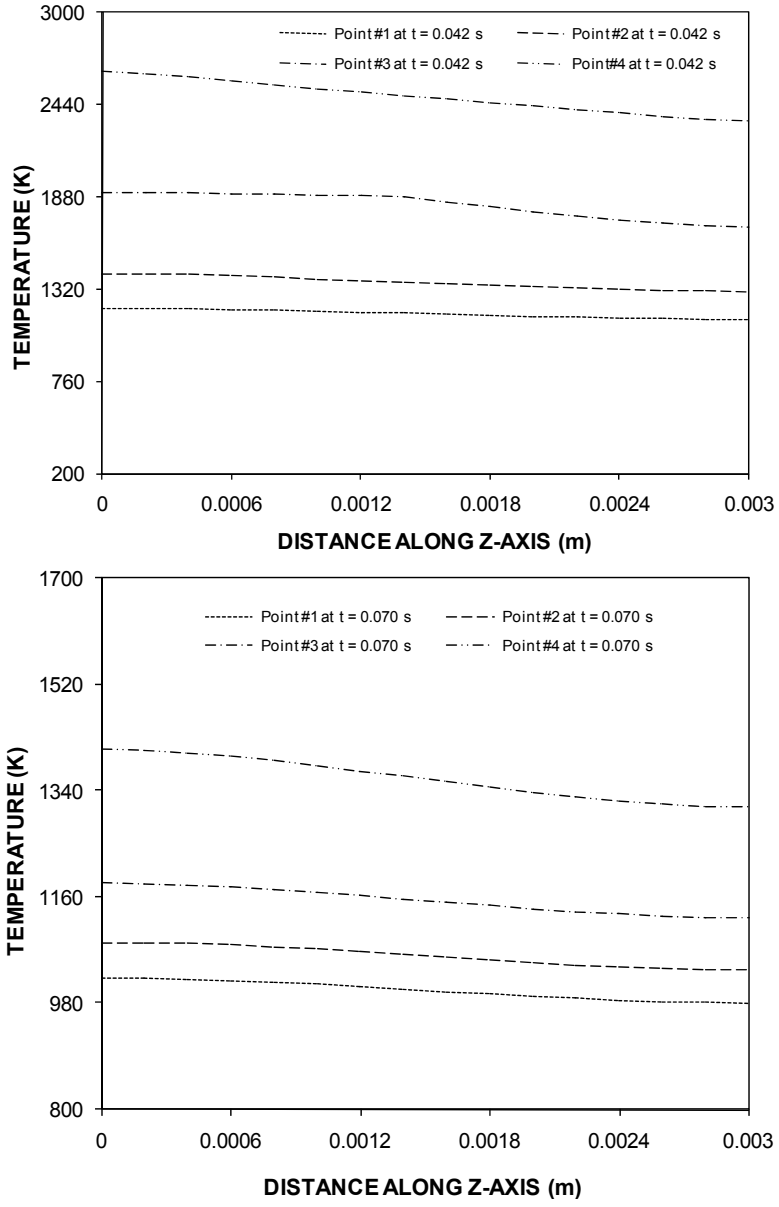

Figure 5.5. *Temperature distribution along the z-axis at two cooling periods*

Figure 5.6 shows von Mises' stress variation along the hole top and bottom circumferences for different time periods while Figures 5.7 and 5.8 show von Mises' stress contours around the cutting section.

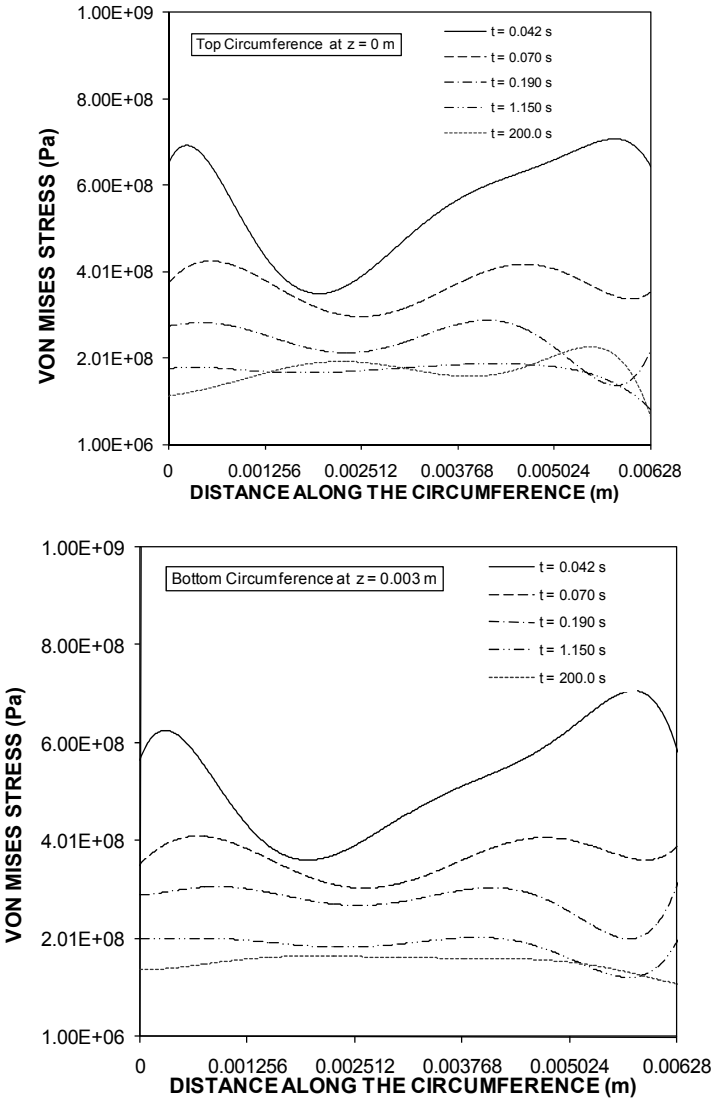

Figure 5.6. *Von Mises' stress distribution around the top and bottom circumference of the hole*

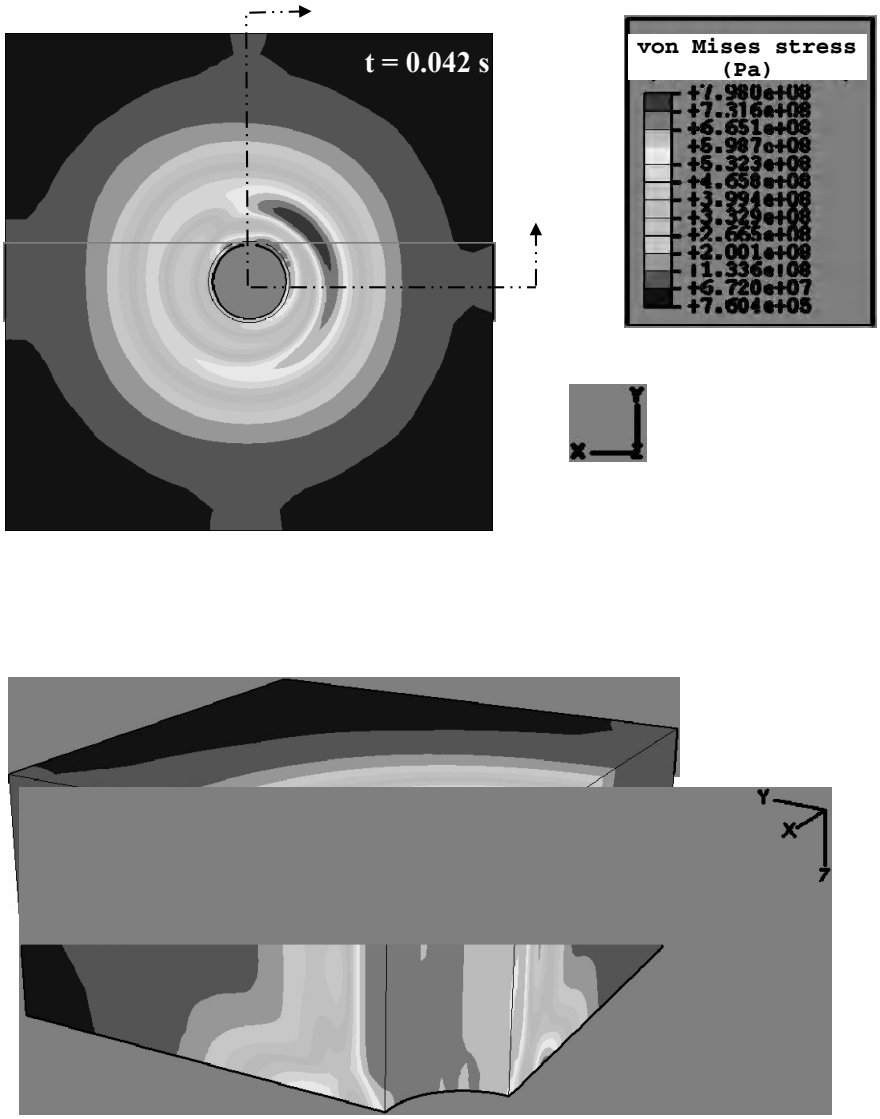

Figure 5.7. *Von Mises' stress contours in the cutting section at t = 0.042 s*

The von Mises' stress attains high values in the region where temperature gradients are high. This corresponds to the region near the neighborhood of the laser beam location. Since the elastic modulus of the substrate material reduces with increasing temperature, the von Mises' stress attains lower values at high

temperature locations. Moreover, the von Mises' stress distribution along the top and bottom circumferences of the hole is not uniformly distributed. This is associated with the laser beam motion, which moves along the circumference of the hole with constant cutting speed. In this case, the cooling rate of each location differs along the hole circumference while resulting in a non-uniform stress distribution.

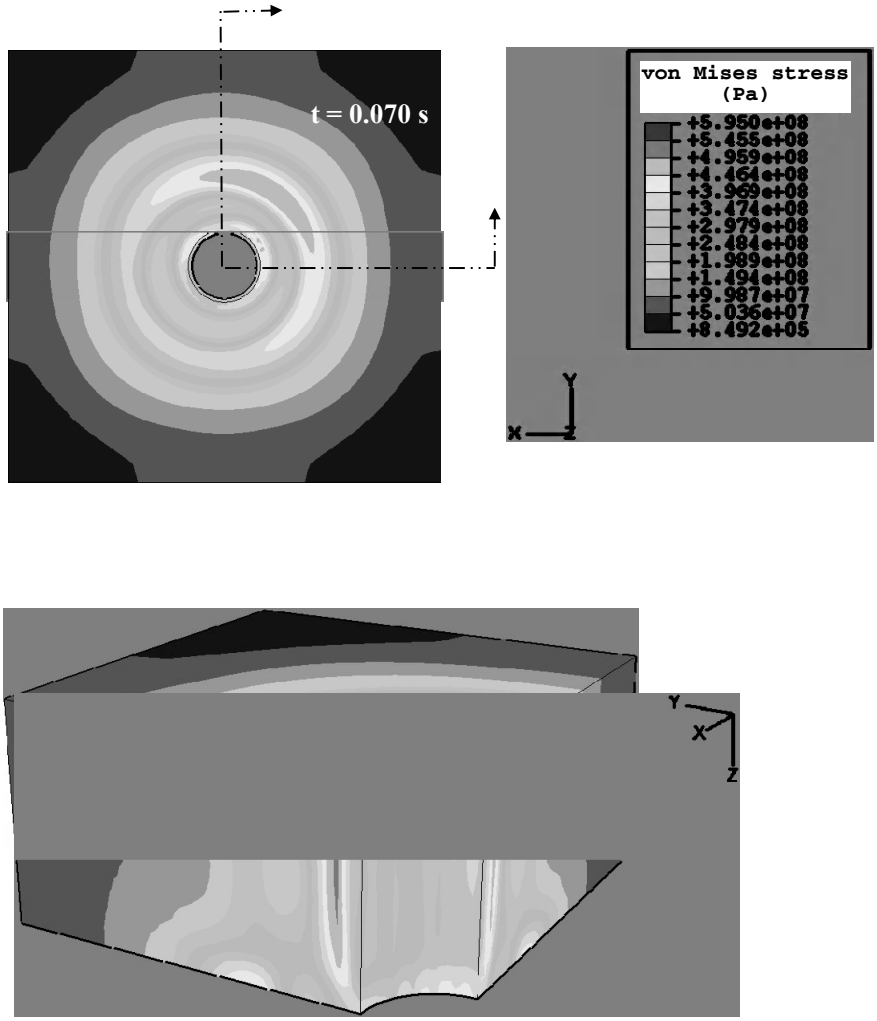

Figure 5.8. *Von Mises' stress contours in the cutting section at t = 0.07 s*

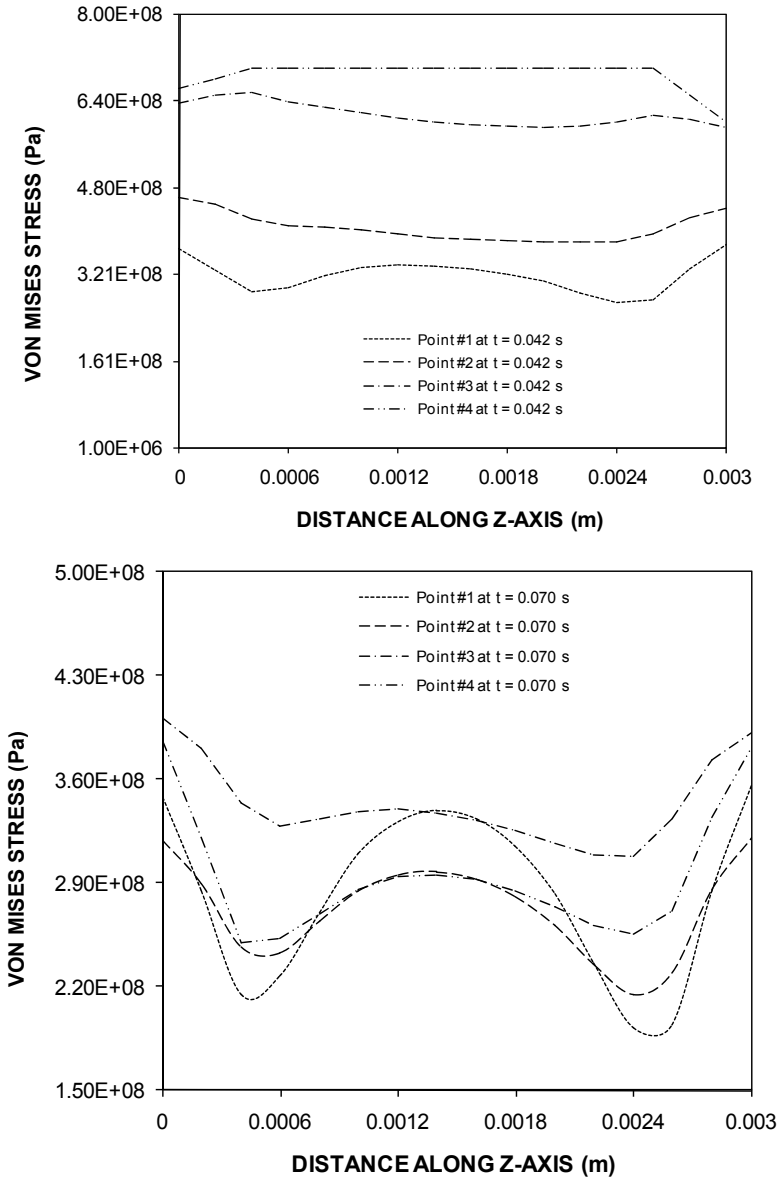

Figure 5.9. *Von Mises' stress distribution along the z-axis for two cooling periods*

As the cooling cycle progresses (t = 200 s), the temperature reduces to initial temperature and von Mises' stress becomes almost uniform along the hole

circumference. This is also true for the bottom circumference. The maximum value of von Mises' stress is slightly higher at the top circumference than that corresponding to the bottom circumference. This is attributed to the formation of relatively higher temperature gradients around the top circumference than around the bottom circumference.

Figure 5.9 shows the von Mises' stress distribution along the z-axis at different locations around the hole circumference for two periods. In the early cutting period, the von Mises' stress attains high and almost uniform values along the hole depth in the z-direction. The von Mises' stress attains low values along the z-axis at location #1. This is because of the attainment of high temperatures along the z-axis at this location (Figure 5.1). Therefore, high temperature lowers the elastic modulus of the substrate material lowering the stress levels along the hole circumference. In the case of cutting duration t = 0.07 s, von Mises' stress reduces in the region close to the front (z = 0 m) and back (z = 0.003 m) of the hole surfaces, which is more pronounced at location #1. However, in the mid-thickness of the work piece (z = 0.0015 m), the von Mises' stress increases. This increase is attributed to the thermal compression of the substrate material in this region during the cooling cycle after completion of the cutting process. It should be noted that the top and the bottom surfaces of the work piece enables free expansion, while at the mid-thickness thermal expansion does not take place freely. Consequently, thermal expansion of the front and back surfaces of the hole result in compression at the mid-thickness of the work piece.

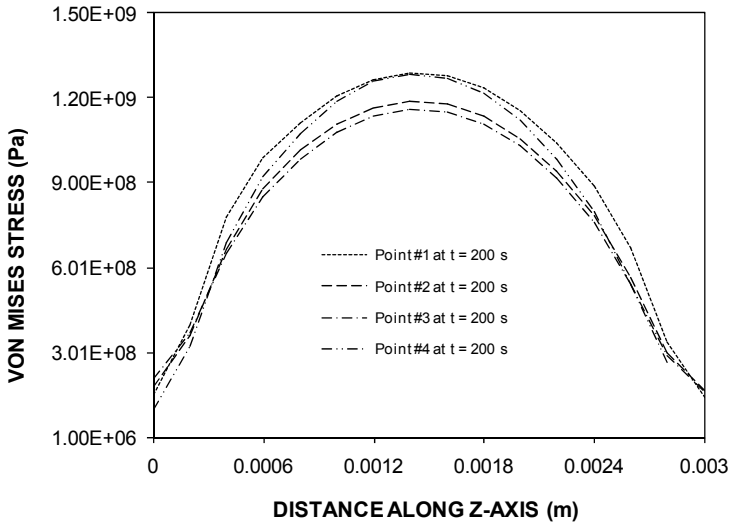

Figure 5.10. *Von Mises' stress distribution along the z-axis after the end of the cooling period*

Figure 5.10 shows the von Mises' stress at the end of the cooling cycle t = 200 s and at different locations around the hole circumference (Figure 5.1), while Figure 5.11 shows the von Mises' stress contour at the end of the cooling cycle.

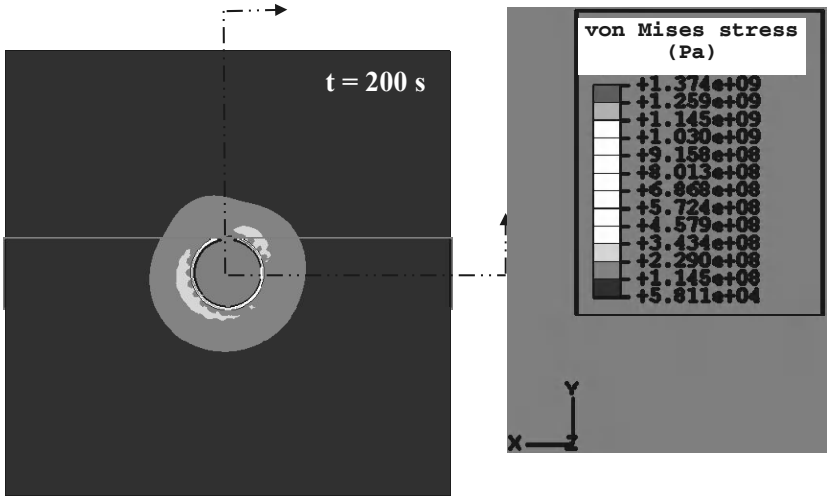

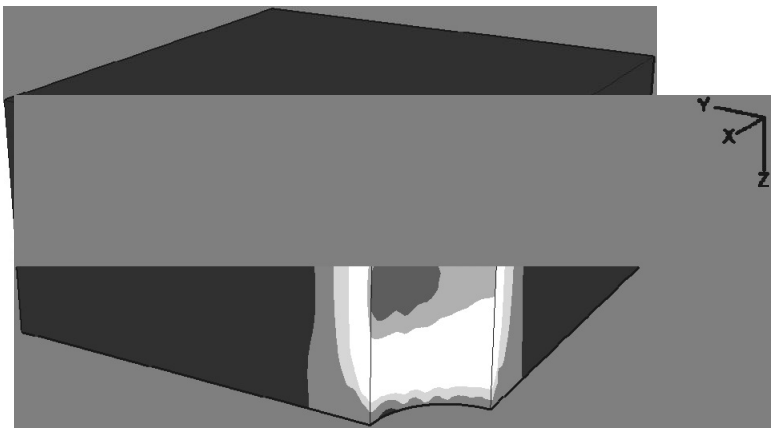

Figure 5.11. *Von Mises' stress contours in the cutting section after the end of the cooling period*

Since the time is long enough and the temperature has reduced to the initial temperature, stress along the z-axis represents the residual stress. The von Mises'

stress reaches its maximum at the mid-thickness of the hole (z = 0.0015 m) for all locations around the hole circumference. It decays towards the hole front and back surfaces. The attainment of high stress levels at the mid-thickness is because of the compressive stresses formed in this region. Consequently, free thermal expansion and contraction in the neighborhood of the hole front and bottom surfaces result in high stress levels in this region. The maximum magnitude of von Mises' stress is in the order of 1.2 GPa, which is extremely high for a hole of 2 mm diameter. In addition, the value of the von Mises' stress at the front (z = 0 m) and back surface (z = 0.003 m) is of the order of 220 MPa. However, the XRD stress measurement reveals that the residual stress at the front surface of the hole is of the order of 280 MPa. When comparing stress predicted at the top and surface of the hole circumference with XRD measurements, it is evident that both results are in good agreement. It should be noted that the measured residual stress is limited to the surface vicinity of the hole front surface due to the limited penetration of the XRD rays.

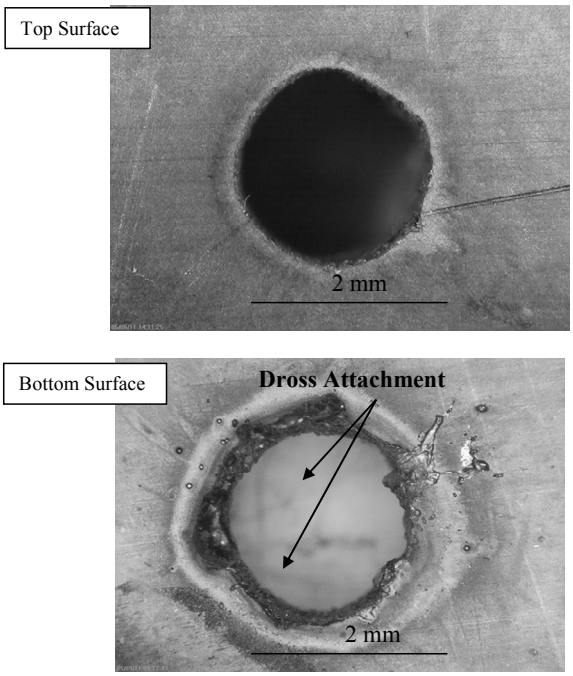

Figure 5.12. *Optical photographs of the top and bottom surface of the laser cut hole*

Figure 5.12 shows optical photographs of the top and bottom surfaces of the laser cut hole. A circular cut with almost no geometric defects is observed from the

optical micrographs. However, some small sideways burning is observed at the top and bottom of the hole surfaces. This is particularly true at the back surface of the work piece. The sideways burning appears as irregularities around the hole circumference. Although nitrogen gas is used at high pressure, the presence of the small amount of oxygen in the cutting section is responsible for the formation of sideways burning around the hole circumference. Since a titanium alloy has a high affinity to oxygen, the formation of sideways burning is almost unavoidable.

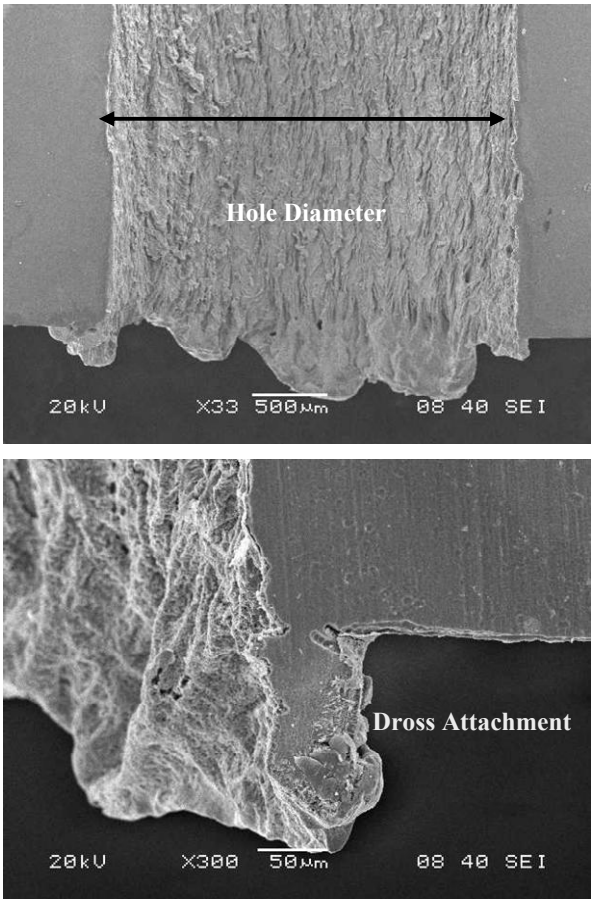

Figure 5.13. *SEM micrograph of a laser hole section*

Figure 5.13 shows a hole cross-section. In this case the striation pattern is evident at the kerf surface. However, striation patterns are formed irregularly due to thermal erosion and uncontrolled melt flow at the kerf surface. The dross attachment

on the back surface of the work piece is evident. This may be the result of blockage of the hole by the molten metal flow during the cutting process. In this case, the assisting gas loses its axial momentum in the hole due to the small hole diameter. This, in turn, lowers the pressure drag acting on the melt flow surface while enabling molten metal accumulation and attachment at the hole exit region. Moreover, a close examination of the SEM micrographs (Figure 5.13) reveals that the heat affected zone is considerably large around the cutting section. However, a dense layer is formed at the surface indicating the rapidly solidified region.

Figure 5.14 shows XRD diffractogram corresponding to the laser cut surface. The occurrence of TiO_2 peaks indicates the presence of oxygen at the cut surface. Since nitrogen is a reactive gas at high temperature, it forms a TiNx compound in the cutting section, which is evident from the TiN_x peak. The formation of TiN_x at the surface region contributes to the microhardness of the kerf surface.

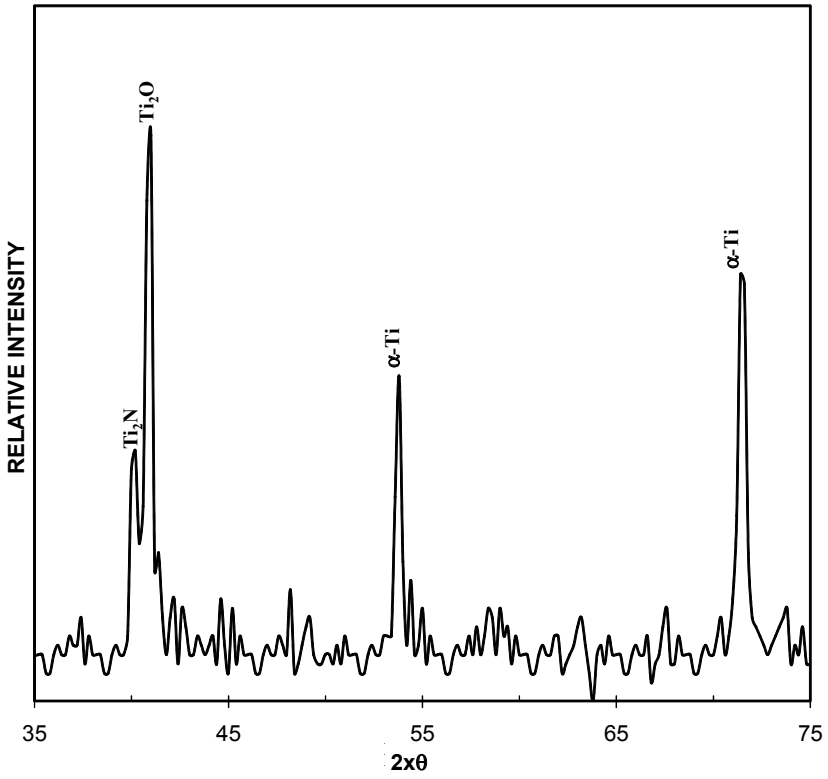

Figure 5.14. *XRD diffractogram of a laser cut surface*

5.6. Conclusion

The laser cutting of a 2 mm diameter hole in a Ti-6Al-4V sheet was carried out. Temperature and stress fields developed around the cutting section were modeled and predicted using the ABAQUS finite element code. The metallurgical and microstructural changes in the cutting section were examined using optical and scanning electron microscopes. The residual stress formed in the vicinity of the cut surface was measured incorporating the XRD technique. The findings were compared with the numerical predictions.

It was found that the temperature at the laser beam location greatly exceeds the liquidus temperature of the substrate material. This, in turn, results in high temperature gradients in the region next to the laser beam location. High temperature gradients cause the formation of high stress levels around the hole circumference. Since the elastic modulus reduces with increasing temperature, the von Mises' stress attains low values in the region of high temperature. The von Mises' stress attains high values at the mid-thickness of the hole. This is attributed to free expansion of the front and back surfaces, which introduce compressive stress at the mid-thickness of the hole. The maximum thermal stress at the end of the cooling cycle is in agreement with the XRD data. Sideways burnings occurred around the hole circumference despite nitrogen being used as an assisting gas. High temperature oxidation reactions in the cutting section were responsible for the formation of the sideways burning. The formation of the oxide compound (TiO_2), as was evident from the XRD diffractogram, was due to the high temperature oxidation reactions that take place in the cutting section. Irregularly formed striation patterns were observed at the kerf surface. The blockage effect of the small hole diameter reduces the axial velocity of the assisting impinging jet. This, in turn, lowers the pressure drag in the hole and the melt accumulation and dross attachment at the hole back surface becomes unavoidable.

5.7. Acknowledgements

The authors acknowledge the support of King Fahd University of Petroleum and Minerals in Dhahran, Saudi Arabia for this work.

5.8. Bibliography

[ABA 09] ABAQUS Theory Manual, Version 6.7, ABAQUS Inc., Pawtucket, USA, 2009.

[ALM 06] ALMEIDA I. A., de ROSSI W., LIMAB M.S.F., BERRATTA J.R., NOGUEIRA G.E.C., WETTER N.U, VIEIRA Jr N.D., "Optimization of titanium cutting by factorial analysis of the pulsed Nd: YAG laser parameters", *Journal of Materials Processing Technology*, vol. 179, pp.105-110, 2006.

[CRS 11] CRS HOLDINGS INC., Alloy Data: Titanium Alloy Ti 6Al-4V, available online at: www.veridiam.com/pdf/DataSheetTitaniumAlloy.pdf, 2011.

[DUB 08] DUBEY A.K., YADAVA V., "Experimental study of Nd:YAG laser beam machining: an overview", *Journal of Materials Processing Technology*, vol. 195, pp. 15-26, 2008.

[MAH 98] MAHER W., TONG K., "Laser cutting of titanium with pulsed and modulated pulsed Nd:YAG lasers", *Proc. SPIE*, vol. 3265, pp. 180-183, 1998.

[PFE 10] PFEIFER R., HERZOG D., HUSTEDT M., BARCIKOWSKI S., "Pulsed Nd:YAG laser cutting of NiTi shape memory alloys: influence of process parameters", *Journal of Materials Processing Technology*, vol.210, p.1918-1925, 2010.

[QI 04] QI L.T., WANG Y., LV S.J., "Study of YAG laser cutting process with titanium alloy sheet", *Proc. SPIE*, vol. 5629, pp. 247-253, 2004.

[RAO 05] RAO B.T., KAULA R., TIWARIB P., NATH A.K., "Inert gas cutting of titanium sheet with pulsed mode CO2 laser", *Optics and Lasers in Engineering*, vol. 43, pp.1330-1348, 2005.

[SHA 06] SHANJIN L., YANG W., "An investigation of pulsed laser cutting of titanium alloy sheet", *Optics and Lasers in Engineering*, vol.44, pp.1067-1077, 2006.

[THA 05] THAWARI G., SARIN S.J.K., SUNDARAJIAN G., JOSHI S.V., "Influence of process parameters during pulsed Nd:YAG laser cutting of nickel-base superalloys", *Journal of Materials Processing Technology*, vol.170, pp.229-239, 2005.

[YIL 11] YILBAS B.S., AKHTAR, S.S., KARATAS C., "Laser trepanning of a small diameter hole in titanium alloy: temperature and stress fields", *J. of Materials Processing Technology*, vol. 211, pp. 1296-1304, 2011.

Chapter 6

Modeling and Simulation of Laser Welding

This chapter deals with the modeling and simulation of the laser welding process using statistical, artificial intelligence and the finite element method. Laser welding is characterized by its high power density, high welding speed, concentrated heat input, high levels of stability and low distortion. The weld bead profile of laser welding depends on many operating process parameters and these parameters must be chosen correctly to obtain the preferred output. The trial-and-error method of selecting weld parameters is not suitable for laser welding as the process is very costly, hence suitable analytical methods are essential for selecting the optimum parameters for welding. In this chapter the influence of laser welding parameters on the weld bead profile of AISI 304 stainless steel butt joints are analyzed based on the Box–Behnken experimental design. Statistical based mathematical modeling is carried out along with neural network modeling and finite element simulation. The Backpropagation algorithm is used for neural network modeling. Many network combinations are tried and finally an optimum network is selected. Mathematical expressions for predicting the depth of penetration and bead-width are extracted from the neural network model.

The transient temperature profiles and weld pool dimensions, depth of penetration and bead width have been determined using the finite element software SYSWELD. Temperature dependent thermophysical properties are considered for the finite element analysis. Finally, the results of mathematical modeling, neural

---

Chapter written by Karuppudaiyar R. BALASABRAMANIAN, Krishnasamy SANKARANARAYANASAMY and Gangusami N. BUVANASHEKARAN.

Lasers in Manufacturing Edited by J. Paulo Davim

network model and finite element simulation models are compared with the experimental values.

6.1. Introduction

Laser welding is a non-contact fusion welding process similar to the electron beam welding process. It is characterized by its high speed, high power density, concentrated heat input and high production rate due to which it is widely used in the manufacturing sector where conventional methods are not suitable. Due to its low heat input, less distortion, low heat affected zone, it is primarily used for the welding of thin sections, heat sensitive and magnetic materials. The weld bead profile of laser welding depends on various parameters and these parameters must be selected correctly to obtain the desired output. The laser welding process is an expensive process where the trial-and-error method of analysis is not suitable. Hence prior to welding a product a thorough understanding of the operating process conditions is essential, which can only be achieved using modeling and simulation. Modeling provides a better understanding of the process and the interactions between the process variables.

6.2. Process mechanisms

Laser beam welding (LBW) is one of the most widely used high energy beam welding processes. LBW is a very concentrated energy source which provides high power density and results in producing a keyhole during welding similar to plasma arc welding or electron beam welding [AVA 08]. Depending on the laser irradiance, two modes of welding are possible: conduction limited welding and deep penetration (keyhole) mode welding. Conduction limited welds are in liquid phase, which are obtained at an irradiance level of less than 10^6 W/cm^2. At these irradiance levels, the focused laser beam using a lens is absorbed by the metal workpiece, generating heat that is rapidly conducted into the metal, thus melting the irradiated surface and the subsurface layers. This process goes on without vaporization of the molten surface layers. In conduction mode welding the surface temperature will be below the boiling point of the substrate and conduction mode heat transfer occurs. Conduction welding is possible when the absorbed energy is sufficient to melt the weld zone, but insufficient for vaporization and plasma formation. Conduction welds, exhibit a low depth-to-width ratio (aspect ratio), which is required when a limited penetration in the thickness direction is desired, especially for heat sensitive parts.

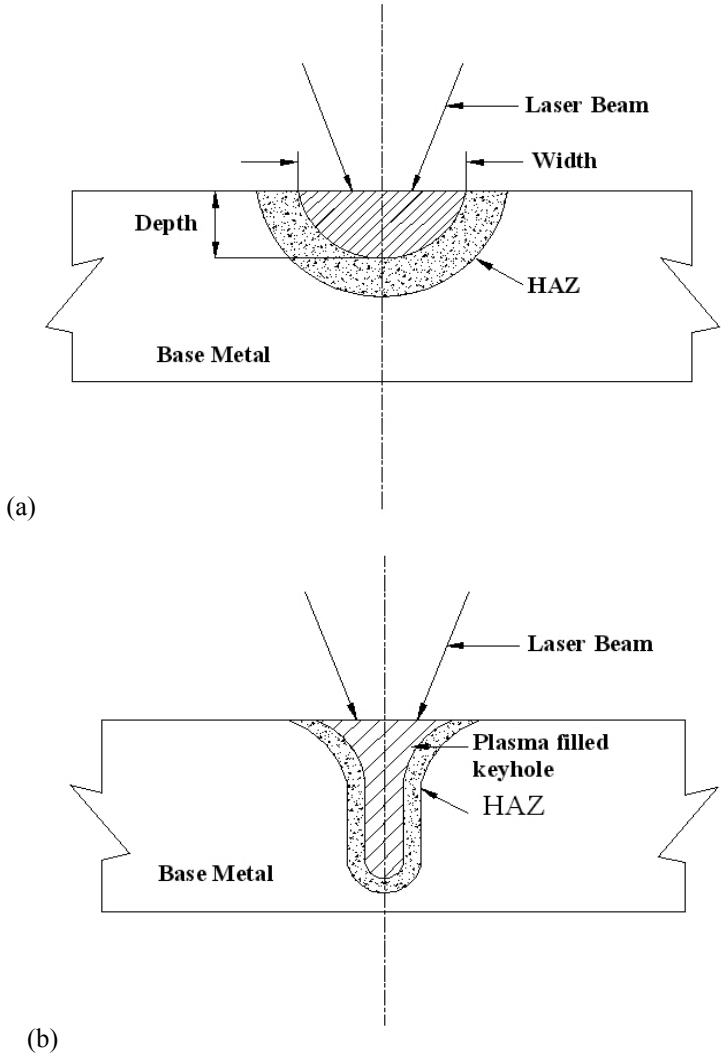

Figure 6.1. *(a) Conduction-limited welding; (b) deep penetration welding*

Deep penetration (keyhole) mode laser welding implies vaporizing of metals, which requires a laser irradiance level in excess of 10^6 W/cm^2. The temperature of the substrate will be more than the boiling point. During this mode, the laser beam melts through the metal work piece thickness and produces a narrow cylinder of liquid metal resulting in a high depth to width ratio. Furthermore, vaporization of the liquid for a finite thickness occurs, producing a column of metal vapor. The vapor

column, commonly referred to as a vapor cavity or keyhole, is surrounded by liquid metal [FRE 99, MAZ 80]. Inside the keyhole the laser radiation is subjected to multiple reflections before it escapes from the cavity. Due to the existence of temperature gradients along the surface and subsurface liquid layers, the surface tension varies dramatically along these liquid layers, promoting localized (Marangoni) convection. When the work piece is subjected to a pass through the laser beam, the metal along the leading edge of the keyhole is melted through its entire thickness. The liquid metal flows around and along the base of the keyhole, eventually re-solidifying at the trailing edge [STE 88].

Figure 6.1 shows typical shapes of (a) conduction limited welding and (b) deep penetration or keyhole welding. Very high power concentration will also be a problem. Power densities higher than 10^7 W/cm^2 may result in excessive vaporization and a loss of material. Most industrial laser welding is autogenous; no filler metal is added to the joint. This is primarily because lasers make relatively small melt puddles and it is hard to get filler wire small enough in diameter to feed the pool without freezing it. KiloWatt – class lasers generate melt puddles in the order of 0.5 to 0.8 mm in diameter, if the filler metals are to be used, the wire should be 0.2 to 0.5 mm in diameter.

6.3. Operating parameter characteristics

The process parameter selection is important, it regulates the laser welding process and can be modified to achieve the specified weld results. Welding quality is strongly characterized by the weld bead geometry, depth of penetration (DOP), bead width (BW), and hence the weld bead geometry plays an important role in determining the mechanical properties of the welded joints. Therefore, the selection of the welding process parameters is essential for obtaining the optimal weld bead geometry. The success of the welding depends on the choice of the above mentioned operating welding parameters. Thus, for a good weld quality the combination of the above parameters must be properly selected. The weld bead geometry and rigidity depends on the welding parameters. The accuracy of welding depends on the material preparation, the joint fit-up and the laser beam-to-joint alignment. The various operating process parameters are:

– beam characteristics:

  - mean power (continuous or pulsed),

  - power density and distribution,

  - spot dimensions,

- beam mode,
- beam angle and wavelength;

– technological parameters:

- welding speed,
- type and flow rate of the shielding gas,
- focal point,
- gap between plates;

– characteristics of the material:

- thermal diffusivity,
- reflectivity,
- weldability,
- chemical composition,
- absorptivity,
- thermal conductivity,
- latent heat,
- thermal expansion coefficient,
- density and thickness,
- atmospheric condition.

6.4. Types

Depending on the type of laser and wavelength desired, the laser medium is gas, liquid or solid. Lasers are commonly classified according to the state or the physical properties of the active medium. Currently, gas, solid-state and semiconductor lasers are used for material processing and more recently fiber lasers are emerging. The gas lasers can be further subdivided into neutral atom lasers, ion lasers, molecular lasers and excimer lasers. The typical lasers that are commercially available for material processing are: (i) gas lasers; (ii) solid state laser – lamp pumped and diode pumped; (iii) semiconductor lasers; (iv) fiber lasers. Wavelengths of presently available industrial lasers cover the entire spectral range from infrared to ultraviolet as shown in Figure 6.2 [LEO 03].

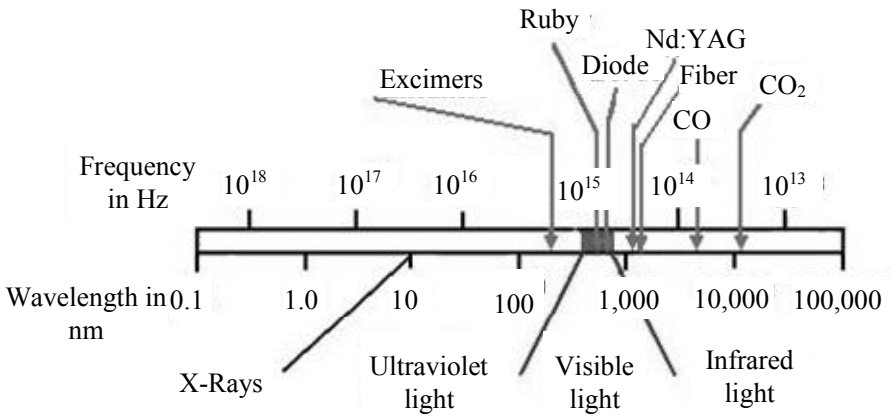

Figure 6.2. *Lasers in the electromagnetic spectrum*

6.4.1. *Gas laser*

The earliest industrial lasers were gas lasers. Gas lasers use high-voltage, low-current power sources to supply the energy required to excite the gas mixture used as a lasing medium. These lasers can operate in both continuous and pulsed mode, and the wavelength of the CO_2 laser beam is 10.6 μm. At this wavelength the fiber optic cable absorbs the laser beam and damages itself, so a rigid lens and mirror delivery system is used. At present, power outputs for gas lasers can be much higher than solid-state lasers, reaching 40 kW. Two types of gas lasers are available: (i) the transverse flow laser; and (ii) the axial flow laser. The laser generated from a CO_2 laser source cannot be transferred via a fiber optic cable (FOC), hence welding has to be done near the laser source itself.

6.4.2. *Solid state laser*

The Nd:YAG laser is a standard solid-state laser source used for industrial precision welding and drilling. Contour cutting is also done with Nd:YAG lasers, because the light from Nd:YAG lasers can be sent through a FOC, and it is easy to integrate into production systems. Nd:YAG lasers may be operated in either pulsed or continuous wave (CW) temporal modes. Pulsed Nd:YAGs have flash lamps, while CW-Nd:YAG lasers use continuous arc lamps. The pumping is accomplished by optical excitation. In a lamp-pumped solid state laser, the lamp and laser rod are positioned side-by-side, inside a reflecting structure that allows a large fraction of the pumping light to reach the laser rod. A significant improvement in the efficiency

and optical performance of Nd:YAG lasers may be affected by pumping with diode lasers rather than lamps. The advantage of using diode pumping is that it reduces the effect of thermal gradients in the laser medium.

6.4.3. *Diode laser*

A diode laser is a laser where the active medium is a semiconductor similar to that found in a light-emitting diode. The most common and practical type of laser diode is formed from a p-n junction and powered by an injected electrical current. A laser diode, like many other semiconductor devices, is formed by doping a very thin layer on the surface of a crystal wafer. The crystal is doped to produce an n-type region and a p-type region, one above the other, resulting in a p-n junction, or diode.

6.4.4. *Fiber lasers*

In recent years fiber lasers have become a possible viable alternative to semiconductor and gas lasers. In a fiber laser the active gain medium is an optical fiber doped with rare-earth elements, such as erbium, ytterbium, neodymium, dysprosium, praseodymium, and thulium. They are related to doped fiber amplifiers, which provide light amplification without lasing. A fiber laser generates the beam inside the fiber, so the delivery of the beam does not require any complicated or sensitive optics. This makes it very suitable and easy to use. The beam is generated and confined inside the small core of the fiber. High power fiber lasers are used for welding, metal cutting and engraving; while low power lasers are used for measurement and data transfer. The commercially available industrial lasers types are: ruby, Nd-glass, Diode, He-Ne, CO_2, Nd:YAG, argon ion, dye, copper and excimer [BAL 05].

6.5. Material considerations

When the laser beam strikes the surface, part of the energy is absorbed and part is reflected. The energy that is absorbed by the surface gets heated up. The absorption of laser irradiation is dependent on many factors like interaction time and the surface property. If the material has a higher reflectivity, then the energy absorption will be minimal. Material with a high thermal diffusivity conducts heat energy faster leading to a greater depth of welding. Melting a material with laser radiation depends on the heat transfer in the material. The heat transfer depends upon the thermal conductivity, density and thermal diffusivity of the material. A high thermal conductivity of the material leads to larger penetration. Based on the material the operating process condition has to be selected. The major problem

based on a material with laser welding is poor absorption of the laser radiation, porosity formation, heat affected zone embrittlement and crack sensitivity.

The difficulty of welding aluminum alloys is due to its highly reflective nature, also the selection of high power will lead to a drop-out as a result of excess fluidity. During the welding of heat resistant alloys like Inconel 718 and Hastelloy, the weld is more brittle and results in cracking and segregation. Laser welding is better suited for titanium alloys due to less grain growth compared to slow processes. The iridium alloy, similar to a heat resistant alloy, has the problem of hot cracking [STE 03]. Welding dissimilar materials is receiving much attention due to the great demand for high quality and high performance industrial products. Joining dissimilar metals is very difficult, especially when the thermal conductivity of each is substantially different (e.g. copper and steel), since this affects the absorption of laser light. The welding of copper is difficult due to its high thermal diffusivity, which transfers away the absorbed energy from the fusion and to be wasted. Laser welding generally produces excellent properties due to rapid cooling which produces a fine structure.

The laser welding of plastics has been actively investigated with the development of diode lasers. Under defocused conditions the plastics are readily joined using low power diode, YAG and fiber lasers. AISI 304 stainless steel is selected as the material for the experimental analysis. It has the following properties; high ductility, excellent drawing, forming and spinning properties. Essentially it is non-magnetic but it becomes slightly magnetic when cold worked. Austenitic stainless steels have a high ductility, low yield stress and relatively high ultimate tensile strength, when compared to typical carbon steel. Austenitic stainless steels weld easily. They are single phase ductile materials. Austenitic stainless steels are good candidates for laser welding if their sulfur and phosphor contents are kept low.

During the welding of stainless steel, prolonged periods of exposure at high temperatures may lead to chromium precipitation on grain boundaries and thus the reduction of corrosion resistance. Specific laser beam welding features, such as high welding speed, small heat-affected zone, and low material exposure at elevated temperatures are beneficial for the welding of stainless steel. AISI 304 stainless steel has excellent forming characteristics. It can be deep drawn without intermediate heat softening – a characteristic that has made this grade dominant in the manufacture of drawn stainless parts, such as sinks and saucepans. Austenitic stainless steels are used in a wide range of applications, including structural support and containment, architectural uses, kitchen equipment and medical products. They are widely used not only because of their corrosion resistance but because they are readily formable, fabricable and durable. The AISI 304 stainless steel is selected as the research work material due to its wide application in industries, especially the automotive industry.

6.6. Applications of laser welding

Laser welding has shown many advantages over traditional welding methods in various applications and is currently used in many industries:

– aerospace;

– automobile;

– bi-medical devices;

– textiles;

– thin metal fabrication;

– food and medical packaging;

– electronics;

– windows and signs;

– visual displays.

Laser welding is a proven joining method for a variety of today's metals, alloys and composites. Diode lasers are used in laser printers, CD and DVD players, lecture pointers, bar-code reading, laser surgery, industrial machining and as directed energy weapons.

As laser welding is a high energy density process, the heating is localized [REA 97], thus the following characteristics are obtained:

– The heat-affected zone is very small, which is beneficial for welding heat-sensitive parts.

– The total heat input is low, which is an important factor for applications like the welding of electronic packages, or when low distortion of the part is desired.

– Due to high energy density, welding rates are high, resulting in economic benefits.

– As the process is a non-contact type there is no possibility of contamination.

– Laser welding can be performed in the atmosphere, without the need for a vacuum as in electron beam welding.

– The welding head connected to the robot is useful for welding complicated design parts.

6.7. Strengths and limitations of laser welding

Laser beam welding offers, amongst others, the following advantages:

– deep and narrow penetration;

– precision welding;

– low and precise heat input;

– small fusion zone volume;

– possibility of joining dissimilar materials;

– narrow heat affected zones;

– low residual stress;

– low weld distortion and limited deformations;

– automated welding;

– high welding speed;

– reduced tendency to spiking, under-bead spatter, incomplete fusion and root bead porosity;

– fixturing is easy and fast;

– very localized heating;

– post-weld treatment is normally not required;

– no vacuum is required.

Today, the automobile and aerospace industries rely on lasers for a clean and non-contact source for joining thin section sheets [MAJ 03].

There are some limitations to laser welding:

– Highly reflective materials cannot be easily welded e.g. aluminum.

– Due to high power density vaporization of volatile alloys is possible.

– The initial cost of the laser source is high.

– The depth of penetration in laser welding is low, except for multi-kiloWatt lasers.

– Safety consideration is important especially working with Nd:YAG lasers.

– Special training is required for machine operators.

– The laser system lacks mobility.

– The flexibility of a welding system to weld different parts and geometries is limited.

– Close fitting and well clamped joints are required.

6.8. Developments and advances in laser welding processes

So far CO_2 and Nd:YAG lasers are frequently used in industry. Recently fiber lasers have penetrated industry. Fiber lasers have good beam quality and are now identified as being highly efficient, bright and high-power lasers. The advantage of a fiber laser is that, the beam transmitted from the fiber, is usually of very high quality and can be focused to a small spot size. It can either be continuous or repetitively pulsed. Due to its exceptional fine focusing power a lot of applications are possible. The other advancement of laser welding is hybrid welding, where a laser and an assisted arc are used. The energy input is given from a laser source, as well as from the gas metal arc torch, a gas tungsten arc torch or a plasma arc torch. The advantage of this combined process is that gap tolerances are relaxed and the addition of a filler metal is possible and provides a method of controlling the metallurgy of the weld metal. Laser welding of plastics using a diode, YAG and fiber lasers of low power under defocused conditions has been actively investigated with the evolution of diode lasers all over the world.

High power lasers for welding are now rapidly developing using a pumping system and fiber coupling. Yb:YAG disk lasers are relatively new and are expected to have higher power, higher efficiency and higher intensity (brightness) in the near future. Laser diode-pumped YAG lasers are capable of delivering brighter and higher-quality beams at higher efficiencies than lamp-pumped YAG lasers. Rod-type lasers, diode-pumped Nd:YAG lasers, slab-type lasers and diode-pumped Nd:YAG lasers have been developed. High power laser diodes or diode lasers that can also be used directly in fiber-coupled mode, are commercially available. A YAG laser can be oscillated in the mode of a continuous wave (CW), normal or modulated pulsed wave (PW) or Q-switching. A second harmonic Nd:YAG laser with a several millisecond time period has recently been developed to melt a copper sheet easily. In recent years, many manufacturers have developed laser welding systems utilizing galvanometric scanners.

Welding with preheating is also nowadays being carried out to produce the required metallurgical properties of the welded parts and to avoid cracking. To increase the laser beam welding capability multiple beam welding is being practiced by using two laser beams together. Laser diode-pumped solid-state lasers, such as

disk and fiber lasers, are being investigated for higher power, better beam quality, more efficiency and fiber delivery [NAS 05]. They are also expected to work as heat sources in place of CO_2 lasers for remote/scanner laser welding because they are more amenable to robotic and fiber delivery. These types of lasers also have the advantage of easier operation, higher productivity and cost reduction. Lots of research work is going on worldwide in the development and improvement of laser sources and in material processing.

6.9. Modeling and analysis of the laser welding process

Analysis of the process is essential to identify the influence of its parameters and to control it to obtain the desired response. The modeling and analysis of process parameters can be achieved using artificial intelligence, statistical analysis and by the finite element method (FEM). Accurate reduction of temperature distribution during experimentation in the molten pool zone is very difficult, as is the prediction of residual stresses; these can be done using the FEM. To determine the fluid flow pattern, pressure and velocity distribution of a fluid, the computation of a fluid flow analysis can be performed. The laser welding process is analyzed based on mathematical modeling, ANN and using the FEM.

6.9.1. *Design of experiments*

Experiments are conducted to study the performance of processes and systems. To understand a process, series of experimental trials have to be conducted and then an analysis is done. Performing experiments randomly and analyzing the process will lead to more cost, time and man power and the resulting outcome will not achieve the target. In order to minimize the experiment and to properly analyze the process parameters, the design of the experiments is essential.

Design of the experiment (DOE) is a planned method for determining the relationship between input factors (Xs) affecting a process and output of that process i.e. responses (Ys). DOE involves designing a set of experiments, in which all the relevant factors are varied systematically [MON 08]. When the results of these experiments are analyzed, they help to identify the optimal conditions, the factors that have the most influence on the responses and those that do not have any effect on the responses, as well as details such as the existence of interactions and effects between the factors. The experimental design is an important tool in the engineering world for improving the performance of a manufacturing process. It also has extensive applications in the development of new processes. DOE is an efficient statistical procedure for planning a series of experiments, such that the obtained data

can be analyzed to yield valid and objective conclusions. It can be used to screen a set of variables to identify those with the most effect, design a series of experiments to investigate the influence and effect of different parameters, optimize an experimental process or retrospectively analyze a set of experimental data.

In the last two decades, the use of DOE has grown at a rapid pace and has been adapted for many applications in different areas. The advantage of conducting experiments based on factorial design is that the factors are varied together instead of one factor at a time. There are many experimental designs available: the factorial design, fractional factorial design, Taguchi technique and response surface methodology. The choice of an experimental design depends on the objectives of the experiment and the number of factors to be investigated.

Response surface methodology (RSM) is one of the most popular DOE methods for deciding the number of experimental trials and the range of parameters. It can also be used to optimize the welding process parameters which provide the best responses of interest. RSM is a collection of statistical and mathematical methods which are useful for modeling and analyzing engineering problems. It quantifies the relationship between the controllable input parameters and the obtained response surfaces. Mathematical or statistical modeling is used to predict the responses and to check the adequacy of the model using the analysis of variance.

6.9.2. *Box–Behnken design*

The Box–Behnken design (BBD), coming under RSM, was devised by George E.P. Box and Donald Behnken in 1960. It is an independent quadratic design, which does not contain fractional factorial design and the parameter combinations are at the midpoints of the process space edges and at the center. These designs are rotatable and require 3 levels of each factor coded, such as -1, 0 and +1. BBD is a rotatable second-order design based on three-level factorial designs. The special arrangement of the BBD levels allows the number of design points to increase at the same rate as the number of polynomial coefficients. BBD requires an experiment number according to the equation:

$$N = k^2 + k + c_p \qquad [6.1]$$

where k is the factor number and c_p is the replicated number of the central point. Viewed as a cube, the BBD consists of a central point and the middle points of the edges, as shown in Figure 6.3.

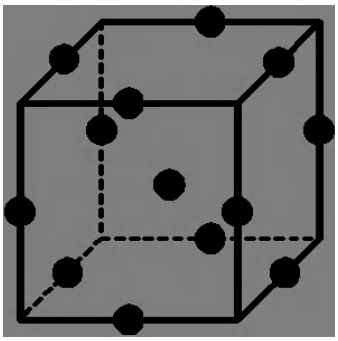

Figure 6.3. *Box–Behnken design for three factors*

For the three-level three-factorial Box–Behnken experimental design, a total of 15 experimental runs are required: one central point, 12 points corresponding to the midpoints of 12 edges and 2 replicates of the central point. In the present analysis 15 butt joint experimental trials are conducted and are then analyzed.

6.9.3. *Artificial neural network*

In the fabrication industries, intelligent material processing requires a precise and consistent output in order to meet the quality standards. Artificial neural networks (ANNs) are computational models, which replicate the functions of a biological network, composed of neurons, and are used to solve complex functions in various applications [YAG 99]. ANN is a new type of computer system, which is based on the primary understanding of the organization, structure, function and mechanisms of the human brain. It is a powerful data modeling tool, which is able to capture and represent complex input/output relationships. In the field of biology, electronics, computer science, mathematics and engineering, ANN is one of the most important research areas. The ANN system consists of three layers, which are input, hidden and output layers. The input layer contains all the input factors. Information from the input layer is processed in the hidden layers, and then the results are sent to the output layer [ABD 08].

The most common type of ANNs that have been used in the literature are feed forward ANNs trained with a backpropagation algorithm [CHA 01, KIM 05, KAN 08]. ANNs are capable of learning patterns by training with a number of known patterns. As in nature, the network function is largely determined by the connections between the elements. Figure 6.4 illustrates how the information is processed through a single node. The node receives weighted activation from other nodes through its incoming connections. First, these are added (summation

function), the result is then passed through an activation function, the outcome being the activation of the node. For each of the outgoing connections, this activation value is multiplied by the specific weight and transferred to the next node. A neural network consists of three main components, namely weights, bias and an activation function. Each neuron receives inputs x_i, $x_{j, \ldots}$ x_n, attached with a weight w_i, which shows the connection strength for that input for each connection. Each input is multiplied by the corresponding weight of the neuron connection. A bias b_i, that can be defined as a type of connection weight with a constant non-zero value added to the summation of weighted inputs ($x_j w_{ij}$), forms the input u_i to the transfer function. The summation of the input weighted function and bias is given as "u_i"

$$u_i = \sum_{j=1}^{N} w_{ij} x_j + b_i \qquad [6.2]$$

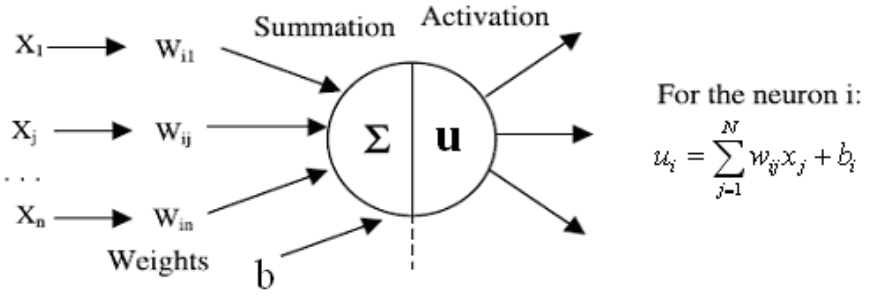

Figure 6.4. *Information processing in an artificial neural network*

Using a generalized least mean square (LMS) algorithm, the backpropagation network (BPN) algorithm minimizes the mean square difference between the real and the desired output. The error function of the BPN algorithm is the average of the square difference between the output of each neuron in the output layer and the desired output [KIM 05]. In the present study, the welding parameters are mapped to the weld dimensions through the internal representation of BPNs. Data obtained (input parameter and output parameter) from the experiments is provided to the network for learning. The algorithm progresses iteratively through a number of epochs. On each epoch, the target and actual outputs are compared and the error is calculated. The error is then propagated backwards through the network and the weights are changed based on the learning algorithm.

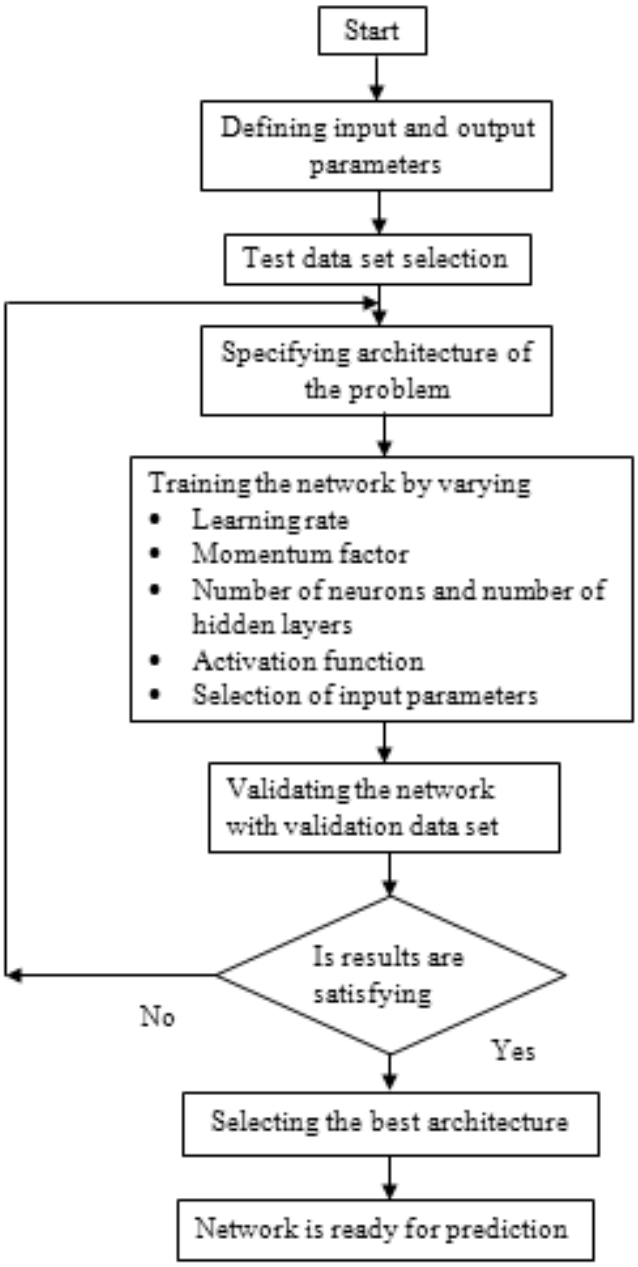

Figure 6.5. *Flow chart depicting the modeling procedure*

This learning process is an iterative process, and learning will stop once an acceptable error is achieved or the set goal is reached, whichever is earlier. When the trained network is presented with a new input (data not used for training), the network responds according to the knowledge it has gained. The application of the ANN for the laser welding process is limited, as the process is expensive and the amount of data required for modeling must be large for better accuracy. The high cost of the material and the process and relatively small batch size production does not allow for the determination of optimum laser parameters by a trial-and-error method for each application. Hence, the ANN is useful for creating a model for welding using the combination of input and output parameters with minimum possible trials. Figure 6.5 represent the steps of neural network modeling of the welding process.

6.9.4. *Finite element analysis*

The finite element analysis of the welding process has been a major topic in welding research for several years, simulating the whole process. The FEM is an efficient and powerful tool for numerically solving mathematical problems. The results of simulations can be used to explain the physical essence of some complex phenomena in the welding process. The simulation of the laser welding process enables the estimation of the weld bead geometry, temperature distribution, transient stresses, residual stresses and distortions. These can be used to evaluate structural misalignments and unexpected failures due to overstressing caused by the superposition of in-service loads and welding induced residual stresses. However, the simulation of the welding process involves the interaction of thermal, mechanical and metallurgical phenomena. It is difficult to measure the temperature of the weldment, especially during the welding process. Many laser welding trials need to be conducted to arrive at the desired process parameters, for given material combinations in the absence of suitable mathematical modeling and analysis.

During laser welding, complicated phenomena such as temperature dependency of the material properties during phase transition (i.e. melting and evaporation) and laser light absorption and reflection in plasma occur in a very short period. Since the laser welding process is characterized by a highly collimated and concentrated beam of energy vaporizing the base metal, it is difficult to provide accurate measurements near the molten zone. Hence FE thermal simulation seems to be more comprehensive. A number of analytical and numerical models of the welding processes have been used by various researchers to evaluate temperature and stress distribution during the welding process and predict the residual stresses and final distortions of structural components. These include analytical models, 2D finite element models and 3D finite element models of laser welding [BAL 08].

It is difficult to measure the temperature of the weldment, especially during the welding process. Many laser welding trials need to be conducted to obtain the desired process parameters, for a given material combination in the absence of suitable mathematical modeling and analysis. The FE simulation is used to predict the temperature distribution in and around the molten zone and the weld bead geometry.

6.10. A case study

In order to exemplify the application of statistical methods, neural networks and the FEM in modeling and the simulation of the welding process, the following case study is presented. In this study, the effect of influencing process parameters (beam power, welding speed and beam angle) on the response (depth of penetration and bead width) is analyzed and modeled to predict the response. These models are used to obtain the response for the given set of input variables.

6.10.1. *Experimental setup*

To conduct the experimental trials a solid-state Nd:YAG laser machine is used. The source is a 2,000 W CW-Nd:YAG laser system interfaced with the CNC controller. Special arrangements are made for the supply of argon inert gas at the interaction zone. The laser head is fixed with fibre optic cable coupling, which can be tilted to the desired angle. The work table can be moved in the X-Y directions under the CNC controller. The source interaction with the base material and the closing of the laser source is controlled by the software. Figure 6.6 shows the schematic sketch of a Nd: YAG laser source.

The size of the sheets taken for butt joint welding trials are 60 mm long × 20 mm wide × 1.6 mm thick. The materials are completely cleaned prior to welding. Argon gas is used as a shielding medium with a constant flow rate of 5 l/min to avoid surface contamination. The faying edges of the sheets are machined to have close fit-up during welding. Before performing trials, it is ensured that the gap is less than half of the laser beam diameter. The focused laser beam is aligned with the center of the specimen to avoid any misalignment; otherwise one side of the material will completely melt while the other side remains partially melted. As the sheet thickness for the experimental trials is 1.6 mm, the process parameters are selected accordingly. The weld bead dimensions for all the specimen coupons are obtained using longitudinal metallographic sections of the welds digitally imaged using an image inspection system.

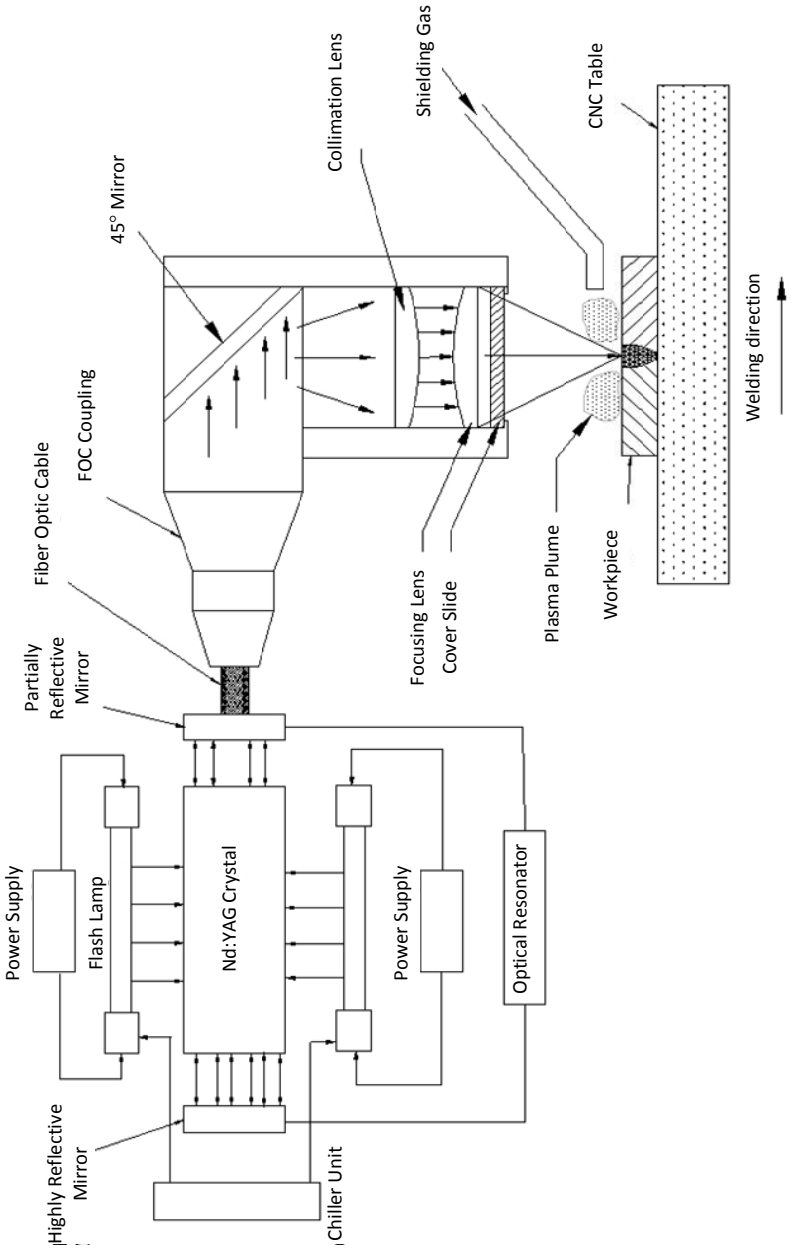

Figure 6.6. *Schematic sketch of a Nd:YAG laser source*

The butt joint experiment variables and levels used for experimental trials are given in Table 6.1.

Variables	-1	0	+1
Beam Power (BP), (Watts)	750	1,000	1,250
Welding speed (WS), (mm/min)	750	1,000	1,250
Beam angle (BA), (degrees)	85	90	95

Table 6.1. *The independent process variables and experimental design levels used*

Figure 6.7 shows the photo macrograph of a specimen welded by a laser operating under the following parameters: laser power 1,250 Watts, beam angle 90^{o} and welding speed 750 mm/min on a stainless steel substrate showing a deep penetration welding (keyhole) mode.

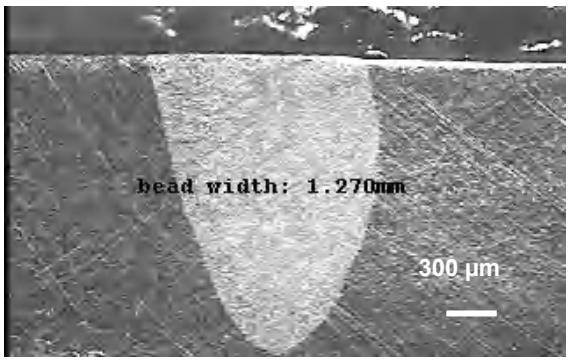

Figure 6.7. *Macrograph of butt joint bead profile*

6.10.2. *Mathematical modeling of butt joint*

The modeling of a butt joint based on a BBD is performed as detailed below:

– Designing a series of experiments for the adequate and reliable measurement of the response of interest.

– Developing a mathematical model of the second order response surface with the best fit.

– Finding the optimal set of experimental parameters that produce a maximum or minimum response value.

– Representing the direct and interactive effects of process parameters through 2D and 3D plots.

The mathematical modeling of a butt joint is performed using all 15 trial data and the effect of each factor on the weld bead geometry is determined. The computer programs for supporting the experimental design and performing the analysis of variance are carried out using Design-Expert V7.

The general form of the second order RSM model is given below [MON 08]:

$$y = \beta_0 + \beta_1 x_1 + \beta_2 x_2 + \beta_3 x_3 + \beta_{11} x_1^2 + \beta_{22} x_2^2 + \beta_{33} x_3^2 + \beta_{12} x_1 x_2 + \beta_{13} x_1 x_3 + \beta_{23} x_2 x_3 \quad [6.3]$$

Where y is the predicted response, β_0 is the model constant; x_1, x_2 and x_3 are independent variables; β_1, β_2 and β_3 are linear coefficients; β_{12}, β_{13} and β_{23} are cross-product coefficients and β_{11}, β_{22} and β_{33} are the quadratic coefficients. All the coefficients mentioned above are estimated using Design-Expert V7 software from the experimental results. A three-factor three-coded level BBD is used to determine the response. The mathematical models in actual form obtained from the above analysis are given below to predict the responses, namely depth of penetration and bead width. To determine the responses (DOP and BW), the input parameters (BP, WS and BA) need to be substituted, in the actual form, in the corresponding equations. The mathematical model in coded and in actual factors is given below.

Final equation in terms of coded factors

DOP = 0.70 + 0.24 * A -0.075 * B + 0.019 * C-0.072* A*B -5.000E-003 * A * C+2.500E-003* B * C -0.052 * A^2+0.085 * B^2-0.048 * C^2 [6.4]

BW = +0.99 +0.23 * A -0.079 * B +1.000E-002 * C -0.050 * A * B +7.500E-003 *A* C+2.500E-003 * B * C -0.051 * A^2 +0.074 * B^2 -0.038 * C^2 [6.5]

Final equation in terms of actual factors

DOP = -16.49750+4.14500E-003 * BP-2.04000E-003 * WS +0.34775 * BA-1.16000E-006*BP*WS -4.00000E-006*BP*BA+2.00000E-006* WS * BA -8.40000E-007*BP^2+1.36000E-006*WS^2-1.90000E-003*BA^2 [6.6]

BW =-11.94000 +2.82167E-003* BP -2.06833E-003 * WS +0.27000 * BA -8.00000E-007*BP*WS +6.00000E-006 * BP * BA +2.00000E-006 * WS * BA -8.13333E-007*BP^2+1.18667E-006*WS^2-1.53333E-003*BA^2 [6.7]

The test for the significance of the regression models, individual model coefficients and the lack-of-fit test are performed using the statistical package

Design Expert V 7. Table 6.2 summarizes the analysis of variance of the quadratic model, and other model terms for the depth of penetration. The same table also shows the other adequacy measures R^2, adjusted R^2 and predicted R^2. The entire adequacy measures are close to 1, which is in reasonable agreement and indicates adequate models. The adequate precision ratio above 4 indicates adequate model discrimination [DES 08]. The model terms are significant, if the probability value (p-value) is less than 0.05 [LEE 00].

Source	Sum of squares	dof	Mean square	F-Value	p-value	Comments
Model	0.56	9	0.063	192.95	< 0.0001	significant
A-BP	0.45	1	0.45	1373.88	< 0.0001	
B-WS	0.045	1	0.045	138.46	< 0.0001	
C-BA	2.81E-03	1	2.81E-03	8.65	0.0322	
AB	0.021	1	0.021	64.69	0.0005	
AC	1.00E-04	1	1.00E-04	0.31	0.603	
BC	2.50E-05	1	2.50E-05	0.077	0.7926	
A^2	0.01	1	0.01	31.31	0.0025	
B^2	0.027	1	0.027	82.08	0.0003	
C^2	8.33E-03	1	8.33E-03	25.63	0.0039	
Residual	1.63E-03	5	3.25E-04			
Lack of Fit	1.18E-03	3	3.92E-04	1.74	0.3851	not significant
Pure Error	4.50E-04	2	2.25E-04			
Cor Total	0.57	14				

$R^2 = 0.9971$, Adj.$R^2 = 0.992$, Pred.$R^2 = 0.965$, Adeq.precision = 52.736.

Table 6.2. *ANOVA table for depth of penetration*

The output shows that the model is significant with a probability value (p-value) 0.0001; hence the model is significant as it is less than 0.05. The probability value

for no-lack-of-fit is 0.3851, which is larger than the reference limit P of 0.05; since larger values of R^2 are more desirable [MON 08]. The Model F-value of 192.95 implies that the model is significant. Adequate precision measures the signal-to-noise ratio. If the adequate precision ratio is greater than 4 then it is desirable. Here the ratio is 52.736, which indicates an adequate signal. It is observed that the effect of the beam angle and the factor associated with the beam angle has the least significance on the responses compared to the other input parameters i.e. beam power and welding speed.

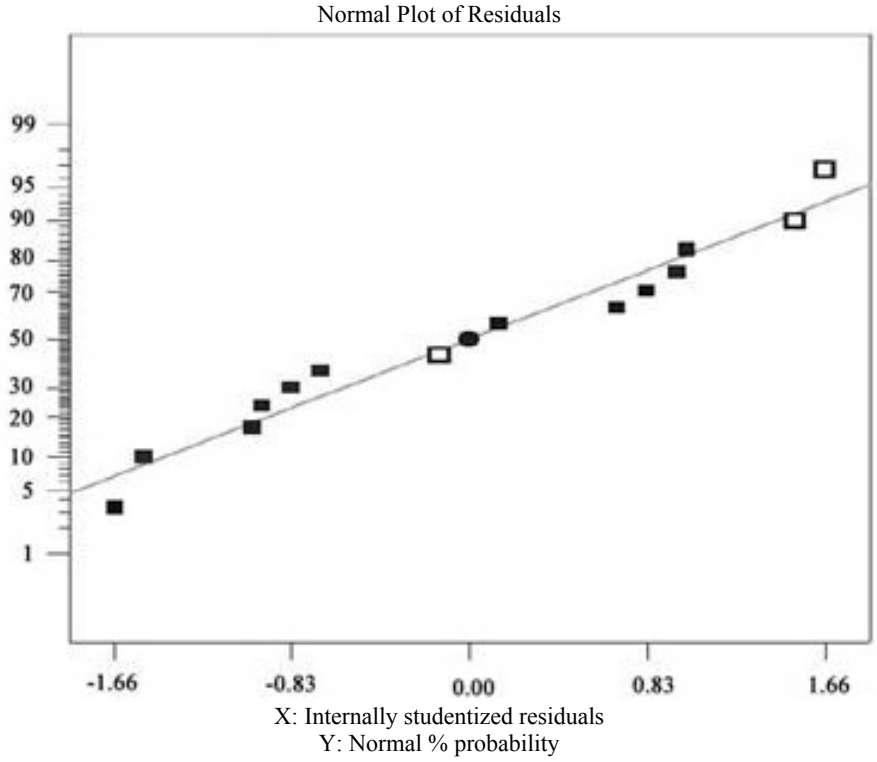

Figure 6.8. *Normal plot of residuals for the depth of penetration*

Figure 6.8 shows the normal plot of residuals for the depth of penetration. The data are very well fitted, lying in the inclined line. Table 6.3 lists the analysis of variance of the quadratic model and other model terms for bead width. The other adequacy measures R^2, adjusted R^2 and predicted R^2 are also given. The adequacy measures are close to 1 for all, which is in reasonable agreement and indicates adequate models. The output shows that the model is significant with the probability value (p-value) 0.0001; hence the model is significant as it is less than 0.05. The

p-value for no-lack-of-fit is 0.3945, which is larger than the reference limit P of 0.05. Hence the model is significant. The Model F-value of 181.36 implies that the model is significant. As stated earlier if the precision ratio is greater than 4 then it is desirable. Here the precision ratio is 48.074, which indicates the adequate signal. It is observed that the effect of the beam angle and the factor associated with the beam angle have the least significance on the responses compared to other input parameters i.e. beam power and welding speed.

Source	Sum of squares	dof	Mean square	F-Value	p-value	Comments
Model	0.54	9	0.06	181.36	< 0.0001	significant
A-BP	0.44	1	0.44	1331.31	< 0.0001	
B-WS	0.05	1	0.05	151.1	< 0.0001	
C-BA	8.00E-04	1	8.00E-04	2.44	0.1793	
AB	1.00E-02	1	1.00E-02	30.46	0.0027	
AC	2.25E-04	1	2.25E-04	0.69	0.4455	
BC	2.50E-05	1	2.50E-05	0.076	0.7936	
A2	9.54E-03	1	9.54E-03	29.06	0.003	
B2	0.02	1	0.02	61.86	0.0005	
C2	5.43E-03	1	5.43E-03	16.52	0.0097	
Residual	1.64E-03	5	3.28E-04			
Lack of Fit	1.18E-03	3	3.92E-04	1.68	0.3945	not significant
Pure Error	4.67E-04	2	2.33E-04			
Cor Total	0.54	14				

$R^2 = 0.9969$, Adj.$R^2 = 0.9914$, Pred.$R^2 = 0.9631$, Adeq.precision = 48.074.

Table 6.3. *ANOVA table for bead width*

6.10.3. *Process parameters interaction effect on the butt joint profile*

The influence of two input parameters on the responses, while the third parameter is kept constant is analyzed and plotted as a surface plot. Figure 6.9 shows the interaction effect of BP and WS on the DOP. As the laser beam incident energy increases, the DOP also increases which is due to the increase of peak power and heat conduction. A maximum DOP is obtained when the BP is at a maximum and the WS is at a minimum. The reason is as the BP increases the amount of heat input increases leading to more melting of metal, resulting in more DOP. As the WS increases the DOP decreases, due to the metal being exposed to the heat source for a shorter time. To obtain more DOP, the laser has to be operated at a high beam power and low welding speed [BAL 09].

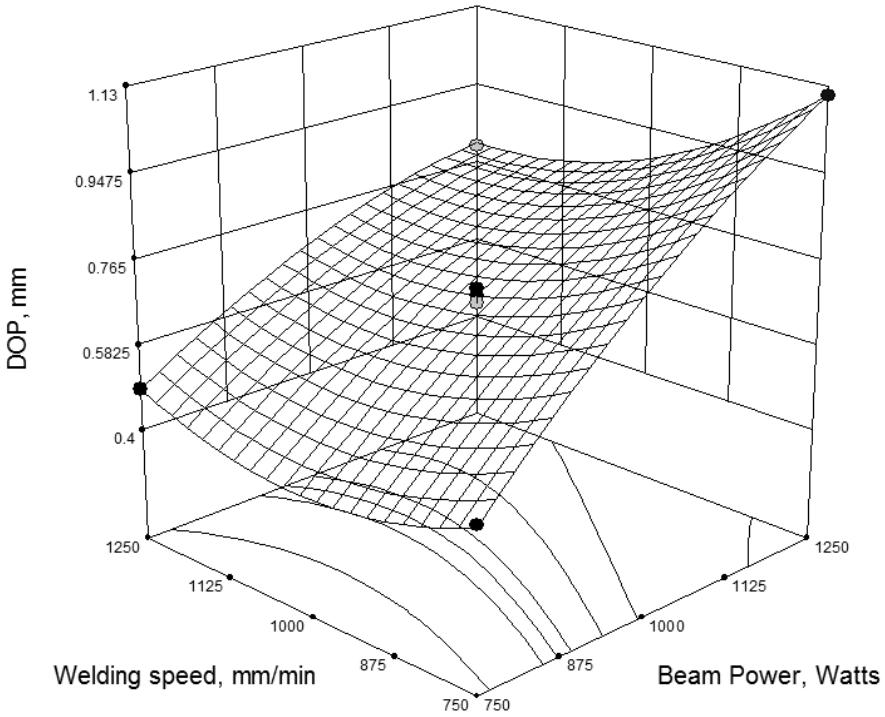

Figure 6.9. *Response surface showing the effect of beam power and welding speed on the depth of penetration*

The interaction effect of beam power and welding speed on the bead width is shown in Figure 6.10. At high beam power and low welding speed the bead width is greater, due to an increase in the heat input and a longer interaction time. At high

welding speeds and low beam powers the bead width is lower due to the high traveling speed of the laser beam over the welding line and less heat input. So to obtain the minimum bead width, the welding has to be performed at a high welding speed. At high beam power and low welding speed the bead width is greater due to the increase in heat input and longer interaction time. At high welding speeds and low beam powers the bead width is less. The welding speed always has an inversely proportional relationship with the heat input. An increase in the welding speed leads to a decrease in the heat input. The role of the welding speed is significant compared to the beam angle on the depth of penetration. At a low welding speed the depth of penetration is greater and at a high welding speed the depth of penetration is less. The maximum depth of penetration is obtained for a 90º beam angle position. It is observed that the beam angle has the least amount of influence on the depth of penetration and the bead width.

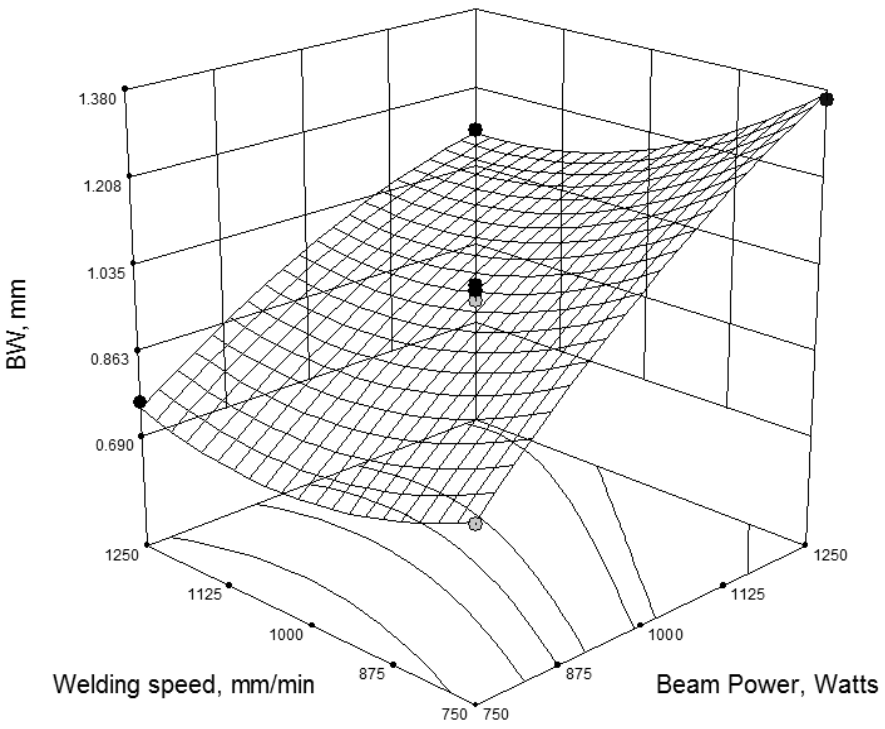

Figure 6.10. *Response surface plot showing the effect of beam power and welding speed on the bead width*

The response surface of Figure 6.11 shows the interaction effect of the welding speed and beam angle on the bead width. At a 90º beam angle the bead width is less, but it is greater for 85º and 95º beam angle positions. When the welding speed is high the bead width is less and when the welding speed is low the bead width is greater. The interaction effect of the beam angle and WS on the bead width infers that to obtain less bead width welding has to be done at a beam angle of 90º and with a high welding speed. An increase in the welding speed leads to a decrease in the bead width. This is due to the high traveling speed of the laser beam over the welding line when the welding speed is increased. Therefore the heat input decreases leading to a lower volume of the base metal being melted, consequently the width of the welded zone decreases. Between the welding speed and the beam angle, the welding speed is the major parameter influencing bead width compared to beam angle.

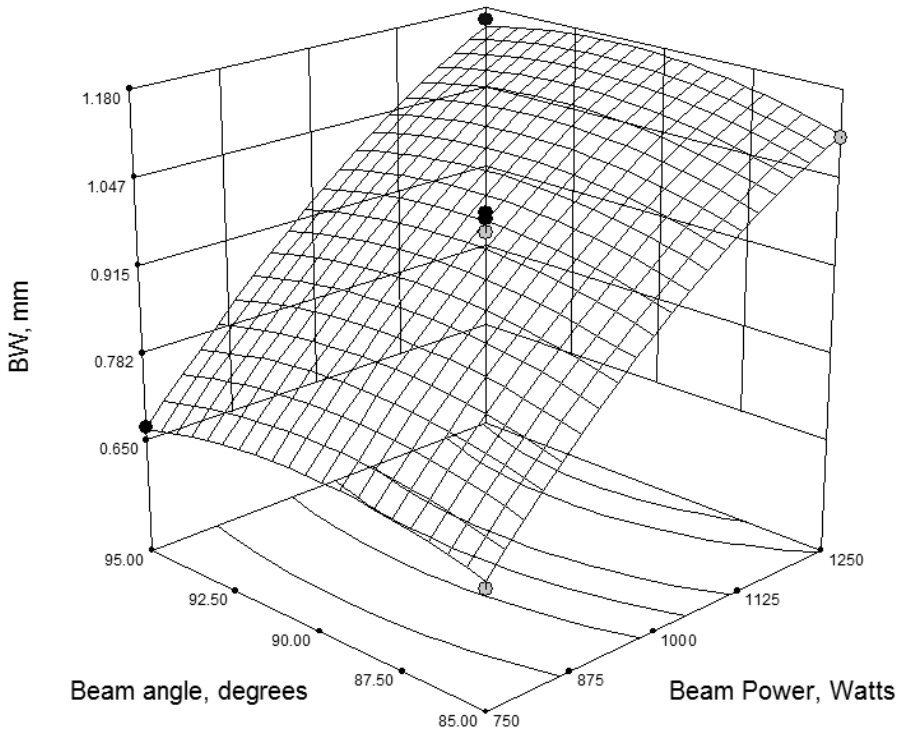

Figure 6.11. *Response surface showing the effect of the welding speed and beam angle on the bead width*

Based on the direct and interaction effects it is observed that beam power is the major parameter influencing the depth of penetration and bead width followed by the welding speed and the beam angle has the least effect on the responses.

6.10.4. *ANN modeling*

The performance of a neural network model mainly depends on the network architecture and parameter settings. The ANN modeling is carried out in two steps: The first step is to train the network with training sets and the second step is to test the network with the data not used for training.

6.10.4.1. *Training a neural network*

A training set is a group of matched input and output patterns. Neural network training is initiated by selecting the number of neurons, number of hidden layers, momentum correction factor, learning rate and activation function [MAT 01]. It is important that all the information the network is required to learn is supplied to the network as a data set. When each pattern is read, the network uses the input data to produce an output, which is then compared to the training pattern, i.e. the correct or desired output. If there is a difference, the connection weights are often altered in such a way that the error is decreased. ANN runs through all the input patterns repeatedly until all the errors are within the required tolerance. The learning process automatically adjusts the weights. The data collected from the butt joint welding trials are used for training the network.

The following are the optimized parameter values set in the MATLAB® program to build the ANN model, which is obtained by conducting several trial combinations:

– learning rate: 0.05;

– learning rate decrement (lr-dec): 0.5;

– learning rate increment (lr-inc): 1.05;

– maximum performance increase (max perf inc): 1.04;

– performance goal: 0.0001.

Network learning is performed until an iteration number of 90,000 times and an error of 0.001, whichever is reached first. The number of hidden layers and the number of neurons in it are determined through a trial-and-error method, in order to accommodate the converged error. Since there are 3 input data, the error of each variable has an error rate of 0.0003.

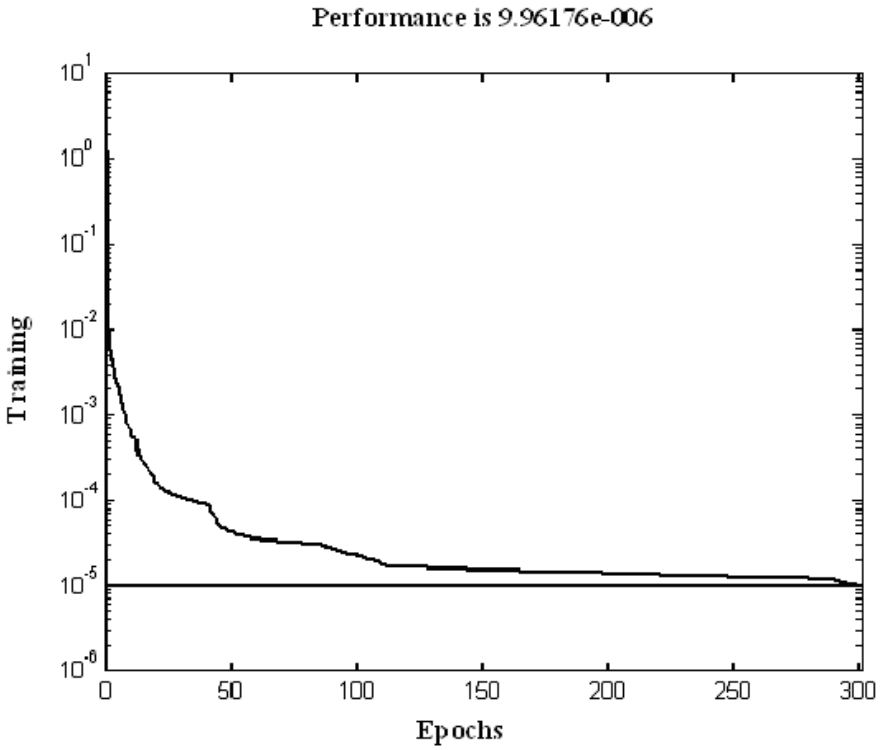

Figure 6.12. *Training result for one hidden layer with four neurons*

The connection weights are increased or decreased as the network training progresses and finally the neural network settles down to a stable cluster of mutually excitatory nodes. In this application 3–12 neurons in the hidden layers are employed. The computations are performed using the NN toolbox of MATLAB®. In order to calculate the DOP and BW, mathematical formulations are derived from the resulting weights and the activation functions used in the ANN. The input layer consists of three neurons (BP, WS and BA) and the output layer consists of two neurons (DOP and BW). Many network combinations are carried out for the analysis. Figure 6.12 shows the decrease of the mean square error (MSE) during the training process of the network with one hidden layer and four neurons in it. The number of neurons (N) in the hidden layer and number of hidden layers (H) are changed to arrive at an optimum neural network for the prediction of laser weld bead geometry of the butt joint. 15 trial data sets are used for training the neural network.

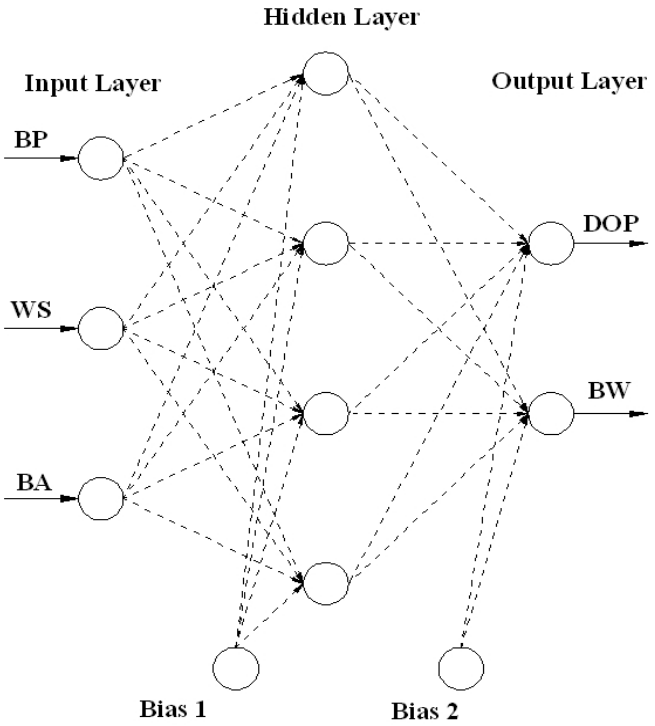

Figure 6.13. *The ANN architecture for a butt joint, one hidden with four neurons*

Figure 6.13 shows the ANN architecture of the final ANN model selected among the nine combinations of networks (1HX3N, 1HX4N, 1HX5N, 2HX3N, 2HX4N, 2HX5N, 3HX3N, 3HX4N, 3HX5N) tested for the analysis. This network reached the best performance goal when compared with other networks. This particular network also gave accurate results for test data compared to other networks. Hence the network (1HX4N), one hidden layer with four neurons is taken up for the butt joint profile prediction. In this network (1HX4N), a hidden layer with a "log-sigmoid" transfer function, the output layer with the "Purelin" transfer function is used for the prediction of DOP and BW. The log-sigmoid transfer function used in the hidden layer is given in the following equation:

$$F(x) = \frac{1}{1+e^{-x}} \qquad [6.8]$$

where x is the weighted sum of the input.

The general form of the "Purelin" transfer function used for the output layer is given as:

$$F(x) = x \qquad [6.9]$$

During training the weights and biases of the network are iteratively adjusted to minimize the network performance function. The weights in the network are initialized to a random number that is uniformly distributed in a small range of values. The range is typically $[(-\alpha/\sqrt{N_i}),(\alpha/\sqrt{N_i})]$, where N_i is the number of inputs to the ith unit and α ranges from 1 to 3. Thus the range can be different for each unit. During the training of the backpropagation algorithm, a generalized least mean square algorithm is used to minimize the error function, which is given as the mean square difference between the model generated output and the actual output (target output) [KIM 05]. In the present study, the welding parameters are mapped to the weld dimensions through the internal representation of backpropagation.

In order to determine the butt weld bead geometry, the following equations are derived from the neural network. In the following equations E_i and F_i are the weighted sum of the input and log-sigmoid activation function, respectively, for the ith neuron of the hidden layer and their values which are extracted from the network. The coefficients obtained (their weights) from the hidden layer neuron are multiplied by the output of the input layers and the last constant value represents the bias term associated with the hidden layer. The trained network is initially analyzed using the same 15 input data set, and it was found that the network gives good results. The weights obtained from the neural network are extracted and make a mathematical formulation. As four neurons are used in the hidden layer four equations for the hidden layer are obtained. The weights are multiplied with the output of the input layer and pass it to the "log-sigmoid" transfer function. The output of the logistic transfer function is multiplied by the weight of the output layer for the prediction of the DOP and BW. As there are two neurons in the output layer, two equations are obtained (i.e. DOP and BW). The mathematical equations derived from the hidden layer are given below.

$$F_1 = \frac{1}{1+e^{-(\,0.433\ BP - \ 0.51\ WS + 0.0475\ BA - 54.957)}} \qquad [6.10]$$

$$F_2 = \frac{1}{1+e^{-(\,0.0089\ BP + 0.0104\ WS + 0.417\ BA - 56.6956)}} \qquad [6.11]$$

$$F_3 = \frac{1}{1+e^{-(\,-0.0951\,BP+\,0.102\,WS+\,0.5248\,BA\,-53.3565)}} \quad [6.12]$$

$$F_4 = \frac{1}{1+e^{-(\,-0.00734\,BP\,+0.0187\,WS\,\,-1.857\,BA\,+159.8554)}} \quad [6.13]$$

The mathematical equations derived from the output layer for the prediction of the depth of penetration and the bead width are given below.

$$DOP = 0.27638F_1 + 0.39604F_2 - 0.35488\,F_3 + 0.17694\,F_4 + 0.50928 \quad [6.14]$$

$$BW = 0.5159\,F_1 + 0.11431\,F_2 + 0.011524\,F_3 + 0.098922\,F_4 + 0.87104 \quad [6.15]$$

6.10.5. *Finite element analysis*

The FEM was used to predict the weld bead dimension and temperature distribution in and around the weld zone. FE analysis offers flexibility in modeling and provides a full field numerical solution [FRE 99]. FE analysis generally consists of three pre-processing steps, which are followed by problem solving and post processing.

The following are the sub-steps of FE analysis:

– definition of the material properties;

– building the model and meshing;

– initializing the boundary conditions;

– modeling the heat source;

– solving the problem;

– result analysis.

To simulate the finite element thermal process of laser beam welding, a finite element software package SYSWELD is employed. The following assumptions are made in the formulation of the finite element simulation:

1) The work piece initial temperature is 30°C.

2) The heat source is moving while the work piece is fixed.

3) All thermo-physical properties for the AISI 304 stainless steel are considered to be temperature dependent.

4) A Gaussian heat flux distribution is applied to the top surface of the metal plate with a conical distribution along the thickness.

5) Free convections and radiations are applied to all external surfaces and no external loads except thermal ones are applied to the mechanical model.

During the laser welding process, many mechanisms take place in the material of the weldment. A very narrow zone under the laser beam is suddenly heated, vaporized and locally fused. After welding and cooling the melt material, assembly of the welded pieces is achieved. The heat transfer of laser beam welding can be calculated by applying heat conduction theory considering the thermal and mechanical aspects of the problem. The assumptions on this are that the dimensional changes during laser beam welding are not significant and that the mechanical work done is negligible compared to the thermal energy changes. Under a moving coordinate system o-xyz with the y-axis along the welding direction, the z-axis along the work piece thickness direction (coinciding with the laser beam centerline), and the origin o at the work piece surface, the governing equation for the heat flow through the work piece is given as:

$$\rho C_p \left[\frac{\partial T}{\partial t} + (-v_w) \frac{\partial T}{\partial y} \right] = \frac{\partial}{\partial x}\left(k \frac{\partial T}{\partial x} \right) + \frac{\partial}{\partial y}\left(k \frac{\partial T}{\partial y} \right) + \frac{\partial}{\partial z}\left(k \frac{\partial T}{\partial z} \right) + q_v(x, y, z) \quad [6.16]$$

where ρ is the density, C_p is the specific heat, v_w is the welding speed, T is the temperature, t is the time, k is the thermal conductivity and $q_v(x, y, z)$ is the volumetric heat source. During the welding process, the heat is supplied to the weld pool by the laser beam. This heat is transferred to the metal by conduction and convection. Part of this heat energy is lost by free convection and radiation. Combined convection and radiation losses are given in the model by creating a skin layer on the surface of the work piece. The heat loss is implemented into the FE code by developing a FORTRAN subroutine [ESI 07].

The natural boundary condition can be defined by:

$$k_n \frac{\partial T}{\partial n} - q + h(T - (T - T_0) + \sigma\varepsilon(T - T^4) = 0 \quad [6.17]$$

where k_n is the thermal conductivity normal to the surfaces that are subjected to radiation, convection and imposed heat fluxes; q is the prescribed heat flux; h is the heat transfer coefficient for convection; σ is the Stefan-Boltzman constant for radiation = 5.67×10^{-8} W/m^2 K^4; and ε is the emissivity. A convection coefficient of h = 25 W/m^2 K [ESI 07], and an emissivity (ε) value of 0.7 are used for stainless steel. The heat flux specified on the work piece surface is given by the incident laser beam. The initial condition for the transient analysis is

$$T(x, y, z, 0) = T_0(x, y, z) \qquad [6.18]$$

where T_0 is the initial temperature. Prior to welding the material is assumed to be at room temperature. In order to simulate the heat distribution and flow in the welding direction, the laser beam is modeled as a 3D moving heat source.

In this study a 3D conical Gaussian heat source, as shown in Figure 6.14, is used to describe the laser beam heat input. When the laser beam is directed at the metal surface, a circular molten pool forms as the heat spreads equally in all directions. When the beam starts moving, melting takes place preferentially at the leading edge, while at the trailing edge the weld metal starts solidifying. When the plate is stationary the beam is in a circular shape and gets elongated into an elliptical shape once the work piece starts moving. The elliptical shape of the weld puddle is affected by the welding speed. At slow speeds, the puddle is slightly elliptical, becoming increasingly elongated as the speed increases, finally becoming a tear-drop shape at high welding speeds. The laser energy applied to make a weld joint is dissipated by conduction, convection and radiation to the base metal, welding fixtures and the environment.

During welding, the heat affected zone (HAZ) does not undergo melting but experiences complex thermal and stress alterations. The imposition of welding thermal cycles on the base material causes changes in the properties of the HAZ. Welding is characterized by the heating rate, peak temperature and cooling rate. Peak temperature decreases rapidly with increasing distance from the weld center-line. In pure metals, melting takes place at a constant temperature by absorption of the latent heat from the heat source; however an alloy has a range of temperature during which it melts. The temperature above which the alloy is completely molten is called the liquidus temperature, and the temperature below which the alloy is completely solid is called the solidus temperature. The temperature range between these two points is called the equilibrium melting (or solidification) temperature range.

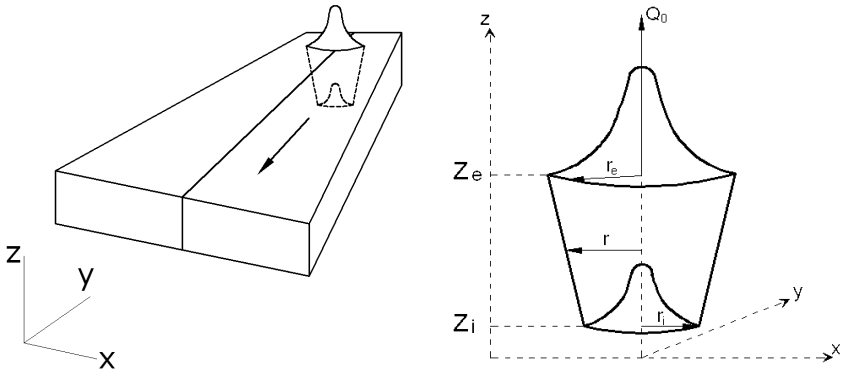

Figure 6.14. *3D conical Gaussian profile of the laser beam*

During laser welding part of the energy generated by the laser source is lost before being absorbed by the material of the work piece, approximately 30% of the nominal power of the laser source. Accordingly, the absorbed energy is considered to be 70% of the laser power [TSI 03]. The simulation of laser welding is done using a cone following the Gaussian distribution of heat flux, which can be computed according to the formula

$$Q_r = Q_0 \exp\left(\frac{-r^2}{r_0^2}\right) \qquad [6.19]$$

where r and r_0 are given as:

$$r = (x^2 + y^2)^{\frac{1}{2}}, \qquad [6.20]$$

$$r_0 = r_e - (r_e - r_i) * (z_e - z) / (z_e - z_i) \qquad [6.21]$$

where:

– Q_r is the source intensity;

– Q_0 is the maximum source intensity;

– r_e is the (x, y) parameter of Gaussian curve in the upper plane at $z = z_e$;

– r_i is the (x, y) parameter of Gaussian curve in the lower plane at $z = z_i$.

In the local reference frame of FE code SYSWELD, it is possible to define the offset of the heat source center (x_0, y_0, z_0) and the angle of the laser beam relative to z axis and oriented by the y axis (a_y). Based on the orientation of the y axis (beam angle), the source intensity Q_r is calculated and applied within the FE model using a FORTRAN subroutine [BAL 08].

Figure 6.15 shows the time history plot for successive nodes along the weld path. The temperature distributions in all the nodes have a similar trend, exhibiting constant heat input on the material. It is noted that the temperature increases as the heat source approaches the respective node and once the heat source crosses the node the temperature decreases gradually to room temperature.

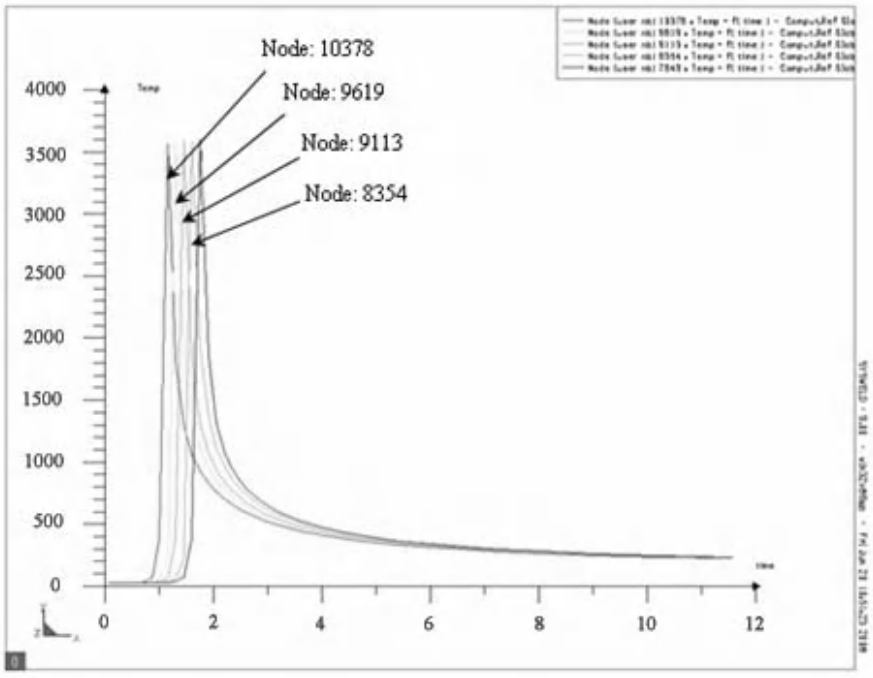

Figure 6.15. *Time history plot for successive nodes along the weld path*

The simulated shape of the butt joint is shown in Figure 6.16 for the parameter set: 1,000 W, 1,000 mm/min and 90º. The shape of the weld bead is simulated in the model by showing the regions where the temperature is above the melting point (1,450ºC) illustrated by the dark triangular area. From here the depth of penetration and bead width can be computed.

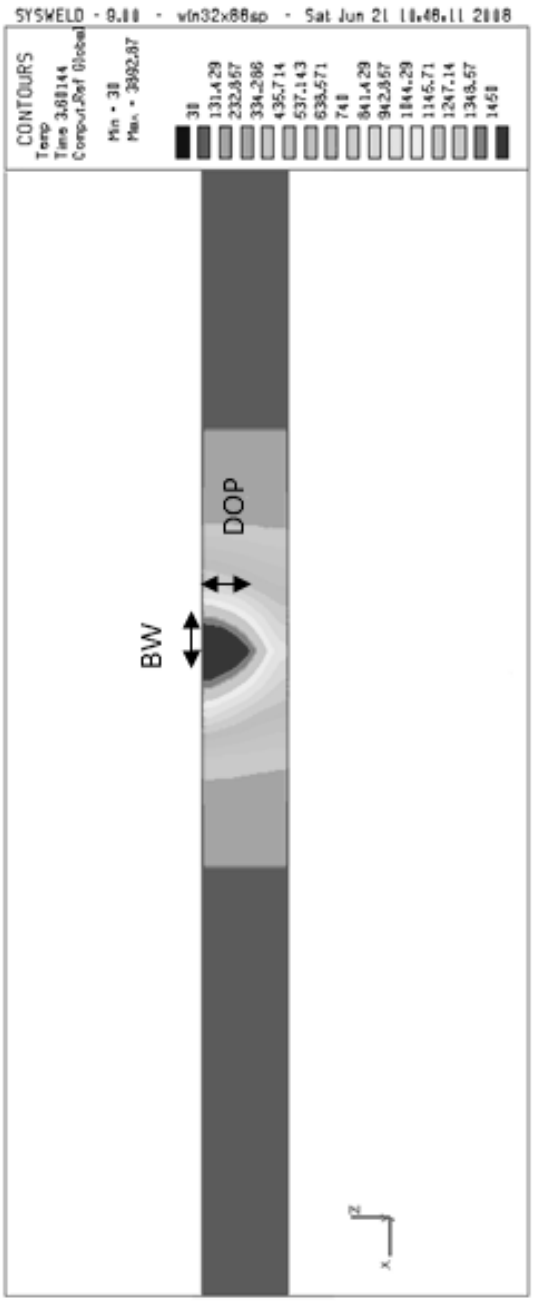

Figure 6.16. *Cross-sectional view with temperature distribution at 3.8 s of simulation of the butt joint*

Figure 6.17. *Comparison of the butt joint fusion zone: (a) measured profile and (b) FEM analysis*

Figure 6.17 shows the experimentally measured profile and the FE simulated profile for the weld bead, which are in good agreement. Although not reported for all the laser power combinations, welding speed and beam angle which have similar agreements are also obtained for the other cases.

6.11. Comparison of statistical analysis, the finite element method and an ANN

The data obtained (response) from statistical modeling, an ANN and by the FEM is compared to identify which gives the closest result to the experimental data. Figure 6.18 shows the comparison of the depth of penetration for the butt joint obtained by experimentally measured values of validation trials and various models namely mathematical modeling, ANNs and the FEM.

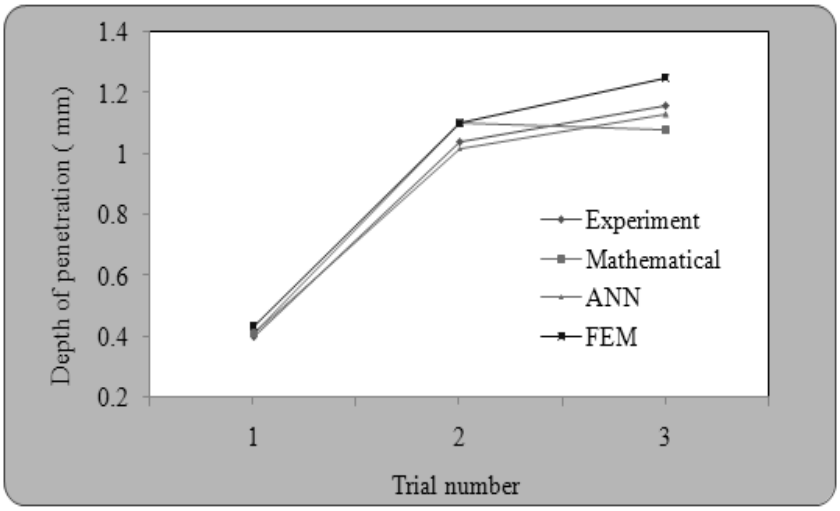

Figure 6.18. *Comparison of the depth of penetration for the butt joint*

Figure 6.19 shows the comparison of bead width versus butt joint obtained by the experimentally measured values of validation trials and various models.

Table 6.4 shows the comparison of experimentally measured values of validation trials with the data obtained mathematically and by the ANN and the FEM for the butt joint. It is observed that the percentage error is around -7.52% to 6.9% for the mathematical model, -4.93% to 2.59% for the ANN model, and -11.27% to 1.92% for the FE simulation.

Sl No	Measured		Mathematical		% error		ANN		% error		FEM		% error	
	DOP (mm)	BW (mm)	DOP (mm)	BW (mm)	DOP	BW	DOP (mm)	BW (mm)	DOP	BW	DOP (mm)	BW (mm)	DOP	BW
1	0.4	0.65	0.41	0.68	-2.5	-4.6	0.41	0.66	-2.5	-1.5	0.44	0.70	-8.7	-7.6
2	1.04	1.33	1.1	1.43	-5.7	-7.5	1.02	1.36	1.9	-2.2	1.02	1.32	1.9	0.7
3	1.16	1.42	1.08	1.45	6.9	-2.1	1.13	1.49	2.5	-4.9	1.25	1.58	-7.7	-11.2

Table 6.4. *Comparison of the experiment value with the mathematical, ANN and FEM values for the butt joint*

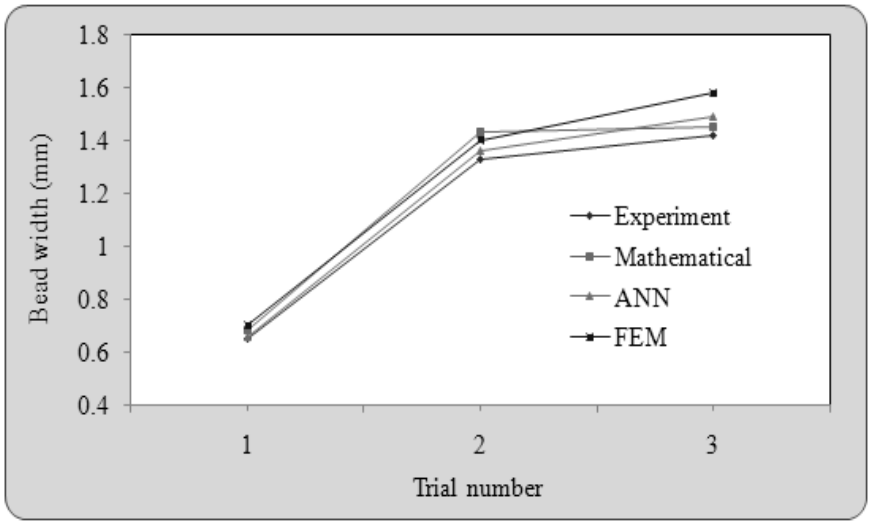

Figure 6.19. *Comparison of the bead width for the butt joint*

Comparing the results obtained by the various models showed that the neural network modeling prediction is closer to the experimental values, followed by the results obtained by regression modeling and then by FE analysis. The main advantage of neural networks is that complex nonlinear relationships can be modeled, potentially incorporating high-order interactions between predictive variables. The error that is a maximum in FEM modeling is due to more assumptions being made on the material properties and conditions.

6.12. Conclusion

Laser welding modeling can be carried out using the statistical method, artificial intelligence and the FEM. Laser welding can be used as a potential source for thin section welding. Laser welding technology is now being intensively investigated worldwide along with the development of new lasers of higher beam quality. The trend of development in lasers and welding processes with lasers or hybrid heat sources is increasing and is recognized as high technology.

Laser welding, combined with other process (hybrid welding), can be used for thicker sections to obtain more penetration in a cost effective manner. However a lot of research is required to analyze the process parameters for a variety of materials. Only limited open source materials are available regarding heat transfer and fluid flow during laser welding. There is tremendous scope for the modeling and

simulation of laser welding processes for the prediction of fluid flow and temperature analysis. The development of online monitoring systems to predict the weld bead geometry during welding will help operators to control the process during the experimentation.

Currently there is no laser available that is suitable for all processes; therefore a laser has to be selected on the basis of a good understanding of its performance and applications. Many novel research works are being undertaken worldwide in laser materials processing, online monitoring, modeling and simulation, theoretical analysis, developments of laser sources and various laser types that are being published in conference journals every year.

6.13. Acknowledgment

The Authors wish to acknowledge the following publishers Elsevier [BAL 10] and Production Engineering Institute [BAL 08], for their kind permission for reusing the texts, tables and figures from previously published material.

6.14. Bibliography

[ABD 08] ABDULKADIR C., AKIF KUTUK M., AHMET E., GUZELBEY IBRAHIM H., "Neural network modeling of arc spot welding", *Journal of Materials Processing Technology*, vol. 202, no. 1-3, pp. 137–144, 2008.

[AVA 08] AVANISH KUMAR D., VINOD YA., "Laser beam machining: a review", *International Journal of Machine Tools & Manufacture*, vol. 48, no. 6, pp. 609-628, 2008.

[BAL 05] BALDEV R., BHANU SANKARA RAO K., *Frontiers in Material Science*, University Press (India) Private Limited, India, 2005.

[BAL 08] BALASUBRAMANIAN K.R., SIVA SHANMUGAM N., BUVANASHEKARAN G., SANKARANARAYANASAMY K., "Numerical and experimental investigation of laser beam welding of AISI 304 stainless steel sheet", *Advances in Production Engineering & Management Journal*, vol. 3, no. 2, pp. 93-105, 2008.

[BAL 09] BALASUBRAMANIAN K.R., Investigations on process parameters, modeling and weld characterization for laser joining of thin section stainless steel, PhD Thesis, National Institute of Technology, Tiruchirappalli, India, 2009.

[BAL 10] BALASUBRAMANIAN K.R., BUVANASHEKARAN G., SANKARANARAYANASAMY K., "Modeling of laser beam welding of stainless steel sheet butt joint using neural networks", *CIRP Journal of Manufacturing Science and Technology*, vol. 3, no.1, pp. 80-84, 2010.

[CHA 01] CHANG W.S., NA S.J., "Prediction of laser spot weld shape by numerical analysis and neural network", *Metallurgical and Material Transactions*, vol. 32B, pp. 723-731, 2001.

[DES 08] DESIGN EXPERT SOFTWARE, V6, User's Guide, Technical Manual, Stat-Ease Inc., Minneapolis, USA. 2008.

[ESI 07] ESI GROUP, SYSWELD, Reference Manual, 2007.

[FRE 99] FREWIN M R., SCOTT D A., "Finite element model of pulsed laser welding". *Welding Journal*, vol. 78, pp. 15-22, 1999.

[KAN 08] KANTI K.M., RAO P.S., "Prediction of bead geometry in pulsed GMA welding using back propagation neural network", *Journal of Materials Processing Technology*, vol. 200, no. 1-3, pp. 300-305, 2008.

[KIM 05] KIM G.H., SEO D S., KANG K.I., "Hybrid models of neural networks and genetic algorithms for predicting preliminary cost estimates", *J. Comput. Civil Eng*., vol. 19, no. 2, pp. 208-211, 2005.

[LEE 00] LEE J.I., UM K.W., "A prediction of welding process parameters by prediction of back-bead geometry", *Journal of Material Processing Technology*, vol.108, no.1, pp. 106-113, 2000.

[LEO 03] LEONARD M., "Laser materials processing", *Laser welding, Laser Kinetics*, Mountain View, California, 2003.

[MAJ 03] MAJUMDAR J.D., MANNA I., "Laser processing of materials", *Sadhana*, vol. 28, no. 3-4, pp. 495-562, 2003.

[MAT 01] MATLAB 6.1, Help Navigator, 2001.

[MAZ 80] MAZUMDER J., STEEN W.M., "Heat transfer model for CW laser material processing", *Journal of Applied Physics*, vol. 51, no. 2, pp. 941-948, 1980.

[MON 08] MONTGOMERY D.C., *Design and Analysis of Experiments*, John Wiley & Sons, New York, 2008.

[NAS 05] NASIR A., *New Developments in Advanced Welding*, Woodhead Publishing Limited, Cambridge, UK, 2005.

[REA 97] READY J.F., *Industrial Applications of Lasers*, Academic Press, 1997.

[STE 88] STEEN W.M., DOWDEN J., DAVIS M., KAPADIA P., "A point and line source model of laser keyhole welding", *J. Phys. D: Appl. Phys*., vol. 21, no.8, pp. 1255-1260, 1988.

[STE 03] STEEN W.M., *Laser Material Processing*, Springer-Verlag Limited, London, 2003.

[TSI 03] TSIRKAS S.A., PAPANIKOS P., KERMANIDIS T.H., "Numerical simulation of the laser welding process in butt-joint specimens", *Journal of Materials Processing Technology*, vol. 134, no. 1, pp. 59-69, 2003.

[YAG 99] YAGNANARAYANA B., *Artificial Neural Networks*, Prentice-Hall, India, 1999.

Chapter 7

Lasers in Surface Engineering

After a brief introduction to laser technology, this chapter describes some lasers in surface engineering techniques, namely, laser surface cladding and laser surface treatments. The use of laser technology to create custom made surfaces is common practice in current industrial applications. It allows engineers to design surfaces with the required properties and, therefore, the efficiency of the materials can be easily improved at lower prices.

One of the industrial fields where laser technology is widely used is the coating industry for improving resistance and tribological behavior of materials, looking for lower friction coefficients and better wear performance. Coating can be carried out using the laser cladding technique, which consists of melting onto a substrate – using the energy provided by a laser beam – a coating material with the desired properties. During this process a mixture of two materials (dilution) is also produced which is of interest to maintain boundedness so that it is as small as possible but at the same time, provides a good bond between the two layers.

Other surface treatment techniques such as plasma spray and arc welding among others, have disadvantages including the presence of porosity, high thermal impact, inadequate bonding of the coating layer to the substrate and the dilution substrate-coating. Cladding's main advantage is its good behavior in all these aspects.

Laser devices can also be used to modify the profile of the surface, laser surface texturing, creating micrometric holes generated with different geometries,

---

Chapter written by Alberto H. GARRIDO, Rubén GONZÁLEZ, Modesto CADENAS, Chin-Pei WANG and Farshid SADEGHI.

Lasers in Manufacturing Edited by J. Paulo Davim

distributions and densities that act as reservoirs of lubricant that can be flowed to the interface during critical lubrication conditions. Similarly, cavities, grooves and valleys created on the surface can trap particles generated by wear, reducing abrasion. The presence of surface irregularities improves lubricant wettability facilitating the formation of lubricating oil film acting as well – at high speed and with sufficient supply of lubricant fluid – as hydrodynamic pressure traps that reduce friction unless it reaches cavitation or turbulence in the grooves.

7.1. Introduction

The laser effect is based on stimulated emission, first described in 1917 by Albert Einstein: "Light particles with energy of a specific frequency could stimulate the electrons in the atom to emit radiant energy as light of the same frequency." Forty-three years later, in 1960, T. H. Main built the first laser. It was a solid state laser that used a ruby as the active medium and was excited by a flash lamp. In 1964, K.N. Patel constructed the first CO_2 laser and in 1966 the first industrial CO_2 laser was built by the engineers for "Coherent Radiation Laboratories". In the seventies the laser began to be used in industrial environments, and is now a useful tool in many industrial, medical, military and scientific applications.

7.2. Characteristics of laser radiation

The practical use of lasers is due to its properties of monochromaticity, coherence, small divergence and emission of light in a beam of well-determined direction, possibility of high radiation, etc. This allows us to concentrate a very high energy in a small surface area.

7.2.1. *Monochromaticity*

Laser light consists of a single wavelength (actually consists of multiple wavelengths within an extremely small scale), as opposed to white light, which is a combination of all colors or wavelengths, and is thus said to be monochromatic. Each wavelength has its own unique properties. It is therefore of the utmost importance to know these characteristics, the most important being transmission through materials. The laser beam energy must be capable of heating the material to be treated and this happens if the material is capable of absorbing the laser energy, an aspect that depends largely on the wavelength of the laser.

7.2.2. *Directionality and divergence*

The directionality is the property of concentrating the entire laser light into a narrow beam that propagates in one direction. The degree of directionality is specified by the beam divergence, which in turn is given by the angle between the centerline of the divergent cone and the edge of the cone. When increasing the average power of excitation to increase the average output power, beam divergence increases. This is because the combination of the internal heat produced by the excitation and the external cooling produced by the circulation of the coolant, promotes an increase of power in the cavity (thermal lens effect). Beam divergence is enhanced with the increasing thermal lens effect in a standard laser resonator.

7.2.3. *Coherence*

It is said that a light source is coherent when all the light waves have the same frequency and phase.

Note that the laser beam is never perfectly monochromatic and not entirely coherent. However, it has a higher degree of monochrome and coherence than any light from another source.

7.3. Advantages of laser devices

The advantages of laser devices are as follows:

– One of their most distinctive is high energy intensity, which can focus on a very small area in a controlled manner.

– No contact between the work piece and the tool is required. Therefore, there is no danger of mechanical deformation of the work piece and the clamping tools are simplified, and it is only necessary to place the piece properly.

– While efficiency in the generation of the laser is around 15% in CO_2 lasers, the overall energy efficiency is greater than that achieved by traditional welding, heat treatment, etc.

– Speed of response and accuracy, which, coupled with the flexibility, allows good integration with robotics (ease of adaptation to computerized controls).

– The thermal cycle that occurs when working with a laser is capable of generating new microstructural changes in materials which modify its properties; this is a field that is undergoing a great deal of research worldwide.

– They are not affected by electromagnetic fields.

– They enable a wide range of powers and energy pulses.

Perhaps one of the main drawbacks of laser systems is their high initial investment cost in comparison with other processes. However, their depreciation may be faster, because of the advantages mentioned above.

7.4. Laser surface cladding

7.4.1. *Introduction*

One of the first citations in the scientific literature referring to laser surface coating dates back to 1966 [COQ 86], and even then the corrosion, fatigue and wear resistance properties due to this technique were already cited. From that date until today, the use of this technique has been widespread, with common use in industrial fields such as shipbuilding [BAN 83], engine manufacturing [CHA 08], turbine building [KAT 00] and tool machining [NUR 09], etc.

Therefore, the importance of this technique in current industry is without doubt, and the research efforts aimed at optimizing and spreading its use are clearly justified.

The main objective of laser cladding is to attach to a substrate, under controlled conditions, a material with different metallurgical properties. This is achieved by melting a thin layer of the substrate to produce a high resistant bond with minimal dilution of the coating material [RIA 96]. As is well known, the microstructure and chemical composition of the coating will depend on the mixing degree of both materials, which in turn is a function of the convection and diffusion processes and of the cooling rates during the liquid-solid phase change and the cooling solid-solid [KOM 90].

Excessive dilution of the coating material to the substrate is one of the problems that plagues the scientific literature [RIA 96, BAN 83], thus appearing as one of the main quality parameters of the coating. Similarly, and for obvious reasons, the presence of cracks and/or pores in the coating is also an indicator of the quality of the cladding. The absence of cracks/pores is preferred because of their high influence on the phenomena of fatigue and wear.

The highly focused interaction between the laser beam and the surface of the materials makes this surface treatment technique an interesting alternative in the development of high quality coatings, since it generates low porosity layers, with good adhesion to the substrate and with a controlled dilution substrate-coating [STE 93].

Among the different types of lasers, those most commonly used for cladding are CO_2, Nd:YAG and, currently, diode lasers.

The CO_2 laser is the most appropriate in those cases with high power, large size and relatively low precision requirements; the Nd:YAG laser has better results in low and medium powers, working on mid-size pieces with high accuracy [ZHA 08]. However the diode laser, due to its characteristics, is presented as particularly suitable for different surface treatment techniques including cladding processes, as it produces layers without or with little porosity that are excellently bonded to the substrate. Moreover, this type of laser, working in focus, develops coating tracks wider than other laser types, with low levels of dilution and less coarse metallurgical structures than that achieved with other lasers. For all these reasons, the high-power diode laser cladding is a more effective process compared to other laser techniques [BAR 03].

Particularly, the use of a diode laser on low laser absorption materials shows, due to its shorter wavelength, better performance than the CO_2 laser, creating more regular coating droplets with lower thermal impact [IWA 05]. It also shows a particular beam profile, low cost per power unit, compact design and high efficiency [BAC 04, HAA 05].

7.4.2. *Process description*

7.4.2.1. *Laser surface cladding of preplaced coatings*

This process is the simplest and most economically resourceful as it does not require auxiliary powder feeder devices. It consists of a previous preparation of the substrate surface by impregnating a layer of coating material (Figure 7.1). Generally, to keep this pre-deposited layer bonded to the substrate, a highly volatile binder is used (alcohol-based [STE 98]), so that its vaporization is easier and, thus, the presence of contaminant particles in the coating decreases. This technique provides great flexibility in selecting the chemical composition of the coating material and its position [IWA 97]. Likewise it enables the modification of cladding properties in a work piece, as it facilitates the possibility of placing layers with different alloys of materials on the substrate to be coated.

A major disadvantage of this technique is the contamination of the coating by the presence of traces of the binder used to deposit the cladding layer. This contamination yields uncertainty in the behavior of the coating, and can increase the presence of pores by the vaporization of the binder.

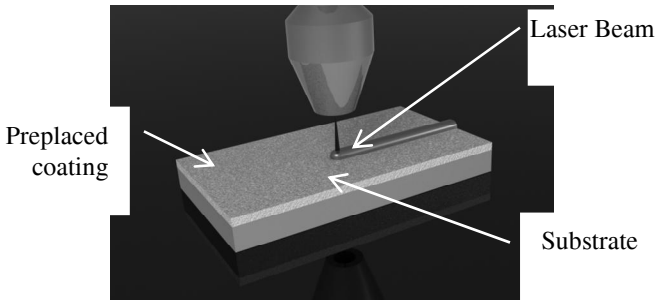

Figure 7.1. *Preplaced coating cladding*

7.4.3. *Process parameters*

Table 7.1 shows the variables involved in the process broken down into two categories: laser and manipulation of the substrate. While parameters such as wavelength, beam mode, etc., are not include as variables because they are imposed by the equipment and materials.

Laser	Material
Power	Coating material
Spot diameter	Substrate material
Velocity	Surface condition
Protection gas	
Focal length	
Power density	
Interaction time	
Specific energy	
Overlapping	

Table 7.1. *Parameters of the laser melt process*

7.4.3.1. *Power density*

The power density is a parameter that measures the power supplied per unit area, i.e. the section of the laser beam incident on the base material. The power density is influenced by the laser power and for the spot diameter.

$$D = Power/(\pi \cdot r^2) = W/cm^2 \qquad [7.1]$$

7.4.3.2. *Specific energy*

The specific energy (E) or energy density is a parameter that measures the energy input per unit area, i.e. the section of the laser beam incident on the base material. This is defined as:

$$E = Power /(d \cdot V) \qquad [7.2]$$

where d is the beam diameter in a direction perpendicular to the movement and V is the speed of relative movement between the beam and the substrate. High specific energy generates high temperature gradients and vice versa. Lasers, therefore, are not suitable for deep heat treatments, which involve high densities of energy and interaction time, as this area of the treated material would evaporate before the heat had been led to a significant depth.

In order to obtain rapid cooling and thus fine structures during laser coating, the specific energy of the process should be as low as possible. A high specific energy leads to coarse grain sizes, increased dilution and distortion. In addition, with low specific energies, the process is more economical and competitive with alternative methods.

7.4.3.3. *Velocity and interaction time*

Interaction time indicates the time that the laser beam interacts with the piece of base material thus determined by the ratio of the velocity of the laser beam over the material to be treated and the area of the beam on its surface.

If the power density remains constant, the sliding velocity of the laser beam will affect the energy received by the piece. If the sliding velocity is too high, the interaction time is too small, which results in insufficient energy transfer. However, low speeds generate greater interaction times. Similarly, high speeds generate high cooling rates, resulting in fine microstructures.

7.5. Laser surface cladding by powder injection

One of the first references in the scientific literature that refers to this technique dates back to 1987 [WEE 87]. In this one-stage technique, the powdered coating material is projected, by means of a nozzle, onto the substrate by a gas stream aimed at the point where the laser beam reaches the surface of the base material (Figures 7.2 and 7.5). The laser beam, as it hits the surface of the substrate, creates a melt pool of base material which is reached by the powder particles. These particles, projected by the carrier gas, are quickly heated as they go through the laser beam on

their way to the melt pool. Thus, the molten particles that fall into the melt pool will create the coating track. Meanwhile the particles that are not able to reach that area will just solidify over the non-melted surface of the substrate. That so, without the required dilution between coating and substrate, the particles that solidify out of the melt pool will not get the right bond with the surface.

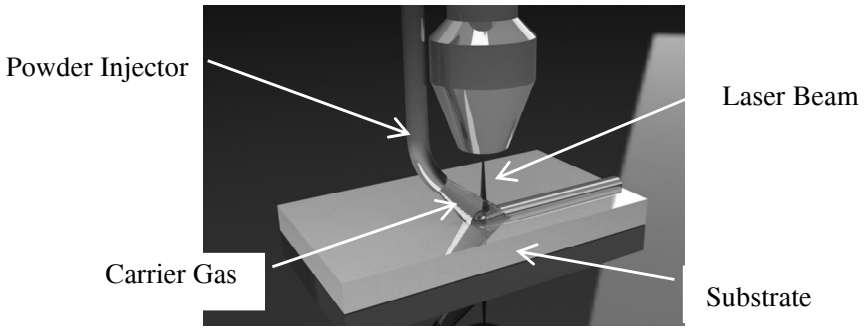

Figure 7.2. *One-stage cladding with a lateral injector*

In this process, the applied power has to be high enough to melt the powder, as it goes through the laser beam, but also low enough to not create a spread melting on the surface of the substrate [YEL 95].

When all the laser-provided energy is used in heating the powder and melting the substrate the cladding process would reach its highest efficiency (Figure 7.3), however, as some of this energy will be reflected and/or not used, the process will have to face a loss of energy.

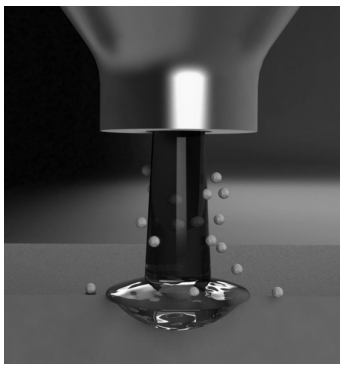

Figure 7.3. *Cladding process*

Small areas can be coated with a single track, while wider areas could require more than one track to be completely coated. In this case, an overlapping process is carried out (Figure 7.4), which leads to the repeated melting of the previously placed tracks and presents good chemical homogeneity and a consistent melt depth [MOH 92].

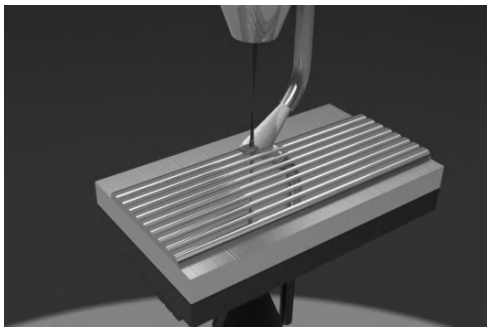

Figure 7.4. *Overlapping*

7.5.1. *Types of powder injection techniques*

7.5.1.1. *Cladding with a lateral injector*

This is the simplest one-stage technique (Figure 7.2) and, consequently, the least expensive. The arrangement of the nozzle enables the defocusing of the laser beam and, thus, the width of the cladding track can be easily modified (Figure 7.4). However this type of process modification requires a strong experimental validation of the results in order to obtain optimal defocusing for a specified track width.

On the other hand, the lateral powder injector requires that the laser beam should always be displaced in the direction of the powder's flow in order to obtain valid results. This is a remarkable disadvantage when complex geometries are required. Furthermore, the lateral injector shows a directional effect on the shape of the coating drop [STE 98] and, compared with coaxial injector, a lower efficiency in the use of the supplied powder [HU 97].

7.5.1.2. *Cladding with a coaxial injector*

The coaxial injection of the powder particles (Figure 7.5) requires a special nozzle (Figure 7.7) that creates a powder flow coaxial with the laser beam. Although it is more expensive than the lateral injection device, it has the important advantage of allowing the laser head to move in any direction, thus it can reach difficult access points which, with the lateral injector, would be impossible [HU 97].

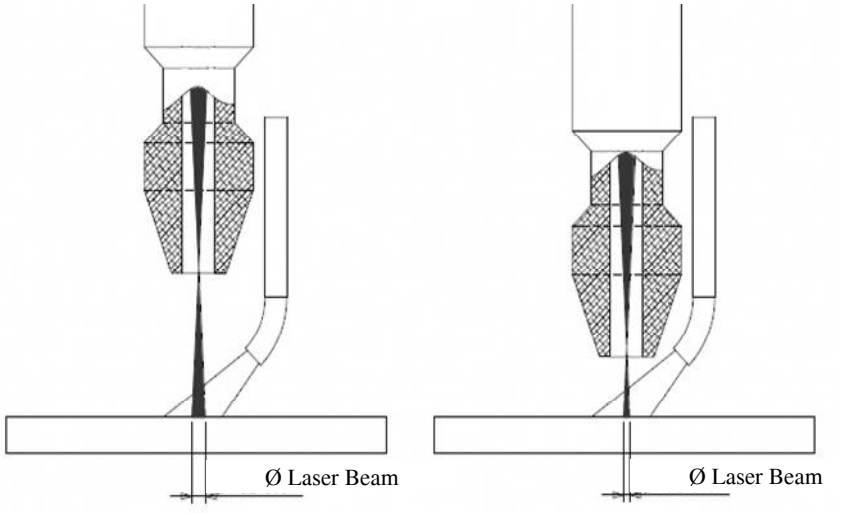

Figure 7.5. *Laser beam defocusing*

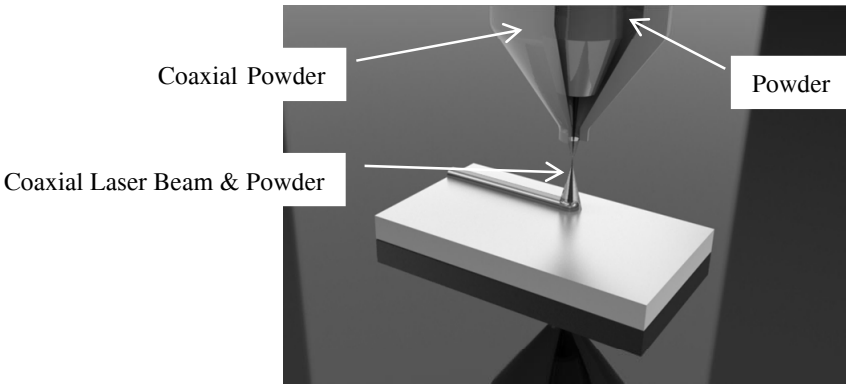

Figure 7.6. *One-stage cladding with a coaxial injector*

Unlike the lateral injector's ability to change the focal point and, in doing so vary the width of the cladding track (Figure 7.4), the main disadvantage of the coaxial injector is that displacing the laser device to change the beam's focus, means displacing the powder nozzle. Therefore, the "focus" of the powder jet will also be modified so the resulting flow could be too thick or too thin and the obtained cladding track will not obtain the required quality (Figure 7.7).

Figure 7.7. *Nozzles for coaxial powder injectors*

The coaxial injection cladding technique presents major advantages as it enables the laser cladding of complex geometries with good control of the coating thickness and dilution. Moreover, the width of the track is not a final requirement as a laser cladding used to be composed of several overlapped tracks.

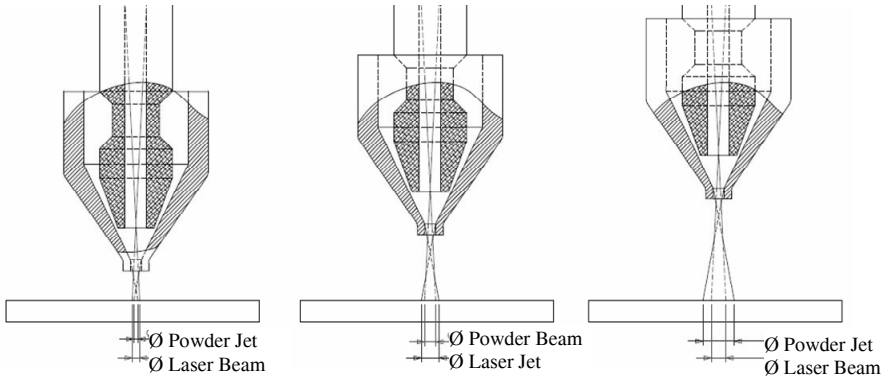

Figure 7.8. *Coaxial powder injector defocusing*

7.6. Energetic study of the cladding process

Laser cladding is a low efficiency process; among its several energy losses the thermal conductivity of the substrate should be remarked upon. This conductivity leads to a thermal energy flow towards the substrate, where it is dissipated and wasted. In spite of this, the energy loss due to the substrate's conductivity can be reduced by increasing the amount of energy supplied to the powder and decreasing the energy supplied to the substrate [PAR 06], which can be achieved by modifying,

among other parameters, the feeding speed of the substrate and the provided powder flow [PAR 05].

The low efficiency of the process can not only be explained by the aforementioned losses, but by a set of them, such as conduction, radiation, convection and reflection. Considering the heat transfer mechanisms involved in the process it can be established [GED 02a] that:

$$P_{laser} = P_u + P_l \quad [7.3]$$

where:

– P_{laser} is the laser nominal power;

– P_u is the useful power used in carrying out the coating and bonding with the substrate;

– P_l is the power loss of the process.

The useful power is used both in the melting of the powder particles (P_{mp}) and the creation of the molten substrate pool (P_{cp}), while the loss energy (P_l) can be classified according to its sources (Figure 7.9):

– P_{sr} is the power reflected by the surface;

– P_{rd} is the power lost by radiation;

– P_{pr} is the power reflected by the powder particles;

– P_{cv} is the power lost by convection;

– P_{cd} is the power lost by conduction (coating-substrate);

– P_p is the power lost by heating particles that fail to reach to the cladding area. This depends on the setup of the powder injector, both in flow and orientation.

$$P_u = P_{mp} + P_{cp} \quad [7.4]$$

$$P_l = P_{sr} + P_{rd} + P_{pr} + P_{cv} + P_{cd} + P_p \quad [7.5]$$

The improvement of the process efficiency means an increase in the energy absorption by the powder particles and a decrease in the energy absorption by the substrate, as an oversized melt pool creates a bigger thermal impact without providing any beneficial result. Decreasing the energy losses is not a realistic goal, because some of the mechanisms that generate them are necessary for the cladding process. It would be impossible to create a melt pool with a temperature lower than

that of the surrounding material and, thus, there will always be heat transfer from the molten material towards the solid material.

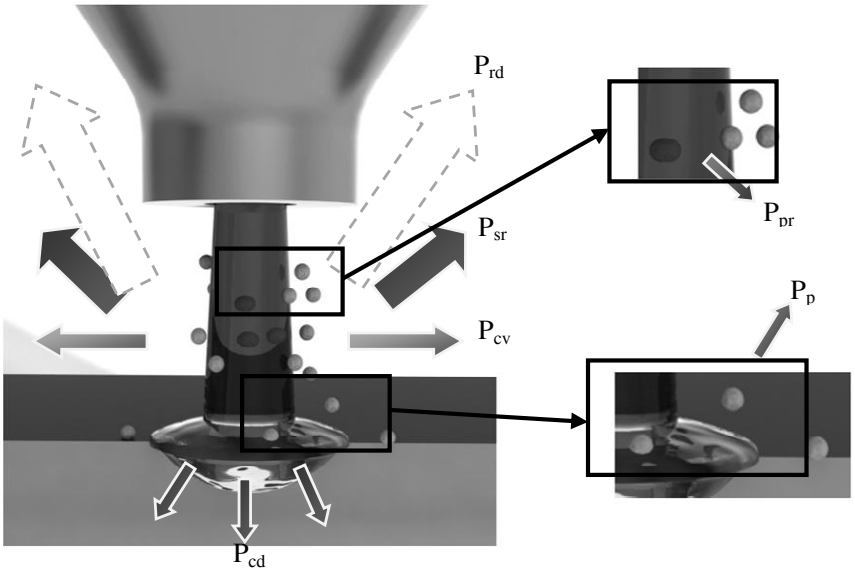

Figure 7.9. *Heat transfer mechanisms of cladding processes*

A CO_2 laser cladding process shows 40% efficiency, with the following energetic outcome [GED 02b]:

– Loss energy:

- P_{sr} =50%
- P_{rd} =1%
- P_{pr} =9%

– Useful energy:

- P_{mp} =10%
- P_{cp} =30%

Therefore, the improvement of the cladding process requires favoring of the substrate surface's energy absorption and also the powder particles' energy absorption before they reach the molten substrate. The laser beam passes through the powder cloud that comes from the nozzle on its way to the substrate area where the

melt pool is located. It is during that path nozzle-molten substrate area that the powder particles are heated and reflect off part of the received energy.

7.6.1. *Energy losses due to reflection off the surface of the cladding area*

The reflectivity of the surface increases as the heated area starts melting, as the melt pool, which is superficially flat, surrounded by inert gas (carrier and/or shielding gas) and free of oxides, shows a greater reflectivity than the solid surface [BLO 96].

The wavelength of the laser beam also influences the reflection of the material, being lower for smaller laser wavelengths [STE 98], so that a Nd:YAG laser (λ = 1.06 µm) performs better than a CO_2 laser (λ = 10.6 µm) in terms of reducing reflection losses. As these losses reach even 50% of the energy emitted by the laser device, their reduction is most interesting as it increases the efficiency of the cladding process.

Diode lasers have wavelengths ranging between 0.4 and 0.8 µm, thus presenting a better behavior for reflection losses. Thus, the diode laser is presented as the best option in order to decrease the losses that have the most influence on the low overall efficiency of the cladding process.

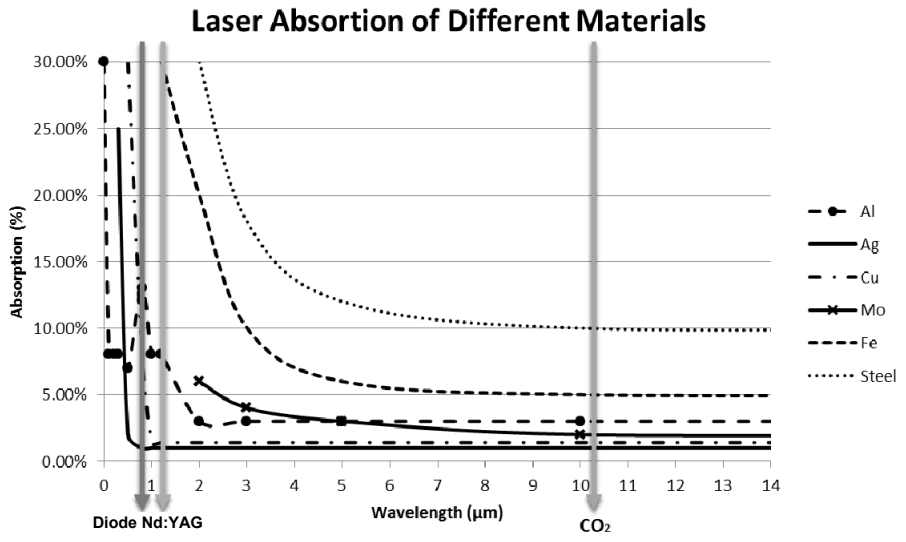

Figure 7.10. *Laser absorption of different materials*

7.6.2. *Energy losses due to radiation*

The radiation losses generated during the cladding process can be determined by studying the spectral emittance (radiant energy per time, area and wavelength units), of a black body (M_{cn}), at a certain temperature (T). Using Planck's Law:

$$M_{\lambda cm}(T)\,d\lambda = \frac{2\pi hc^2}{\lambda^5}\frac{1}{e^{\frac{hc}{\lambda k_B T}}-1}\,d\lambda \qquad [7.6]$$

where:

– h is Planck's constant, h=6.62·10-34 J·s;

– c is the speed of light, c=3×10^8 m/s;

– k_B is Boltzmann's constant, k_B=1.3806503×10^{-23} J/K

– λ is the wavelength.

By integrating Planck's Law for all wavelengths, the Stefan–Boltzmann Law is obtained:

$$M_{cn}(T) = \sigma \cdot T^4 \qquad [7.7]$$

where σ is Stephan-Boltzmann's constant, σ=5.6693×10^{-8} $W\cdot m^{-2}\cdot K^{-4}$.

For a material that does not entirely absorb or emit radiation, the spectral emittance is obtained by multiplying the black body's emittance by the spectral emissivity (ε_λ), which generally depends on the frequency and the temperature:

$$\varepsilon_\lambda = \varepsilon_\lambda(\lambda, T) \le 1 \qquad [7.8]$$

Those bodies in which the emissivity does not depend on the wavelength are called gray bodies:

$$\varepsilon_\lambda(\lambda, T) = \varepsilon_\lambda(T) \qquad [7.9]$$

That so, for a gray body:

$$M\lambda(\lambda, T) = \varepsilon_\lambda(\lambda, T)\cdot M_{\lambda cm}(\lambda, T) \qquad [7.10]$$

$$M_{\lambda}\left(\lambda,T\right)=\varepsilon\left(\lambda,T\right)\cdot\sigma\cdot T^{4} \quad [7.11]$$

Stephan–Boltzmann's law states that the emitted radiation is proportional to the fourth power of the absolute temperature of the material, therefore the higher the temperature of the body the greater the radiation energy transfer:

$$P_{rad}=k\cdot T^{4} \quad [7.12]$$

$$P_{rad}=\sigma\cdot A\cdot T^{4} \quad [7.13]$$

where:

– σ is the Stephan–Boltzmann constant, σ=5.6693·10-8 W·m-2·K-4;

– T is the surface temperature of the melt pool [K];

– A is the surface area of the melt pool [m2].

7.6.3. *Energy losses due to convection*

The energy losses due to convection phenomenon can also be calculated from the equations that describe that heat transfer mechanism:

$$\dot{q}=h\cdot\left(T-T_{\infty}\right) \quad [7.14]$$

$$Q=h\cdot A\cdot\left(T-T_{\infty}\right) \quad [7.15]$$

where:

– h is the heat transfer coefficient, h=100 W/m^{2}K [PRE 95];

– A is the surface area [m^2];

– T is the surface temperature [K];

– T_{∞} is the carrier and/or shielding gas temperature [K].

It must be remarked that the heat transfer mechanism is a forced convection as the powder feeding and area protection require gas streams.

7.6.4. *Energy used in creating and bonding the coating*

During the cladding process several layers are created, each of them with different compositions and characteristics. At the deepest region, a heat affected zone (HAZ) can be found which is made up of the substrate material but is modified by the laser energy. Close to this zone, is located the area where the laser energy melts the substrate and, over it, a region where an alloy, composed of the substrate and coating material (dilution), solidifies. Finally, the coating zone is located in the upper layer; it is metallurgically bonded to the substrate and composed of the molten powder (Figure 7.11).

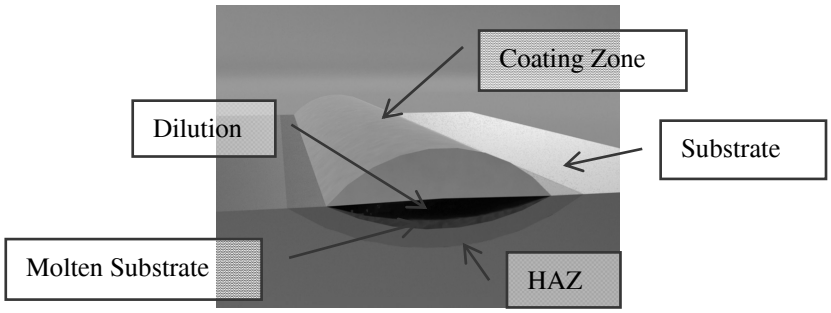

Figure 7.11. *Cladding regions*

The coating material melting process can be divided into two stages.

a) Increase of the material's temperature until the melting point:

$$P_{\Delta T} = A \cdot v \cdot \rho \cdot C_p \cdot \Delta T \qquad [7.16]$$

where:

– A is the molten section area [m^2];

– v is the scanning speed [m/s];

– ρ is the material's density [g/m^3];

– C_p is the specific heat [$J/(g \cdot K)$];

– ΔT is the temperature increase [K].

b) Absorption of thermal energy to change phase from a solid to a liquid:

$$P_{sol-liq} = A \cdot v \cdot \rho \cdot H_f \qquad [7.17]$$

where H_f is the latent heat [J/g].

Taking into account both stages of the melting process:

$$P_u = A \cdot v \cdot \rho \cdot \left(C_p \cdot \Delta T + H_f \right) \qquad [7.18]$$

According to the relationship between the useful energy and the obtained melting, it is obvious that lasers that reduce the reflectivity of the substrate require a more critical power setup in order to avoid an oversized molten area in the substrate.

As the melt pool is surrounded by a shielding inert gas and it is free of oxides, reducing its reflectivity is not easy. Nevertheless it is much easier to increase the power absorption by the powder particles just by increasing their average diameter, always within the limits that allow a proper coating to be carried out.

An important conclusion [GED 02a] is that the amount of energy absorbed in heating the substrate does not vary with the output power, as it is determined by the amount of energy that the substrate needs to absorb before it starts melting. Thus any increase in absorbed energy becomes available energy for the melting process.

7.7. Control parameters of laser surface cladding

Both, the melting of the injected powder and of the substrate's surface, are functions of the energy supplied by the laser beam and turned into temperature. It is desirable to obtain a uniform distribution of the temperature as this process contributes to obtaining a more homogeneous cladding layer and more constant properties throughout the coating. Obviously, an important factor in the transformation of the energy supplied to the material in temperature will be its absorptivity, which depends in turn, and for a given material, on the type of laser used. Thus, materials with lower absorptivity require shorter wavelengths.

Consequently, one of the first variables to be considered will be the energy provided by the laser device as well as the capacity, according to its wavelength, of energy absorption/diffraction of the material.

In particular cases, chemical reactions can also affect the results, as in the case of aluminum and iron interactions, where aluminothermic reactions can increase the amount of energy present in the surface treatment – not by modifying the absorption of radiation but by increasing the energy of the reaction [HUA 08].

The particle size of the coating powder has a great influence on its energy absorptivity, the smaller the particles, the easier it is to melt them. Thus, the mean size of the powder particles becomes another influential factor in laser cladding.

The laser cladding process is usually controlled by three different parameters: the power of the laser beam, the scanning speed of the device and the powder feeding rate [OLI 05]. However, many other parameters are involved, as during the laser process several phenomena occur: mass and heat transfer, fluid mechanics, phase changes, etc. With such a high number of parameters controlling the process, it is common practice to group them according to relations [OLI 05] and/or to maintain some of them as constant, making statistical study and the evaluation of their influence on the final results of the laser cladding process possible.

We should also consider the need to use different gases during the laser running and the powder feeding; as it is necessary to take into account the flows of shielding, auxiliary and carrying gases, as well as the powder feeding rate used during the process.

The deposition of the powder into the melt pool is a function of its mass flow, but also of the scanning speed of the device, which jointly moves the injector and the laser beam. Thus, a lower speed of the device will correspond to a greater energy input per unit area, producing variations in the thermal impact of the substrate, in the formation of the melt pool and in the heating of the powder particles which are sent out at the substrate.

As a result, as the input variables are set:

1) P is the laser device power [kW];

2) S is the scanning speed [mm/min];

3) M is the powder mass flow [g/min];

4) G_s is the shielding gas flow [l/min];

5) G_a is the auxiliary gas flow [l/min];

6) G_c is the carrying gas flow [l/min].

To determine the quality of the resulting coating, a set of output parameters must be stated, thus its study will enable isolation of the effects of the input variables on

the results. Consequently, the features to be observed should include the width, height and penetration of each cladding track [XIO 07], the area of its cross-section, the dilution, and, according to its working behavior, the presence of cracks and/or pores.

As a result, as the output variables are set:

1) W is the track width [mm];

2) H is the track height [mm];

3) D is the dilution [%];

4) A is the area of the cross section [mm^2];

5) P_{por} is the presence of pores [%];

6) P_{cr} is the presence of cracks [%].

7.8. Widely used materials and alloys

According to the required properties of the coating, different types of cladding materials can be considered [ERD 05, VIN 080]:

– Impact resistance: lowly alloyed ferrous coatings (< 12% Cr alloy, C, Si+Ni, Mn, W, Mo, V).

– Corrosion and erosion resistance: highly alloyed ferrous coatings (< 50% Cr, Mn, Mo, alloy C+Ni, Co, B, W, V).

– High hardness at high temperatures: coatings of nickel base alloys (5÷25 Ni+Cr, 2÷4%, 5% Si+C, B).

– Oxidation and corrosion resistance: cobalt based alloys coatings (Co+Cr, 4÷15% 20÷35% W, 0, 8÷2, 5% C+Si, Ni, Fe).

– Abrasion resistance: oxide-based ceramic material coatings (Al_2O_3, Cr_2O_3, ZrO_2, TiO_2, SiO_2, etc.), carbides (WC, Cr_2, C_3, SiC, etc.), nitrides, borides and cermets (metal or alloy + ceramic WC-Co, CrC-NiCr, etc.).

7.9. Laser surface treatments

7.9.1. *Introduction*

The laser has some remarkable properties for surface treatment. The electromagnetic radiation of a laser beam is absorbed by the first atom layers in

opaque materials (such as metals), and there are no associated expulsions of hot gases, swirl flows or even radiation reflected outside the optically-defined area of the beam. In fact, energy can be precisely stimulated in the surface only where needed.

7.9.2. *Laser hardening*

Improving the wear resistance of a material could be one of the reasons for considering laser hardening, but it also enhances the fatigue and impact resistance as a result of residual stresses introduced into the surface. The tenacity of the base metal is maintained, while a hard layer on the surface is carried out. In this process, the laser beam comes into contact with the material while it moves over the surface heating it without reaching the melting point.

The depth of hardening is directly proportional to the power of the laser and inversely proportional to the scanning speed; however, its dependence on the diameter of the focus is more complex.

7.9.3. *Laser surface melting*

In this type of treatment, the surface is melted by the laser beam in an inert gas environment. The aims of this process are the homogenization of the material, the refinement of its microstructure, the generation of rapid solidification structures and the sealing of surfaces.

The obtained result is controlled by the proper uses of power, speed and spot diameter parameters.

7.9.4. *Laser surface texturing*

7.9.4.1. *Process description*

The laser surface texturing (LST) process consists of achieving micrometric pockets with different shapes, surface distributions and densities. The main function of these dimples is to act as lubricant reservoirs, retaining the lubricant fluid so it can be supplied to the contact area if needed during starving lubrications regimes. Moreover, the micro-pockets can work as wear debris retainers decreasing the abrasion of contact areas.

The presence of surface irregularities (Figure 7.12) improves the wettability of the material, favoring the formation of the lubricant film. Furthermore, at high

speeds and with a sufficient supply of a fluid lubricant, it can also increase the hydrodynamic pressure and, therefore, friction losses can be reduced provided that cavitation and turbulence at the pockets are avoided.

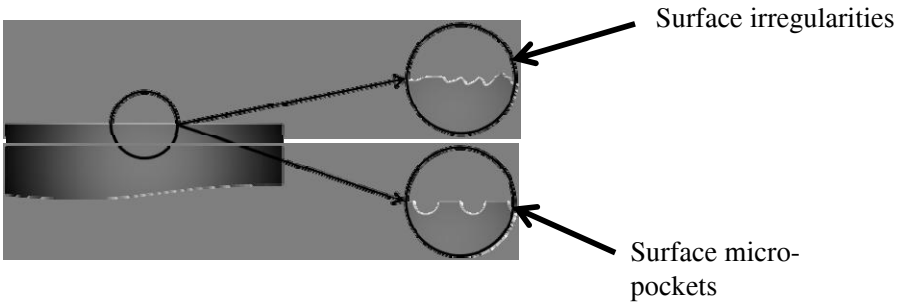

Figure 7.12. *Surface irregularities and micro-pockets*

7.9.4.2. *Surface texturing techniques*

The surface texturing process has been widely studied and different texturing techniques have been stated, all of which have their advantages and disadvantages. It should be noted that most of them have been developed for a specific industrial sector, as a result, and thus it cannot be said that there is a single texturing technique that fits all industrial processes. On the other hand, it can be stated that an industrial process can have one or more texturing techniques that fit it.

Surface texturing has been a common approach to enhance tribological performance over the past 20 years. It can provide two lubrication mechanisms: a) to generate an additional pressure to separate two mating surfaces under fully flooded conditions; b) to provide additional lubricant under starved conditions. Surface texturing can be performed using the following techniques: vibrorolling, grinding, waterjet, electrical discharge machining (EDM), shot peening, the LIGA process, the laser multi-layer process, and laser surface texturing (LST).

Vibrorolling: is the plastic deformation of the layers below the surface of the specimen (Figure 7.13) by applying a high loaded hard tool (ball or rounded diamond). This technique generates a series of surface grooves with a configurable, but difficult to modify, path. It is thus an economical process but is restricted to a limited number of available surface geometries [VOL 02].

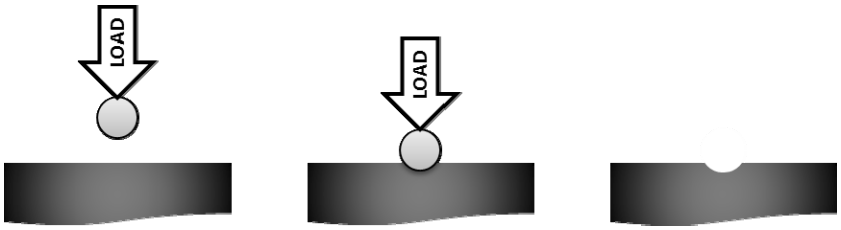

Figure 7.13. *Vibrorolling*

In grinding, profiled rollers are used to generate tracks consistent with the shape of the roller (Figure 7.14) by printing on the surface under load. Different roller profiles generate different textured surfaces. This technique is economical but not very flexible. The change of the texturing patterns requires the replacement of engraved rollers [STE 07].

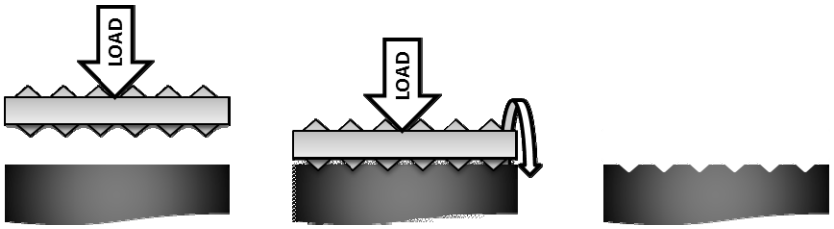

Figure 7.14. *Grinding*

Waterjet is an alteration of the surface geometry, compatible with texturing. It is generated by the incision of a stream of high pressure water mixed with abrasive particles, although the result is more like a blasting than controlled diameter and depth texturing (Figure 7.15). It is a method of low thermal stress but with little or no control over the geometry of the dimples [ARO 02].

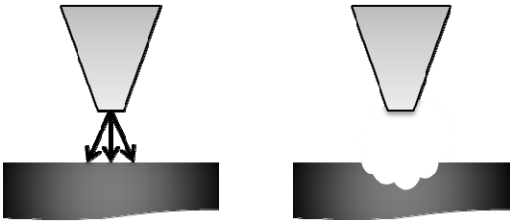

Figure 7.15. *Waterjet*

In electrical discharge machining (EDM) micro-cavities are generated by using electro-erosion of the surface of the specimen (Figure 7.16). The specimen is immersed in a solution, which is a major constraint in the performance of the process. The generation of projections is also remarkable as they alter the surface roughness of the work piece [GUU 07].

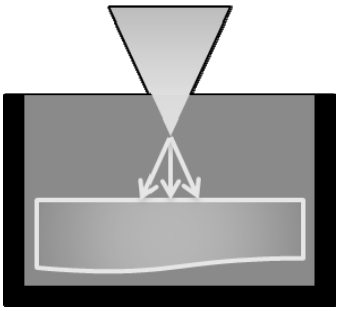

Figure 7.16. *Electrical discharge machining*

In shot peening the round glass, ceramic or metallic particles are shot at the target surface to create plastic deformations. The process is simple and inexpensive with interesting changes in the surface properties (surface roughness, geometric stress concentration factor and cold work) [MYL 11]. However, the patterns are irregular and difficult to control. During the process, the particles may be introduced into the work piece.

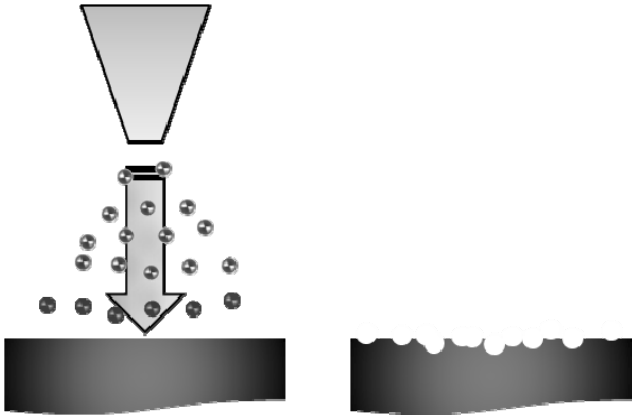

Figure 7.17. *Shot peening*

The LIGA process is broadly applied to fabricate the microstructures of MEM developments. It can perform high quality features, and the surface roughness is simply achieved at less than 10 nanometers. A large field of textures with a high depth-width ratio can be manufactured. Since a fine surface quality results in less surface roughness effects, the experiments can be easily compared to numerical studies [STE 04].

In the laser multi-layer process a laser textured mask with a uniform thickness is attached to a base with a shear-resistant thin-film adhesive, as shown in Figure 7.17. This manufacturing process is able to create dimples with a uniform depth and with a clean and smooth profile. A high depth-width ratio and complex shape are simply generated without a high cost. This approach has been applied to study the lubrication mechanism in the transition between fully flooded and starved conditions [STE 04].

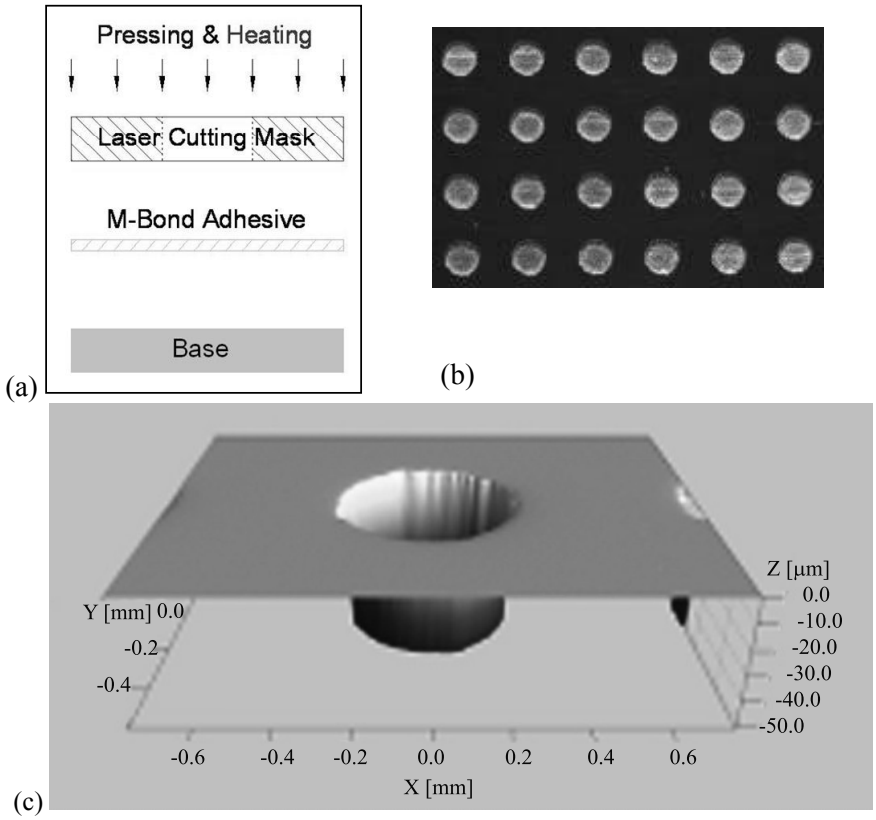

Figure 7.18. *Laser multi-layer process: (a) fabrication; and (b) and (c) textured specimen*

In laser surface texturing (LST) the generation of laser micro-holes can be regulated by different phenomena, each presenting different results. The search for one formation mechanism or another depends on the desired results in terms of shape, depth, and profile. The most common input parameters of a laser texturing process typically include: power, time, spot diameter, defocusing, frequency, impulse profile and the number of shots.

The wavelength of the laser beam is not considered as it usually depends on the nature of the device. When the realization of micro-drill is done with a single pulse, the shot frequency does not influence the results. The laser frequency does influence the results because the energy absorption of the material depends on it, with higher performances of shorter wavelengths in those materials having a lower coefficient of energy absorption.

The large number of parameters of a laser device that can modify the energy and energy density incident on the surface generates a large number of combinations for obtaining the desired results. If we add the possibility of programming impulse profiles the combinations are almost infinite as each set of parameters can be studied with all kinds of profiles: step, constant, linear, and so on. LST has been widely used to enhance the lubrication performance in industry, such as in magnetic storage devices [ZHO 03, KOM 03], mechanical seals [ETS 97], piston rings [RYK 06, RYK 02, BOL 05], thrust bearings and scroll compressors [VAI 09].

7.10. Laser surface texturing techniques

Laser surface texturing is widely used as a surface treatment to improve friction behavior [HIG 11a] both in industrial and scientific fields. It is currently used in enhancing the performance of internal combustion engines [ETS 09, BOR 08, RYK 06], biomechanical applications [FAS 09, GÖT 04], manufacturing processes [KAW 09, WAG 08] and in a wide range of different uses.

The laser generation of micro-pockets can be regulated by different phenomena, each of them achieving different results. Thus, according to the required results, in terms of shape, depth, profile, etc., different kinds of LST will be carried out with different kinds of process control mechanisms.

7.10.1. *Melting*

As the first of the LST mechanisms, melting is the simplest and easiest to achieve because it does not involve removing material. It can be fast and economic without necessarily requiring a post-surface treatment. Melting occurs when the

incidence of the laser beam on the surface only generates a melt area that will quickly solidify so that there will be no modification of the balance of material mass; instead it will be of the surface profile (Figure 7.19). As the shape of the melt and solidified area depends on the behavior of the melt pool, more particularly on the gradient of surface tension γ against temperature T [DU 05], the surface profile of the melt area can be predicted.

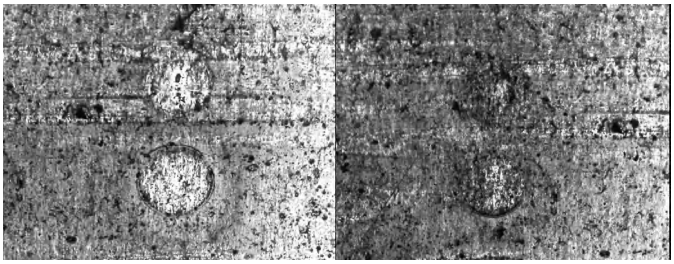

Figure 7.19. *Nd:YAG laser surface melting*

Since in pure metals and alloys, the surface tension generally decreases with the increase in temperature, the gradient $d\gamma/dT$ is negative in most of those materials. However the presence of sulfur significantly changes the surface tension of the solvent and its presence can even reverse the trend of the variation of γ with T and turn the gradient $d\gamma/dT$ into a positive value. These factors affect the flows in the melt, where the surface material moves towards areas of higher surface tension.

Hence, the shape of the melt depends on the behavior of the material's surface tension. As the temperature profile remains the same, the variation of the surface tension behavior involves a different surface tension profile and, as a result, a different mass flow. Thus, in the case of a negative gradient $d\gamma/dT$ the surface profile presents a valley-shaped profile, while in the opposite case the profile shows a hat-like profile (Figure 7.20).

Figure 7.20. *Different surface profiles (valley, left; hat, right)*

7.10.2. *Vaporization*

The sudden vaporization of surface material requires a high energy density applied for a short time, i.e. the laser device uses short pulses with relatively high energy peaks. However, the main factor to be taken into account is the energy level used, while the pulse duration remains at a second level of importance [IAN 98]. Therefore to increase the rate of vaporized material, raising energy is more efficient than increasing the pulse duration [HIG 11b].

7.10.3. *Melting and vaporization:*

Laser texturing processes involve the modification of the surface of the material by removing material under the action of a laser beam. As this beam hits the surface a thin layer of material melts (Figure 7.21) and, if the energy is high enough, it is then vaporized generating a vapor jet (Figure 7.22) that leaves the surface. This ejected jet creates a recoil pressure that pushes the liquid material in the melt pool toward its perimeter [SOV 07].

Figure 7.21. *Simulation of the initial melting of the surface*

The surface of the molten metal layer quickly reaches the vaporization temperature, generating a stream of metal vapor escaping from the surface, while creating a recoil pressure that deforms the molten surface, forwarding the liquid metal to the edge of the micro-pocket.

During this stage the melt pool temperature remains constant at the vaporization temperature, using the remaining energy to carry out the phase change.

Figure 7.22. *Simulation of the recoil pressure*

The presence of this rim (Figure 7.23) usually requires a surface grinding stage after the texturing process. In some cases the rim shape resembles the valley effect created by melting spots on materials with a negative gradient $d\gamma/dT$, so that, if that is the required shape, no further treatment is needed.

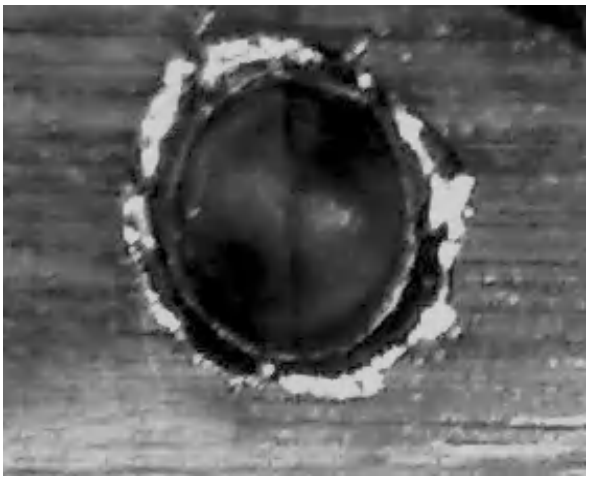

Figure 7.23. *The rim due to the recoil pressure*

7.10.4. *Melting and gas injection*

An interesting LST technique is to melt a surface volume of the material and subsequently remove it by the action of an inert gas jet stream. Its interest lies in the advantage of requiring less energy input with a lower thermal impact on the material. On the other hand, it has the drawback of projecting drops of molten material onto the surface of the work piece which solidify both on the surface and inside adjacent micro-pockets.

In those cases where this LST process is carried out, its prime objective is to ensure the complete removal of molten material before it solidifies in or outside the micro-pocket (Figure 7.24). To achieve this goal, an auxiliary inert gas jet stream is required; in fact the pitch of the nozzle is critical to obtain the right result [LAL 00].

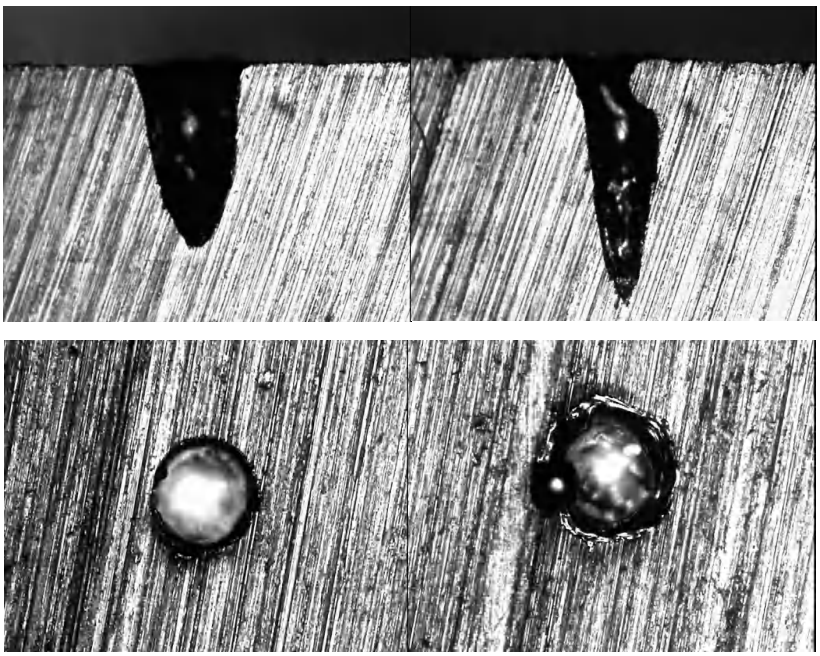

Figure 7.24. *Right (left) and wrong (right) air-assisted molten material removal*

When texturing is carried out at low energy levels, the surface melting of the affected material is controlled by convection and thermocapillarity phenomena [SIM 05], whereas at high energy levels the material can suddenly vaporize [YE 02] together with the presence of the molten material.

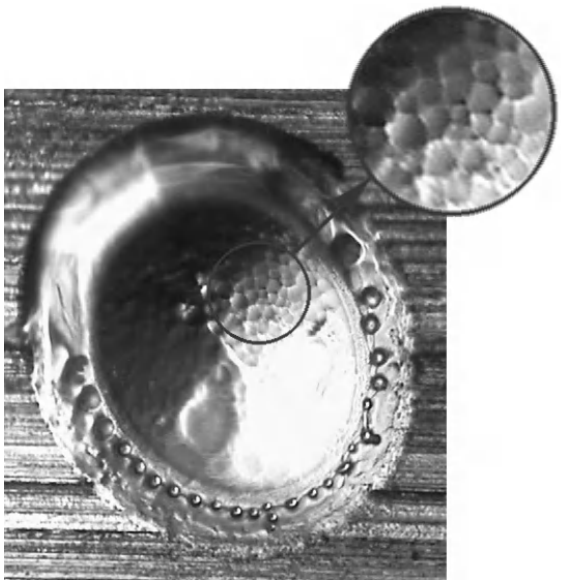

Figure 7.25. *Marangoni's cells*

The Marangoni convection phenomena – for which characteristic cells can be observed in the LST micro-pocket carried out with a CO_2 laser device and shown in Figure 7.25 – are due to a thermal gradient generated in the melt pool by the incidence of the laser beam (Figure 7.26). Therefore a thermal flow appears in the molten material (Figure 7.27).

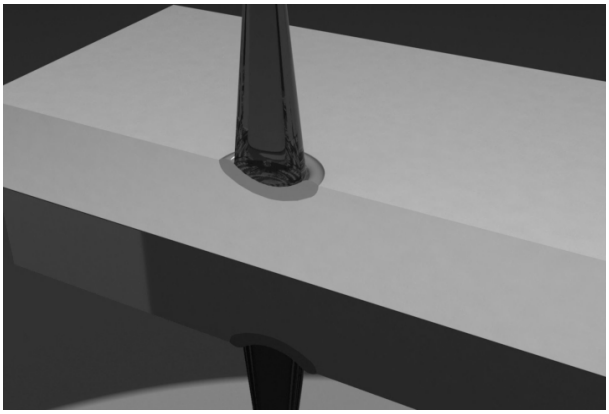

Figure 7.26. *Simulation of the laser beam incidence*

This thermal gradient generates a density differential between the upper areas of the melt pool and the lower areas. This difference creates the mass flow (Figure 7.28) which regulates the mass transfer and movement in the melt pool.

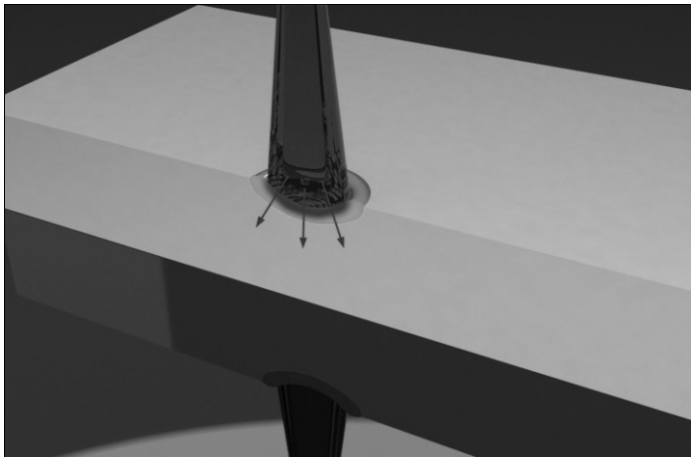

Figure 7.27. *Thermal flow*

Another factor that controls the mass flow during laser texturing is the thermocapillarity [KIM 08], which is produced by the changes of the surface tension due to the fluctuations of the melt pool's temperature [DU 05].

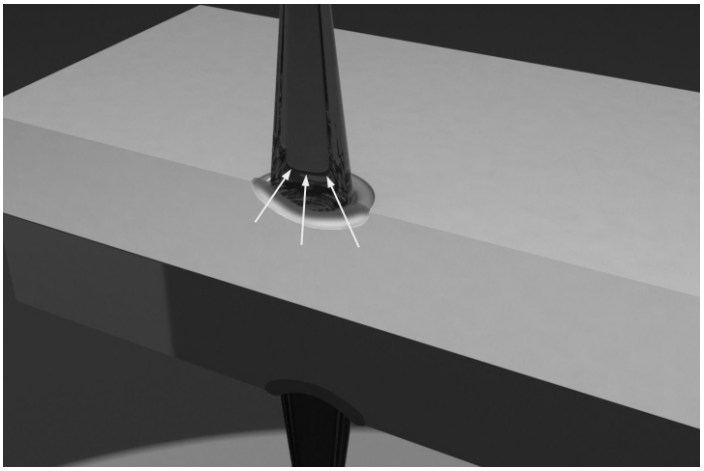

Figure 7.28. *Mass flow*

When the laser beam hits the surface of the material and melts it, the temperature at and near the laser spot increases, thus the surface tension is modified (usually it decreases as temperature raises), which in turn generates a shear force on the surface of the melt pool that creates mass and thermal flow [LON 99].

As was already mentioned, in those cases where high energy density is applied the material can suddenly vaporize creating a rim on the surface of the material and surrounding the micro-pocket. This vaporization also creates a mass flow in the melt pool to move the molten material toward the edge of the dimple [SOV 07].

The three mechanisms mentioned tend to form a rim around the micro-pocket (Figure 7.29) that most authors subsequently corrected, either by laser polishing [VIN 08] or mechanical polishing [ZUM 09, ZUM 07].

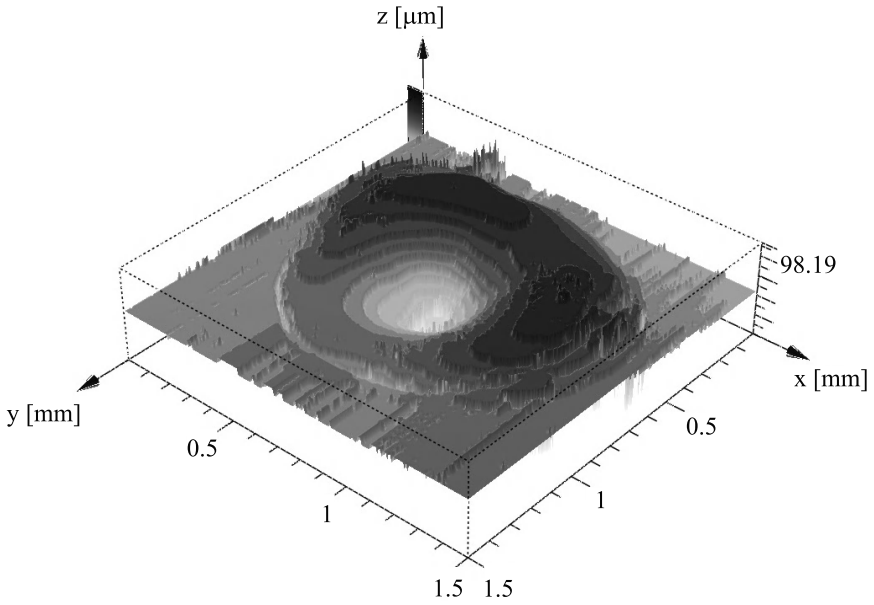

Figure 7.29. *Confocal microscopy of a micro-pocket*

7.10.5. *Process parameters*

The most common control parameters of a laser texturing process usually include: power, pulse duration, spot diameter, defocusing, pulse frequency, pulse profile and the number of pulses (Figure 7.30). For practical purposes the laser

beam's wavelength is not considered to be a parameter as it depends on the laser device.

When the micro-pocket is performed with a single pulse, the pulse frequency, of course, does not affect the results. Not so the laser frequency, which, as was already mentioned, modifies the material absorption of the laser energy, with better behavior for shorter wavelength laser devices on those materials with lower energy absorption coefficients.

The large number of available parameters that modifiy the energy and the energy density supplied to the surface turns into a large number of possible combinations to achieve the required micro-pocket. If the capacity of chosing different pulse profiles is added, the number of pulse combinations is almost endless, as each set of parameters could be studied with all kinds of profiles: step, constant, linear, etc. (Figure 7.31).

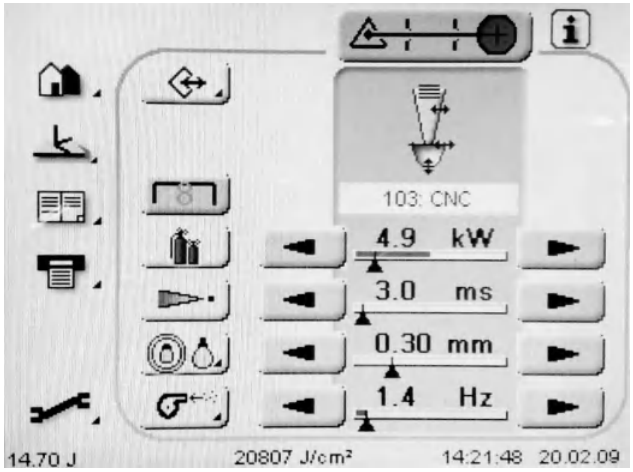

Figure 7.30. *Control parameters of a Nd:YAG laser device*

In those cases where only the surface melting is required to modify the surface profile, lower energies and shorter pulse durations should be used to minimize the material vaporization. In contrast, if the sudden vaporization of the material is the goal of the laser surface texturing process, higher energies and short pulse durations should be programmed.

The possibility of modifying the pulse profile (Figure 7.31) becomes another important and very powerful control parameter. The modification of the peak values, their location in time, the use of different steps, the pulse duration, etc., generate

different results for the same energy level. That is, by changing the pulse profile the peak power, and its location in time, can be modified without altering the total supplied energy.

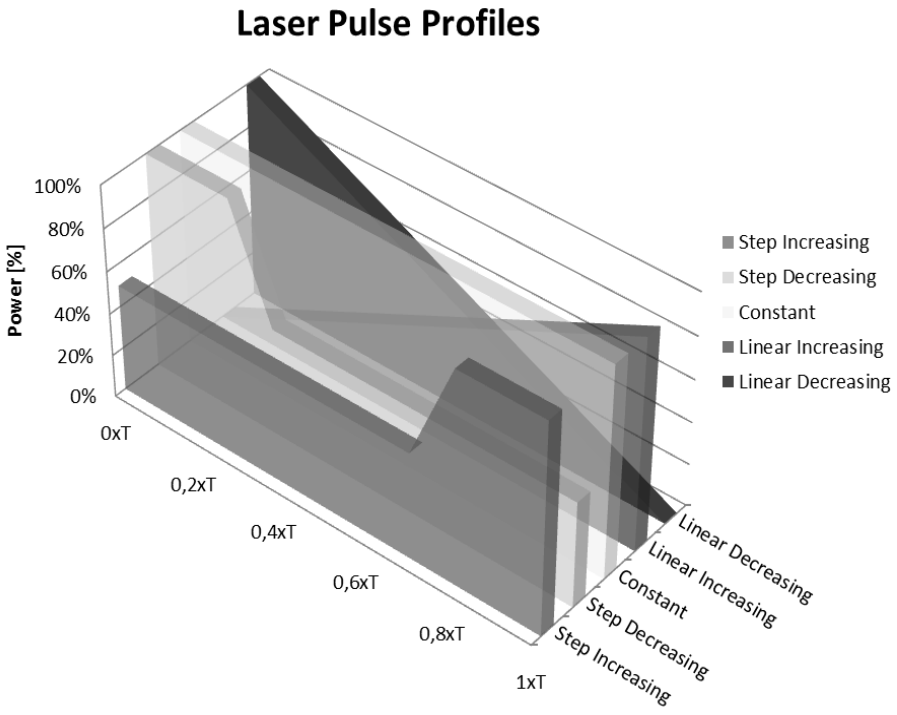

Figure 7.31. *Pulse profiles*

By programming different pulse profiles (Figure 7.32) the LST control mechanism can be chosen, generating a molten material volume before its vaporization, programming a high energy peak to reach sudden vaporization with low previous melting, etc.

The increase in the instantaneous energy density, for a given pulse energy, reduces the phenomenon of vaporization during the rapid melting and solidification of the material [DU 05].

According to the required results the power peak can move forward or backward in the time duration of the pulse, favoring the re-melting of the micro-pocket area, in the first case, and increasing the vaporization in the second case.

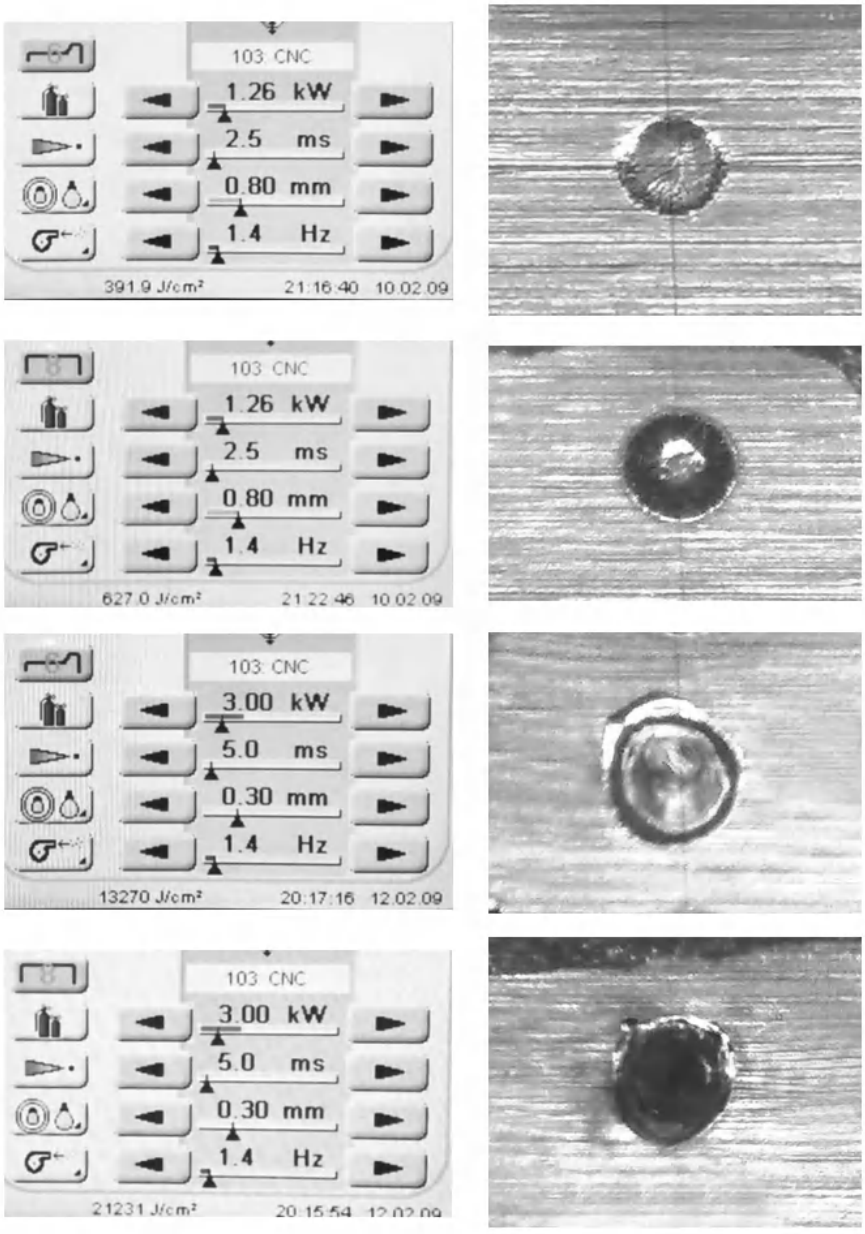

Figure 7.32. *Control parameters and the obtained micro-pockets*

The defocusing of the laser beam also modifies the generation of the melt pool and/or the vaporization of the material, so that a very small defocusing favors vaporization, although if it is too big, it can lead to a failed melting of the material.

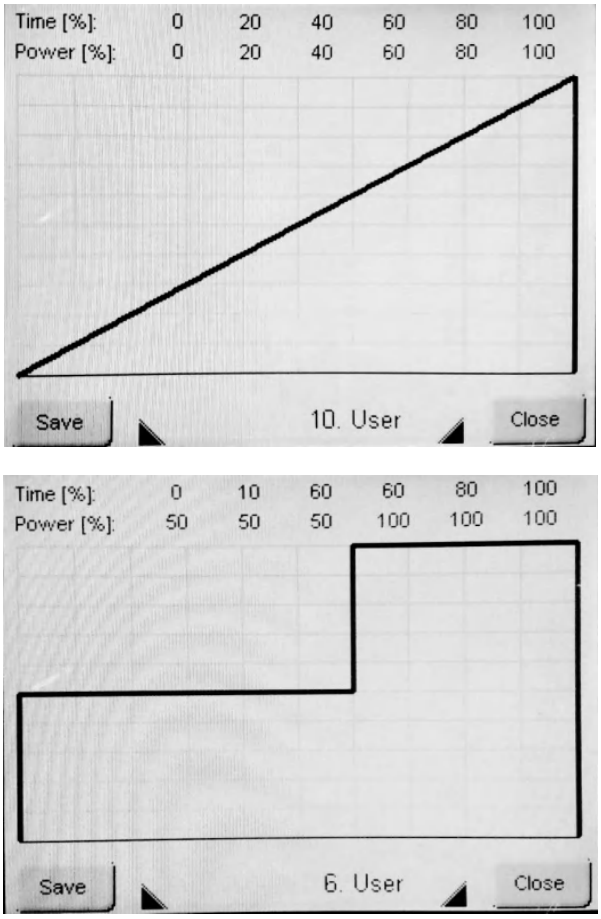

Figure 7.33. *Different pulse profiles*

The values of the control parameters have to be set according to the desired effect on the material's surface (Figure 7.34). Note that those values are different if what is expected is sudden vaporization, melting, melting and vaporization, vaporization and re-melting, etc.

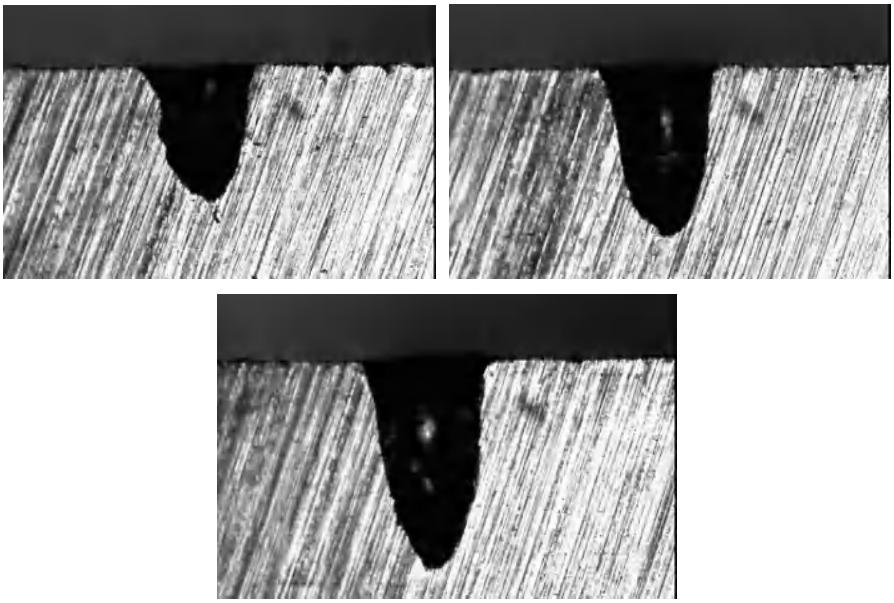

Figure 7.34. *Different effects on micro-pocket formation*

Taking into account all the refereed parameters it can be stated that a LST process should at least include the following input variables:

– P: laser power [kW];

– D: spot diameter [mm];

– t: pulse duration [ms];

– P_P: pulse profile;

– G_a: auxiliary gas flow.

However, those variables can be changed or removed according to the considered effect, i.e. if just a surface melting is carried out, the auxiliary gas flow is no longer required.

Frequency of the pulse has not been considered as it produces a very similar effect to the one obtained by increasing the power (it changes the micro-pocket's diameter and depth) [VIL 09] and therefore is not considered as a relevant variable [DU 05].

7.11. Characterization of laser surface texturing

7.11.1. *Geometry*

To study the results of a LST process, most of the authors consider geometric and surface distribution factors. In those cases where the laser device is used as a machining tool, the shapes of the micro-pocket are almost endless. However the most common shapes would be circular, semicircular, ellipsoidal, semi-ellipsoidal, triangular, hexagonal and trapezoidal.

In the simplest case, the micro-pocket is carried out with a single laser shot, subsequently, the obtained shape is circular (Figure 7.35). Thus, the following factors are considered as characteristic parameters of the dimple [VIN 08]:

– O: micro-pocket's diameter [μm];

– D: micro-pocket's depth [μm].

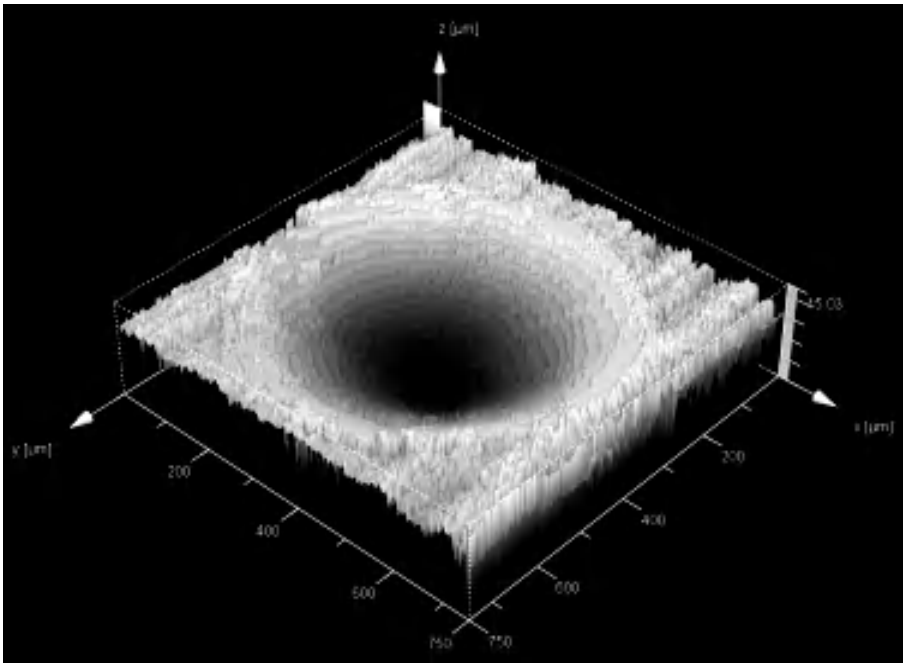

Figure 7.35. *Characterization of micro-pockets*

Sometimes, these two parameters can be handled as a single parameter because a D/O ratio can be established. It has to be remarked upon that D/O ratios greater than 0.5 do not substantially modify the LST behavior [WAN 11, WAN 09].

7.11.2. *Density*

Once each micro-pocket is rightly defined, its distribution on the material's surface needs to be established. Generally this is done by obtaining the texturing density (ρ) that represents the percentage of textured area against the total area.

$$A_{micro-pocket} = \pi \cdot \frac{\phi^2}{4} \quad [7.19]$$

$$A = L^2 \quad [7.20]$$

$$\rho = \frac{A_{micro-pocket}}{A} \cdot 100 = \frac{\pi \cdot \phi^2}{4 \cdot L^2} \cdot 100$$

where:

– $A_{micro\text{-}pocket}$ is the micro-pocket's area;

– A is the total surface area;

– $\emptyset$ is the micro-pocket's diameter;

In tribology applications, it currently cannot be stated that there is an optimum value of density that works for all cases. In addition, Vilhena [VIL 09] establishes a practical range of texturing densities from 6.7% up to 26.8%, while Li [LI 10] considers a range from 1.8% up to 11.2%. However other authors [HIG 11a] study the relation of the texturing density according to the contact area, stating that the LST process has to take into account the size of the contact area.

7.12. Bibliography

[ARO 02] AROLA D., MCCAIN M.L., KUNAPORN S., RAMULU M., "Waterjet and abrasive waterjet surface treatment of titanium: a comparison of surface texture and residual stress", *Wear*, vol. 249, pp. 943-950, 2002.

[BAC 04] BACHMANN F., RATH W., AUERBACH V., "High power diode lasers for hardening and cladding applications", *Haerterei-Technische Mitteilungen*, vol. 59, no. 3, pp. 217-223, 2004.

[BAN 83] BANAS C., "Lasers effective for attaching Cu-Ni Cladding to ship steel", *Welding and Metal Fabrication*, vol. 51, no. 6, pp. 297-299, 1983.

[BAR 03] BARNES S., TIMMS N., BRYDEN B., PASHBY I., "High power diode laser cladding", *Journal of Materials Processing Technology*, vol. 138, no. 1-3, pp. 411-416, 2003.

[BLO 96] BLOEHS W., GRÜNENWALD B., DAUSINGER F., HÜGEL H., "Recent progress in laser surface treatment: I. Implications of laser wavelength", *Journal of Laser Applications*, vol. 8, no. 1, pp. 15-23, 1996.

[BOL 05] BOLANDER N.W., SADEGHI F., GERBER G.R., "Piston ring friction reduction through surface modification", *Proceedings of the 2005 Fall Technical Conference of the ASME Internal Combustion Engine Division*, ASME, New York, pp. 663-671, 2005.

[BOR 08] BORGHI A., GUALTIERI E., MARCHETTO D., MORETTI L., VALERI S., "Tribological effects of surface texturing on nitriding steel for high-performance engine applications", *Wear*, vol. 265, pp. 1046-1051, 2008.

[CHA 08] CHANG S.-S., WU H.-C., CHEN C., "Impact wear resistance of stellite 6 hardfaced valve seats with laser cladding", *Materials and Manufacturing Processes*, vol. 23, no. 7, pp. 708-713, 2008.

[COQ 86] COQUERELLE G., COLLIN M., FACHINETTI J.L., "Laser cladding and alloying", *Proceedings of the 3rd International Conference on Lasers in Manufacturing*, pp. 197, IFS Ltd, Los Angeles, CA, 1986.

[DEO 05] DE OLIVEIRA U., OCELIK V., DE HOSSON J.TH.M., "Analysis of coaxial laser cladding processing conditions", *Surface and Coatings Technology*, vol. 197, pp. 127-136, 2005.

[DU 05] DU D., HE Y.F., SUI B., XIONG L.J., ZHANG H., "Laser texturing of rollers by pulsed Nd-YAG laser", *Journal of Materials Processing Technology*, vol. 161, pp. 456-461, 2005.

[ERD 05] ERDEMIR A., "Review of engineered tribological interfaces for improved boundary lubrication", *Tribology International*, vol. 38, pp. 249-256, 2005.

[ETS 97] ETSION I., HALPERIN G., GREENBERG Y., "Increasing mechanical seal life with laser-textured seal faces", *15th International Conference on Fluid Sealing BHR Group*, pp. 3-11, 1997.

[ETS 09] ETSION, I., SHER, E., "Improving fuel efficiency with laser surface textured piston rings", *Tribology International*, vol. 42, pp. 542-547, 2009.

[FAS 09] FASASI A.Y., MWENIFUMBO S., RAHBAR N., CHEN J., LI M., BEYE A.C., ARNOLD C.B., SOBOYEJO W.O., "Nano-second UV laser processed micro-grooves on Ti6Al4V for biomedical applications", *Materials Science and Engineering*, vol. 29, pp. 5-13, 2009.

[GED 02a] GEDDA H., POWELL J., WAHLSTRÖM G., LI W.-B., ENGSTRÖM H., MAGNUSSON C., "Energy redistribution during CO_2 laser cladding", *Journal of Laser Applications*, vol. 14, no. 2, pp. 78-82, 2002.

[GED 02b] GEDDA H., POWELL J., KAPLAN A., "A process efficiency comparison of Nd:YAG and CO_2 laser cladding", *Welding in the World, Le Soudage Dans Le Monde*, vol. 46, pp. 75-86, 2002.

[GÖT 04] GÖTZ H.E., MÜLLER M., EMMEL A., HOLZWARTH U., ERBEN R.G., STANGL R., "Effect of surface finish on the osseointegration of laser-treated titanium alloy implants", *Biomaterials*, vol. 25, pp. 4057-4064, 2004.

[GUU 07] GUU Y.H., HOU M.T.-K., "Effect of machining parameters on surface textures in EDM of Fe-Mn-Al alloy", *Materials Science and Engineering A*, vol. 466, pp. 61-67, 2007.

[HAA 05] HAAKE J.M., ZEDIKER M.S., "Heat treating and cladding operations with high-power diode lasers", *Proceedings of SPIE – The International Society for Optical Engineering*, pp. 76-86, 2005.

[HAE 00] HAEFKE H., GERBIG Y., DUMITRU G., ROMANO V., "Microtexturing of functional surfaces for improving their tribological performance", *Proceedings of the International Tribology Conference*, pp. 217-221, 2000.

[HIG 11a] HIGUERA GARRIDO A., GONZÁLEZ R., CADENAS M., HERNÁNDEZ BATTEZ A., "Tribological behavior of laser-textured NiCrBSi coatings", *Wear*, vol. 271, pp. 925-933, 2011.

[HIG 11b] HIGUERA GARRIDO A., GONZÁLEZ R., CADENAS M., VIESCA J.L., "NiCrBSi coatings textured by Nd-YAG laser", *Int. J. Surface Science and Engineering*, vol. 5, pp. 75-97, 2011.

[HU 97] HU Y.P., CHEN C.W., MUKHERJEE K., "Analysis of powder feeding systems on the quality of laser cladding", *Advances in Powder Metallurgy and Particulate Materials*, vol. 3, pp. 21.17-21.31, 1997.

[HUA 08] HUANG K., LIN X., XIE C., YUE T.M., "Microstructure and wear behaviour of laser-induced thermite reaction Al_2O_3 ceramic coatings on pure aluminum and AA7075 aluminum alloy", *Journal Wuhan University of Technology, Materials Science Edition*, vol. 23, no. 1, pp. 89-94, 2008.

[IWA 97] IWAMOTO H., SUMIKAWA T., NISHIDA K., NISHIDA M., ARAKI T., "The formation of NiCrAlY cladding with preplaced method", *Yosetsu Gakkai Ronbunshu/Quarterly Journal of the Japan Welding Society*, vol. 15, no. 2, pp. 267-271, 1997.

[IWA 05] IWATANI S., OGATA Y., UENISHI K., KOBAYASHI K.F., TSUBOI A., "Diode laser cladding on a5052 aluminium alloy for wear resistant", *Proceedings of the ASME Summer Heat Transfer Conference*, pp. 295-301, 2005.

[KAT 00] KATHURIA Y., "Some aspects of laser surface cladding in the turbine industry", *Surface and Coatings Technology*, vol. 132, no. 2-3, pp. 262-269, 2000.

[KAW 09] KAWASEGI N., SUGIMORI H., MORIMOTO H., MORITA N., HORI I., "Development of cutting tools with microscale and nanoscale textures to improve frictional behavior", *Precision Engineering*, vol. 33, pp. 248-254, 2009.

[KIM 08] KIM Y.-D., KIM W.-S., "A numerical analysis of heat and fluid flow with a deformable curved free surface in a laser melting process", *International Journal of Heat and Fluid Flow*, vol. 29, pp. 1481-1493, 2008.

[KOM 90] KOMVOPOULOS K., NAGARATHNAM K., "Processing and characterization of laser-cladded coating materials", *Journal of Engineering Materials and Technology, Transactions of the ASME*, vol. 112, no. 2, pp. 131-143, 1990.

[KOM 03] KOMVOPOULOS K., "Adhesion and friction forces in microelectromechanical systems: mechanisms, measurement, surface modification techniques, and adhesion theory", *J. Adhes. Sci. Technol.*, vol. 17, no. 4, pp. 477-517, 2003.

[LAL 00] LALLEMAND G., JACROT G., CICALA E., GREVEY D.F., "Grooving by Nd:YAG laser treatment", *Journal of Materials Processing Technology*, vol. 99, pp. 32-37, 2000.

[LI 10] LI J., XIONG D., DAI J., HUANG Z., TYAGI R., "Effect of surface laser texture on friction properties of nickel-based composite", *Tribology International*, vol. 43, pp. 1193-1199, 2010.

[LON 99] LONGTIN J.P., HIJIKATA K., OGAWA K., "Laser-induced surface-tension-driven flows in liquids", *International Journal of Heat and Mass Transfer*, vol. 42, pp. 85-93, 1999.

[MYL 11] MYLONAS G.I., LABEAS G., "Numerical modelling of shot peening process and corresponding products: residual stress, surface roughness and cold work prediction", *Surface and Coatings Technology*, vol. 205, pp. 4480-4494, 2011.

[NUR 09] NURMINEN J., NÄKKI J., VUORISTO P., "Microstructure and properties of hard and wear resistant MMC coatings deposited by laser cladding", *International Journal of Refractory Metals and Hard Materials*, vol. 27, no. 2, pp. 472-478, 2009.

[PAR 05] PARTES K., SEEFELD T., SEPOLD G., VOLLERTSEN F., "High efficiency laser cladding at elevated processing speed", *24th International Congress on Applications of Lasers and Electro-Optics, ICALEO 2005 – Congress Proceedings*, pp. 621-628, 2005.

[PAR 06] PARTES K., SEEFELD T., SEPOLD G., VOLLERTSEN F., "Increased efficiency in laser cladding by optimization of beam intensity and travel speed", *Proceedings of SPIE - The International Society for Optical Engineering*, vol. 6157, no. 615700, 2006.

[PRE 95] PRESCOTT P.J., JACOBS H.R., SEYED-YAGOOBI J., PULKOWSKI J., GRIGOROPOULOS C.P., MOON T.J., LAVINE A.S., OOSTHUIZEN P.H., BAYAZITOGLU Y., "Transport phenomena in materials processing", *American Society of Mechanical Engineers, Heat Transfer Division*, vol. 317-2, pp. 321, 1995.

[RIA 96] RIABKINA-FISHMAN M., ZAHAVI J., "Laser alloying and cladding for improving surface properties", *Applied Surface Science*, vol. 106, pp. 263-267, 1996.

[RYK 02] RYK G., Klingerman Y., Etsion I., "Experimental Investigation of Laser Surface Texturing for Reciprocating Automotive Components", *Tribology Transactions*, vol. 45, pp. 444-449, 2002.

[RYK 06] RYK G., Etsion I., "Testing piston rings with partial laser surface texturing for friction reduction", *Wear*, vol. 261, pp. 792-796, 2006.

[SIM 05] SIM B.-C., KIM W.-S., "Melting and dynamic-surface deformation in laser surface heating", *International Journal of Heat and Mass Transfer*, vol. 48, pp. 1137-1144, 2005.

[SOV 07] SOVEJA A., JOUVARD J.M., GREVEY D., "Metal surface laser texturing: multiphysics modelling of a single impact effect", *Proceedings of the COMSOL Users Conference*, 2007.

[STE 93] STEEN W.M., WATKINS K.G., "Coating by laser surface treatment", *Journal de Physique IV*, vol. 3, 1993.

[STE 98] STEEN W.M., *Laser Material Processing*, Springer, 1998.

[STE 04] STEPHENS L.S., SIRIPURAM R., HAYDEN M., MCCARTT B., "Deterministic micro asperities on bearings and seals using a modified liga process", *Journal of Engineering for Gas Turbines and Power*, vol. 126, pp. 147- 154, 2004.

[STE 07] STEPIEN P., "Grinding forces in regular surface texture generation", *International Journal of Machine Tools & Manufacture*, vol. 47, pp. 2098-2110, 2007.

[TUE 98] TUERSLEY I.P., HOULT T.P., PASHBY I.R., "Nd-YAG laser machining of SiC fibre/borosilicate glass composites. Part I. Optimisation of laser pulse parameters", *Composites Part A: Applied Science and Manufacturing*, vol. 29, pp. 947-954, 1998.

[VAI 09] VAIDYA A., SADEGHI F. "Experimental investigation of orbiting thrust bearing using wide and shallow circular pockets", *ASHRAE Transactions*, vol. 115, no. 2, pp. 668-675, 2009.

[VIL 09] VILHENA L.M., SEDLACEK M., PODGORNIK B., VIZINTIN J., BABNIK A., MOZINA J., "Surface texturing by pulsed Nd:YAG laser", *Tribology International*, vol. 42, pp. 1496-1504, 2009.

[VIN 08] VINCENT C., MONTEIL G., BARRIERE T., GELIN J.C., "Control of the quality of laser surface texturing", *Microsystem Technologies*, vol. 14, pp. 1553-1557, 2008.

[VOL 02] VOLCHOK A., HALPERIN G., ETSION I., "The effect of surface regular microtopography on fretting fatigue life", *Wear*, vol. 253, pp. 509-515, 2002.

[WAG 08] WAGNER K., VÖLKL R., ENGEL U., "Tool life enhancement in cold forging by locally optimized surfaces", *Journal of Materials Processing Technology*, vol. 201, pp. 2-8, 2008.

[WAN 09] WANG C., SADEGHI F., WERELEY S.T., CHUNG H., "Investigation of fluid flow out of a microcavity using Mpiv", *STLE Tribology Transactions*, vol. 52, pp. 817-832, 2009.

[WAN 11] WANG C., SADEGHI F., WERELEY S.T., RATEICK R.G. JR., SCOT R., "Experimental investigation of lubricant extraction from a micropocket", *STLE Tribology Transactions*, vol. 54, no. 3, pp. 404-416, 2011.

[WEB 96] WEBBER T., "Laser material processing", in WEBBER, T. (ed.), *Laser Weld Overlay*, Taylor & Francis Inc. and Marcel Dekker Inc., 1996.

[WEE 87] WEERASINGHE V.M., STEEN W.M., "Laser cladding with pneumatic powder delivery", *Applied Laser Tooling*, pp. 183-211, 1987.

[XIO 07] XIONG Z., ZENG X., "Morphology and quality control of laser cladding layers using low order mode CO_2 laser", *Journal of Huazhong University of Science and Technology*, vol. 35, no. 1, pp. 147-149, 2007.

[YE 02] YE X.-H., CHEN X., "Importance of Marangoni convection in laser full-penetration welding", *Chinese Physics Letters*, vol. 19, pp. 788-790, 2002.

[YEL 95] YELLUP J., "Laser cladding using the powder blowing technique", *Surface and Coatings Technology*, vol. 71, no. 2, pp. 121-128, 1995.

[ZHA 08] ZHANG A.-F., ZHU G.-X., ZHOU Z.-M., LU B.-H., "Comparison of cladding characteristics on CO_2 laser, Nd: YAG laser and excimer laser", *Heat Treatment of Metals*, vol. 33, no. 6, pp. 14-18, 2008.

[ZHO 03] ZHOU L., KATO K., VURENS, TALKE F.E., "The effect of slider surface texture on flyability and lubricant migration under near contact conditions", *Tribology International*, vol. 36, no. 4-6, pp. 269-277, 2003.

[ZUM 07] ZUM GAHR K.H., MATHIEU M., BRYLKA B., "Friction control by surface engineering of ceramic sliding pairs in water", *Wear*, vol. 263, pp. 920-929, 2007.

[ZUM 09] ZUM GAHR K.-H., WAHL R., WAUTHIER K., "Experimental study of the effect of microtexturing on oil lubricated ceramic/steel friction pairs", *Wear*, vol. 267, pp. 1241-1251, 2009.

List of Authors

Syed S. AKHTAR
Mechanical Engineering Department
King Fahd University of Petroleum and Minerals
Dhahran
Saudi Arabia

Esther T. AKINLABI
Department of Mechanical Engineering Science
University of Johannesburg
South Africa

Stephen A. AKINLABI
Department of Mechanical Engineering Science
University of Johannesburg
South Africa

Karuppudaiyar R. BALASUBRAMANIAN
Department of Mechanical Engineering
National Institute of Technology
Tiruchirappalli
India

Denise BELLISARIO
Department of Mechanical Engineering
University of Rome Tor Vergata
Italy

Pankaj BHARGAVA
Raja Ramanna Centre for Advanced Technology.
Indore
India

Lasers in Manufacturing Edited by J. Paulo Davim

Gangusami N. BUVANASHEKARAN
Laser Materials Processing Division
Welding Research Institute, BHEL
Tiruchirappalli
India

Modesto CADENAS
Mechanical Engineering Department
University of Oviedo
Gijon
Spain

J. Paulo DAVIM
Department of Mechanical Engineering
University of Aveiro
Portugal

Alberto H. GARRIDO
Mechanical Engineering Department
University of Oviedo
Gijon
Spain

Rubén GONZÁLEZ
Mechanical Engineering Department
University of Oviedo
Gijon
Spain

Omer KELES
Mechanical Engineering Department
Gazi University
Turkey

Lalit M. KUKREJA
Raja Ramanna Centre for Advanced Technology
Indore
India

Atul KUMAR
Raja Ramanna Centre for Advanced Technology
Indore
India

Tshilidzi MARWALA
Faculty of Engineering and Built Environment
University of Johannesburg
South Africa

Christ P. PAUL
Raja Ramanna Centre for Advanced Technology
Indore
India

Ayukt K. PATHAK
Raja Ramanna Centre for Advanced Technology
Indore
India

Fabrizio QUADRINI
Department of Mechanical Engineering
University of Rome Tor Vergata
Italy

Farshid SADEGHI
Mechanical Engineering Department
University of Purdue
West Lafayette
USA

Krishnasamy SANKARANARAYANASAMY
Department of Mechanical Engineering
National Institute of Technology
Tiruchirappalli
India

Loredana SANTO
Department of Mechanical Engineering
University of Rome Tor Vergata
Italy

Mohammad SHEIKH
School of Mechanical, Aerospace and Civil Engineering
The University of Manchester
UK

Mukul SHUKLA
Department of Mechanical Engineering Technology
University of Johannesburg
Johannesburg
South Africa
and
Mechanical Engineering Department
Motilal Nehru National Institute of Technology
Allahabad
India

Erica A. SQUEO
Department of Mechanical Engineering
University of Rome Tor Vergata
Italy

Maturose SUCHATAWAT
School of Mechanical, Aerospace and Civil Engineering
The University of Manchester
UK

Chin-Pei WANG
University of Purdue
West Lafayette
USA

Bekir S. YILBAS
Mechanical Engineering Department
King Fahd University of Petroleum and Minerals
Dhahran
Saudi Arabia

Index

Lasers in Manufacturing Edited by J. Paulo Davim

H

I

L

M

N, O

P